Interaction between aerosols and convective boundary-layer dynamics over land

Eduardo Wilde Barbaro

Thesis committee

Promotors

Prof. Dr M.C. Krol
Professor of Air Quality and Atmospheric Chemistry
Wageningen University

Prof. Dr A.A.M. Holtslag
Professor of Meteorology
Wageningen University

Co-promotor

Dr J. Vilà-Guerau de Arellano
Associate professor, Meteorology and Air Quality Group
Wageningen University

Other members

Dr G. Feingold, National Oceanic and Atmospheric Administration, Boulder, USA
Prof. Dr H.J.J. Jonker, Delft University of Technology, the Netherlands
Prof. Dr T. Röckmann, Utrecht University, the Netherlands
Prof. Dr R. Uijlenhoet, Wageningen University

This research was conducted under the auspices of the SENSE Research School

Interaction between aerosols and convective boundary-layer dynamics over land

Eduardo Wilde Barbaro

Thesis

submitted in fulfillment of the requirements for the degree of doctor
at Wageningen University
by the authority of the Rector Magnificus
Prof. Dr M.J. Kropff,
in the presence of the
Thesis Committee appointed by the Academic Board
to be defended in public
on Friday 20 March 2015
at 4 p.m. in the Aula.

E. Wilde Barbaro
Interaction between aerosols and convective boundary-layer dynamics over land
x + 183 pages.

PhD thesis, Wageningen University, Wageningen, NL (2015)
With references, with summaries in Dutch, English and Portuguese.

ISBN 978-94-6257-265-2

"Time, time, time,
See what's become of me
While I looked around for my possibilities
I was so hard to please
But look around
Leaves are brown
And the sky is a hazy shade of winter

Hang on to your hopes, my friend
That's an easy thing to say
But if your hopes should pass away
Simply pretend that you can build them again
Look around
The grass is high
The fields are ripe
It's the springtime of my life"

Simon, P.F. (1968). A hazy shade of winter. *Bookends*, **4(B)**, Columbia Records.

Contents

"Little boxes all the same
There's a green one and a pink one
And a blue one and a yellow one
And they're all made out of ticky-tacky
And they all look just the same"

Reynolds, M. (1967). Little boxes. *Sings the Truth*, **3(A)**, Columbia Records.

1 Introduction

In this thesis we study the interplay between aerosols and physical processes happening in the lowest portion of the atmosphere near the surface at the daily scale. In this Introduction, we will first outline the relevance of this research, after which we will present our theoretical framework and research objectives.

1.1 Aerosols and the environment

Aerosols are defined as solid or liquid particles suspended in the atmosphere and play a major role in the Earth system. Arguably, the most fundamental impact of aerosols is on human health (Oberdorster *et al.*, 2005). Tiny (< 1 μm) anthropogenic aerosols (e.g. combustion-generated) penetrate into the circulatory system causing detectable damage to the heart and lungs (Oakes *et al.*, 2014). Natural aerosols, such as pollen, can be carried by the wind away from its source (Chamecki *et al.*, 2009) and may cause severe allergies (Wallin *et al.*, 1991; D'Amato *et al.*, 1998). The marine biota are also strongly affected by aerosols via deposition of nutrients (Carslaw *et al.*, 2010).

Aerosols also strongly interact with weather and climate. According to several studies (Kaufman *et al.*, 2002; Niyogi *et al.*, 2007; Arneth *et al.*, 2010; Zubler *et al.*, 2011b; Myhre *et al.*, 2013; Hosseinpour & Wilcox, 2014) aerosols strongly interact with

a number of phenomena, ranging from global to the local scale. Stevens & Feingold (2009) showed that aerosols have an intricate relation with clouds, affecting the radiation arriving at the Earth's surface, and precipitation (Uijlenhoet & Sempere Torres, 2006; Cirino *et al.*, 2014). In Fig. 1.1 we illustrate three materials commonly observed in the atmosphere as small particles (typically < 10 μm).

Figure 1.1: Small particles of sea salt (left), dust (middle), and volcanic ash (right) are commonly observed in the atmosphere. Image copyright: Katherine Mann.

The aerosol properties, such as amount, size, and chemical composition (as depicted in Fig. 1.1), vary widely depending on the land-surface characteristics (e.g. oceans, rural areas, urban areas, deserts) and their sources (e.g. anthropogenic or natural) - see Ramanathan (2001). Aerosols interact on different spatial scales, and are present in all sort of environments, as illustrated in Figure 1.2.

Concerning the global scale, Liu & Mauzerall (2007) found evidence of inter-continental transport of sulfate aerosols emitted specially in East Asia, North America and Europe. Another example of inter-continental transport of aerosols is shown in Fig. 1.2a, where we notice a heavy load of Saharan dust traveling over the Atlantic Ocean (close to Cape Verde). Depending on the active weather systems, the dust is transported to very different locations (Schepanski *et al.*, 2009). Israelevich *et al.* (2012) found significant loads of Saharan dust over the Mediterranean sea, and Swap *et al.* (1992) showed that Saharan dust is intimately connected to rain systems in the Amazon rainforest. Recently, Longo *et al.* (2013) argued that the buoyancy generated by the fires in the Amazon is closely related to intense deep convection, and introduces a strong perturbation to the climate system. The interaction between aerosols, cloud formation, and precipitation is of crucial importance for the climate system. This interaction is known as aerosol indirect effect. The indirect effect is defined as the

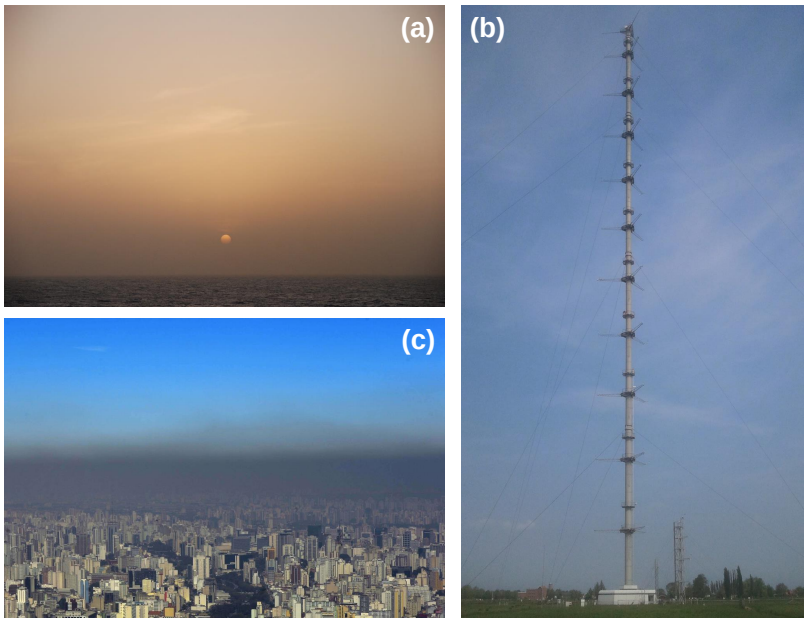

Figure 1.2: (a) Saharan dust traveling over the Atlantic ocean (N 14.8748° W 23.0002°) in 2009 (b) slightly polluted air over Cabauw (the Netherlands) in 2011 (c) heavily polluted atmosphere in Sao Paulo (Brazil) in 2013. Images copyright: (a) John Kalisch, IFM-GEOMAR, and (c) Terra.com.br website, editorial branch division for sustainability (author: Marcelo Pereira).

mechanism by which aerosols alter microphysics, radiative properties, and lifetime of clouds (Feingold *et al.*, 2003; Roelofs & Jongen, 2004; Boucher *et al.*, 2013).

The indirect effect of aerosols is also important in regional scale studies (Andreae & Rosenfeld, 2008; Bangert *et al.*, 2011). Feingold *et al.* (2010) showed significant oscillations in precipitation rate due to the influence of aerosols on the formation and size of cellular cloud fields. The transport of aerosols is also a critical phenomenon at regional scale. Athanasopoulou *et al.* (2008) noted sea salt entering significant distances into coastal areas for Greece. Rodhe *et al.* (1972) observed a significant transport of anthropogenic aerosols (sulfate and soot) in Sweden between urban and non-urban areas. Schaap *et al.* (2010) showed that on average the aerosol found in Cabauw (the Netherlands) is a mixture mostly composed of carbonaceous aerosols, inorganic aerosols, mineral dust, and a fraction of sea salt (Fig. 1.2b). In addition, both chemical composition and burden of aerosols vary significantly depending on the transport imposed by the weather systems acting in the region (Hamburger *et al.*,

2011).

Besides the interaction at larger scales, aerosols are strongly coupled to the diurnal cycle, and the thermodynamics of the lower atmosphere (Angevine *et al.*, 1998b; Zhang *et al.*, 2010; Grell & Baklanov, 2011). We observe in Fig. 1.2c, a cloudless day at the polluted urban area of Sao Paulo (Brazil). We can clearly identify a heavy layer of pollutants close to the surface, visibly distinguished from the clean layer of air above. These pollutants were emitted mostly by automobile traffic (e.g. soot) and also consist of dust re-suspended from the soil (Castanho & Artaxo, 2001).

Although the environments shown in Fig. 1.2 are very different, they all share the fact that the presence of aerosols influences the physics and chemistry of the lower atmosphere (Baklanov *et al.*, 2014). Note, however, that aerosols are not only emitted at the surface. Aerosols are also formed from gas-phase precursors of natural or anthropogenic origin. Moreover, it is common to observe aerosols forming complex mixtures, e.g. black carbon mixing with nitrates or sulfates, or coating dust. It is anyhow clear that the lowest layers of the atmosphere play an important role in mixing and transporting aerosols (Andreae & Crutzen, 1997). In the next section we will therefore describe the physics of the lowest layers of the atmosphere, the so-called atmospheric boundary layer (ABL), when heated by sunlight during daytime.

1.2 Aerosols in the atmospheric boundary layer

1.2.1 A classical clear ABL

We first introduce in Fig. 1.3a the main processes governing the development of the diurnal ABL without the presence of aerosols. The available energy at the surface, mainly driven by the incoming solar radiation (see Chapter 2), evaporates water from the soil and vegetation, and warms the surface and the atmospheric layers above. As a result, the evaporation and heat fluxes at the surface organize upward turbulent motions (thermals) transporting moisture and heat to higher altitudes. In that way, most of the available energy at the surface is transferred to the atmosphere by means of evaporation and heat, forming what is know as the surface energy balance (SEB). This transport by thermals occurs at a timescale of minutes through an efficient process called convective turbulence. Due to the convective character of the diurnal ABL we refer to it as convective boundary layer (CBL).

Heat and moisture are not only exchanged at the surface, but also at the top of the CBL, with a non-turbulent layer called free-atmosphere (Stull, 1988; Garratt, 1992). This process is shown in Fig. 1.3, where the most energetic eddies are able to engulf air from the free-troposphere, normally characterized by higher potential temperatures

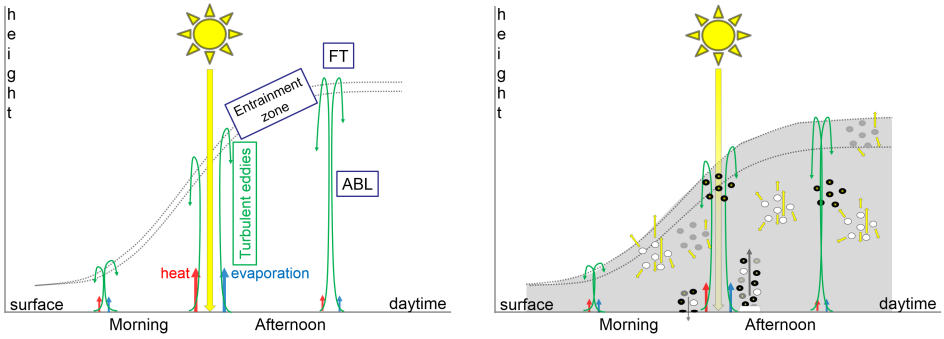

(a) Clear ABL **(b) Polluted ABL**

Figure 1.3: Schematic of the land-ABL evolution during the day showing in (a) the classical clear ABL, and (b) an ABL in which aerosols are disturbing the land-ABL system. The yellow arrows in both panels denote the downward solar radiation. The surface fluxes are indicated in (a) as well as the turbulent eddies and the entrainment zone between the ABL and free-troposphere. (b) The different colors for the aerosols represent their interaction with solar radiation: black (strongly absorbing), gray (moderately absorbing), and white (purely scattering). Note in (b) the surface emission and deposition processes. Adapted from Stull (1988).

and lower amounts of water vapor compared to the CBL. This processes is known as entrainment.

Note that the turbulent transport and mixing are directly connected to the dispersion of pollutants. In particular, aerosols (emitted and formed in the CBL) are transported in the boundary layer (Fig. 1.3b) and may influence its evolution. In the next section we will briefly discuss the role of aerosols disturbing the evolution of the CBL.

1.2.2 The polluted ABL

In Fig. 1.3b we introduce surface processes, such as emission and deposition of aerosols or trace gases. Aerosols, depending on their characteristics (see Fig. 1.1), absorb (e.g. black carbon) or scatter (e.g. sea salt, sulfate and nitrate aerosols) solar radiation, interacting differently with CBL dynamics. For example, Yu *et al.* (2002) and Arneth *et al.* (2010) have shown that aerosols interact with radiation affecting the coupling between the surface and the CBL. Closely connected with the subjects studied in this thesis, Oliveira *et al.* (2002) and Codato *et al.* (2008) showed by means of detailed

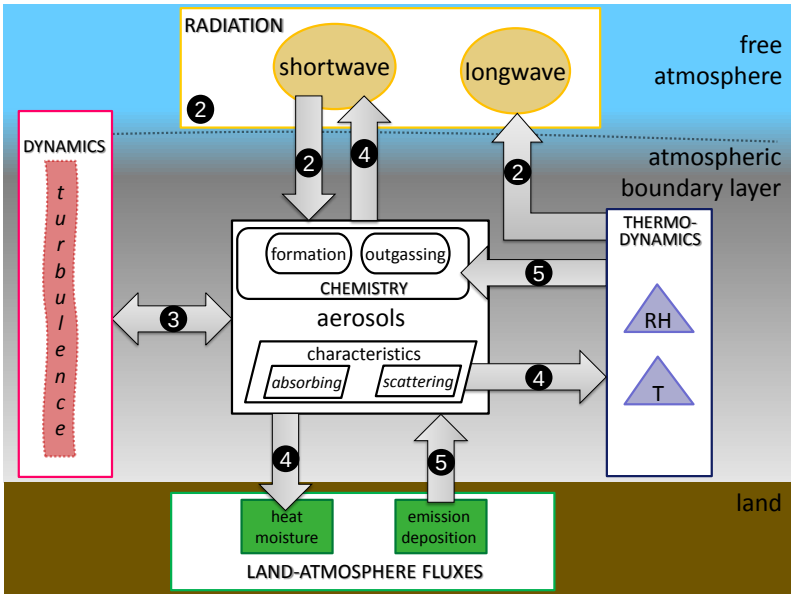

Figure 1.4: The land-CBL system influenced by the presence of aerosols, and the interactions investigated in this thesis. The numbers inside the arrows indicate the Chapter these processes are studied. Figure inspired by the feedback-diagram first proposed by Ek & Mahrt (1994).

observations that pollution in Sao Paulo (see Fig. 1.2c) has altered the urban climate by diminishing the solar radiation at the surface, both locally and at the regional scale.

We use Fig. 1.4 as a road map to introduce the fundamental concepts of the land-CBL system and the different couplings studied in this thesis.

1.2.3 Radiation-Aerosols-Thermodynamics coupling

We notice from Fig. 1.4 that the interaction between aerosols and solar radiation occurs through two distinct processes, called scattering and absorption (Liou, 2002). Whereas absorption of radiation leads to a warming of the CBL, scattering leads to a cooling effect (Jacobson, 1998; Yu *et al.*, 2002). The cooling effect is explained by the fact that some of the scattered radiation is reflected back to space, i.e. not being absorbed by the aerosols, neither reaching the surface. This process leads to a reduction in the total energy confined within the CBL (Li *et al.*, 1997). The opposite is observed for strongly absorbing aerosols. The heating promoted by absorption of

radiation due to aerosols also influences the vertical distribution of energy within the CBL. In that way, aerosols alter the CBL thermodynamics and its energetics. Note that the amount of radiation reaching the surface is strongly determined by the aerosol characteristics shown in Fig. 1.4 (Hatzianastassiou *et al.*, 2005; Wang *et al.*, 2009). We explore these couplings in detail in Chapters 3 and 4.

1.2.4 Radiation-Aerosols-Surface coupling

It is important to emphasize that the perturbations caused by aerosols at the surface are significantly larger than at the top of the atmosphere (TOA) because at the surface aerosols alter the SEB as well (Forster *et al.*, 2007). To study the impact of aerosols on global climate, their radiative effect at the TOA is the relevant quantity (more reflected radiation means a cooling effect) (Myhre *et al.*, 2013). At the TOA, Ramanathan *et al.* (2001) showed instantaneous values as small as -7 Wm^{-2}, and the last IPCC report suggests diurnally-averaged values smaller than -1 Wm^{-2} (Boucher *et al.*, 2013), see also Bellouin *et al.* (2013). In contrast, the impact of aerosols at the surface is more representative for the local scales (Gregory *et al.*, 2004). Specially for partially absorbing aerosols, Ramanathan *et al.* (2001) showed that radiative disturbances at the surface are many times larger than at the TOA. Haywood *et al.* (2003), using aircraft measurements, found instantaneous values as large as -130 Wm^{-2} in the CBL. Tripathi *et al.* (2005) show diurnal averages ranging from -31 Wm^{-2} to -98 Wm^{-2} for moderately to highly polluted industrial cities in India. Note that these disturbances impose a reduction of the solar radiation at the surface ranging within 10-30% during daytime (Yu *et al.*, 2002). This coupling and its feedbacks on turbulence are studied in Chapters 3 and 4 of this thesis.

1.2.5 Aerosols-Chemistry coupling

As illustrated in Fig. 1.4, surface exchanges are an important source (or sink) of gases and aerosols in the CBL (Ganzeveld & Lelieveld, 1995). Guenther *et al.* (1995) discussed the role of thermodynamics (temperature and moisture) and solar radiation on the emissions of volatile organic compounds at the surface. Dentener & Crutzen (1994) demonstrated by means of of a three-dimensional transport model that ammonia emissions and deposition are strongly coupled to the temperature close to the surface. In addition to the surface processes, Krol *et al.* (2000), using a three-dimensional model, showed that turbulence induces significant perturbations in the concentration of chemicals within the CBL. These gases are important aerosol precursors. Besides being emitted and deposited at the surface, aerosols also participate in

chemical reactions and affect important chemical cycles, including nitrogen and sulfur compounds (Andreae & Crutzen, 1997). Jacobson (1998) showed that photolysis frequencies strongly depend on the absorbing and scattering properties of aerosols. Moreover, a significant amount of chemical reaction rates are temperature dependent (Vilà-Guerau de Arellano *et al.*, 2011). Therefore, the reactivity of most compounds in the CBL is directly related to the CBL thermodynamics. It is also known that the thermodynamics of the CBL impacts aerosol formation (Harrison & Pio, 1983; Nenes *et al.*, 1998; Neuman *et al.*, 2003). In a recent study, Aan de Brugh *et al.* (2013) showed for ammonium nitrate aerosol that the turbulent mixing in the CBL in combination with a temperature-dependent partitioning of atmospheric nitrate (between the gas and aerosol phases) leads to a strong interaction between CBL dynamics and aerosol formation. The interaction between aerosols, thermodynamics, and chemistry is discussed in Chapter 5.

In the next section we will briefly introduce how aerosols have been studied from the observational perspective and in terms of numerical modeling.

1.3 Observing and modeling aerosols in the atmospheric boundary layer

Several measurement campaigns have established a comprehensive database of meteorological observations (Angevine *et al.*, 1998b; Masson *et al.*, 2008) often including radiosondes of the CBL vertical structure. However, only a few campaigns have combined these observations with detailed aerosol and chemical observations (Kulmala *et al.*, 2011; Jager, 2014). Several studies indicated that the lack of observational data sets leads to major uncertainties in the aerosol representation in numerical models (Li *et al.*, 1997; Zhang *et al.*, 2010).

The same is noted from the numerical perspective, Haywood & Boucher (2000) and Haywood *et al.* (2003) showed that a reliable representation of the aerosol optical properties and their spatial distribution is necessary to reduce the uncertainty concerning the role of aerosols in the climate system. According to Kinne *et al.* (2013) a significant part of this uncertainty is due to the poor understanding of the tropospheric aerosol characteristics and their sources and feedbacks. Carslaw *et al.* (2010), in a comprehensive review, propose that the complexity of the couplings between aerosols and the land-atmosphere system complicates the quantification and understanding of the individual processes. According to Stevens & Feingold (2009) and Baklanov *et al.*

(2014) the coupling of atmospheric thermodynamics, aerosol transport, chemical reactions, and atmospheric composition in numerical models will remain a challenge over the next years.

The pioneering works of Zdunkowski *et al.* (1976) and Ackerman (1977) studied for the first time the impact of the absorption of solar radiation within the CBL by means of simplified numerical models. They concluded that aerosols (by absorbing solar radiation) redistribute heat in the CBL, affecting its thermodynamics - see also Jacobson (2001a). Quijano *et al.* (2000) and Raga *et al.* (2001), also using one-dimensional numerical models, showed that besides their characteristics and amount, the vertical distribution of aerosols also influences the dynamics of the CBL.

In order to numerically simulate the interaction between turbulent eddies (see Fig. 1.3), surface, aerosols, and radiation, large-eddy simulation (LES) is the best available tool (Wyngaard, 2010). LES has been widely used to simulate turbulent flows in the atmosphere since it solves explicitly the turbulent eddies transporting properties, like moisture, heat, and aerosols, and only parameterizes the smaller eddies. Because it explicitly solves most of the turbulent spectrum, LES allows us to investigate in great detail the vertical structure of the CBL. For instance, Aan de Brugh *et al.* (2013) used LES to study surface observations of ammonium nitrate aerosols that form in the colder upper CBL. They showed that downdrafts carry air masses that are rich in ammonium nitrate towards the surface, and that this vertical mixing is fundamental to interpret the surface observations. The one-dimensional models mentioned in the previous paragraph do not resolve the turbulent eddies and hence have to parameterize the transport and chemistry associated with them. However, existing parametrizations focus on the transport of temperature and inert scalars, and may not be suitable if physical or chemical processes proceed at timescales similar to the CBL mixing timescale (Vilà-Guerau de Arellano & Duynkerke, 1995).

Due to the significant increment in computer power since the last decades, a few integrating LES studies appeared coupling some of the mechanisms shown in Fig. 1.4. Within the context of our research, Feingold *et al.* (2005) studied the suppression of clouds by coupling their formation to aerosols, CBL dynamics, and radiation, but kept the surface properties fixed. Ouwersloot *et al.* (2013) quantified the transport of chemicals by shallow-cumulus clouds, without accounting for the role of aerosols in cloud formation. Neglecting emissions and deposition of aerosols at the surface, Aan de Brugh *et al.* (2013) showed that the phase transition of ammonium nitrate is strongly coupled to the CBL dynamics.

In conclusion, studies accounting for the role of aerosols in the fully coupled land-CBL system are still lacking. Specifically at diurnal scales, only in the last decade a few studies appeared that couple aerosols to CBL thermodynamics, radiation, land

surface, and chemistry (Yu *et al.*, 2002; Riemer *et al.*, 2003; Wong *et al.*, 2012) and even fewer using LES (Jiang & Feingold, 2006; Lee *et al.*, 2014). In the next section we will discuss how we deal with the challenges mentioned here. We will also position our work in terms of originality in relation to previous studies.

1.4 General objectives and strategy

In this thesis we will show that even relatively low loads of aerosols - such as measured at Cabauw (Fig. 1.2b) - play a very relevant role in the surface-CBL system at a diurnal time scale. The main objective of our research is to understand and quantify the impact of aerosols on the radiation field, CBL thermodynamics, chemistry and the SEB. The interactions involving aerosols in the CBL are still not well understood because of the lack of quality measurements and high resolution numerical simulations accounting for the aerosol couplings within the land-CBL system, e.g. Jiang & Feingold (2006). Thus, we place emphasis on the interaction between aerosols and the turbulent field by explicitly simulating the three-dimensional turbulent structures in the CBL using LES. By doing so, we are also able to augment our understanding on the role of aerosols disturbing the entrainment zone. Because LES is computationally demanding, it is very convenient to have complementary tools to study the wide range of conditions in which aerosol can affect the surface and CBL thermodynamics and chemistry. Therefore, we also use mixed-layer theory and a single column model. These models also provide us with a framework to interpret the LES results. Finally, the LES results shown in this thesis might serve as benchmark to evaluate the performance of other coupled numerical models that do not explicitly resolve the turbulent field (e.g. WRF-CHEM model, see Grell *et al.* (2005)).

One of the innovative aspects in this thesis is the extension of previous work (Ackerman, 1977; Venkatram & Viskanta, 1977; Angevine *et al.*, 1998b; Cuijpers & Holtslag, 1998; Krol *et al.*, 2000; Raga *et al.*, 2001; Yu *et al.*, 2002; Haywood *et al.*, 2003; Aan de Brugh *et al.*, 2013) to deal with the several couplings described in Fig. 1.4. To evaluate our modeling efforts we take advantage of (i) a complete observational data set (EUCAARI-CESAR) combining information about aerosol, radiation, fluxes, and chemistry measurements at the surface, with detailed information of the atmospheric vertical structure (Kulmala *et al.*, 2009, 2011). We will present carefully designed numerical experiments in which aerosols, radiation, and CBL dynamics fully interact. These numerical experiments are conducted using various models that are briefly outlined below.

1.4.1 Numerical models

1.4.1.1 DALES

We resolve the integration at diurnal scales of radiation-chemistry-surface-atmosphere by means of an LES platform. We use the Dutch Atmospheric LES (DALES) model as described by Heus *et al.* (2010), coupled to a land-atmosphere module (Ganzeveld *et al.*, 1998; van Heerwaarden *et al.*, 2009), a chemistry module (Vilà-Guerau de Arellano *et al.*, 2011; Aan de Brugh *et al.*, 2013), and a radiative transfer code (Joseph *et al.*, 1976). In that way, our numerical framework enables us to accurately simulate the dynamics of the CBL and, at the same time, account for the interactions of aerosols with radiation, the surface, and chemistry. We pay special attention to the quantification of the aerosol effects on the vertical structure of the CBL, focusing also on its entrainment characteristics. Our LES framework also allows us to understand the formation and transport of aerosols within the CBL.

1.4.1.2 Non-eddy resolving models

We also take advantage of a zeroth-order mixed-layer model (Lilly, 1968; Tennekes, 1973; van Heerwaarden *et al.*, 2009) coupled to the same radiation, chemistry and land-surface models used in DALES. This model helps us to interpret and extend our LES results to different aerosol characteristics. Furthermore, we use the Wageningen University Single-Column Model (WUSCM), described in detail by Aan de Brugh *et al.* (2012), to parameterize the interaction between 3D turbulence and chemistry in an one-dimensional framework. This latter aspect is important for the representation of aerosols in non-eddy resolving models, like WRF-CHEM.

1.5 Research questions and outline

Aiming to disentangle the aerosol-CBL dynamics interplay (Fig. 1.4) we have formulated four general research questions. We answer these questions in Chapters 2 to 5 adopting different strategies:

Question 1 How can we effectively model the impact of aerosols on the radiation budget?

A crucial part of our research is to understand the radiation budget of the CBL. Therefore, in Chapter 2 we will discuss the most important concepts and assumptions

concerning the radiative transfer model employed in this thesis. Firstly, we will introduce the broadband two-stream Delta-Eddington (Shettle & Weinman, 1970; Joseph *et al.*, 1976) model. We will discuss its accuracy to obtain the solar radiation within the CBL for both clear and polluted situations. We will also investigate the role of pollution disturbing the atmospheric emission of longwave radiation. We aim to approximate the atmospheric emission of longwave radiation - even under polluted conditions - by means of a simple empirical formula depending on the atmospheric temperature and water vapor pressure close to the Earth's surface.

Question 2 What are the effects of aerosol heat absorption on the vertical structure of the CBL?

To answer this question we will design in Chapter 3 a process study aiming at investigating the impact of vertical distribution of aerosols on the turbulent fluxes, surface forcing, vertical structure and heat budget of the CBL. To support the analysis and discussion of the LES results we also employ mixed-layer theory. Our approach is inspired by the numerical experiments designed by (i) Lilly (1968) to investigate the role of longwave radiation in the development of shallow cumulus clouds, and by (ii) Tennekes (1973), in terms of experimental design and interpretation of the dynamics in a dry convective CBL, and by (iii) Bretherton *et al.* (1999), who studied entrainment by using an archetype boundary layer full of radiative-active smoke and by simulating radiative cooling at the top of stratocumulus clouds.

We also investigate if, by absorption of radiation within the CBL, aerosols can alter the interchange of properties between the top of the CBL and the free-atmosphere. Our aim is to understand the role of aerosols disturbing the upper CBL characteristics (Ackerman, 1977; Raga *et al.*, 2001) and weakening the turbulent eddies depending on the aerosols vertical distribution within the CBL.

Question 3 How do the CBL dynamics and land-surface react to the radiation absorbed and scattered by aerosols during the day?

To address this question, in Chapter 4 we use DALES interactively coupled to radiation and the land surface. Besides the numerical component, we also take advantage of an observational data set containing information about the CBL vertical structure and surface (Kulmala *et al.*, 2011). To further quantify the aerosol effects on the land-CBL system we study the responses of the surface and CBL dynamics to a wide range of aerosol loads and characteristics. Since this type of study requires hundreds of numerical simulations we use our zeroth-order mixed-layer platform. In

that way, we are able to investigate and quantify the response of the SEB to the aerosol absorption and scattering of solar radiation.

Question 4 What is the impact of CBL thermodynamics and chemistry on aerosol formation, transport and deposition?

In Chapter 5 we extend the work of Aan de Brugh *et al.* (2013) by using DALES coupled to chemistry and to emission and deposition fluxes. We study the formation and transport of ammonium nitrate aerosol within the CBL placing special emphasis on understanding and representing processes, such as the surface deposition flux and turbulent transport of gases and aerosols. We investigate the impact of CBL turbulence and chemistry on nitrate deposition and evaluate how the WUSCM parameterizes the interaction between 3D turbulence and the gas-aerosol conversion of nitrate (explicitly solved in DALES).

Finally, in Chapter 6 we summarize the main results of this thesis. A general discussion placing the research presented in this thesis in perspective is given in Chapter 7, alongside some future recommendations.

"Here comes the Sun, here comes the Sun
And I say it's all right
Little darling, the smiles returning to the faces
Little darling, it seems like years since it's been here"

Harrison, G. (1969). Here comes the Sun. *Abbey Road*, **1(B)**, Apple Records.

2

Radiation modeling: theory, assumptions and verification

Part of Section 3 of this Chapter is published as:
Barbaro, E., Oliveira, A.P., Soares, J., Codato, G., Ferreira, M.J., Mlakar, P., Boznar, M.Z. & Escobedo, J.F. (2010). Observational characterization of the downward atmospheric longwave radiation at the surface in the city of Sao Paulo. *Journal of Applied Meteorology and Climatology*, **49**, 2574–2590

2.1 Introduction

A crucial aspect of our research is to understand the effect of aerosols on (i) radiation, (ii) turbulent fluxes, and (iii) thermodynamics of the CBL. We start this section by introducing the fundamentals of radiative transfer theory used for the studies in Chapters 3, 4 and 5. We discuss the effect of aerosols on shortwave radiation, and longwave radiation, and stress the importance of accounting for the impact of aerosols on the surface energy budget and on the thermodynamics of the CBL. Throughout all this Chapter the term shortwave (SW) refers to the solar radiation band carrying the most energetic wavelengths ($< 5\mu$m), and longwave (LW) refers mostly to the radiation emitted by the Earth ($> 5\mu$m). The emission from the atmosphere happens in a much larger wavelength due to the acute difference between the atmospheric temperature (200-300 K) and the temperature of the Sun ($\approx$ 5800 K). Therefore, for the shortwave band at atmospheric temperatures the emission of SW radiation can safely be neglected (Liou, 2002).

The net-available energy at the surface (Q_{NET}) is a key component of the energy budget in the CBL. It is given by the sum of the shortwave and longwave radiation components:

$$Q_{NET} = SW_{\downarrow} + SW_{\uparrow} + LW_{\downarrow} + LW_{\uparrow}, \tag{2.1}$$

where, $SW_{\downarrow}$ is the downward solar radiation (positive) that reaches the surface, and $SW_{\uparrow}$ is the upward diffuse radiation reflected by the surface (negative). $LW_{\downarrow}$ is the incoming longwave radiation (positive) at the surface and the $LW_{\uparrow}$ (negative) is the longwave radiation emitted by the surface. Note that, as introduced in Chapter 1, the perturbations to the energy budget at the surface due to the direct effect of aerosols are much larger than at the top of the atmosphere (Forster *et al.*, 2007).

At various places in this thesis we evaluate the impact of aerosols on the thermodynamics of the CBL. The SW radiation absorbed by the aerosols directly contributes to the heating rate (HR) of air parcels (Gao *et al.*, 2008). Other factors that influence the HR are (i) absorption of shortwave radiation (heating) by gas phase constituents (e.g. ozone, water vapor, NO_2) and (ii) emission of longwave radiation (cooling). We will show in Chapter 3 that there are two (equivalent) ways to calculate the vertical aerosol HR within the CBL: (i) divergence of the net-irradiance ($F = SW_{\downarrow} + SW_{\uparrow}$) and (ii) the product between total actinic flux (ϕ) and aerosol layer absorption (σ_a). Both expressions are shown below:

$$HR_{SW} = \frac{1}{\rho c_p}\frac{\partial F}{\partial z}$$
$$HR_{\phi} = \frac{1}{\rho c_p}\sigma_a \phi \ , \tag{2.2}$$

where ρ is the air density, and c_p is the heat capacity of the air. Whereas the former expression is widely used in meteorological studies (Angevine *et al.*, 1998b; Masson *et al.*, 2008) the latter prevails in air quality and chemistry studies (Conant, 2002; Gao *et al.*, 2008).

The main objective of this Chapter is threefold. Firstly, we explain that to resolve the shortwave band of the radiation components we use the broadband two-stream Delta-Eddington (DE) model (Shettle & Weinman, 1970; Joseph *et al.*, 1976) implemented in DALES (Heus *et al.*, 2010). We extend the original code in DALES to account for the presence of scattering and absorbing aerosols. Here we show that under clear-sky conditions our broadband two-stream DE is of sufficient accuracy (i) to calculate the correct amount of available energy at the surface for both clear and polluted situations, and (ii) to represent the total heating within the CBL by describing the aerosol properties using a single representative wavelength (550 nm). In order to verify the representativeness of our assumptions we compare the results obtained with the DE model against a multiband radiative transfer code (LibRadtran - see Mayer & Kylling (2005)), which is able to account for the atmospheric composition, aerosol vertical distribution, and gaseous SW absorption, and LW cooling. Note that by using the LibRadtran model we are explicitly solving the aerosol properties in a wavelength-dependent fashion. In Chapter 4 we further extend the validation of the DE model against observations of global, direct, and diffuse radiation at the surface taken at Cabauw, the Netherlands.

Secondly, we will motivate the choice of the Brunt's formula (Brunt, 1932) in DALES to calculate the incoming downward LW radiation at the surface under clear-sky conditions. According to this expression, the downward longwave radiation at the surface during clear-sky days can be reliably approximated by the atmospheric temperature and water vapor pressure at screen level, and thus does not depend on the aerosol characteristics. To show the validity of these assumptions we analyze a 9-year data set containing 5-minute-averaged measurements of incoming LW radiation and meteorological parameters taken on a micrometeorological platform located in Sao Paulo (Brazil). Additionally, in Chapter 4 we compare the results obtained with Brunt's formula with observations taken at Cabauw (the Netherlands). Concerning

the upward LW radiation, we assume that the surface is a black body, i.e. its emissivity is equal to unity (Holtslag & de Bruin, 1988), and its calculation depends only on the surface skin temperature (van Heerwaarden & Vilà-Guerau de Arellano, 2008).

Lastly, as an illustration of the importance of a proper representation of the aerosols in our numerical framework, we will show the relevance of solving simultaneously the radiation, energy budget and turbulence for a canonical CBL.

2.2 The shortwave radiation model

One of the outstanding issues concerning the interaction between aerosols and radiation is the fact that the most significant interference happens in the range of wavelengths comparable to the size of the aerosols, i.e. typically up to a few microns at most (Seinfeld & Pandis, 2006). Around 70% of the energy emitted by the Sun is contained within wavelengths smaller than 1 μm. At around 4 μm the accumulated energy arriving at the top of the atmosphere (also called total solar irradiance) reaches approximately 99% of its maximum magnitude (1366 Wm^{-2}). In Fig. 2.1 we show the solar irradiance curve at the top of the atmosphere and at the surface for a typical mid-latitude atmosphere.

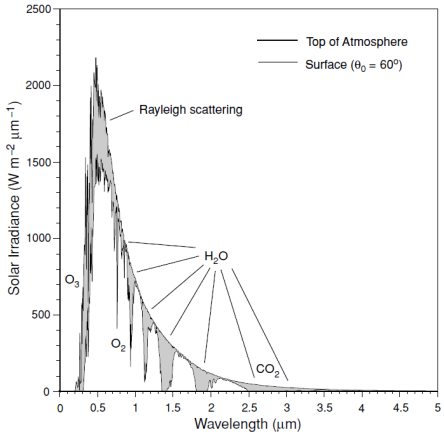

Figure 2.1: Solar irradiance curve at the top of the atmosphere (top curve) and at the surface (bottom curve) for a solar zenith angle of 60° calculated using the MODTRAN 3.7 program. The atmosphere is assumed cloudless and clear (i.e. no aerosols). The absorption and scattering regions (and the responsible mechanisms) are indicated in gray. Adapted from Liou (2002).

We observe in Fig. 2.1 that the solar irradiance at the top of the atmosphere (top curve) is attenuated by different processes until it arrives at the surface (bottom curve). Moreover, the maximum of the solar irradiance curve is at around 550 nm. Hence the choice of 550 nm to represent the aerosol properties. Note in Fig. 2.1 that the atmosphere is assumed clear, so the effect of aerosols and clouds in extincting *SW* radiation is not accounted for. Since molecules are typically a few nanometers in size, the strongest interaction between solar radiation and air molecules is in the ultraviolet and visible part of the spectrum. Ozone is the main absorber of ultraviolet radiation (< 0.4 μm). Within the visible range ($0.4 - 0.7$ μm) mainly Rayleigh scattering is responsible for attenuating *SW* radiation. In the near- and medium-infrared range ($\approx 0.7 - 6.0$ μm), water vapor and CO_2 are the most important contributors for the extinction of *SW* radiation. Note that other gases, e.g. NO_2, also contributes slightly to the extinction of *SW* radiation.

In this thesis we will investigate the response of the surface (shading) and CBL thermodynamics (heating/cooling) to the presence of aerosols. Thus, the total solar irradiance reaching the surface depends upon (besides geographical, astronomical and surface parameters) the reflectivity (r), transmissivity (t), and absorptivity (a) of the atmosphere (Pinker & Laszlo, 1992). In Fig. 2.2 we sketch these processes:

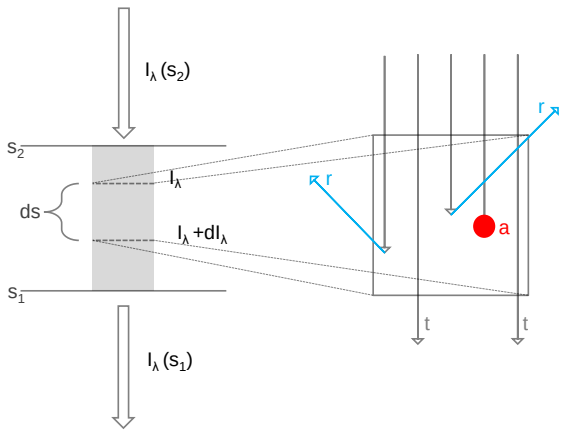

Figure 2.2: Extinction of irradiance traversing an infinitesimal medium due to absorption (red circle), and scattering (blue arrows). Adapted from Liou (2002).

Here I is the irradiance at a given wavelength λ and ds is an infinitesimal path length. To exemplify the interaction between the atmospheric properties and "photons" (represented by the arrows), we sketch r, t, and a for the medium in Fig. 2.2. Energy is

conserved for the transfer of irradiance through a scattering and absorbing medium (Palmer & Bass, 1994). Thus, in Fig. 2.2 the transmissivity of the medium equals to 40% (i.e. 2 "photons" are directly transmitted), the absorptivity equals to 20% (1 "photon" is absorbed), and two "photons" are scattered resulting in 40% reflectivity.

2.2.1 Aerosol interaction with SW radiation

In our research we mostly focus on the effects of aerosols on the shortwave band through scattering and absorbing radiation. Thus, assuming that dI depends only on the optical properties of the atmosphere and on the path length, and neglecting multiple scattering from other directions, we can mathematically express the change in irradiance traversing the path ds (for any wavelength) as:

$$\frac{dI}{kds} = -I, \tag{2.3}$$

where k is the atmospheric extinction coefficient (in m^{-1}) and represents the optical properties of the atmosphere, and I is the irradiance (in Wm^{-2}). The term on the rhs denotes the reduction in irradiance due to absorption and scattering. Integrating Eq. 2.3 results in the irradiance at position s_1 that reads:

$$I(s_1) = I(s_2) \exp\left(-\int_{s_1}^{s_2} kds\right), \tag{2.4}$$

where s_2 and s_1 and ds are indicated in Fig.2.2. Eq. 2.4 is known as Beer-Lambert law. It states that the attenuation in radiation (in the absence of multiple scattering from other directions) depends upon the optical properties of the medium and the path length (Swinehart, 1962). The term $\int_{s_1}^{s_2} kds$ in Eq. 2.4 represents the total extinction of radiance over the path and is called optical depth (τ). The extinction caused exclusively by aerosols is called aerosol optical depth (AOD). Kaufman (1993), in a comprehensive study showed for different areas around the globe that the measured AOD (at 550 nm) over land varies from very small values (determined by a small stratospheric aerosol burden (Junge *et al.*, 1961)) in non-polluted areas up to values as large as 1.5 for very polluted situations (e.g. biomass burning). In short, the aerosol optical depth represents the overall importance of the particles in removing radiation from the incident beam (Wallace & Hobbs, 2006).

Eq. 2.4 represents the fraction of the SW radiation transmitted to the surface conserving its direction (i.e. the orientation of the Sun) throughout the atmosphere, and is called *direct solar radiation*. However, a significant part of the radiation that reaches the surface comes in the indirect form, i.e. due to scattering processes. In the atmosphere, scattering is mainly generated by molecules, clouds (water droplets

and ice crystals), and aerosols (Palmer & Bass, 1994). The *SW* radiation reaching the surface after being scattered throughout the atmosphere (therefore changing its orientation) is called *diffuse radiation*. The sum of direct and diffuse radiations is called global *SW* radiation (or simply *SW* radiation). The absorbing properties of an aerosol layer can be measured by the single scattering albedo (SSA). This is defined as the ratio of scattered radiation (independent of the scattering direction) over the total extinction. The SSA measures the relative importance of scattering and absorption processes. Recent studies showed that SSA over land varies approximately within the range 0.7-1.0 (Jacobson, 2001b; Tripathi *et al.*, 2005). For instance, a value as low as 0.7 means that 70% of the incoming solar radiation will be scattered and 30% absorbed, most of the absorption happening within the CBL (Coakley *et al.*, 1983; Angevine *et al.*, 1998b). As we will show in this thesis (Chapters 3 and 4), the radiation absorbed within the CBL due to the presence of aerosols has a major role in controlling the vertical distribution and partitioning of energy in the land-atmosphere system. Scattering and absorption are fundamental physical process associated with the interaction between particles (or molecules) at all wavelengths (Liou, 2002). For example, in Fig. 2.1 we observe the significant role of Rayleigh scattering (air molecules and gases) in attenuating the ultraviolet and visible parts of the *SW* radiation. Molecules scatter radiation approximately equally in the forward or backward directions (i.e. isotropically). In contrast, large particles (typically > 0.1 μm) tend to scatter radiation towards the forward direction, a process referred to as Mie scattering. The physical property of an aerosol layer that determines the direction of the scattering is called asymmetry factor (g). g varies from -1 (totally backward scattering) to 1 (totally forward scattering). In that way, the asymmetry factor for molecules, i.e. Rayleigh scattering, is zero, whereas for large particles, e.g. cloud droplets and ice crystals, g reaches values close to 0.9. A typical value for the asymmetry factor of (sub-micron) aerosol particles is around 0.6 (Andrews *et al.*, 2006; Kassianov *et al.*, 2007).

The aerosol optical depth, single scattering albedo and asymmetry factor are the three key properties to determine the direct effect of aerosols in the climate system (Boucher *et al.*, 2013). The presence of aerosols increases or decreases the total reflectivity of the atmosphere. It therefore depends on the aerosol properties whether aerosols exert a warming or cooling effect on the climate (Wallace & Hobbs, 2006) - evaluated at the top of the atmosphere (TOA). As discussed in Chapter 1, aerosols exert a much stronger effect at the surface if compared to the TOA. For example, totally scattering aerosols (SSA is equal to unity) reduce the amount of *SW* radiation reaching the surface (due to back-scattering) without absorbing any *SW* radiation, and therefore are responsible for a negative direct radiative effect at the surface (i.e.

cooling). In contrast, absorbing aerosols (SSA smaller than unity) can exert either a positive or negative net-effect in the atmosphere. If its absorbing properties are significant, for instance black carbon, as discussed in Chapter 3, the heating caused by absorption of *SW* radiation may compensate the cooling effect caused by the reduction in the amount of *SW* radiation reaching the surface. We will further discuss both situations in Chapter 4.

2.2.2 The two-stream broadband Delta-Eddington model

Throughout this research we assume that variations in the intensity of all atmospheric quantities are much larger in the vertical direction compared to the horizontal ones. Thus, it is convenient to measure linear distances normal to the Earth surface. As a consequence, the atmosphere can be divided into parallel layers of infinite extensions in the horizontal directions. This approximation is called plane-parallel atmosphere and is used in numerous radiative transfer solvers (Mayer & Kylling, 2005; Seinfeld & Pandis, 2006). By applying this assumption, we observe in Fig. 2.2 that the distance ds can be normalized by writing $ds = dz/cos(\theta)$, where dz is an infinitesimal of the distance normal to the surface and θ denotes the inclination to the upward normal (i.e. the zenith angle). In the situation shown in Fig. 2.2, $cos(\theta)$ equals to unity, since the ray of light already coincides with the normal to the surface. Substituting ds in Eq. 2.4, results in the term $\int_{z_1}^{z_2} kdz/cos(\theta)$. This term represents the optical depth over the distance normal to the surface.

Since our main interest is the understanding of the interplay between aerosols and CBL thermodynamics, we divide the entire atmosphere into an aerosol-free Rayleigh layer situated above an aerosol layer embedded in the CBL. In Fig. 2.3 we sketch our numerical setup. The numbers (1370 Wm^{-2}, 900 Wm^{-2}, and 850 Wm^{-2}) indicate typical amounts of radiation arriving at the most representative heights in our setup: TOA, top of the CBL, and surface, for a mid-latitude CBL at noon. The aerosol burden and properties are representative of a continental CBL (Hewitt & Jackson, 2009).

In order to calculate the *SW* radiation fluxes within the aerosol layer, we use a two-stream broadband Delta-Eddington (DE) model. The DE model fulfills our purposes and provides accurate calculations of the direct and diffuse components of the integrated *SW* radiation (Shettle & Weinman, 1970; Joseph *et al.*, 1976; Liou, 2002). As we discussed above, the temporal evolution of the AOD, SSA and g are needed to calculate the *SW* radiation vertical profile within the aerosol layer. Following the derivation of the radiative transfer equations discussed in Shettle & Weinman (1970) and Joseph *et al.* (1976) we present here in short how to obtain the diffuse (I_D) and

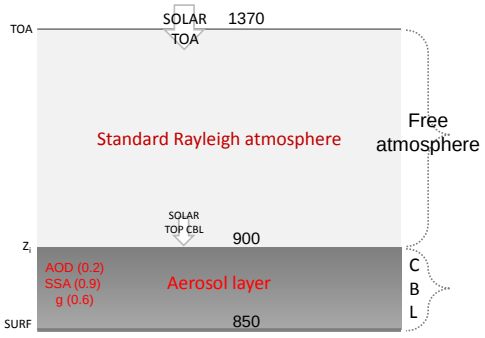

Figure 2.3: Sketch of the separation between free-troposphere (assumed as a standard Rayleigh atmosphere) and CBL (containing the aerosol layer) adopted in our study. The radiation model is used to calculate the diffuse and direct partitioning due to Rayleigh scattering and the aerosols within the CBL. The numbers displayed at the TOA, top of the CBL, and surface, are indicative of typical values of downward radiation (in Wm^{-2}) for a continental mid-latitude CBL ($\theta \approx 30°$) at noon. The numbers in red (in the aerosol layer) indicate typical aerosol burden and properties for a continental CBL.

direct (I_{DIR}) broadband radiation using the DE model. Differently from Shettle & Weinman (1970) our interest is in the radiative fluxes only, therefore, we show the azimuthally integrated form (omitting the wavelength dependence) of the radiative transfer equation for the diffuse radiation (I_D):

$$\mu \frac{dI_D}{d\tau} = -I_D + \frac{\omega}{2} \int_{-1}^{+1} P\ I_D\ d\mu + \frac{1}{4} \omega F_0 P e^{-\tau/\mu} \tag{2.5}$$

where ω is the single scattering albedo, P is the so-called phase function, $\mu = cos(\theta)$, and F_0 is the solar irradiance perpendicular to the direction of incidence at the top of the domain. In Eq.2.5 we quantify the production of diffuse radiation due to multiple scattering (second term on the rhs) and the conversion of direct radiation ($F_0 e^{-\tau/\mu}$) into diffuse radiation (last term rhs).

The phase function P is related to the asymmetry factor (g), since P defines the direction of an incident ray of light after the scattering event. As shown in Joseph *et al.* (1976) the most efficient way to describe P is to approximate it by a Dirac delta function and a two term expansion:

$$P(cos(\iota)) = 2f\delta(1 - cos(\iota)) + (1 - f)(1 + 3g^{'} cos(\iota)), \tag{2.6}$$

where f is the fraction of the scattering relative to the forward contribution, and ι is the angle between incident and scattered radiances, and $g^{'}$ is the asymmetry factor of the truncated phase function. By calculating P using Eq. 2.6 we are already assuming the *delta*-Eddington approximation. In that way, the diffuse radiation after a scattering event is written as a fraction going in the same direction of incidence (first term on the rhs) and a fraction whose direction depends on the asymmetry of the particle (last term on the rhs). Note that Shettle & Weinman (1970) approximated the phase function without correcting for the forward scattering (i.e. assuming $f = 0$, the so-called Eddington approximation). The advantage of the delta-Eddington approximation is the fact that the error of this approximation tends to decrease as the asymmetry factor approaches unity. The δ-transformation is very important for polluted and cloudy atmospheres since aerosols and cloud droplets scatter radiation strongly in the forward direction. Joseph *et al.* (1976) showed that f must be equal to g^2, because g^2 is exactly the second moment of the original phase function P. Assuming Eq. 2.6 to have the same asymmetry factor as the original phase function (i.e. without the *delta* correction) we obtain

$$g = \frac{1}{2}\int_{-1}^{+1} cos(\iota)P(cos(\iota))d(cos\iota) = f + (1-f)g^{'} \tag{2.7}$$

and finally:

$$g^{'} = \frac{g}{1+g}. \tag{2.8}$$

In order to substitute the phase function in Eq. 2.5 we re-write it as:

$$P(\mu,\mu') = 2f\delta(\mu-\mu') + (1-f)(1+3g'\mu\mu') \tag{2.9}$$

where μ and μ' are respectively the directions of the radiation beam before and after the interaction with the particle. In that way, (similarly to the derivation for g) it is possible to use the same Eddington equation for the diffuse radiation (Eq.2.5) except by the optical properties corrected as follows:

$$\begin{aligned} \tau' &= (1-\omega f)\tau \\ \omega' &= \frac{(1-f)\omega}{1-\omega f}. \end{aligned} \tag{2.10}$$

Substituting the transformed (') aerosol properties in Eq.2.5, and separating the diffuse radiation according to the Eddington assumption:

$$I_D = I_0 + \mu I_1, \tag{2.11}$$

we obtain:

$$\begin{aligned} \frac{dI_1}{d\tau'} &= -3(1-\omega')I_0 + \tfrac{3}{4}\omega' F_0 e^{-\tau'/\mu} \\ \frac{dI_0}{d\tau'} &= -(1-\omega' g')I_1 + \tfrac{3}{4}\omega' g' \mu F_0 e^{-\tau'/\mu}. \end{aligned} \tag{2.12}$$

Finally, the diffuse irradiance (I_D) is given by:

$$I_D = (I_0 \pm 2/3 I_1) \tag{2.13}$$

where the $\pm$ represents the downward(+) and upward(-) components. The solutions for I_0 and I_1 are shown in Shettle & Weinman (1970) in their Eq. 12 (albeit for the Eddington approximation). We reproduce them here including the delta-Eddington assumptions:

$$\begin{aligned} I_0^i \tau' &= C_1^i e^{-k_i \tau'} + C_2^i e^{+k_i \tau'} - \alpha_i e^{-\tau'/\mu} \\ I_1^i \tau' &= P^i (C_1^i e^{-k_i \tau'} - C_2^i e^{+k_i \tau'}) - \beta_i e^{-\tau'/\mu} \end{aligned} \tag{2.14}$$

The terms k_i, P_i, α_i and β_i are given below:

$$\begin{aligned} k_i &= [3(1-\omega_i')(1-\omega_i' g_i')]^{1/2}, \\ P_i &= [3(1-\omega_i')/(1-\omega_i' g_i')]^{1/2}, \\ \alpha_i &= 3\omega_i' F_0 \mu^2 [1 + g_i'(1-\omega_i')]/4(1-k_i^2\mu^2), \\ \beta_i &= 3\omega_i' F_0 \mu [1 + 3g_i'(1-\omega_i')\mu^2]/4(1-k_i^2\mu^2). \end{aligned} \tag{2.15}$$

where the index i refers to the ith layer. The constants C_1 and C_2 are determined depending on the boundary conditions (Shettle & Weinman, 1970), i.e. the terms k, P, α, and β calculated at the top of the domain and at the surface, in addition to the surface albedo. Based on Eq.2.13 and on the solutions of the DE method given in Eqs. 2.14 and 2.15 we can write the broadband downward and upward global SW radiation as:

$$\begin{aligned} SW_\downarrow^i &= (I_0^i + (2/3)I_1^i) \quad + \mu F_0 e^{-\tau_i'/\mu}, \\ SW_\uparrow^i &= (I_0^i - (2/3)I_1^i). \end{aligned} \tag{2.16}$$

In our research the value F_0 is calculated based on the broadband atmospheric net-transmissivity from the top of the atmosphere to the top of the aerosol layer following Burridge & Gadd (1974) - see also Stull (1988) and provides the total downward SW radiation used as an upper boundary condition for the DE radiative transfer calculations (Heus *et al.*, 2010). The Rayleigh scattering above the aerosol layer is calculated based on the Elterman (1968) standard profile. Here, we integrate all the Rayleigh optical depth and use the downward radiation at the top of the aerosol layer, to obtain the direct/diffuse partitioning of the SW radiation in the first layer of the model (as shown in Fig. 2.4).

In Eq 2.16 the last term on the rhs of the downward component represents the broadband direct radiation also calculated with the corrected τ'. This is explained by the fact that scattered radiation traveling in very nearly the same direction as the incident beam can also be considered direct radiation - see Eq. 2.6 (Joseph *et al.*, 1976; Liou, 2002). Following Shettle & Weinman (1970) we also assume the surface as being Lambertian, therefore all the reflected radiation is diffuse (Madronich, 1987).

Similarly to Haywood *et al.* (2001); Myhre *et al.* (2003) and Bellouin *et al.* (2013) we assume the wavelength of 0.55 μm as representative for the aerosol properties and Rayleigh scattering. We choose 0.55 μm as a representative wavelength since it is located at the peak of the solar irradiance curve - see Fig.2.1. In Chapter 4 we show that in spite of this simplification, our results show a satisfactory agreement with the radiation observations (also in terms of partitioning between the direct and diffuse components) enabling us to quantify the role of aerosols on the (thermo)dynamics of the boundary layer during daytime. We are aware, however, that small errors are introduced by neglecting the aerosol wavelength dependence.

We have further verified our assumptions concerning (i) the use of a simple broadband DE code, and (ii) assuming a single wavelength for the aerosol properties as representative for the whole spectrum. To do so, we use a more accurate radiative transfer model (libRadtran - see Mayer & Kylling (2005)), which is able to account for spectral multiband calculations as well as for aerosol wavelength dependence. To solve the radiative transfer in libRadtran we use the disort solver described in Stamnes *et al.* (2000). Vertically, the SW radiation is calculated at 200-meters intervals within the CBL. Since we are interested in the comparison of broadband irradiances calculated by the DE radiative transfer code implemented in our LES and libRadtran we employ the most accurate band parametrization available in libRadtran (correlated-k approximation). In that parametrization the solar spectrum (Fig. 2.1) is divided in 148 sub-bands and the absorbing cross sections are obtained as shown in Kato *et al.* (1999) and Mayer & Kylling (2005).

We have designed three academic numerical experiments using the same LES framework as described in Chapters 4 and 5. The initial and boundary conditions are presented in Table 2A.1 in Appendix 2A. In our LES, concerning CBL dynamics, and radiation, and land-surface, the simulations correspond to a typical cloudless, mid-latitude continental boundary layer during summer over grassland. To facilitate the comparison with the libRadtran vertical profiles of direct and diffuse radiation we do not allow diurnal variation of solar radiation during the entire simulated period. The aerosol properties in our LES experiments are prescribed (and held constant during the whole simulated time) as follows:

- CLE: clear case (control) without aerosols
- SCA: heavily polluted CBL filled with purely scattering aerosols
- ABS: heavily polluted CBL filled with strongly absorbing aerosols

In the context of our experiments the term "heavily polluted" means AOD(550 nm) = 0.6 and "strongly absorbing" refers to SSA(550 nm) = 0.7 (Kaufman, 1993). We use an asymmetry factor equal to 0.6 for all our experiments (Andrews *et al.*, 2006). In libRadtran we prescribe our atmosphere as standard mid-latitude up to 50 km with the following constituents: N_2, O_2, O_3, CO_2, water vapor, and NO_2. We have designed two sets of experiments using libRadtran. The only difference between the two sets is the aerosol wavelength treatment. In the first set we have kept the aerosol properties wavelength independent (similarly to DE in DALES), whereas in the second the aerosol optical depth is scaled following the Ångström equation $\beta\lambda^{-\alpha}$. To mimic the AOD in the DALES experiments (0.6) we have chosen $\alpha = 1.4$ and $\beta = 0.26$. These values are representative of a continental polluted atmosphere (Jacovides *et al.*, 2005; Toledano *et al.*, 2007). To ensure consistency in the comparison between the model results we use the same single scattering albedo and asymmetry factor in the DE and LibRadtran. In Fig. 2.4 we show the vertical profiles of the global and diffuse *SW* radiation within the CBL for both the DE and libRadtran integrations.

We confirm in Fig.2.4 that aerosols significantly extinct *SW* radiation within the CBL compared to the clear case. The differences in the amount of *SW* radiation reaching the surface and leaving the CBL for the polluted cases compared to the control case are summarized in Tables 2A.2 (SCA minus CLE) and 2A.3 (ABS minus CLE). We note more global radiation reaching the surface for the purely scattering case if compared to the absorbing case. The reason is because in the absorbing case a significant amount of *SW* radiation remains within the CBL, leading to a

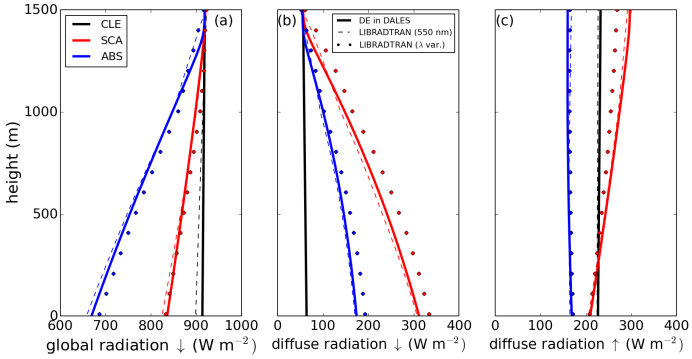

Figure 2.4: Vertical profiles of (a) downward global, and (b) downward diffuse, and (c) minus upward diffuse *SW* radiation within the CBL. The continuous lines indicate the DE model in DALES and the dashes (fixed aerosol properties) and circles (wavelength-dependent aerosol optical depth) the libRadtran runs. The experiments are indicated in the caption.

homogeneous heating rate of approximately 13 K day^{-1}. Our DE in DALES is able to reproduce the augment in the diffuse radiation if aerosols are present within the CBL. Since purely scattering aerosols scatter all the incident light, the diffuse radiation increases by almost a factor of 5 if compared to the clear experiment. Both at the surface and at the top of the CBL, the DE model in DALES correctly captures the impact of aerosols in the outgoing *SW* radiation. Whereas the CBL filled with absorbing aerosols reflects less radiation back to space, we observe an increase at the top of the CBL for the scattering aerosols.

Note that the instantaneous perturbations at the top of the CBL found here compared to the control case (in the order of 50 Wm^{-2}) are much larger than the local instantaneous forcing of aerosols discussed in the IPCC report (e.g. 7 Wm^{-2}, see Ramanathan *et al.* (2001)) because these are extreme cases. The increase in the effective albedo indicates that the CBL is cooling if scattering aerosols are present. The opposite is observed for absorbing aerosols. In Chapter 4 we will quantify the impact of aerosols on the diurnal average of the effective albedo for a mid-latitude CBL in the Netherlands.

In conclusion, the results obtained with the DE model in DALES for the *SW* radiation under polluted conditions are of sufficient accuracy to calculate the effect of aerosols on surface energy budget at the surface (see Eq. 2.1). The error, relative to the control experiment, we make with DE in DALES compared to the libRadtran simulations remains around 5-15%, as suggested by Liou (2002). The errors are small

also relative to the same experiment (Halthore *et al.*, 2005). Note that the polluted cases evaluated here are extreme (heavily polluted CBLs, extremely high/low single scattering albedos, radiation flux kept at the zenith), and were designed to evaluate the limitations of our approach. In reality, under typical aerosol and astronomical conditions, smaller errors are expected. In Chapter 4 we will validate our numerical setup against two typical mid-latitude boundary layers observed in the Netherlands.

The last assumption to be considered concerning the radiation treatment is that in our DE calculations we do not take into account gaseous absorption within the CBL. That means we assume the overall radiative impact of gaseous absorption (in the total HR of the CBL) to be negligible in comparison to that due to aerosols. Angevine *et al.* (1998b), also simulating a mid-latitude CBL, found near cancellation between cooling rate (due to long wave emission, see next section) and gaseous absorption (water vapor, ozone, oxygen and CO_2) within the CBL for a fixed solar zenith angle of 30°. However, absorption by water vapor is not confined to the optically thin limit (Solomon *et al.*, 1987) and will vary throughout the day, whereas the LW radiation cooling remains almost constant (changing less than 5% during the day).

To further investigate this issue, we simulate in libRadtran the same experiment discussed in detail in Chapter 4 (without aerosols) for different times during the day. The objective is to quantify the error we make by not taking into account SW gaseous absorption and LW cooling in the total HR calculation for a typical mid-latitude CBL. The result is shown in Fig. 2.5.

Our results agree with Angevine *et al.* (1998b) showing near cancellation between gaseous SW radiation absorption and LW radiation cooling during most of the convective period. Early in the morning and late in the afternoon slight discrepancies are observed (smaller than 0.7 K/day). We expect this small bias to have a negligible influence on our findings for the whole convective period. We will show in Chapter 4 that early in the morning, when the difference is more significant, the heat budget equation is dominated by the divergence of the turbulent heat flux rather than the contribution of the aerosol heating rate. Moreover, the cancelation of SW gaseous absorption and LW cooling is consistent between all our numerical experiments independent of the amount of aerosols. As a result, we expect that our approach properly represents the aerosol HR during the convective period. In the next section we describe the treatment of the LW radiation in our modeling framework, and the possible interaction between LW radiation and aerosols.

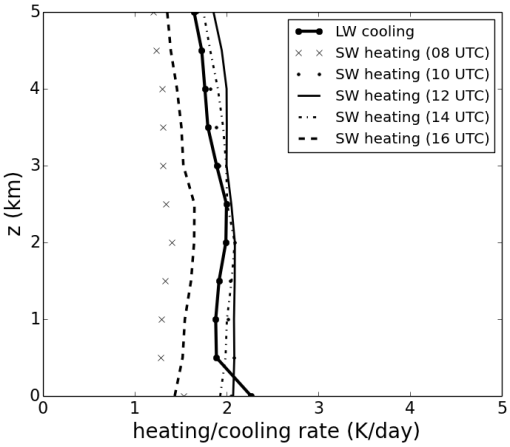

Figure 2.5: Contribution of *SW* gaseous absorption (heating) and *LW* cooling (almost invariant during the day) to the total heating rate. To improve visualization we show *LW* cooling as positive. The times are displayed in the caption.

2.3 The longwave radiation model

Section 2.2 dealt only with scattering and absorption of shortwave radiation in the atmosphere due to gases and aerosols (see Fig. 2.2). The radiation emitted in the infrared part of the spectrum (roughly between 5 μm and 100 μm) is also important for the calculation of the surface energy budget (see Eq. 2.1). Due to the much larger wavelengths compared to the shortwave band, the radiation propagated in that region is called *longwave radiation* (*LW* radiation). In Fig. 2.6 we show an example of the emission spectrum of the Earth's atmosphere (for a cloudless situation).

The profile observed in Fig. 2.6 can be framed by calculating the Planck function spectra (B(λ, T)) for blackbody temperatures within 200-300 K. The term blackbody refers to a surface able to absorb all the incident radiation (Wallace & Hobbs, 2006). We can add to Eq. 2.3, the contribution of the atmospheric emission:

$$\frac{dI}{kds} = -I + \pi B(T). \tag{2.17}$$

Assuming again the plane parallel approximation, and (i) isotropic emissions, and (ii) the infrared emission at the top of the atmosphere equal to zero, i.e. πB(T_{TOA}) = 0, we can find a solution to I (hereafter in this Chapter referred to as *LW*) for

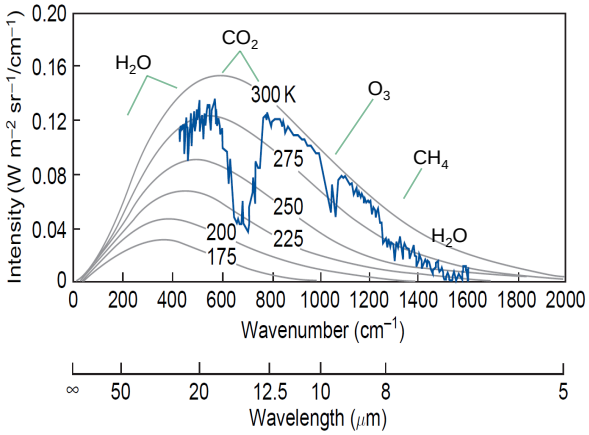

Figure 2.6: Measurements of monochromatic radiation emitted from the Earth observed from the Nimbus 4 satellite (blue curve) as a function of wavenumber and wavelength. The gray curves represent the theoretical Planck blackbody spectra. The major absorbers and the region of absorption of *LW* radiation are indicated in the figure. Adapted from Liou (2002); Wallace & Hobbs (2006) and Huang *et al.* (2013).

both the upward and downward components (Brutsaert, 1975; Liou, 2002; Wallace & Hobbs, 2006):

$$\begin{aligned} LW(z)_{\downarrow} = & \int_{\infty}^{z} \pi B(T) \frac{\partial \epsilon(z)}{\partial z} dz \\ LW(z)_{\uparrow} = & \pi B(T)\epsilon(0) + \int_{0}^{z} \pi B(T) \frac{\partial \epsilon(z)}{\partial z} dz. \end{aligned} \tag{2.18}$$

The term $\epsilon(z)$ is the (column) emissivity compared to a blackbody, i.e. $\epsilon(z) = 1$ for a blackbody medium. The total flux density emitted by a *blackbody* can be obtained by integrating the Planck function over the entire wavelength domain (Liou, 2002):

$$\pi B(T) = \sigma T^4, \tag{2.19}$$

where σ is the Stefan-Boltzmann constant ($\sigma = 5.67 \times 10^{-8}$ Wm^{-2} K^{-4}) and T is the absolute temperature. Note that in the upward *LW* radiation component the first term on the rhs represents the surface emission. This term is absent in the downward component because $\pi \mathrm{B}(T_{TOA}) \approx 0$. The integral term in both equations represents the total atmospheric contribution.

Our first interest is to obtain the downward and upward components of the *LW* radiation at the surface (z=0) in order to calculate the net-available energy Q_{NET}, see

Eq. 2.1. We also will show that the impact of aerosols on the *LW* radiation band is normally small. Concerning the upward component, similarly to Holtslag & de Bruin (1988) and van Heerwaarden *et al.* (2009), we assume the surface as a blackbody, i.e. $\epsilon(0) = 1$, and therefore the broadband upward longwave radiation becomes simply:

$$LW_{\uparrow} = \sigma T_{surface}^{4}. \tag{2.20}$$

Note that the integral in Eq. 2.18 for the upward component disappears at surface. For the downward *LW* radiation reaching the surface the integral term in Eq. 2.18 can be empirically approximated by:

$$LW_{\downarrow} = \epsilon_0 \sigma T_0^4, \tag{2.21}$$

where T_0 is the air temperature near the ground (screen level) and ϵ_0 is called the effective atmospheric emissivity (Brutsaert, 1975). The effective emissivity is a bulk atmospheric property that indicates the capability of the atmosphere to emit longwave radiation as consequence of their composition and thermal stratification (Brutsaert, 1975; Malek, 1997; Long & Turner, 2008; Grobner *et al.*, 2009). Ohmura (2001), Dürr & Philipona (2004) and Bosveld *et al.* (2014) showed that majority of the downward longwave radiation in a cloudless boundary layer comes from the warm and moist lowest atmospheric layers (90% within the first 1000 m). Hence, a fast and reliable way to estimate the downward *LW* radiation at the surface for clear-sky conditions is to use Eq. 2.21 and to parameterize the effective emissivity as a function of the temperature and/or vapor pressure (e_0) at screen level, $\epsilon_0 = f(T_0, e_0)$ (Brunt, 1932; Swinbank, 1963; Brutsaert, 1975; Prata, 1996; Crawford & Duchon, 1999; Niemela *et al.*, 2001; Iziomon *et al.*, 2003; Finch & Best, 2004; Bilbao & de Miguel, 2007; Flerchinger *et al.*, 2009; Bosveld *et al.*, 2014). Most of the formulas available in literature that estimate the effective emissivity are based on empirical relations derived from observations (Brunt, 1932; Niemela *et al.*, 2001), other formulas use an approximation of the radiative transfer equation (e.g. Brutsaert's formulation) or simply use a mathematical fitting to estimate directly the incoming *LW* radiation at the surface (Dilley & Obrien, 1998). As we will show in this Section for a polluted CBL in Sao Paulo (Brazil) and in Sections 4 and 5 for a semi-rural site in Cabauw (the Netherlands) the formula of Brunt (Brunt, 1932) is the most appropriate for the calculation of the surface energy budget (Eq. 2.1) under clear-sky conditions in our modeling framework. However, these findings may be altered by the presence of clouds.

Clouds can be approximated as blackbodies in the longwave band, increasing the net-emissivity of the atmospheric column and therefore the incoming *LW* radiation arriving at the surface. More specifically, this effect becomes even more important

for lower clouds, e.g. *Stratus*, because of the combination of the blackbody emissivity and high temperatures (Niemela *et al.*, 2001). Aerosols may also have an effect on the downward *LW* radiation arriving at the surface depending on their size, concentration and absorption properties (Tegen *et al.*, 1996). On the whole, if clouds and aerosols are present, estimates of the effective emissivity range widely between 0.6-0.95 (Staley & Jurica, 1972). However, in the clear-sky days discussed in this thesis, Sao Paulo (this Section) and Cabauw (Chapters 4 and 5), the effective emissivity remains within the range 0.7-0.8.

Concerning the impact of aerosols and clouds on *LW* radiation, we will present an analysis of measurements made in the city of Sao Paulo (Brazil) - see Barbaro *et al.* (2010). We use for this purpose a comprehensive set of measurements of downward *LW* radiation, and other standard meteorological variables (temperature, and specific humidity, and solar radiation). The meteorological measurement platform is located at the top of the 4-story building of the Institute of Astronomy, Geophysics and Atmospheric Sciences (IAG) of the University of Sao Paulo, in the western portion of the city of Sao Paulo, at 744 m above mean sea level (23°33'35" S; 46°43'55" W) (Oliveira *et al.*, 2002). Screen air temperature and water vapor represent the data measured at 1.5 m above the roof surface. The incoming *LW* radiation measurements were carried out without any horizontal obstruction, so they can be considered valid for a sky-view factor equal to 1 (Jonsson *et al.*, 2006). The measurements were taken between 1997 and 2006 with a sampling frequency of 0.2 Hz and stored as 5-minute averages. The results shown in this Section for downward *LW* radiation at the surface in Sao Paulo (during winter) are comparable to the measurements in Cabauw (as we will show in Chapter 4) for spring and autumn conditions.

To characterize the aerosol loading, we use hourly values of PM_{10} measurements carried out at the surface continuously during 8 years, from 1998 to 2005, in a monitoring air quality surface station, located in the city of Sao Paulo. The station of C. Cesar, closely located to the measurements location, was used here for the observations of particulate matter. The PM_{10} notation is used to describe the particles with 10 micrometers or less in diameter. Therefore, PM_{10} includes also the fine particulate matter ($PM_{2.5}$). The PM_{10} data was measured by the Sao Paulo State Environmental Agency (CETESB), using the Beta Attenuator Method. The major sources of PM_{10} in urban areas are vehicles and industries and in rural areas biomass burning associated to harvesting (Velasco, 2005). Most of the particulate matter in Sao Paulo is generated locally by dust (re-suspended) and by combustion of fossil oil, the later having a strong absorbing character (Castanho & Artaxo, 2001; Sanchez-Ccoyllo *et al.*, 2008). Additionally, in Sao Paulo, the systematic penetration of sea breeze during

the afternoon also brings moisture and (highly scattering) maritime aerosol to Sao Paulo (Codato *et al.*, 2008).

We evaluate the performance of 10 empirical expressions (see Table 2A.4) available in the literature for clear-sky conditions to estimate LW radiation at the surface (see Eq. 2.21). These expressions are useful for us since they can be efficiently implemented in our numerical framework, to provide trustworthy estimates of the LW radiation reaching the surface. Based on the very high PM_{10} concentrations measured in Sao Paulo, here we extend the empirical formulas and will try to find a relation between PM_{10} observations and incoming LW radiation at the surface.

To keep this section as concise as possible, we refer the reader to Barbaro *et al.* (2010) for a detailed description of the meteorological data, as well the methodology to remove glitches from LW radiation observations. There, we also explained how to improve the pyrgeometer (device that measures the LW radiation) precision using the heat balance equation and neural network technique to correct for the dome emission effect.

2.3.1 Diurnal variability of LW radiation and effective emissivity

Based on Malek (1997) and Long & Turner (2008), a subset of LW measurements including only clear-sky days was used to isolate the mean cloud effect on the LW radiation in Sao Paulo. Between 1997 and 2006 we identified 138 days that could be classified as cloud free (Barbaro *et al.*, 2010). As expected, the seasonal distribution of clear-sky days indicates a maximum frequency during winter (dry season) and minimum during summer. The largest number of clear-sky days occurs in August, the driest month of the year (not shown). Therefore, in Fig. 2.7 to ensure robustness in the comparison, we consider the observations carried in Sao Paulo only in August, the month with the largest number of clear-sky days.

We find in Fig. 2.7a if only clear sky days are considered, that the diurnal variation of downward LW radiation shows a smaller intensity but a larger amplitude. This result indicates that the presence of clouds not only increases the intensity of the downward LW at the surface (325 ± 11 Wm^{-2} at 0900 LT and 345 ± 12 Wm^{-2} at 1800 LT), because clouds emit in the atmospheric window, but also decreases its diurnal cycle amplitude, due to the relatively constant cloud base temperature during the day. Air temperature and water vapor differences between all and clear days are apparent mostly during daytime, when clear sky values of air temperature increase and water vapor values decrease more than for all sky conditions (Figs. 2.7b,c). We will show in Chapter 4 that measurements in Cabauw show a similar diurnal variability and magnitude for the downward LW radiation at the surface.

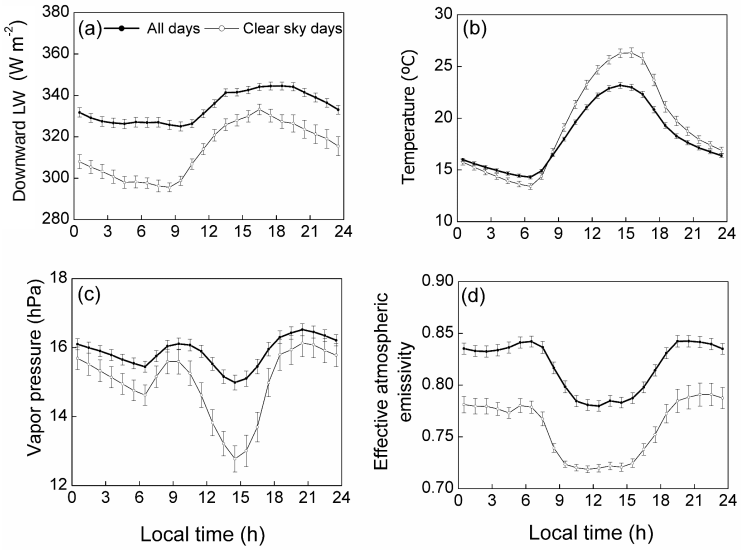

Figure 2.7: Diurnal variation of monthly-averaged hourly values of (a) downward LW radiation, (b) air temperature, (c) air vapor pressure and (d) effective atmospheric emissivity ($LW/\sigma T^4$) at the surface. The thick black lines indicate the monthly-averaged hourly values for August of the entire data set. The thin lines indicate the monthly-averaged values for clear-sky day observations for August of the entire data set. The error is given by the vertical bars.

In Fig. 2.7d we observe the differences in the effective emissivity (defined as $LW_{\downarrow}/\ \sigma T^4$) between all-sky and clear-sky conditions remain relatively constant and equal to $0.060\pm\ 0.007$, or about $7\pm1\%$ during the entire day, indicating that the presence of clouds mainly increases the effective emissivity but does not alter its diurnal evolution. The daytime drop in the effective emissivity, observed in both clear-sky and all-sky conditions, can be explained in terms of the boundary-layer thermodynamics. Early in the morning the screen level temperature and vapor pressure start to increase before the LW radiation, due to the shallow boundary layer confined below the capping inversion formed during the night. At the end of the convective period, the screen level temperature decreases earlier than the incoming LW radiation (due to the negative sensible heat flux at the surface). This delay between temperature and incoming LW radiation is explained by the fact that measurements of incoming LW radiation at the surface are not only influenced by the surface variability, but also by the boundary-layer vertical structure (Grobner *et al.*, 2009).

2.3.2 Effect of aerosols in the downward LW radiation at the surface

We show in Fig. 2.8 the diurnal variation of monthly-averaged hourly values of PM_{10} for Sao Paulo during August (1998-2005).

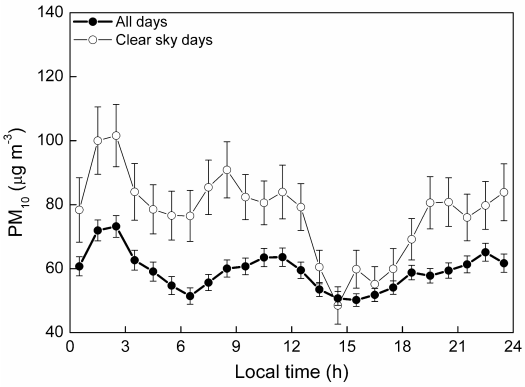

Figure 2.8: Diurnal variation of monthly averaged hourly values of PM_{10} in August for Sao Paulo. The full black circles indicate the hourly average values based on all days of August from 1998 to 2005. The open circles indicate the hourly average for all the clear-sky days during the same time frame. The error is given by the vertical bars.

The diurnal variation in Fig. 2.8 shows the highest concentrations of PM_{10} during clear-sky conditions. Similarly, Castanho & Artaxo (2001) also found considerable differences between diurnal variation of particulate matter concentration during cloudy and clear-sky days. The winter averaged-value for PM_{10} obtained by Castanho & Artaxo (2001) (77 μgm^{-3}) are similar to the clear-sky values obtained in this study. Note that these values are significantly above the limit of 50 μgm^{-3} determined in 2005 by the European legislation on air quality for the 24-hour average of PM_{10} concentrations (Priemus & Schutte-Postma, 2009). Moreover, the PM_{10} is higher during the night due to the stability of the boundary layer.

Despite the large aerosol concentration and the fact that a significant fraction of the aerosol in Sao Paulo is generated from fuel combustion, with an absorbing character, we found that the diurnal pattern of PM_{10} does not show a clear correlation with the incoming LW radiation at the surface. A similar lack of correlation was noted by Jonsson *et al.* (2006) for African cities located in similar latitudes to Sao Paulo. Their work proposes as a possible explanation that the PM_{10} presents a considerable diurnal variation, but the mass of particles in the vertical air column and the optical

depth are about the same during day and night periods. Given the fact that nearby rural areas at the latitude of Sao Paulo are also contaminated it is difficult to deduce how much of the pattern of PM_{10} observed in Sao Paulo is related to local or more regional sources.

In order to further confirm that we can neglect the aerosol influence on the *LW* radiation reaching the surface during clear-sky days we performed a principal components analysis (PCA) to obtain the minimum number of independent variables able to explain the downward *LW* radiation variance. The PCA is a statistical technique that can be used to reduce the variables dimensionality (Harman, 1976; Henry, 1991) in order to replace the inter-correlated variables by a smaller number of independent variables (Kessler *et al.*, 1992; Wilks, 2011). Table 2.1 shows the factor loadings of the principal component analysis for the clear-sky days between 1998 and 2005.

Table 2.1: Factor loadings and communalities obtained for all the clear-sky days during the August months between 1998 and 2005.

Variable	Factor 1	Factor 2	Communalities
Air temperature	94.5%	$<<$ 0.1%	94.5%
Longwave radiation	47.1%	33.6%	80.7%
Vapor pressure	0.1%	89.8%	89.9%
Relative humidity	73.0%	25.6%	98.6%
PM_{10}	0.1%	1.7%	1.8%

We observe in Table 2.1 that the downward *LW* radiation during clear-sky days is associated with two factors, which are able to explain 80.7% of the incoming *LW* radiation variance. Besides the incoming *LW* radiation, factor 1 explains air temperature and relative humidity. The vapor pressure is not explained by factor 1, but it is strongly explained by factor 2. This factor does not explain the air temperature and explains poorly the relative humidity. Moreover, factors 1 and 2 are not related to PM_{10} concentration at the surface. Therefore, the incoming *LW* radiation can be estimated using solely air temperature, following the factor 1, and vapor pressure, following the factor 2. These results and the poor correlation between PM_{10} and downward *LW* radiation at the surface ($R^2 = 0.17$) confirm that there is not a distinguishable relation between them.

Our results in Chapters 3 and 4 (under clear-sky conditions) confirm that the effect of strongly absorbing aerosols (e.g. black carbon) on the atmospheric temperature (e.g. $\approx$ 1.5 K temperature increase during the afternoon) is not strong enough to significantly alter the incoming *LW* radiation at the surface (≈ 5 Wm^{-2}). This value is even within the 5% accuracy of *LW* radiation measurements with commercially

available pyrgeometers (Fairall *et al.*, 1998; Payne & Anderson, 1999; Philipona *et al.*, 2001, 2004; Burns *et al.*, 2003; Marty, 2003). Note that our findings are in agreement with the physical drivers chosen in all the empirical formulas available in the literature used to calculate LW radiation at the surface, i.e. they all depend on temperature and vapor pressure. That result confirms the robustness of the conclusion reached for Sao Paulo (see also Jonsson *et al.* (2006)). In Chapter 4 we will show that good results are obtained in the estimation of incoming LW radiation at the surface without accounting for any aerosol information.

2.3.3 Representing the downward LW radiation for clear-sky days in our numerical framework

Our intent here is to find a simple empirical expressions to estimate the incoming LW radiation at the surface under clear-sky conditions, which could be easily implemented in our LES to evaluate the energy budget at the surface (Arnfield & Grimmond, 1998; Martilli *et al.*, 2002; Offerle *et al.*, 2003; Karam *et al.*, 2010). In Fig. 2.9 we present results calculated by 10 different formulations based on Prata (1996) and Niemela *et al.* (2001) used here to estimate the downward LW radiation for clear sky days at the surface (see Table 2A.4).

The performance of all 10 empirical formulas can be compared by analyzing the mean bias error (MBE), root mean square error (RMSE) and the index of agreement d. The mean bias error indicates the mean deviation and provides information about the long term performance of the model. Here, a positive MBE indicates that the model overestimates the observations. The root mean square

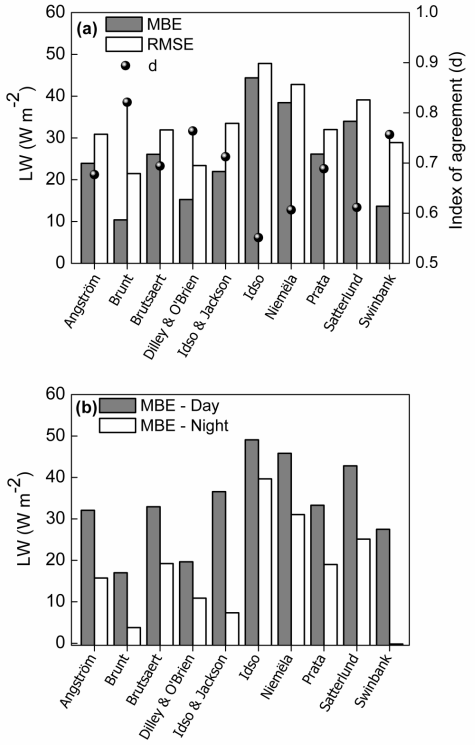

Figure 2.9: Performance of the 10 expressions (see Table 2A.4) used to estimate the incoming LW radiation at the surface in terms of (a) MBE, RMSE and index of agreement d, for the entire period and (b) MBE for day and nighttime periods.

error indicates how well the modeled value approaches the observations. It provides the short-term performance of the model. Smaller RMSE are associated with better estimates. The index of adjustment d varies between 0 and 1 and indicates the level of fitness between estimates and measurements (Willmott, 1982). It can be applied in order to make a cross comparison between the estimates and the observations. Values close to 1 indicate a good performance of the estimates with respect to the observations.

We note from Fig. 2.9 that all expressions overestimate the incoming LW radiation at the surface. The expression of Brunt presents the best results, with the smallest MBE, RMSE and the biggest d (Fig. 2.9a). In addition, all the expressions perform better during nighttime (Fig 2.9b), because all of them are very sensitive to air temperature and vapor pressure variations (Ulden & Holtslag, 1985), which are more prominent during daytime. Moreover, the boundary layer is shallower during the night and the effective emissivity can be better estimated by the screen parameters.

Based on its good general performance shown here, we have chosen to implement the Brunt's formula $[(0.52+0.065\sqrt{e_0})\sigma T_0^4$, see Brunt (1932)] in our numerical framework. We will show in Chapters 4 and 5 that it also provides good estimates for the downward LW radiation at the surface in Cabauw. In DALES the first level of the model (typically located at around 10 m above the surface) is assumed as being equivalent to the screen level. Here, we have also shown that the impact of aerosols in the LW band is negligible, therefore in the next Chapters we devote our attention to the interaction between aerosols and the SW radiation band.

2.4 The interplay among radiation, aerosols, thermodynamics, and surface in the CBL

Earlier in this section (Fig. 2.4) we introduced three case studies to demonstrate the performance of the DE model in DALES. To finalize this section, we shortly demonstrate the relevance of studying the atmospheric turbulent flow coupled to the radiation and to the aerosol properties (AOD, SSA and g). How these properties are explicitly calculated in DALES and their dependence on surface emissions and chemistry will be discussed in Chapter 5. In Chapter 5 we will also discuss the effects of CBL dynamics on the aerosol properties. Here, for simplicity, we only consider the interaction between aerosols and SW radiation.

In Fig. 2.10 we show how aerosols disturb the temporal evolution of three important CBL variables (height, potential temperature and turbulent kinetic energy):

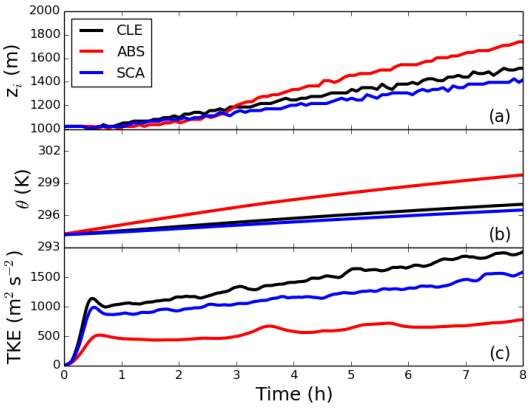

Figure 2.10: Temporal evolutions of (a) boundary-layer height, defined as the height where the buoyancy flux is minimum, (b) CBL-averaged potential temperature and (c) integrated TKE within the CBL. The three experiments are indicated in the legend.

We notice in Fig. 2.10 that the boundary-layer height increases, compared to a clear atmosphere (CLE), if the CBL is filled with a heavy load of absorbing aerosols (ABS). In contrast, it decreases for the CBL filled with scattering aerosols (SCA). Here, the boundary-layer height is estimated as the height where the buoyancy flux is minimum (as shown in Chapter 3).

In SCA, due the reduction in Q_{NET} (by about -68 Wm^{-2}) compared to CLE (not shown), the CBL receives less energy and therefore grows less. For ABS, the reduction in Q_{NET} is even stronger (about -207 Wm^{-2}) because of the absorptive character of the aerosols (see Fig. 2.4a). However, the aerosols heat the CBL uniformly at a rate of approximately 13 K day^{-1}, supplying the CBL with energy and counterbalancing the shading (cooling effect) at the surface. As a net effect, the CBL reaches higher levels since the heating modifies the CBL thermodynamics. We will explore the relation between CBL growth and different aerosol properties in detail in Chapters 3 (for an academic CBL) and 4 (for a realistic CBL based on Cabauw data). The fact that the CBL height for the ABS experiment is shallower during the first hours of the simulation is explained by the increased relative importance of the net-radiative flux (Q_{NET}) during that time (Edwards *et al.*, 2014). We also discuss that issue in Chapter 4. The differences in the average potential temperature within the CBL (warmer for ABS and cooler for SCA) is also explained by the interplay between surface fluxes and the radiation leaving the CBL (see Fig. 2.4c).

The turbulent kinetic energy (TKE) is also strongly affected by the aerosols. The decrease in the TKE is explained only by the reduction in the *turbulent* surface fluxes, therefore the largest impact is noted for ABS. The heating (energy) promoted by the aerosols in ABS is non-turbulent and therefore does not augment TKE. Nevertheless, a heterogeneous vertical distribution of the aerosols also affect the TKE. This will be discussed in detail in Chapter 3.

In summary, in this Chapter we have explained the fundamentals of radiative transfer used throughout this thesis and the importance of accounting for the aerosol properties in the shortwave radiation band. We have also justified our assumptions concerning the radiative transfer model used in DALES by comparing it with a more sophisticated radiative transfer code. With respect to the longwave band, we have shown that aerosols are not relevant to estimate the incoming longwave radiation at the surface. We have presented a study based on the characterization of an observational data set to select the best representation of the incoming LW radiation at the surface. Finally, we have presented an example of a canonical CBL that illustrates the impact of aerosols on the surface energy budget and CBL thermodynamics.

2A Appendix: Tables

Table 2A.1: LES initial and prescribed values for CLE, SCA and ABS experiments. The land-surface properties are taken from the CESAR2008 case (Table 4.1).

Dynamics and radiation properties			
Initial boundary-layer height, z_i [m]		1000	
Geostrophic wind, (U_g, V_g) [m s^{-1}]		(0, 0)	
Large-scale vertical velocity, (w_s) [m s^{-1}]		0	
Global radiation ↓ (top CBL), [Wm^{-2}]		920	
Zenith angle [°]		35	
Heat, Moisture and Extinction	**θ (K)**	**q (g kg^{-1})**	**β_a (km^{-1})**
$z < 1000$ m	294	2	0.6
$z > 1000$ m	$296 + 6 \times 10^{-3}$ $(z - 1000)$	0.0	0.0
Numerical settings			
Spatial domain, (x,y,z) [m]		(8640, 8640, 3000)	
Spatial resolution, (dx,dy,dz) [m]		(60, 60, 15)	
Integration total time [h]		8	
Aerosol properties (0.55 μm)	**CLE**	**SCA**	**ABS**
Aerosol optical depth, τ [-]	0.0	0.6	0.6
Single scattering albedo, ω [-]	–	1.0	0.7
Asymmetry parameter, g [-]	–	0.6	0.6

Table 2A.2: Differences (in Wm^{-2}) between SCA and CLE experiments.

	DE in DALES	LibRadTran (λ var.)	LibRadTran (550 nm)
global ↓ (surf.)	-75	-66	-73
diffuse ↓ (surf.)	248	273	243
diffuse ↑ (top)	62	48	65

Table 2A.3: Differences (in Wm^{-2}) between ABS and CLE experiments.

	DE in DALES	LibRadTran (λ var.)	LibRadTran (550 nm)
global ↓ (surf.)	-243	-214	-239
diffuse ↓ (surf.)	110	128	106
diffuse ↑ (top)	-70	-61	-57

Table 2A.4: Empirical expressions used to estimate the downward atmospheric longwave radiation at the surface for clear sky conditions (Prata 1996; Niemela 2001). e_0, T_0 and σ are respectively the water vapor pressure (hPa), and air temperature (K) measured at screen-level, and Stefan Boltzmann constant (5.67x10^{-8} Wm^{-2}K^{-4}).

Author (Year)	**Expression**
Ångström (1918)	$(0.83 - 0.18 \times 10^{-0.067 e_0})\sigma T_0^4$
Brunt (1932)	$(0.52 + 0.065\sqrt{e_0})\sigma T_0^4$
Swinbank (1963)	$(9.2 \times 10^{-6} T_0^2)\sigma T_0^4$
Idso-Jackson (1969)	$[1 - 0.261 \exp(-7.77 \times 10^{-4}(273 - T_0)^2)]\sigma T_0^4$
Brutsaert (1975)	$1.24 \left(\frac{e_0}{T_0}\right)^{1/7} \sigma T_0^4$
Satterlund (1979)	$1.08 \left[1 - \exp(-e_0^{\frac{T_0}{2016}})\right] \sigma T_0^4$
Idso (1981)	$\left[0.7 + 5.95 \times 10^{-5} e_0 \exp(\frac{1500}{T_0})\right] \sigma T_0^4$
Prata (1996)	$\left\{1 - \left(1 + 46.5 \left(\frac{e_0}{T_0}\right)\right) \exp\left[-\left(1.2 + 3\left(46.5 \left(\frac{e_0}{T_0}\right)\right)\right)^{0.5}\right]\right\} \sigma T_0^4$
Dilley and O'Brien (1998)	$59.38 + 113.7 \left(\frac{T_0}{273.16}\right)^6 + 96.96\sqrt{18.6 \left(\frac{e_0}{T_0}\right)}$
Niemela (2001)	$[0.72 + 0.009\,(e_0 - 2)]\,\sigma T_0^4$

"You may say I'm a dreamer
But I'm not the only one
I hope someday you'll join us
And the world will be as one"

Lennon, J.W. (1971). Imagine. *Imagine*, **1(A)**, Apple Records.

3

Impacts of aerosol shortwave radiation absorption on the dynamics of an idealized convective atmospheric boundary layer

Published as:
Barbaro, E., Vilà-Guerau de Arellano, J., Krol, M.C. & Holtslag, A.A.M. (2013). Impacts of Aerosol Shortwave Radiation Absorption on the Dynamics of an Idealized Convective Atmospheric Boundary Layer. *Boundary-Layer Meteorology*, **148**, 31–49

Abstract

We investigated the impact of aerosol heat absorption on convective atmospheric boundary-layer (CBL) dynamics. Numerical experiments using a large-eddy simulation model enabled us to study the changes in the structure of a dry and shearless CBL in depth-equilibrium for different vertical profiles of aerosol heating rates. Our results indicated that aerosol heat absorption decreased the depth of the CBL due to a combination of factors: (i) surface shadowing, reducing the sensible heat flux at the surface and, (ii) the development of a deeper inversion layer, stabilizing the upper CBL depending on the vertical aerosol distribution. Steady-state analytical solutions for CBL depth and potential temperature jump, derived using zero-order mixed-layer theory, agreed well with the large-eddy simulations. An analysis of the entrainment zone heat budget showed that, although the entrainment flux was controlled by the reduction in surface flux, the entrainment zone became deeper and less stably stratified. Therefore, the vertical profile of the aerosol heating rate promoted changes in both the structure and evolution of the CBL. More specifically, when absorbing aerosols were present only at the top of the CBL, we found that stratification at lower levels was the mechanism responsible for a reduction in the vertical velocity and a steeper decay of the turbulent kinetic energy throughout the CBL. The increase in the depth of the inversion layer also modified the potential temperature variance. When aerosols were present we observed that the potential temperature variance became significant already around $0.7\ z_i$ *(where* z_i *is the CBL height) but less intense at the entrainment zone due to the smoother potential temperature vertical gradient.*

3.1 Introduction

How shortwave (SW) radiation and aerosols interact in the atmosphere is one of the largest uncertainties in climate prediction (Satheesh & Ramanathan, 2000; Tripathi *et al.*, 2005; Johnson *et al.*, 2008). Aerosols modify the vertical profile of radiative heating by absorbing and scattering radiation (Quijano *et al.*, 2000). Depending on the amount and nature of aerosols, the effects on the convective atmospheric boundary layer (CBL) evolution, structure and thermodynamics may differ significantly (Forster *et al.*, 2007). More specifically, the CBL's heat budget and the surface fluxes are modified when radiation is scattered or absorbed, thus allowing less radiation to reach the surface (Charlson *et al.*, 1992; Jacobson, 1998; Raga *et al.*, 2001; Yu *et al.*, 2002; Liu *et al.*, 2005; Li *et al.*, 2007; Johnson *et al.*, 2008; Malavelle *et al.*, 2011). Extending previous studies, we address here the response of the CBL, driven by surface and entrainment fluxes, to aerosol heat absorption.

A proper calculation of the mean heating rates ($\overline{HR}$, henceforth only HR) relies on the availability of both radiation and aerosol measurements. However, only a few observational campaigns have been based on a trustworthy database of both meteorological and air-quality data (Masson *et al.*, 2008). The pioneering works of Zdunkowski *et al.* (1976) and Ackerman (1977) studied for the first time the impact of aerosol SW radiation absorption within the CBL. Zdunkowski *et al.* (1976) showed that HR can locally be as high as 4 K h^{-1} but the overall effect of the polluting aerosol layer is a cooling of the lower CBL due to a reduced surface sensible heat flux. Since then, several studies have followed: Angevine *et al.* (1998b) measured HR in the lower troposphere of around $4 - 5$ K day^{-1} for the FLATLAND series of experiments. Tripathi *et al.* (2005) found via a field campaign in Kampur, located in urban-continental India, that aerosol SW absorption leads to a HR of about 1.8 K day^{-1}. Malavelle *et al.* (2011) found HR associated with SW absorption in West Africa as high as 1.2 K day^{-1}, with 0.4 K day^{-1} as a diurnal mean.

Where surface effects are concerned, Yu *et al.* (2002) showed that less solar radiation reaches the surface due to both aerosol backscattering and absorption, thereby suppressing the growth of the CBL. They also showed that aerosol heat absorption destabilises the upper CBL (see also Johnson *et al.*, 2008).

With respect to the impact on the upper CBL, Ackerman (1977), and more recently Raga *et al.* (2001), have indicated that aerosols induce changes in the vertical structure of the CBL by redistributing heat and affecting the dynamics of the entrainment zone. Raga *et al.* (2001) found for Mexico City HR of 20 K day^{-1} when the absorbing aerosols are located in the upper CBL.

The impact of aerosols on the vertical structure of the CBL has been investigated by means of various methodologies: satellite data (Kaufman *et al.*, 2002), observations made in experimental campaigns (Angevine *et al.*, 1998b; Johnson *et al.*, 2008; Masson *et al.*, 2008), numerical modelling (Cuijpers & Holtslag, 1998; Yu *et al.*, 2002) and combinations of these techniques (Liu *et al.*, 2005; Wong *et al.*, 2012). A process study on how aerosol heating by *SW*-absorbing aerosols influences the turbulent fluxes, surface forcing, vertical structure and heat budget of the CBL is still lacking, however.

The interaction between the turbulence and *SW* radiation, leading to upper CBL stabilization induced by the aerosol absorption of heat, is still not well understood, mainly due to (i) a scarcity of reliable measurements and (ii) a lack of high resolution three-dimensional simulations of the CBL that take the aerosol absorption effect into account. Facing all the limitations of measurements, especially in obtaining aerosol vertical profiles, high-resolution large-eddy simulation (LES) numerical experiments are the best available tool for a systematic study of the impact of absorption on the dynamics of the CBL. LES has been widely used to simulate turbulent flows in the atmosphere since it explicitly resolves large-scale turbulence and parametrizes the smaller eddies (Moeng, 1984; Nieuwstadt & Brost, 1986; Moeng & Wyngaard, 1988; Sullivan *et al.*, 1994).

We therefore take advantage of the capability of LES to investigate the CBL structure and to obtain a better understanding of the impacts of aerosol heat absorption on the CBL dynamics. We pay special attention to the quantification of the aerosol effects on the vertical structure of the CBL, focusing on its entrainment characteristics.

This Chapter is organized as follows: Sect. 3.2 describes the fundamental concepts of radiative transfer theory related to heat absorption. In Sect. 3.3 we explain the design of the numerical experiments and the models used. The aerosol absorption effects in disrupting the CBL's dynamics characteristics are described in Sect. 3.4. The impacts of aerosols on turbulent fluxes, horizontal velocities, potential temperature variances and CBL vertical structure are discussed in Sect. 3.5 and the results are summarized in Sect. 3.6.

3.2 Theoretical framework

Here we describe the impact of the absorbing aerosols on the heat budget and their interaction with the turbulent field. We also introduce the necessary concepts of the radiative transfer theory used in this work. We use as a process illustration the 1D conservation equation of the potential temperature $\bar{\theta}$ for a horizontally homogeneous dry CBL (Stull, 1988; Garratt, 1992):

$$\frac{\partial\overline{\theta}}{\partial t} = -\frac{\partial\overline{w'\theta'}}{\partial z} - w_s\frac{\partial\overline{\theta}}{\partial z} + \overline{HR}\ . \tag{3.1}$$

Here the left-hand term in Eq. 3.1 expresses the potential temperature ($\bar{\theta}$) tendency within a well-mixed CBL. The first term on the right-hand side is the potential temperature turbulent vertical flux divergence, the second describes the vertical advection of potential temperature and the third is the radiation term (or heating rate). Based on radiative transfer theory (see Madronich, 1987), the heating rate (in K s^{-1}) already integrated over the wavelength (λ) can be calculated using either the convergence of the net radiative flux density ($\bar{F}$) or the total actinic flux ($\bar{\phi}$) and the aerosol layer absorption (σ_a, in m^{-1}). Both expressions read:

$$\overline{HR}_F = \frac{1}{\rho c_p}\frac{\partial\bar{F}}{\partial z}\ , \tag{3.2}$$

$$\overline{HR}_\phi = \frac{1}{\rho c_p}\sigma_a\bar{\phi}\ , \tag{3.3}$$

where ρ is the air density, c_p is the heat capacity.

Eq. 3.2 has been used to calculate the heating rate as the divergence of the net radiative flux density between two vertical levels (Lilly, 1968; Stull, 1988; Garratt, 1992; Duynkerke *et al.*, 1995). Here, we are interested in the aerosol heating rates, $HR > 0$, therefore we express it in terms of the convergence of the net radiative flux density. To calculate *HR*, Conant (2002) and Gao *et al.* (2008) used the actinic flux and the aerosol layer absorption efficiency, i.e. the amount of radiation absorbed by the aerosols within the layer, as described in Eq. 3.3. In both cases, the *SW* radiation absorbed by the aerosols is directly translated into heat when ideal thermal contact with the ambient air is assumed (Gao *et al.*, 2008).

Both approaches are suitable since the data required by Eq. 3.2 are widely available (Angevine *et al.*, 1998b; Bretherton *et al.*, 1999) and Eq. 3.3 is predominantly used in air-quality studies, e.g. photolysis rate calculations (Landgraf & Crutzen, 1998; Stockwell & Goliff, 2004). Note that combined, Eqs. 2 and 3 relate the actinic flux to the divergence of net radiative flux density by the amount of absorbing aerosols within the layer (Madronich, 1987; De Roode *et al.*, 2001; Conant, 2002). When there are no absorbing aerosol particles (i.e. $\sigma_a(\lambda) = 0$), the net radiative flux density remains constant (see Madronich, 1987; De Roode *et al.*, 2001). However, when absorbing aerosols are present, radiation is absorbed within the layer, leading to warming. The interaction of aerosols with *SW* radiation is described by: (i) the single-scattering albedo $\omega_0(\lambda)$, (ii) the asymmetry factor g, and (iii) the optical depth

$\tau(\lambda)$, (Liou, 2002), where $\omega_0(\lambda)$ is defined as the ratio between the scattering and the extinction of radiation (therefore unitless). The asymmetry factor g denotes the relative strength of forward scattering. For both Rayleigh and isotropic scattering, $g = 0$. $\tau(\lambda)$ is a unitless and integrated property of an atmospheric column and represents the degree to which aerosols prevent the transmission of light. Based on the radiative parameters discussed here, in Sect. 3.3 we design numerical experiments attempting to investigate the impact of light-absorbing aerosols on the dynamics of the CBL.

3.3 Methodology

3.3.1 Model description

We study the response of turbulence to aerosol heat absorption by means of two different model approaches, LES and a mixed-layer (MXL) model, where the inversion layer is represented by an infinitesimal inversion-layer depth (zero-order jump model - (see Lilly, 1968)). Numerical experiments carried out with the LES technique enable us to understand the modifications to the state variables and calculate explicitly second-order moments in the CBL with aerosols. The LESs also enable us to investigate the impact of aerosol *SW* radiation absorption on the vertical structure of the CBL. Mixed-layer theory (zero- and first-order) is here employed to support the analysis and discussion of the LES results. With the zero-order MXL model we repeat the experiments as in the LES and derive expressions for boundary-layer height and inversion-layer strength equilibrium based on Lilly (1968) and Garratt (1992). By using the first-order MXL equations (Betts, 1974; Duynkerke *et al.*, 1995; Sullivan *et al.*, 1998; Van Zanten *et al.*, 1999; Pino & Vilà-Guerau de Arellano, 2008) we can investigate how the entrainment zone responds to the presence of absorbing aerosols.

The CBL time evolution change due to the aerosol heat absorption is also further analyzed. Isolating the effects of heat absorption within the CBL, and eliminating any other sources of disruption as far as possible, we perform all the analyses after reaching a boundary-layer depth in equilibrium. The conceptual/academic idea of studying a CBL in equilibrium is not new and has been used quite commonly in CBL studies (see Bretherton *et al.*, 1999; Vilà-Guerau de Arellano & Cuijpers, 2000). Our approach is inspired by the method used by (i) Lilly (1968) to investigate the role of longwave radiation in the development of shallow cumulus clouds, and by (ii) Tennekes (1973), in terms of experimental design and dynamics interpretation of a dry convective CBL, and by (iii) Bretherton *et al.* (1999), who studied entrainment by using an archetype boundary layer full of radiative active smoke and by simulating radiative cooling at the top of stratocumulus clouds.

To quantify the impact of the aerosols on the radiation field we use the 1D Tropospheric Ultraviolet and Visible (TUV) radiative model (Madronich, 1987). TUV calculates the net radiative flux density ($\bar{F}$) and actinic flux ($\bar{\phi}$) vertical profiles as functions of aerosol concentration and characteristics. As outlined above, the heating rates are calculated according to Eqs. 3.2 and 3.3, and should be equivalent. We then prescribe the *HR* vertical profiles in our LES.

Here we employ the Dutch Atmospheric Large-Eddy Simulation (DALES) model (Heus *et al.*, 2010) to explicitly simulate the 3D structure of the CBL using vertical and horizontal high resolution and the interaction of turbulence with the heating rate due to aerosol *SW* radiation absorption. The parametrized eddies, solved by sub-grid parametrizations, are determined by a filter that depends explicitly on the numerical grid size (see Sullivan *et al.* (1994) for details).

Fig. 3.1 schematically presents the profiles of $\bar{\theta}$, sensible heat flux $\overline{w'\theta'}$ and *HR*. The dashed lines indicate the zero-order mixed layer approach of the vertical profiles. Definitions such as boundary-layer height (z_i), inversion-layer potential temperature jump ($\Delta\theta$) and entrainment depth (δz) (Betts, 1974; Sullivan *et al.*, 1998), used several times throughout this work, are also shown in Fig. 3.1.

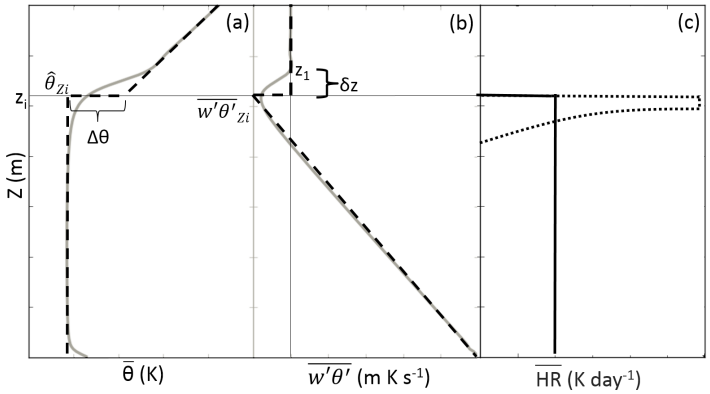

Figure 3.1: Vertical profiles of (a) potential temperature, (b) buoyancy flux and (c) *HR* profiles when the heating rate is located at the top (dotted-line) or uniformly distributed in the CBL (continuous line). Here δz is the entrainment depth ($\delta z = z_1 - z_i$), and z_i is the boundary-layer height based on the minimum buoyancy flux and z_1 stands for the vertical level (above z_i) where the buoyancy flux first reaches zero. $\hat{\theta_{zi}}$ is the temperature and $\overline{w'\theta'_{zi}}$ the buoyancy flux at z_i level. In (a) and (b) the black-dashes represent the zero-order MXL approach and the grey continuous lines represent the LES.

The zero-order MXL model assumes a well-mixed CBL with constant vertical profiles of the state variables within the CBL (flux profiles are therefore linear). The entrainment zone (interface between the CBL and the free troposphere) is represented by an infinitesimal inversion layer (zero-order approach), i.e. $\delta z = 0$ (Lilly, 1968; Betts, 1974). The MXL model expressions for the evolution in time of the potential temperature, inversion jump and CBL height, explicitly considering the impact of radiation absorption, are based on Garratt (1992). The equation for the temporal evolution of the potential temperature is the vertically integrated conservation equation for potential temperature (Eq. 3.1), considering explicitly the *HR* term.

$$\frac{\partial < \bar{\theta} >}{\partial t} = \frac{1}{z_i}\left(\overline{w'\theta'}_0 + w_e \Delta\theta\right) + \frac{1-r}{\rho c_p}\frac{\Delta F}{z_i} \ , \tag{3.4a}$$

$$\frac{\partial \Delta\theta}{\partial t} = \gamma_\theta w_e - \frac{\partial < \bar{\theta} >}{\partial t} \ , \tag{3.4b}$$

$$\frac{\partial z_i}{\partial t} = w_e + w_s - \frac{r}{\rho c_p}\frac{\Delta F}{\Delta\theta} \ , \tag{3.4c}$$

where $< \bar{\theta} >$ is the bulk average potential temperature, z_i is the boundary-layer height, $\overline{w'\theta'}_0$ is defined as the sensible heat flux at the surface, w_e is the entrainment velocity, $\Delta\theta$ is the infinitesimal inversion-layer jump, ΔF (defined as positive) is the absorbed net radiative flux density, r is the fraction of ΔF occurring immediately below the inversion layer, in analogy to the radiative cooling immediately above prescribed by Lilly (1968), γ_θ is the potential temperature lapse rate in the free troposphere, and w_s is the subsidence velocity. To close the mixed-layer equation system (Eqs. 3.4b and 3.4c) the entrainment ratio $\beta_{w\theta}$ is defined as being constant and held equal to 0.2 (Stull, 1988). Note that the *HR* term is defined as being proportional to the divergence of the net radiative flux density, (i) over the whole CBL when $r = 0$, or (ii) confined to the inversion layer when $r = 1$.

As a first step we use the zero-order MXL model to derive simple relations that explicitly take heat absorption into account, for CBL height and the inversion-layer jump. Our primary aim is to determine how the aerosol absorption of *SW* radiation perturbs a CBL in equilibrium. We define the equilibrium as $\frac{\partial z_i}{\partial t} = \frac{\partial \Delta\theta}{\partial t} = 0$ (note $\frac{\partial < \theta >}{\partial t} \neq 0$), in order to isolate the aerosol *SW* absorption from other physical mechanisms, such as diurnal variations. Therefore, we analyze our results after the CBL has reached equilibrium between entrainment and subsidence velocities.

Using Eqs. 3.4a - 3.4c under equilibrium conditions, we found the following expressions for both z_i and $\Delta\theta$:

$$z_i = \frac{1}{\gamma\,|w_s|}\left[\overline{w'\theta'_0}(1+\beta_{w\theta}) + (1-r)\frac{\Delta F}{\rho c_p}\right] \ , \tag{3.5a}$$

$$\Delta\theta = \frac{1}{|w_s|}\left[\beta_{w\theta}\overline{w'\theta'_0} - r\frac{\Delta F}{\rho c_p}\right] \ . \tag{3.5b}$$

The boundary-layer height and inversion-layer jump solutions thus depend on, (i) the sensible heat flux at the surface, (ii) the entrainment rate, (iii) the stability of the free atmosphere, as seen only in Eq. 3.5a, (iv) the vertical distribution of the absorbing aerosols, (v) the absorbed net radiative flux density, and (vi) the subsidence velocity.

As a next step, we use LES to investigate how the boundary-layer turbulent structure is modified by the presence of *SW* absorbing aerosols in a dry CBL.

3.3.2 Design of numerical experiments

We consider a dry, shearless and non-chemical reactive CBL in equilibrium integrated for 30 hours to ensure steady-state. By simulating an idealized boundary layer in equilibrium, we are able to study how the balance of the entrainment (promoting growth) and subsidence (suppressing growth) is perturbed only by the aerosol absorption rather than other possible physical mechanisms (such as radiation scattering). Our experiments are designed to study systematically: (i) the decreased sensible heat flux at the surface, and (ii) the modifications of the entrainment zone due to aerosol heat absorption. Special attention is paid to the vertical structure of the CBL, turbulent transport and heat budget modifications. The initial and boundary conditions of our LES experiments are described in Table 3.1. We kept the design of the MXL model experiments as close as possible to the LES. Despite the non-applicable vertical and horizontal resolutions for the MXL model, the only difference lies in the infinitesimal inversion-layer depth (see Table 3.1: heat) if compared to the finite value prescribed in our LES.

The numerical experiment “CONTROL” simulates a clear CBL (i.e. no absorbing aerosols) in equilibrium driven only by sensible heat flux at the surface. The experiments “UNI” (urban average UNIform aerosol concentration) and “TOP” simulate the same boundary-layer properties as in CONTROL but locating an aerosol layer (i) uniformly within the CBL for UNI, and (ii) located at the upper 200 m of the CBL for TOP (Fig. 3.1c). The experiment CONTROL-SH is identical to the CONTROL case (i.e. no absorbing aerosols) but with the same sensible heat flux as in UNI and

Table 3.1: Initial and prescribed values used for DALES, MXL and TUV (aerosol properties) models for the CONTROL, CONTROL-SH, UNI and TOP experiments. All the properties except CBL height and the potential temperature are kept constant during the simulations. The subscripts 0 and i indicate values at the surface and the entrainment zone, respectively.

Boundary-layer properties			
	Initial boundary-layer height, z_i [m]		1000
	Large-scale subsidence velocity, w_s [m s^{-1}]		
		$z < 1000$ m	$-2 \times 10^{-2} \left(\frac{z}{z_i}\right)$
		$z > 1000$ m	-2×10^{-2}
	Geostrophic wind, (U_g, V_g) [m s^{-1}]		$(0, 0)$
	Integration total time [h]		30
	Spatial domain, (x,y,z) [m]		$(12800, 12800, 2000)$
	Spatial resolution, (dx,dy,dz): [m]		$(50, 50, 10)$
Heat			
	Surface sensible heat flux, $\overline{w\theta}_0$ [K m s^{-1}]		
		CONTROL	0.1
		CONTROL-SH	0.08
		UNI	0.08
		TOP	0.08
	Potential temperature profile [K]		
	DALES	MXL	
$z < 1000$ m	288.0	$z < 1000$ m	288.0
1000 m $< z <$ 1010 m	$288.0 + 10^{-1}(z - 1000)$	-	
$z > 1010$ m	$289.0 + 6 \times 10^{-3}(z - 1000)$	$z > 1000$ m	$289.0 + 6 \times 10^{-3} z$
Aerosol properties			
	Aerosol layer absorption efficiency ($z<$ 1000 m), σ_a [m^{-1}]		25×10^{-6}
	Aerosol optical depth, τ(500 nm)		0.2
	Asymmetry factor, g		0.61
	Single scattering albedo, ω		0.9
	Aerosol specific density [g cm^{-3}]		2
	Average particle radius [nm]		100
	Total aerosol concentration [μg m^{-3}]		20
	Absorbed SW radiation [K m s^{-1}]		
		CONTROL	0.0
		CONTROL-SH	0.0
		UNI	0.02
		TOP	0.02

TOP. Doing so, enables us to isolate the effect of the surface heat flux on the CBL dynamics. Notice that the CONTROL-SH experiment mimics a boundary layer where the surface heat flux decreases by the same amount as in UNI and TOP, assuming a clear CBL.

In UNI and TOP, the shadowing effect at the surface due to aerosol absorption is taken into account by reducing the sensible heat flux at the surface by the same amount as the heat absorbed within the CBL. Thus, both the UNI and TOP experiments are comparable to CONTROL, since the total heat introduced in the system always remains constant. The total heat input (HI) in m K s^{-1} reads:

$$HI = \overline{w'\theta'_0} + \int_0^{zi} \overline{HR}\, dz \ , \tag{3.6}$$

where $\int_0^{zi} \overline{HR} dz = 0$ for the CONTROL case. We thus ensure that the three numerical experiments are energy consistent and that the impact on the CBL dynamics is due to the amount and vertical distribution of the aerosols.

We use the TUV model to obtain realistic vertical profiles of actinic flux and net radiative flux density for the CONTROL and UNI experiments and then calculate the atmospheric heating rate by means of Eqs. 3.2 and 3.3. The specified aerosol properties τ, ω_0, g (Table 3.1) in TUV are based on previous studies, and are representative of an urban, moderately polluted CBL (Raga *et al.* (2001); Yu *et al.* (2002) and references therein; Hewitt & Jackson (2009)). The molecular absorption of O_3 and NO_2 is not considered. The TUV model maximum wavelength range integration $\lambda[230 - 1000]$ nm, $\delta\lambda = 2$ nm and vertical resolution $\Delta z = 30$ m are used. The surface albedo is 0.2. No radiative transfer code is used to calculate HR for the TOP experiment. Instead, similar to Bretherton *et al.* (1999), we integrate the HR profile obtained for the UNI case and place the total heat in the upper 200 m of the CBL by using an exponential decay with a maximum at the top of the CBL. By doing so, we ensure that the amounts of energy absorbed in UNI and TOP are the same.

In Fig. 3.2 we show the radiation fields calculated by TUV and the subsequent HR calculated based on Eqs. 3.2 and 3.3 for UNI and on the exponential decay for the TOP experiment.

The constant net radiative flux density vertical profile shows that no SW absorption takes place either in the free atmosphere and within the CBL for CONTROL (see Eq. 3.2). Within the CBL, in the UNI experiment the absorbing aerosols linearly reduce the net radiative flux density at the surface by about 20 Wm^{-2}, in agreement with the values obtained by Yu *et al.* (2002) for similar aerosol properties. Rayleigh scattering is responsible for the slightly diminished actinic flux (dashed lines) towards

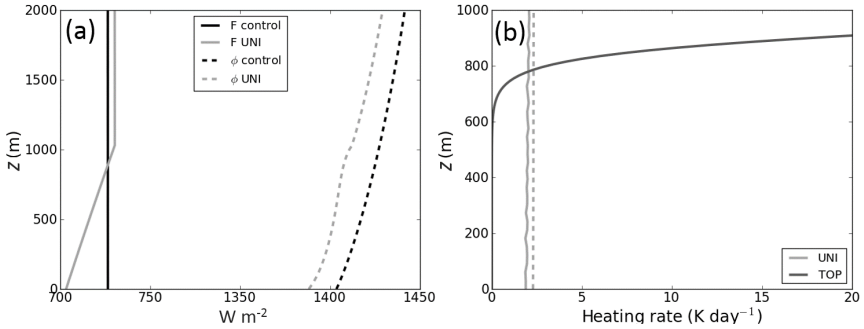

Figure 3.2: (a) Profiles of the net radiative flux density (continuous lines) and actinic flux (dashed lines); (b) the respective HR vertical profiles. In (b) the continuous line for UNI represents the heating rate calculated based on the net radiative flux density divergence (Eq. 3.2). The dashed line is the heating rate based on actinic flux and aerosol layer absorption efficiency (Eq. 3.3). Note that the heating rate obtained for the TOP experiment is based on the exponential decay. To improve visualization, the vertical scale is different and the HR peak (25 K day^{-1}) for the TOP case is not shown.

the surface. The smaller ϕ observed in UNI is caused by the SW absorption throughout the CBL. Since there are no aerosols in the free atmosphere (i.e. $\sigma_a = 0$ above 1000 m) the net radiative flux density profiles are constant in height.

In Fig. 3.2b we observe that the absorption of SW radiation by aerosols significantly heats the CBL by 1.8 K day^{-1}, uniformly distributed for the UNI case and by about 25 K day^{-1} at $z = 1000$ m (peak not shown) when concentrated at the upper CBL (for TOP experiment). It is important to mention that HR calculated based on the net radiative flux density divergence (Eq. 3.2) and the total actinic flux (Eq. 3.3) for the UNI case (dashed and full-light grey lines in Fig. 3.2b) are equivalent. Since meteorological and air-quality experiments are not designed with the same aim in mind (Bierwirth *et al.*, 2010; Wong *et al.*, 2012), synchronized and reliable measurements of net radiative flux density and actinic flux are difficult to obtain. The results showed in Fig. 3.2b open an alternative path to the HR calculation by using two different radiative quantities. The slightly larger HR observed in the calculation based on the actinic flux profile is due to the assumed constant aerosol absorption coefficient within the CBL (see Angevine *et al.*, 1998b). Moreover, the TUV model integrates the wavelength only up to 1000 nm, missing therefore a part of the solar spectrum. This assumption should only affect the actinic flux results since in the net flux density approach we are interested in the divergence of the flux canceling any contribution.

The *HR* profiles are comparable to previous work: Raga *et al.* (2001) with a similar set-up as the one used in the TOP experiment found *HR* as large as 30 K day^{-1} supported by observations in Mexico City. In the UNI case, HR is comparable to the results of Angevine *et al.* (1998b); Jochum *et al.* (2004) and Tripathi *et al.* (2005), who found 4 K day^{-1}, 6 K day^{-1} and 2 K day^{-1} respectively. The *HR* values obtained for both UNI and TOP experiments are prescribed in our LES.

3.4 Effects of aerosol heat absorption on the CBL characteristics

We start by studying the CBL height and entrainment zone responses to the aerosol heat absorption. Table 3.2 summarizes the main CBL characteristics for the three experiments after 30 hours of LES.

Table 3.2: CBL properties after 30 h of simulation; w_* is the convective velocity scale, and Ri_δ is the bulk Richardson number at the entrainment zone.

Case	w_* (m s^{-1})	z_i (m)	$\Delta\theta$ (K)	δz (m)	Ri_δ	$\beta_{w\theta}$
Control	1.50	1040	1.1	110	15.0	0.16
UNI	1.38	955	0.61	130	11.3	0.14
TOP	1.34	860	0.1	210	1.61	0.14

In Table 3.2, δz is the entrainment depth ($\delta z = z_1 - z_i$, see Fig. 3.1), where z_i is the boundary-layer height based on the minimum buoyancy flux and z_1 is the vertical level (above z_i) at which the buoyancy flux first reaches zero. Ri_δ is the bulk Richardson number calculated for the entrainment zone (Sullivan *et al.*, 1998), where:

$$Ri_\delta = \alpha \Delta\theta \frac{z_i}{w_*^2} \tag{3.7}$$

and α is the buoyancy parameter. We see from Table 3.2 that the aerosol absorption of SW radiation makes the ABL shallower by 8.2% and 17.3% for the UNI and TOP simulations respectively. Moreover, in UNI and TOP, the potential temperature jump is weaker and the entrainment zone is deeper and less stable. The entrainment ratio for UNI and TOP experiments is equally decreased (12.5%) compared to the CONTROL experiment, which identifies the surface flux as the driving mechanism controlling the entrainment rate. By focusing on the depth of the entrainment zone, we find that the aerosol heat absorption, besides destabilizing (decreasing Ri_δ), also deepens the

entrainment zone (EZ) by 18% and 91% in UNI and TOP respectively. Since the effects are more pronounced in the TOP experiment, the stability and depth of the entrainment zone depend not only on the amount of aerosols, but also on their vertical distribution. Accordingly, the combination of processes indicates that the aerosol heat absorption has a significant effect on both the surface and the entrainment zone. Further analysis of the CBL vertical structure is therefore needed for an understanding of the changes in the turbulent field caused by the absorption of heat within the CBL (Fig.3.2b). Fig. 3.3 shows the instantaneous profiles of the potential temperature calculated by LES, where the arrows represent the wind vector in the CBL. In the left-hand side of each figure we also plot the 1-hour horizontally-averaged potential temperature.

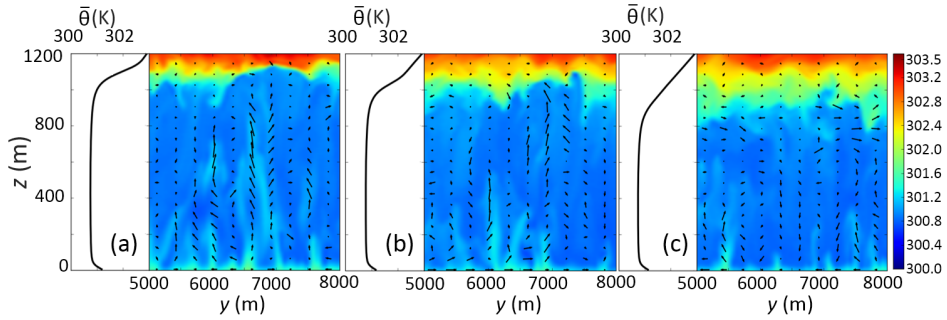

Figure 3.3: 1-hour slab averaged potential temperature $\bar{\theta}$ and y-z cross-sections of the θ field for experiments (a) CONTROL, (b) UNI and (c) TOP after 30 h of simulation. The arrows represent the instantaneous wind field $(\vec{V}, w^{'})$. To improve visualization we show only a sub-part of the horizontal domain (y) $5000 - 8000$ m. Note that due to the cycle boundary conditions and horizontal homogeneity the cross-section location in the x-direction is arbitrary.

The lighter colours within the CBL highlight thermals transporting warmer air, therefore ascendant motion (see wind field), while the darker zones show the subsidence motion. The intensity of the vertical movements is more pronounced for the CONTROL case. The diminution in the vertical motion magnitude between CONTROL (maximum 2.4 ms^{-1}), UNI (maximum 2.0 ms^{-1}) and TOP (maximum 1.6 ms^{-1}) is explained by the shadowing effect at the surface by the aerosol SW radiation absorption. Since less sensible heat flux is prescribed for UNI and TOP the turbulent kinetic energy (TKE) is also reduced. This will be discussed in detail in the next section. Even though the effect of the smaller surface heat flux for UNI and TOP

explains the reduced vertical motions this is not sufficient to enable us to understand all the observed changes. Comparing the UNI and TOP experiments (both with identical surface heat fluxes) we find weaker thermals and updrafts/downdrafts for the latter. We also observe that for TOP the vertical motions are weakened throughout the CBL while in CONTROL and UNI this occurs mostly at higher levels. This indicates a combined effect changing not only the surface heat flux but also the atmospheric structure (as suggested by Ackerman (1977) and Raga *et al.* (2001)). The earlier potential temperature stabilization ($\bar{\theta}$ vertical profile) in the vicinity of the entrainment zone observed for UNI, and more significantly for TOP, is explored in detail in Sect. 3.5.

Fig. 3.4 shows the approach to equilibrium of the boundary-layer height and potential temperature inversion jump calculated using the DALES and MXL models.

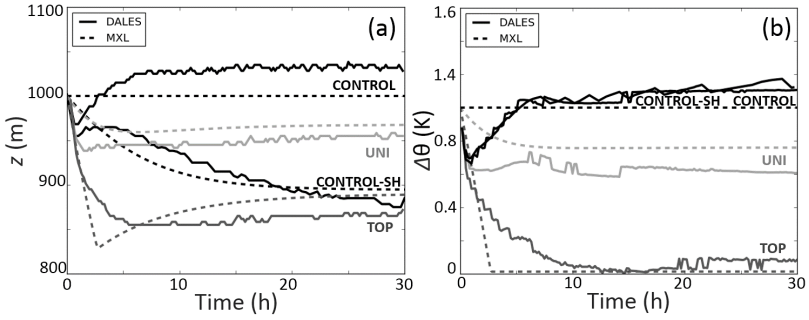

Figure 3.4: Evolution of (a) CBL height and (b) inversion-layer jump. The continuous lines indicate LES and the dashed lines MXL results.

We observe that UNI and CONTROL reach the equilibrium situation for both CBL height and potential temperature inversion jump two to three hours earlier than TOP. This is explained by the already well-mixed aerosol initial profile in UNI and the absence of aerosols in CONTROL. The aerosol layer in the TOP experiment disturbs the inversion-layer jump more strongly (Fig. 3.4b), which means that more time is needed to reach a new equilibrium state. The MXL model results are comparable to the LES in all cases. The satisfactory agreement enables us to provide a mathematical/physical interpretation of the results (Eqs. 3.5a and 3.5b).

As Fig. 3.4a shows, we find that the CBL depth is smaller in both the UNI (955 m) and TOP (860 m) experiments, agreeing with the findings of Yu *et al.* (2002) and Wong *et al.* (2012). Eq. 3.5a predicts that, in the absence of the absorption of heat (no aerosols, $\Delta F = 0$) and with the same atmospheric conditions (subsidence and

free atmospheric stability), the CBL depth depends only on the surface heat flux and the entrainment rate, in the absence of other large-scale forcing. Since $r = 1$ for the TOP experiment, Eq. 3.5a has the same solution for both CONTROL-SH ($\Delta F = 0$) and TOP (as also shown in Fig. 3.4a). The CONTROL-SH experiment has less total energy within the system but the same subsidence profile as CONTROL, which means that equilibrium is reached at a later stage. The MXL model also reproduces CONTROL-SH. The different MXL model solutions, depending on where the heat absorption occurs, show that the effects of the aerosol absorption depend not only on the amount (affecting ΔF) but also on the vertical distribution (r) of aerosols.

Fig. 3.4b shows the temporal evolution of the potential temperature inversion-layer jump. The $\Delta\theta$ temporal evolution for CONTROL-SH follows the CONTROL experiment, as Eq. 3.5b also shows. Note that we define $\Delta\theta$ as the difference between the average potential temperature from the surface until z_i and a linear extrapolation from the free-atmosphere potential temperature lapse-rate to the same level (see Fig. 3.1a). Since the potential temperature inversion-layer jump is smaller in TOP (0.1 K) than UNI (0.6 K), a priori the entrainment zone is less stable (see Table 3.2) and should lead to a deeper CBL. However, the weakening of the potential temperature inversion jump does not lead to an increase in the depth of the CBL (Fig. 3.4a). Rather, the CBL becomes shallower when $\Delta\theta$ is smaller. This apparent contradiction indicates that the aerosol layer at the top of the CBL, besides reducing the potential temperature jump, stabilizes the lower layers by extending the inversion depth (see Fig. 3.3c). Zdunkowski *et al.* (1976); Ackerman (1977); Jacobson (1998) and Raga *et al.* (2001) have already described this effect but were unable to quantify it explicitly. In the next section we investigate the vertical structure of the CBL and the entrainment zone in more detail.

3.5 Impact of aerosol heat absorption on the entrainment zone

The aerosol absorption of *SW* radiation changes both the surface and the EZ. Here we focus on the response of the dynamics to the aerosol heat source in the upper CBL and in the entrainment zone. The cross-sections in Fig. 3.3 have already shown that the temperature and wind fields change depending on the vertical distribution of the aerosols. We therefore first investigate the atmospheric stability below the EZ by calculating the horizontally-averaged potential temperature anomaly and characterize its strength by the squared Brunt-Väisälä frequency (N^2),

$$N^2 = \alpha \frac{\partial \bar{\theta}}{\partial z} \ . \tag{3.8}$$

The potential temperature anomaly profile is defined as $\theta^{'} = \bar{\theta} - < \bar{\theta} >$, where $< \bar{\theta} >$ is the bulk average potential temperature (see Eq. 3.4a). The results are presented in Fig. 3.5.

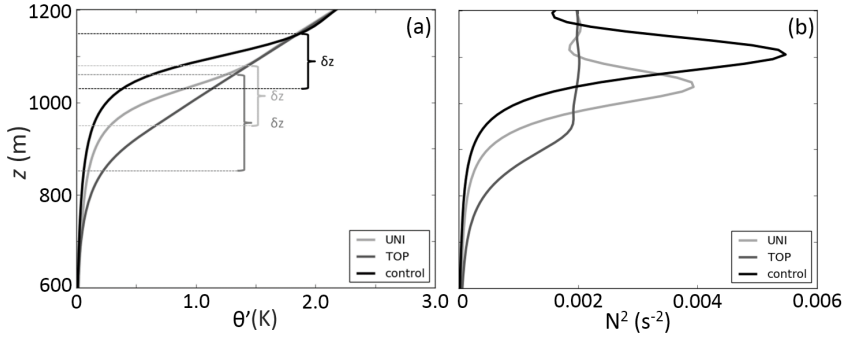

Figure 3.5: Vertical profiles of the last-hour horizontally averaged (a) potential temperature anomaly, and (b) squared-Brunt-Väisälä frequency. In (a) we also identify the entrainment zone depth. To improve visualization, $\theta^{'}$ and N^2 are shown only from 600 m to 1200 m.

A significantly earlier rise of $\theta^{'}$ and N^2 for the UNI and TOP experiments is found, corroborating the lower CBL stratification observed in Fig. 3.3. In Fig. 3.5a, the deepening of the entrainment zone depth for UNI and TOP (see also Table 3.2, δz) can also be seen. The $< \bar{\theta} >$ is independent of the aerosol absorption of heat in all the experiments, showing that our simulations conserve energy. As already indicated by the different values of the Richardson number (Table 3.2), N^2 indicates a less stable stratified EZ in the TOP experiment (Fig. 3.5b). The N^2 profiles reach the same value in the free atmosphere, since $\frac{g}{\theta_0}\gamma = 2 \times 10^{-4}$ s^{-2} for the three experiments. The N^2 peak at the entrainment zone is not observed for the TOP experiment because of the smaller $\Delta\theta$ (Fig. 3.4b) leading to a less stable entrainment zone. Moreover, $N^2 = 0$ below 600 m (not shown) since the layer is well-mixed.

3.5.1 Heat budget of the entrainment zone

The main differences among the experiments lie in the changes in the EZ vertical structure caused by the aerosol heat absorption. However, the LES results indicate

that the minimum of the entrainment flux ($\beta_{w\theta} = 0.14-0.16$) and average entrainment velocity (20 mm s^{-1}) are similar in all the three experiments. In turn, an increased EZ depth can be observed for the UNI and TOP experiments (see Table 3.2).

Since the inversion-layer depth becomes relevant to our analysis we use the first-order mixed layer (1-MXL) theory, in which a finite entrainment depth is assumed instead of an infinitely small depth, to support the LES data interpretation. The 1-MXL model was used earlier by Sullivan *et al.* (1998) and Pino & Vilà-Guerau de Arellano (2008) for the same purpose. The entrainment heat budget expression for the 1-MXL considering radiation absorption is derived after vertically integrating the heat conservation equation (Betts, 1974; Sullivan *et al.*, 1998; Van Zanten *et al.*, 1999; Pino & Vilà-Guerau de Arellano, 2008),

$$w_e \Delta\theta = \overline{w'\theta'}_{z_i} + \delta z \frac{\partial \hat{\theta_{zi}}}{\partial t} - \int_{z_i}^{z_1} \overline{HR} dz \ . \tag{3.9}$$

Betts (1974) first presented the equation without considering the radiation contribution (last term in the right-hand side), but Van Zanten *et al.* (1999) later incorporated *HR* in terms of the divergence of net radiative flux density to study longwave radiative cooling of stratocumulus clouds. Here, for the first time, we apply it in terms of the integral of the heating rate within the entrainment depth.

Following the derivation of Betts (1974), and taking the radiation term into account as in Van Zanten *et al.* (1999), and using the same methodology as suggested by Sullivan *et al.* (1998), we can conveniently re-write Eq. 3.9 in terms of the bulk Richardson number defined in Eq. 3.7:

$$\frac{w_e}{w_*} = \frac{(\beta_{w\theta} + \beta_{\delta z} - \beta_{HR})}{Ri_\delta^n} \ , \tag{3.10}$$

where $\beta_{w\theta} = \overline{w'\theta'}_{z_i} / \overline{w'\theta'}_0$, $\beta_{\delta z} = \left(\delta z \frac{\partial \hat{\theta}}{\partial t}\right) / \overline{w'\theta'}_0$, $\beta_{HR} = \int_{z_i}^{z_1} \overline{HR} dz / \overline{w'\theta'}_0$ and "n" is the Richardson number's power-law index as proposed by Fernando (1991) and used by Pino & Vilà-Guerau de Arellano (2008). This notation is convenient since it enables us to investigate the effects of the surface heat flux ($\beta_{w\theta}$), entrainment depth ($\beta_{\delta z}$) and *SW* radiation absorption (β_{HR}) calculated by the LES individually. Table 3.3 shows the contribution of each term to the entrainment heat budget (Eq. 3.10).

Despite the slight reduction observed in the absolute entrainment rate of UNI and TOP ($0.16 - 0.14$) its relative importance to the heat budget significantly decreases from around 55% to 23%. Moreover, the term that includes the dependence of the EZ depth is significant for all the experiments, being $45-49\%$ of the total contribution to the entrainment heat budget (Sullivan *et al.*, 1998; Van Zanten *et al.*, 1999). However, the absolute value increases in the TOP experiment, indicating a wider EZ (see δz in

Table 3.3: Heat budget at the EZ. Individual contributions (absolute and relative - in %) of each term in Eq. 3.10 are calculated by the LES for the last hour of simulation.

	$\beta_{w\theta}$	$\beta_{\delta z}$	β_{HR}	n	$\frac{w_e}{w*}\Big\vert_{DALES}$	$\frac{(\beta_{w\theta}+\beta_{\delta z}-\beta_{HR})}{Ri^n}$
Control	−0.16(55.2%)	0.13(44.8%)	–	1.1	0.014	0.015
UNI	−0.14(40%)	0.17(48.6%)	0.04(11.4%)	1.2	0.015	0.015
TOP	−0.14(23.0%)	0.28(45.9%)	0.19(31.1%)	5.5	0.015	0.017

Table 3.2 and Fig. 3.5). The β_{HR} term in UNI and TOP represents respectively 11% and 31% of the total contribution to the entrainment heat budget. This increased β_{HR} contribution for TOP is to be expected, since the aerosol heating is concentrated in the upper CBL. The index values (n) in Eq. 3.10 in CONTROL and UNI agree well with those proposed by Pino & Vilà-Guerau de Arellano (2008). For the TOP case, the potential temperature inversion jump is drastically reduced (0.1 K, Fig. 3.4b), resulting in a different $n = 5.5$. Fernando (1991) and Sullivan *et al.* (1998) have already pointed out that $Ri < 14.0$ needs a different power-law index. The TOP results also indicate a deeper EZ due to the major contribution of the aerosol heat absorption term (β_{HR}) to the EZ heat budget.

The last two columns in Table 3.3 refer to the comparison of the Eq. 3.10 right- and left-hand sides calculated independently with the LES. The agreement for all the cases shows that 1-MXL theory satisfactorily explains the changes in the EZ heat budget when aerosol absorption takes place. Heat absorption may therefore be as important as entrainment deepening in the EZ heat budget. High-resolution models like LES are needed to accurately calculate the gradients in the entrainment zone and to properly quantify the effect of aerosol heat absorption.

3.5.2 Entrainment zone high-order statistics

We have observed that aerosol heat absorption (i) weakens the potential temperature jump, and (ii) deepens the EZ. Here we investigate the second-order statistical moments for velocity and temperature to further quantify the impact of aerosol heat absorption.

In Fig. 3.6 we show the vertical profiles of the horizontal velocity variances and the turbulent kinetic energy for the three cases under study.

We observe in Fig. 3.6a typical values for a CBL (Sullivan *et al.*, 1998). Close to the top of the CBL, however, the gradients of the horizontal velocity variance are different due to the modifications in the EZ depth and potential temperature inversion jump. The horizontal variance maximum observed in the CONTROL experiment

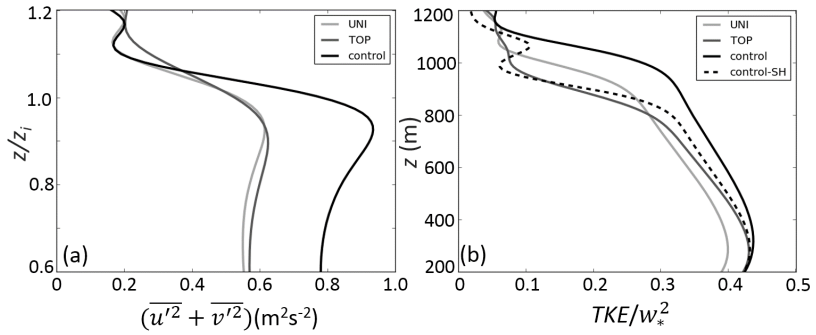

Figure 3.6: Vertical profiles of the last-hour horizontally averaged (a) horizontal velocity variance and (b) normalized turbulent kinetic energy for CONTROL, UNI, TOP and CONTROL-SH (only for TKE). To focus more clearly on the upper CBL characteristics, the horizontal velocity variance is shown from $0.6 - 1.2$ z/z_i.

between $0.8 < z/z_i < 1.0$ indicates a transfer from vertical to horizontal motions when the updrafts encounter the strong inversion layer (see also Fig. 3.3a). The same behaviour (though less intense) is observed in UNI. In TOP, the decreased potential temperature jump and the deeper entrainment zone lead to a weaker variance onset since less momentum is transferred from the updrafts (Sullivan *et al.*, 1998). We quantify the ratio of the vertical velocity variance to the horizontal one, $\frac{\overline{w'^2}}{\overline{u'^2}+\overline{v'^2}}$, to determine the degree of anisotropy in the CBL. Our results show less pronounced vertical motions in TOP (0.42) than in the CONTROL (0.50) and UNI (0.49) experiments, indicating more conversion of vertical motions into horizontal ones within the CBL (see also Fig. 3.3c).

In Fig. 3.6b we show the dimensionless TKE vertical profile for all the experiments also including CONTROL-SH to bring out the contribution of the reduced surface sensible heat flux to the TKE profile. Since our intention is to compare the different TKE vertical structures, this figure is not normalized by z_i. For TOP, closer to the surface the TKE behaviour is totally explained by the surface heat forcing (the TKE profile follows CONTROL-SH). However, above around 400 m the TKE vertical profile for TOP shows a steeper decrease compared to CONTROL-SH, indicating that the CBL vertical structure is altered. The physical explanation is as follows: in the cases of CONTROL and UNI, the updrafts find less resistance than in TOP to raise within the mixed-layer and reach the EZ.

The modifications of the EZ characteristics are further quantified with an analysis

of the potential temperature variance. We present in Fig. 3.7 the vertical 1-hour average $\overline{\theta'^2}$ profile.

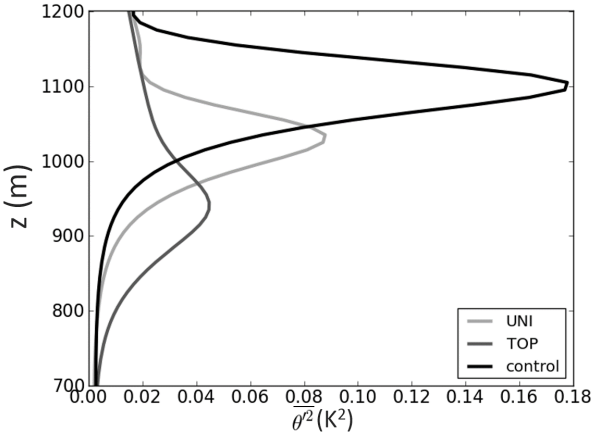

Figure 3.7: Vertical profiles of the last-hour horizontally-averaged $\bar{\theta}$ variance. In order to focus more clearly on the upper CBL characteristics, the potential temperature variance is shown from 700 m to 1200 m.

The $\overline{\theta'^2}$ maximum for the three experiments is found within the EZ. The earlier onset of the $\overline{\theta'^2}$ for UNI and TOP experiments corroborates the lower stratification observed in $\theta^{'}$ and N^2 profiles (Fig. 3.5). The aerosol heat absorption affects the magnitude of the $\bar{\theta}$ variance by reducing it by 47% and 75% in UNI and TOP respectively. The weaker potential temperature jump leads to less $\overline{\theta}$ variance at the top of the CBL. A sharper maximum in $\overline{\theta'^2}$ can be observed in CONTROL and UNI if compared to TOP. Analysing the $\overline{\theta'^2}$ budget enable us to study the responsible physical mechanism that leads to the decrease in the potential temperature variance. Following Stull (1988), Mauritsen *et al.* (2007), Zilitinkevich *et al.* (2007), and Zilitinkevich *et al.* (2008), the potential temperature variance budget (explicitly considering the radiation term) reads:

$$\frac{1}{2}\frac{D\overline{\theta'\theta'}}{Dt} = -\overline{w'\theta'}\left(\frac{\partial\bar{\theta}}{\partial z}\right) - \frac{1}{2}\frac{\partial\overline{w'\theta'\theta'}}{\partial z} - \frac{1}{\rho c_p}\overline{\theta'\frac{\partial F'}{\partial z}} - \epsilon_d \ , \tag{3.11}$$

where the term in the left-hand side is the tendency of the potential temperature variance. The first term on the right-hand side is the production of potential temperature variance, the second indicates the variance vertical transport, the third is the production/destruction of variance due to radiation absorption (also called ϵ_R) and

the fourth is the dissipation of potential temperature variance. Fig. 3.8 shows the vertical profiles of the $\bar{\theta}$ variance budgets in all cases.

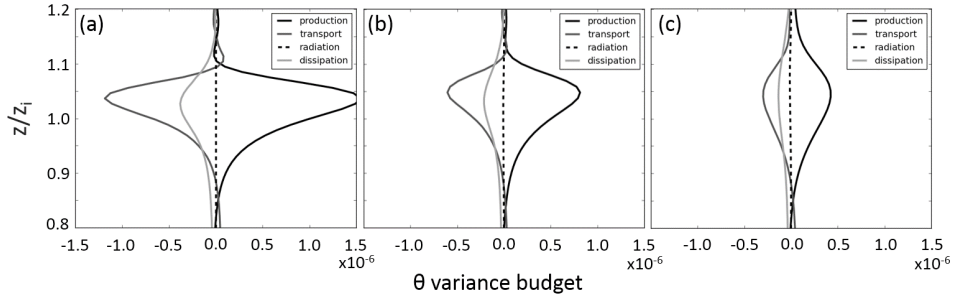

Figure 3.8: Budget of the last-hour horizontally-averaged potential temperature variance normalized by $w_*\theta_*/z_i$ for (a) CONTROL, (b) UNI and (c) TOP. To focus on the EZ characteristics, the budgets are shown from $(0.8-1.2)z/z_i$.

The production term $\left[\overline{w'\theta'}\left(\frac{\partial\bar{\theta}}{\partial z}\right)\right]$ is reduced for both UNI and TOP by different magnitudes due to the diminution in the $\left(\frac{\partial\bar{\theta}}{\partial z}\right)$, (see Fig.3.5b), since the entrainment rates of UNI and TOP are identical. The transport term indicates that all the $\bar{\theta}$ variance is constrained within the EZ since it is transported to the same place as where it is produced and dissipated. The ϵ_R term is not significant for any of the simulations remaining around $1-10\%$ of ϵ_d for all the cases (Stull, 1988).

The vertical profiles of the potential temperature anomaly (Fig.3.5a), Brunt-Väisälä frequency (Fig.3.5b), together with the TKE decreasing and conversion to horizontal movements for TOP (Fig.3.6b) signify that the upper CBL becomes stably stratified at lower heights. In short, we find that in the presence of aerosols, the initially sharper potential temperature gradient at the entrainment zone becomes less strong (Fig. 3.5b), but wider and more stratified. This further confirms the decrease in $\bar{\theta}$ variance (Fig. 3.7) caused by the diminished $\bar{\theta}$ vertical gradient (Figs. 3.5b and 3.8) at the top of the CBL.

3.6 Conclusions

We studied the impact of the aerosol heat absorption on the convective atmospheric boundary-layer (CBL) dynamics. Idealised CBL flows characterized by aerosols distributed (i) uniformly in the whole CBL or (ii) only within the CBL's upper 200 m were compared with a clear, i.e. no aerosols, CBL case. All the experiments were

simulated using the large-eddy simulation (LES) technique. For all the cases the CBL was designed in such a manner that the entrainment velocity was compensated by the subsidence motions, yielding to a constant CBL depth after sufficiently lengthy integration.

We first investigated how the absorbing aerosols perturb the CBL depth-equilibrium by shadowing the surface. We found reduced CBL depth and potential temperature inversion jump when aerosols were present, although these were more intense when the aerosols were concentrated only at the top of the CBL. To further support the analysis of the LES results, we used mixed-layer theory to derive steady-state analytical solutions for boundary-layer depth and potential temperature jump at the inversion layer. In spite of their simplicity, the mixed-layer results agreed well with the LES data for all the experiments.

The reduction in the surface heat flux enabled us to partially explain the shallower CBLs, but not the different equilibrium depths. Our explanation is the following: besides the reduced surface heat flux, the LES results also showed changes in the entrainment zone (EZ) stratification profile. On the one hand, the potential temperature inversion jump becomes weaker as a result of the heat absorption, while on the other, we observed the EZ depth increasing 18% and 91% when aerosols were uniform or concentrated at the top of the CBL.

The impact of aerosols on modifying the stratification of the upper mixed-layer was also corroborated by the larger values of the potential temperature anomaly and the Brunt-Väisälä frequency at lower levels. The combination of these mechanisms explained the different characteristics of the CBL for different vertical distribution of aerosols.

We further studied the aerosol heat absorption effects on the vertical structure of the CBL by quantifying the heat budget at the EZ. Even though the minimum entrainment flux fell by 12.5% when aerosols were present (controlled by the surface forcing), the heat budget analysis confirmed the more significant deepening of the EZ when the aerosols were found only at the top of the CBL.

To complete our analysis, we studied the aerosol heat absorption impact on the velocity and potential temperature variance profiles. The horizontal velocity variance profiles showed that aerosol absorption of heat reduces the horizontal velocity peak at the top of the CBL because less momentum is transferred from the updrafts when the inversion layer was weaker.

When aerosols are located solely at the top of the CBL, the reduced vertical motions throughout the CBL corroborated the steep decrease in turbulent kinetic energy. This was explained by the broadening of the stable stratified region already

below the EZ, weakening the turbulent eddies at lower levels. The ratio $\frac{\overline{w'^2}}{\overline{u'^2}+\overline{v'^2}}$ on average diminished when aerosols were at the top of the CBL, indicating earlier conversion of vertical motion into horizontal components.

The peak in the variance of the potential temperature in the EZ was reduced but an earlier onset was observed. Its budget further explained how the reduced potential temperature gradient observed when aerosols are present was the responsible physical mechanism for diminishing the $\bar{\theta}$ variance.

To conclude, this study evidenced the importance of high resolution models to properly simulate the effects of aerosol absorption of radiation on the dynamics of the CBL. Moreover, we have demonstrated that in addition to the properties of the aerosols, the vertical distribution is an important characteristic to properly describe the CBL height evolution and the dynamics of the EZ. In a future study we plan to include explicitly the effects of the *SW* diurnal cycle and an on-line coupling between the aerosol layer and the *SW* radiation field.

"All together now
All together now
All together now
All together now"

Lennon, J.W. and McCartney, J.P. (1969). All together now. *Yellow Submarine*, **3(A)**, Apple Records.

4

Aerosols in the convective boundary layer: shortwave radiation effects on the coupled land-atmosphere system

Published as:
Barbaro, E., Vilà-Guerau de Arellano, J., Ouwersloot, H.G., Schroter, J.S., Donovan, D.P. & Krol, M.C. (2014). Aerosols in the convective boundary layer: Shortwave radiation effects on the coupled land-atmosphere system. *Journal of Geophysical Research: Atmospheres*, **119**, 5845–5863

Abstract

By combining observations and numerical simulations, we investigated the responses of the surface energy budget and the convective boundary layer (CBL) dynamics to the presence of aerosols. A detailed data set containing (thermo)dynamic observations at CESAR (Cabauw Experimental Site for Atmospheric Research) and aerosol information from the European Integrated Project on Aerosol, Cloud, Climate, and Air Quality Interactions (IMPACT/EUCAARI) was employed to design numerical experiments reproducing two typical clear-sky days, each characterized by contrasting thermodynamic initial profiles: (i) residual layer above a strong surface inversion, and (ii) well-mixed CBL connected to the free troposphere by a capping inversion, without the residual layer in between. A large-eddy simulation (LES) model and a mixed-layer (MXL) model, coupled to a broadband radiative transfer code and a land-surface model, were used to study the impacts of aerosols on shortwave radiation. Both the LES model and the MXL model results reproduced satisfactorily the observations for both days. A sensitivity analysis on a wide range of aerosol properties was conducted. Our results showed that higher loads of aerosols decreased irradiance imposing an energy restriction at the surface, delaying the morning onset of the CBL and advancing its afternoon collapse. Moderately to strongly absorbing aerosols increased the heating rate contributing positively to increase the afternoon CBL height, potential temperature and to decrease Bowen ratio. In contrast, scattering aerosols were associated with smaller heating rates and cooler and shallower CBLs. Our findings advocate the need for accounting for the aerosol influence in analyzing surface and CBL dynamics.

4.1 Introduction

Tropospheric aerosols influence the Earth's climate by absorbing and scattering shortwave (SW) radiation (Boucher & Anderson, 1995; Stier *et al.*, 2007; Paasonen *et al.*, 2013). Depending on the aerosol characteristics (Liu & Ou, 1990; Wang *et al.*, 2009), chemical composition (Yu & Zhang, 2011) and vertical distribution (Knapp *et al.*, 2002; Raut & Chazette, 2008; Sakaeda *et al.*, 2011), their effects on the surface radiation/energy budgets range from negligible to very significant (see also Kaufman *et al.* (2002); Matthias & Bosenberg (2002); Forster *et al.* (2007); Arneth *et al.* (2010); Costabile *et al.* (2013)). More specifically, aerosols modify the convective boundary layer (CBL) dynamics changing its depth, vertical structure and entrainment zone characteristics (Ackerman, 1977; Venkatram & Viskanta, 1977; Zhang *et al.*, 2010; Barbaro *et al.*, 2013).

In this Chapter we study observations of typical mid-latitude CBLs formed over grassland characterized by different mechanisms governing their growth: (i) break-up of a strong surface inversion and (ii) well-mixed CBL growth due to entrainment. We emphasize the importance of the vertical distribution of aerosol extinction (optical depth ~ 0.2 and single scattering albedo ~ 0.9) on the CBL growth, the engulfing of the aerosol layer during the morning transition and the subsequent influence on the (i) surface energy budget (SEB) and (ii) thermodynamic state diurnal variation.

Very few data sets combine aerosol measurements, radiation observations, surface and detailed CBL vertical structure data. Therefore, these processes have been normally investigated separately or by means of simplified CBL numerical models (Venkatram & Viskanta (1977); Tunved *et al.* (2010)), regional models (see Baklanov *et al.* (2014) for a complete review), mesoscale models ((Zhang *et al.*, 2010; Wong *et al.*, 2012)) and climate models combined with satellite observations and aerosol parameterizations (Haywood *et al.* (1999); Chen *et al.* (2013)).

Previous studies have shown that very broad ranges of aerosol optical depth (AOD, expressed as τ) and single scattering albedo (SSA, expressed as ω) are found in the atmosphere. Kaufman (1993) summarizes several measurements of τ (at 550 nm) varying from non-polluted cases ($\tau \approx 0$) up to very polluted situations ($\tau \approx 1.5$) for different areas around the globe. Zubler *et al.* (2011a) present diurnal means of τ for thirteen AERONET stations (all at 550 nm) varying on average between 0.14 and 0.29. Hewitt & Jackson (2009) suggest τ ranging from 0.2 up to 0.8 for polluted continental conditions. For the northern India region, Tripathi *et al.* (2005) obtained averaged τ values (at 500 nm) of around 0.77 ± 0.29. Israelevich *et al.* (2012) found that heavy loads of Saharan dust are transported over the Mediterranean sea with τ values up to 0.6 (at 550 nm). For the single scattering albedo, Jacobson (2001b)

estimated an annually global averaged at $\omega \approx 0.85$ (at 550 nm) over land. Lyamani *et al.* (2010) found ω as low as 0.65 ± 0.07 (at 670 nm) for Granada, an urban location in Spain. Tripathi *et al.* (2005) obtained $\omega \approx 0.76$ (at 500 nm). Takemura *et al.* (2002) simulated global distributions of ω (at 550 nm) varying between 0.8 and 1.0.

With respect to observations, by isolating the aerosol impacts on the *SW* radiation, Hatzianastassiou *et al.* (2005) and Wang *et al.* (2009) have shown that detailed aerosol temporal evolution and vertical profiles are needed to reproduce the observed direct/diffuse partitioning and global irradiance (see also Meywerk & Ramanathan (1999) and Singh *et al.* (2010)). The available observational campaigns studying the aerosol impacts on the troposphere (e.g. de Wekker *et al.* (2004) and Johnson *et al.* (2008)) focused mainly on instrument comparisons and data validation without discussing in detail how the aerosols influence the boundary-layer vertical structure and the CBL heat budget. At the same time, experiments aiming to understand (urban) boundary-layer turbulent processes (Angevine *et al.* (1998b) and Masson *et al.* (2008)) do not further explore how the aerosol *SW* radiation absorption and scattering affect the SEB or the redistribution of heat throughout the CBL.

Regarding numerical modeling, Li *et al.* (1997) and Zhang *et al.* (2010) mentioned that the lack of observational data leads to major uncertainties in the aerosol representation. They argued that numerical studies need more observations to improve our understanding of the complex interaction of aerosols and *SW* radiation, the land-atmosphere system and the CBL vertical structure. None of the studies mentioned above have merged detailed aerosol information to a three-dimensional high resolution model able to reproduce detailed CBL dynamics. Here, extending previous studies (e.g. Venkatram & Viskanta (1977) and Yu *et al.* (2002)), we systematically investigate and quantify how the surface fluxes respond to the aerosol absorption and scattering of *SW* radiation. By doing so, we also consider the subsequent impact of the aerosols on the diurnal evolution of the CBL dynamics. Our approach integrates at diurnal scales radiation-surface-atmosphere using a large-eddy simulation (LES) model coupled to a land-atmosphere model and a radiative transfer code. We also design a parameter space to study typical τ and ω conditions aiming to further quantify the aerosol effects on the land-atmosphere system.

This Chapter is organized as follows: Sect. 4.2 describes the numerical models, the available observations and the experimental design. The validation of the models is discussed in Sect. 4.3. In Sect. 4.4 we present a sensitivity analysis varying the amount and the aerosol characteristics. The main results are summarized in Sect. 4.5.

4.2 Description of the numerical models

We use the Dutch Atmospheric LES (DALES version 3.2, see Heus *et al.* (2010) for a full description of the model) to explicitly simulate the most energetic dynamical structures of the CBL and parameterize the scales smaller than the adopted numerical grid size (Moeng, 1984). The SW radiation is represented by means of the broadband Delta-Eddington (DE) approximation (Joseph *et al.*, 1976). To connect the radiation budget to the surface energy budget, we use the land-surface (LS) model described in van Heerwaarden *et al.* (2010) and references within.

Concerning the radiation calculations, in this work we effectively divide the atmosphere into an aerosol free Rayleigh layer which sits above an aerosol layer subdivided according to the DALES vertical spatial resolution (see Table 4.1). In order to calculate the SW radiation fluxes within the aerosol layer, the two-stream DE approximation fulfills the purposes of this Chapter while providing rapid and precise calculations of the direct and diffuse components of the SW radiation (Shettle & Weinman, 1970; Joseph *et al.*, 1976; Liou, 2002). To calculate the aerosol SW radiation absorption and scattering, the method requires the temporal evolution of the τ, ω and the asymmetry parameter (g), see Liou (2002). The Rayleigh scattering above the aerosol layer is calculated based on the Elterman (1968) standard profile. The atmospheric net transmissivity from the top of the atmosphere to up to the top of the aerosol layer is parameterized following Burridge & Gadd (1974) - see also Stull (1988) - and provides the total downward SW radiation used as an upper boundary condition for the aerosol layer DE radiative transfer calculations. Here, we neglect the contribution of gaseous SW radiation heating and longwave (LW) radiation cooling to the CBL total heating rate (HR). As a result, in our simulations the HR is entirely due to the effect of the aerosols. According to Angevine *et al.* (1998b) and Stull (1988) and further corroborated by radiative transfer simulations using the libRadtran code (Mayer & Kylling, 2005) the heating due to gaseous SW radiation absorption and the LW cooling nearly offset each other from 9.5 UTC to 15.5 UTC for mid-latitudes (not shown). In contrast, for the morning and afternoon transitions the LW radiation cooling is larger than the SW radiation gaseous absorption. For the cases discussed here the differences remain smaller than -0.7 K day^{-1}. Note that a full radiation treatment might yield smaller values of HR both early in the morning and late in the afternoon. However, we expect that this bias has a small influence on our findings for the convective period since the neglect of SW gaseous absorption and LW cooling is consistent between the numerical experiments independent of the amount of aerosols. Moreover, early in the morning the divergence of the turbulent heat flux is the dominant term in the potential temperature budget equation (see

Sect. 4.4). As a result, we expect that our approach produces a proper representation of the effect of the aerosol HR during the convective period. Here we focus only on the convective period, therefore the impact of aerosols and the HR imbalance on the stable boundary layer has not been analyzed.

The vertical HR profile is calculated directly by taking the divergence of net radiation, which is obtained from the SW calculation at a single wavelength. We select the wavelength of 555 nm as representative for the aerosol properties, and the ground is assumed to be a Lambertian surface (Madronich, 1987) with an albedo of 0.25 (Beljaars & Bosveld, 1997; van Heerwaarden *et al.*, 2010). The downward longwave (LW) radiation is prescribed by the clear-sky empirical formula proposed by Brunt (1932) and the upward LW radiation assumes the surface emissivity taken as unity (Holtslag & de Bruin, 1988).

Concerning the land-surface model, the surface resistance is calculated by means of the Jarvis-Stewart model (Jarvis, 1976), the energy budget and the soil temperature equations are based on Duynkerke (1991) and the soil moisture equations are based on Noilhan & Planton (1989). We couple the radiation model and the surface model to our LES to account for the effects of aerosols on SW radiation and on the land-atmosphere system.

To further quantify the aerosol impact on the land-atmosphere system, we use a 0^{th}-order mixed-layer (MXL) model (Lilly, 1968; Garratt, 1992) to perform a series of systematic simulations exploring a wide range of ω and τ. To this end, the same radiation and land-surface models used in our LES are implemented in the MXL model (Heus *et al.*, 2010; van Heerwaarden *et al.*, 2010). The MXL model used here is an extension of that described by van Heerwaarden *et al.* (2010) and Barbaro *et al.* (2013), with the inclusion of the DE model for the SW radiation calculations. The simplified CBL dynamics in the MXL model assumes a well-mixed CBL with constant vertical profiles of the state variables. In the MXL model, the entrainment zone is represented by an infinitesimally thin inversion layer (0^{th}-order approach, see Lilly (1968) and Betts (1974)) and the entrainment ratio is defined as being constant and held equal to 0.2 (Stull, 1988).

4.2.1 Observational data set

The numerical experiments are based on observations taken at CESAR (Cabauw Experimental Site for Atmospheric Research). CESAR (www.cesar-observatory.nl) is located in a flat terrain covered with grass in the Netherlands (51.97 °N, 4.93 °E). Observations of radiation, surface fluxes and thermodynamic variables along the 213

m mast (2, 10, 20, 40, 80, 140 and 200 m) are measured at a 10 Hz frequency (Beljaars & Bosveld, 1997). From 2006 on, CESAR became part of the Baseline Surface Radiation Network (BSRN) and diffuse and direct shortwave radiation components were integrated to the radiation data set (Knap *et al.*, 2010). The prescribed CESAR land-surface information is based on the Cabauw climatological values described in van Heerwaarden *et al.* (2010).

In May 2008, the intensive observational campaign called European Integrated Project on Aerosol, Cloud, Climate, and Air Quality Interactions (IMPACT/EUCAARI) took place in Cabauw (see Kulmala *et al.* (2009, 2011) for details). During the campaign, several additional meteorological observations were collected, including vertical profiles from radiosondes, detailed aerosol information and remote sensing data. In view of this unique data set, May 8^{th} 2008 (henceforth called CESAR2008) is chosen as a control case because of its cloudless conditions, constant weak to moderate easterly winds ranging from 4-6 m s^{-1} and the absence of large-scale heat advection. The chemistry and radiation of the CESAR2008 have already been described in detail - see Derksen *et al.* (2011); Mensah *et al.* (2012); Aan de Brugh *et al.* (2013) and van Beelen *et al.* (2014) for atmospheric chemistry and Wang *et al.* (2009) for clear-sky radiative closure. The CESAR2008 synoptic conditions and the pollution situation over Cabauw were summarized by Hamburger *et al.* (2011) and Grob *et al.* (2013). Both the aerosol optical properties and the loadings represent typical continental aerosols transported from central Europe (Poland and Germany) over the Netherlands due to the easterly circulation associated with the persistent anticyclone located over Denmark, northern Germany and the Benelux states. The synoptics conditions observed around the CESAR2008 campaign - Scandinavian High, Ridge Central Europe and high over Central Europe - are commonly observed in Europe during the month of May (James, 2006).

As we will show, CESAR2008 case is characterized by a residual layer (RL) above a surface inversion. The RL well-mixed vertical structure allows a rapid CBL growth after the break-up of the morning potential temperature inversion. To complement our analysis, we study another convective day with a well-mixed boundary layer at CESAR (September 25^{th} 2003 - henceforth called CESAR2003). This day is characterized by negligible large-scale heat advection, constant moderate winds (4-7 m s^{-1}), very few clouds and the absence of a residual layer. For a complete description of the CBL (thermo)dynamics and the synoptics, see Casso-Torralba *et al.* (2008). The synoptic situation observed for CESAR2003 - anticyclone associated with South Easterly winds - is similar to CESAR2008. The CESAR2003 dynamics and land surface properties have been systematically studied. Van Heerwaarden *et al.* (2010) described the feedbacks and forcings of the CBL dynamics and land surface on the time evolution of

evapotranspiration. Pino *et al.* (2012) quantified the relation between CBL dynamics and CO_2 budget and surface exchanges. Since the aerosol observations were only available during the IMPACT/EUCAARI campaign, τ, ω and g values are assumed to be representative of a typical day in the Netherlands ($\overline{PM}_{2.5} = 22.7 \mu g m^{-3}$, see Schaap *et al.* (2009)), resulting in the same aerosol properties for both numerical experiments. To ensure that the aerosol layer is engulfed by the CBL, and in absence of any observational evidence, we assume an idealized initial aerosol layer height (h_a) of 600 m. By using this value we obtain the closest match between the numerical experiments and the CESAR observations of (thermo)dynamic variables. Variations around h_a have very little impact on the CBL (thermo)dynamics evolution, however.

4.2.2 Experimental design

We present in Fig. 4.1 the temporal evolutions of τ, ω and g for the CESAR2008 case. The aerosol observations described in Fig. 4.1 are prescribed in our MXL and LES simulations by means of fitting functions (red dashes). The initial vertical profile of the aerosol extinction coefficient is prescribed, as shown in Fig. 4.2c. The scalar spatial evolution is solved simultaneously with the other thermodynamic variables in the LES (three-dimensional) and MXL (bulk) models for every time step. By constraining the aerosol properties we aim for an accurate simulation of the *SW* radiation, with a special focus on the reproducibility of its direct and diffuse components.

In Fig. 4.2 we present the mast data (06 UTC) and radiosonde vertical profile (10 UTC) for (a) potential temperature and (b) specific humidity, and (c) the aerosol extinction coefficient (α_a) obtained from a LIDAR profile. The combination of the radiosondes (representing the mixed layer) and the mast data (surface layer) is used to prescribe the initial conditions for our LES and MXL experiments (red vertical profiles). Note that we adapt the MXL model to also take into account the vertical extension of the layer above the developing CBL (residual layer). As long as the RL is present, air is entrained into the boundary layer from the RL with an entrainment ratio held constant and equal to 0.2. When the mixed-layer and the residual layer connect, the lower ground inversion disappears and the mixed-layer merges with the RL. At that moment, entrainment between the mixed-layer and the free-troposphere becomes active, also with an entrainment ratio of 0.2.

The 06 UTC initial profiles of θ and q in the surface layer are based on mast observations (up to 200 m) in order to reproduce the thermodynamics of the morning potential temperature inversion jump. For potential temperature, at 200 m the radiosonde and the mast data coincide and the radiosonde data are taken as initial profile for the well-mixed layer and the free-atmosphere. For specific humidity we

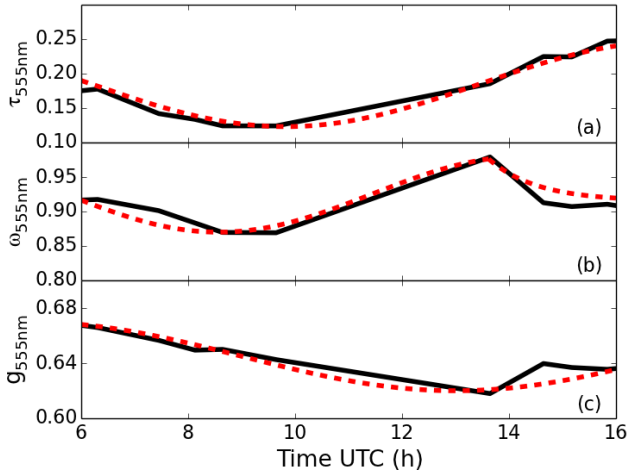

Figure 4.1: Aerosol (a) optical depth, (b) single scattering albedo and (c) asymmetry parameter (all at 555 nm) observed diurnal evolution. The dashes in (a), (b) and (c) represent the prescribed values in the LES and MXL models.

note a discrepancy between radiosonde and mast data of about 1 g kg $^{-1}$ at 200 m height. We follow the mast data closer to the surface and above 800 m the radiosonde is considered to be representative for the initial condition in the upper atmosphere.

The LIDAR profile (06 UTC) is measured using a backscatter LIDAR operating at 355 nm. The LIDAR data was inverted using the Klett-Fernald method (Klett, 1985) assuming a value of the LIDAR backscatter-to-extinction ratio (S) of 50($\pm$20) sr^{-1}. The uncertainty in S can result in significant uncertainty in the resulting aerosol extinction profile. However, here, the LIDAR profile is simply scaled to the corresponding 555 nm τ value and the resulting extinction profile is then used as a qualitative indication of the aerosol extinction vertical profile. The LIDAR profiles, however, are not trustworthy below 500 m because the transmitted beam and the receiver telescope field-of-view do not fully overlap (Biavati *et al.*, 2011). We therefore assume a well-mixed aerosol extinction profile below 500 m down to the surface.

As observed in Fig. 4.2, CESAR2008 is characterized by a residual layer extending from 200 m to around 1700 m - also containing the aerosol layer - see Fig. 4.2c. This boundary layer prototype enables us to study the role of aerosols in delaying/advancing the break-up of the inversion layer and subsequent onset of the morning CBL.

The main difference between the CESAR2008 and CESAR2003 cases is the absence of a residual layer in the latter. Therefore, the CBL growth during the morning transition in CESAR2008 is driven by the rapid incorporation of the well-mixed RL, while in CESAR2003 the CBL growth is more continuous and is driven by entrainment and surface heat fluxes. To study the impact of the aerosols on the CBL development we design two extra LES numerical experiments (called CLEAR and AERO+) for each CESAR control simulation. The experiments "CLEAR" and "AERO+" simulate the same boundary-layer and surface properties as in CESAR2003/CESAR2008. The difference lies only in the τ: for the "CLEAR" simulations τ is set to zero, and for the "AERO+" simulations the τ is tripled compared to the control cases. The AERO+ loadings are therefore characteristic of a moderately polluted urban area (Tripathi *et al.*, 2005; Hewitt & Jackson, 2009), Saharan dust (Zubler *et al.*, 2011b; Israelevich *et al.*, 2012; Kinne *et al.*, 2013) or biomass burning (Myhre *et al.*, 2003).

The initial and boundary conditions of the LES experiments are described in Table 4.1. Note that we keep the design of the MXL model experiments as close as possible to the LES.

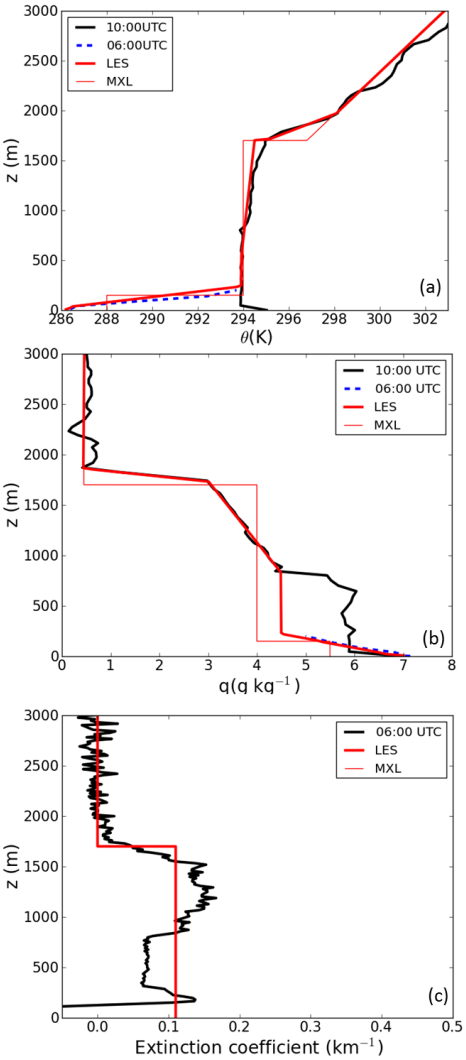

Figure 4.2: Vertical profiles of (a) potential temperature (b) specific humidity and (c) aerosol extinction coefficient. The continuous black lines are radiosondes [(a) and (b)] and LIDAR measurements (c). The blue dashed lines [(a) and (b)] are the CESAR mast observations. The red continuous lines represent the initial profiles at 06 UTC for the LES model (thick) and for the MXL model (thin).

Table 4.1: LES initial and prescribed values for CONTROL, AERO+ and CLEAR experiments for both CESAR2008 and CESAR2003 data sets. The UTC time (t) is given in hours.

Boundary-layer properties		**CESAR2008**	**CESAR2003**
Initial boundary-layer height, z_i [m]		150	114
Initial residual layer height [m]		1700	600
Initial aerosol layer height, h_a [m]		1700	600
Geostrophic wind, (U_g, V_g) [m s^{-1}]		$(8, 0)$	$(6, 3)$
Large-scale vertical velocity, (w_s) [m s^{-1}]		0.0	0.0
Spatial domain, (x,y,z) [m]		$(12800, 12800, 3000)$	$(12800, 12800, 3000)$
Spatial resolution, (dx,dy,dz) [m]		$(50, 50, 15)$	$(50, 50, 12)$
Integration total time [h]		12	12
Heat and moisture vertical profiles	**θ (K)**	**q (g kg^{-1})**	**α_a (km^{-1})**
CESAR2008			
$z < 250$ m	$286.0 + 0.032\ z$	$7.1 - 0.01\ z$	0.11
$250 < z < 800$ m	294.0	4.5	0.11
$800 < z < 1700$ m	$294 + 0.0006\ (z - 800)$	$4.5 - 0.0016\ (z - 800)$	0.11
$1700 < z < 1950$ m	$294.5 + 0.012\ (z - 1700)$	$3.1 - 0.0093\ (z - 1700)$	0.00
$z > 1950$ m	$298.1 + 0.0045\ (z - 1950)$	0.3	0.0
CESAR2003			
$z < 114$ m	284.0	4.3	0.30
$114 < z < 138$ m	$284.0 + 0.167\ (z - 114.0)$	$4.3 - 0.033(z - 114.0)$	0.30
$138 < z < 600$ m	$288.0 + 0.0036\ (z - 138.0)$	$3.5 - 0.0012(z - 138.0)$	0.30
$z > 600$ m	$288.0 + 0.0036\ (z - 138.0)$	$3.5 - 0.0012(z - 138.0)$	0.00
Land-surface properties		**CESAR2008**	**CESAR2003**
Volumetric water content $[m^3 m^{-3}]$		0.43	0.39
Saturated volumetric water content $[m^3 m^{-3}]$		0.60	0.60
Volumetric water content field capacity $[m^3 m^{-3}]$		0.491	0.491
Volumetric water content wilting point $[m^3 m^{-3}]$		0.314	0.314
Vegetation fraction [-]		0.9	0.9
Temperature top soil layer [K]		286.5	282.0
Temperature deeper soil layer [K]		289.5	285.0
Leaf area index [-]		2	2
minimum resistance transpiration [-]		110	110
minimum resistance soil evaporation [-]		50	50
Surface albedo [-]		0.25	0.25
Leaf area index [-]		2	2
Aerosol properties (555 nm)			
Single scattering albedo, ω [-], t< 13.62 h		$0.925 + 0.055 \cos(31.5\ (t + 20))$	
Single scattering albedo, ω [-], t> 13.62 h		$0.975 - 0.06(1 - \exp(15.0 - 1.1\ t))$	
Asymmetry parameter, g [-]		$0.645 + 0.025 \cos(22.5\ (t + 27))$	
Aerosol optical depth, τ [-]			
CONTROL		$0.185 + 0.062 \cos(24.75\ (t + 12))$	
AERO+		$0.555 + 0.186 \cos(24.75\ (t + 12))$	
CLEAR		0.0	

4.3 Model Validation

We start by validating the MXL and LES numerical experiments against the observations (CESAR2008 and CESAR2003). In Fig. 4.3 we show the temporal evolution of the simulated and observed radiation/energy budget, boundary-layer height, potential temperature and specific humidity for CESAR2008. We present in Fig. 4.4 the results obtained for the CESAR2003 case. Note that we use the same radiation transfer model and the land-surface parametrization in the MXL and LES models. Therefore, the validation of the radiation/energy budget of the MXL is omitted. The sensible (SH) and latent (LE) heat fluxes are directly measured by means of the eddy-correlation technique. The surface energy budget imbalance is proportionally distributed over SH and LE according to the Bowen ratio ($\beta = \frac{SH}{LE}$); see Beljaars & Bosveld (1997); Twine *et al.* (2000) and Foken (2008) for further details. The CBL height is retrieved from the wind profiler measurements by the modified maximum signal-to-noise-ratio detection algorithm described by Bianco & Wilczak (2002).

We see in Fig. 4.3a that the DE radiative transfer calculations constrained by aerosol observations (Fig. 4.1) accurately reproduce the SW radiation components for this clear-sky day. The LW radiation components are also well captured. It is observed in Fig. 4.3b that we are able to reproduce the global SW radiation (SWD), with a small mean bias error and root mean square error ($MBE = 2.1$ Wm^{-2} and $RMSE = 8.4$ Wm^{-2}, respectively). Also, the diffuse SW observations are well reproduced ($MBE = 7.0$ Wm^{-2} and $RMSE = 9.7$ Wm^{-2}). Our results are comparable to the more advanced radiation modeling study of Wang *et al.* (2009) - using a spectrally-resolved doubling adding radiation transfer model - for the same day. We show in Fig. 4.3c that also the modeled net radiation agrees with the observations. The prescribed land-surface properties (e.g. soil moisture, temperature and field capacity) are based on van Heerwaarden *et al.* (2010) and observations taken at CESAR. Combined with the radiation terms, this leads to an accurate reproduction of the surface fluxes (SH, LE and the soil heat flux).

A proper determination of the surface fluxes is crucial for an accurate simulation of the CBL height evolution, Fig. 4.3(d). Both the LES and the MXL models are able to capture the break-up of the potential temperature inversion and the subsequent engulfing of the RL. The timing of this break-up differs only 10-20 minutes from the wind profiler observations. The RL from the previous day is then incorporated in the mixed-layer and the boundary layer grows further to around $1600 - 1700$ m. After 11 UTC the sensible heat flux (~ 110 Wm^{-2}) diminishes, reaching negative values already around 15.5 UTC. Therefore, the boundary layer grows fairly little after 11 UTC (~ 400 m in 6 hours). The 7 K temperature increase at 10 m from

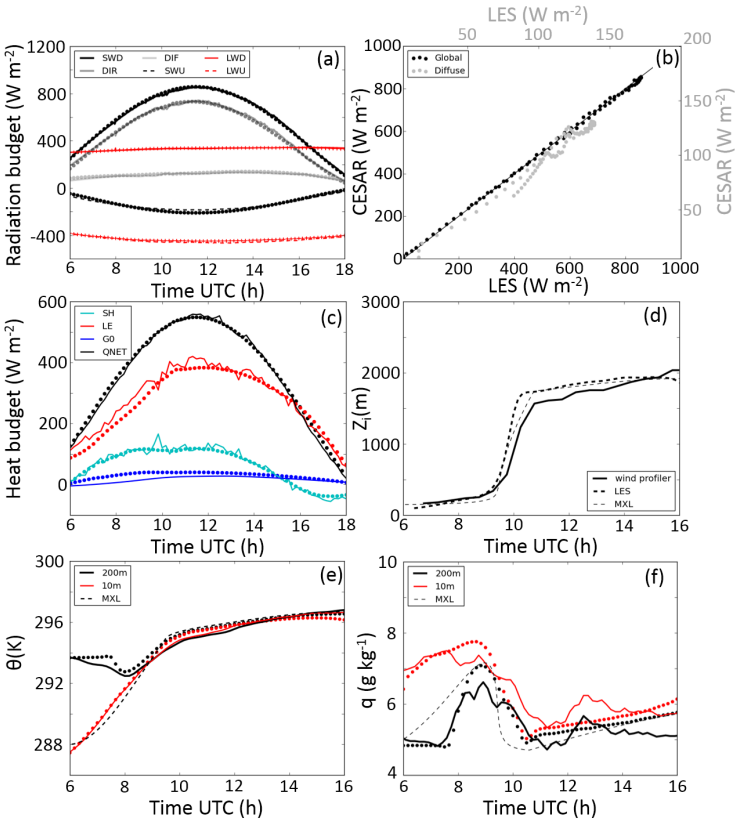

Figure 4.3: LES and MXL validation against the CESAR2008 data set. (a) Temporal evolution of the radiation budget. The dots represent the LES data and the continuous lines represent observations. The dark gray line is the direct SW radiation and the light gray line is the diffuse SW radiation. SWD and LWD (solid lines) are respectively the downward components of the observed SW irradiance (black) and LW radiation (red) - analogue for the upward components (SWU and LWU - dashed lines). All the downward components include error bars, although these are too small to be depicted. (b) Global (left Y-axis) and diffuse (right Y-axis) SW radiation scatter plot - the thin black line is a 1:1 reference line. (c) Temporal evolution of surface energy budget. SH, LE and G_0 are respectively the sensible, latent and soil heat fluxes; $Q_{NET} = (SWD + LWD + SWU + LWU)$ is the net-radiation. Temporal evolution of (d) boundary-layer height, (e) potential temperature and (f) specific humidity. The dashes in (d-f) indicate the MXL model results - omitted for (a), (b) and (c) - see text.

06 UTC till 10 UTC is well reproduced, Fig. 4.3(e), as well as the time at which 10 m and 200 m θ observations converge (09 UTC), indicating the formation of a well-mixed CBL. Finally, the specific humidity evolution, Fig. 4.3(f), compares well with the observations, capturing the entrainment of drier air from the layers above (mainly from 8.5 UTC to 10.5 UTC). Next, in Fig. 4.4 we present the same validation for the CESAR2003 case.

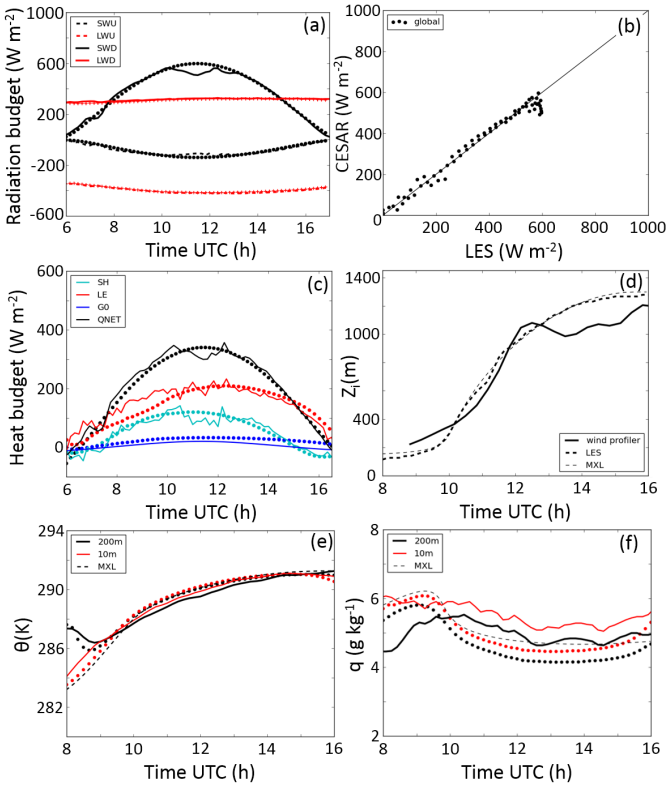

Figure 4.4: Same as Fig 4.3 but for CESAR2003 case. Note in (a) and (c) that we have extended the x-axis to show the complete diurnal cycle of SW radiation and Q_{NET}.

Although we do not have information on the aerosol optical properties, the comparison with observations is also satisfactory for all the variables. Again, the radiative transfer calculations reproduce the observed SW radiation fluxes, except the downward SW at the middle of the day when scattered clouds were observed (Pino *et al.*,

2012). Our hypothesis is that these clouds are located in the upper troposphere, therefore not affecting the downward LW radiation measured at the surface, since most of the LW emission (90%) comes from the lowest 1000 m of the atmosphere (Dürr & Philipona, 2004). We find in Fig. 4.4b that the drop in the observed SWD does not affect the good fit between LES and the observations, but considerably enlarges the MBE (8.1 Wm^{-2}) and $RMSE$ (32.3 Wm^{-2}) if compared to the CESAR2008 values. Notwithstanding, both MBE and $RMSE$ decrease by a factor of 3 by simply excluding the SWD observations during the cloudy period. In Fig. 4.4(c) the modeled surface fluxes match the observations, showing, in Fig. 4.4(d) a continuously growing CBL. This indicates that the prescribed initial conditions are appropriate (see Casso-Torralba *et al.* (2008)). The potential temperature, Fig. 4.4(e) and the specific humidity Fig. 4.4(f) evolutions also show that we are able - with the LES and the MXL models - to capture the physics that drive the CBL evolution. A similar good agreement between the LES and the MXL models is found by Pino *et al.* (2006), albeit without the coupling to a land-surface model.

4.4 Aerosol effects on the surface fluxes and aerosol heating rate

In this section, we aim to further analyze the impact of aerosol scattering/absorption on the surface SW radiation and on the CBL vertical structure. To this end, we compare the CESAR2008 and CESAR2003 control experiments to the CLEAR ($\tau = 0$) and AERO+ (tripled $\tau_{CONTROL}$) simulations - see Table 4.1. Since our findings are similar for both cases under study we focus only on the results for CESAR2008.

We first quantify the aerosol impact on (i) the net SW radiation at the surface and above the CBL and (ii) the SEB. In Fig. 4.5 we show the temporal evolutions of (a) the net SW radiation differences compared to the CONTROL experiment at 2500 m (always above the CBL) and at the surface, (b) the surface flux ratios relative to the CONTROL experiment, and (c) Bowen ratio.

As shown in Fig. 4.5a, aerosols directly reduce the net irradiance at the surface. The differences between the AERO+ and CONTROL experiments range from -43 Wm^{-2} (08 UTC) down to -69 Wm^{-2} (15 UTC) less available energy at the surface. In turn, an increase of up to 46 Wm^{-2} (at 16 UTC) is observed for the CLEAR experiment compared to CONTROL. These results are in agreement with the findings of Tripathi *et al.* (2005) who show diurnal averages ranging from -31 Wm^{-2} to -98 Wm^{-2} less available energy for moderately to highly polluted industrial cities in India.

Haywood *et al.* (2001) obtained a clear-sky direct solar radiative effect as strong as -60 Wm^{-2} for Saharan dust. Myhre *et al.* (2003) show values roughly between -50 Wm^{-2} and -90 Wm^{-2} for biomass burning aerosol in Southern Africa.

At the top of the CBL we also observe less (more) available energy for AERO+ (CLEAR) experiments. The differences, however, are significantly smaller than at the surface because scattering aerosols increase the outgoing *SW* radiation at the top of the CBL due to backscattering. The temporal variation of ΔSW_{NET} is explained by the diurnal cycle of the irradiance and by the temporal evolution of the aerosol properties (see Fig. 4.1c).

The impact of the aerosols on the SEB is presented in Fig. 4.5b. For AERO+ (the opposite response is found for CLEAR), the aerosol *SW* radiation attenuation throughout the aerosol layer causes a relatively small reduction of LE, ranging from -20% up to -10% during the day. The ratio $\left(\frac{SH_{AERO+}}{SH_{CONTROL}}\right)$ is also reduced but, in contrast, shows a more pronounced diurnal variation. The physical explanation is as follows: under the studied surface conditions, i.e. well-watered grassland, LE uses the available surface energy more efficiently compared to SH (see Gentine *et al.* (2011); Bateni & Entekhabi (2012)). Since the reduction in LE is much less pronounced than in SH, the evaporation (not shown) for AERO+ compared with CLEAR decreases relatively little ($5-15\%$). From 10.5 UTC

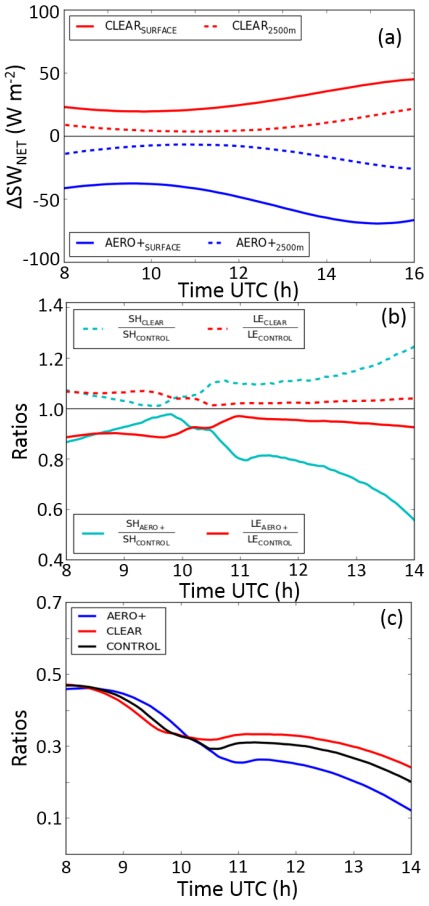

Figure 4.5: Temporal evolution of the (a) net *SW* radiation difference compared to CONTROL at 2500 m (dashed line) and at the surface (continuous lines), (b) SH and LE ratios referent to the CONTROL experiment and (c) Bowen ratio. The thin black line in (a) and (b) represents the reference case. Note that in (a) we have extended the x-axis to 16 UTC in order to show the maximum/minimum differences in the *SW* net-radiation compared to CONTROL. The results are shown only for CESAR2008.

on, the attenuation of SW radiation by aerosols leads to a stronger reduction of the irradiance, diminishing the available energy at the surface and therefore strongly decreasing SH. As a result, aerosols diminish β (Fig. 4.5c) by about 50% more for AERO+ than for CLEAR in the afternoon.

We show in Figs. 4.6a and 4.6b the 10-min averaged CBL heat budget components as a function of height for 09 UTC and 13.5 UTC. Similarly to Angevine *et al.* (1998b) and Barbaro *et al.* (2013) we calculate the two contributions of the heat budget: (i) potential temperature turbulent vertical flux divergence, ($-\frac{\partial \overline{w'\theta'}}{\partial z}$, TD_θ) and (ii) aerosol heating rate ($\frac{\partial \overline{SW}_{NET}}{\partial z}$, HR). To complete the CBL vertical structure analysis we also show the potential temperature vertical profile at 09 UTC and 13.5 UTC (Fig. 4.6c).

As we observe in Fig. 4.6a, the turbulent sensible heat flux divergence is the main contributor to the very rapid increase of the potential temperature (dilution of the 8 K inversion layer jump) during the morning period, i.e. $\mathrm{TD}_\theta >> HR$. Values up to 45 K day^{-1} close to the surface are observed for this case at 09 UTC. During the afternoon, the HR (Fig. 4.6b) becomes as relevant as TD_θ contributing 15% and 49% to the CBL heat budget (at 500 m) for the CONTROL and AERO+ experiments, respectively. We show in Fig. 4.6b that increasing τ (AERO+) leads to an approximately linear increase of the absorption of SW radiation (Sakaeda *et al.*, 2011). Note that, despite the well-mixed aerosol vertical distribution, the HR induced by the

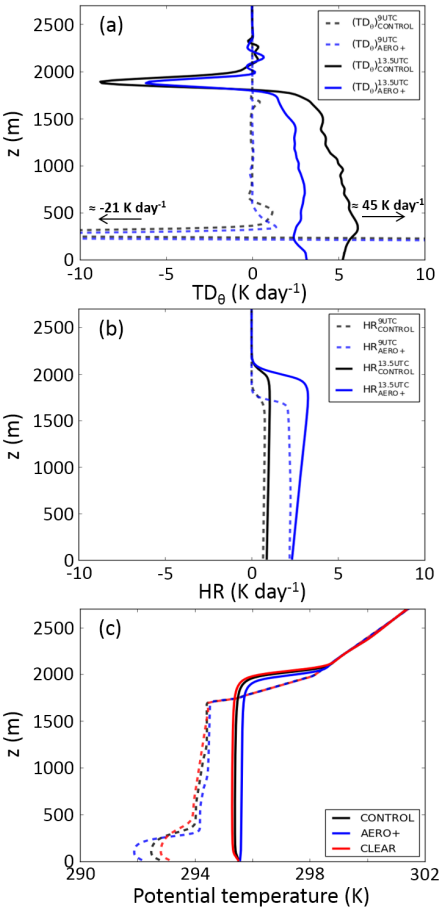

Figure 4.6: Vertical profiles of (a) potential temperature turbulent vertical flux divergence (TD_θ), (b) aerosol HR and (c) potential temperature. To improve visualization, in (a) the max/min of the turbulent term at 09 UTC is indicated in the figure. In all panels, the dashed lines (lighter tones) represent 09 UTC and the continuous lines (darker tones) represent 13.5 UTC. The results are only shown for CESAR2008.

absorbing aerosols is larger at the top of the CBL. The reason is the higher SW downward radiation flux at higher levels, especially for larger optical depths (AERO+). Therefore, the temporal evolution of the HR vertical profile is mainly driven by (i) the CBL dynamics, (ii) the diurnal cycle of irradiance and (iii) changes in both the aerosol properties and aerosol depth (see also Penner *et al.* (1994)). Note that for the HR, the decrease in solar irradiance at larger zenith angles is compensated by the increase in path length of the light through the atmosphere.

In analyzing the potential temperature vertical profiles, we find for the AERO+ experiment that during the morning the CBL is colder and the residual layer is warmer (-0.6 K and $+0.2$ K, respectively) in comparison to the CONTROL experiment (dotted lines in Fig. 4.6c). The explanation is that during the morning $\mathrm{h}_a > z_i$ (see Fig. 4.7b). In this situation, aerosols are also present in the residual layer, reducing the amount of SW radiation at the surface (see Fig. 4.5a) and heating the residual layer (see Fig. 4.6b). Later, the aerosol layer becomes part of the CBL, slightly increasing the CBL potential temperature by about 0.25 K at 13.5 UTC, (continuous lines in Fig. 4.6c).

4.4.1 Impact of the aerosols on the CBL depth development

In this section we quantify the aerosol impact on the break-up of the morning inversion layer and on the CBL collapse in the afternoon. The overall aerosol effect on the temporal evolution of the CBL height (z_i) for weakly absorbing aerosols ($\omega > 0.9$) is summarized in Fig. 4.7. During the morning, aerosols tend to delay the break-up of the ground inversion layer ($\sim$ 40 min for AERO+). The final CBL height for the CESAR2008 case is less influenced by the aerosols because of the well-mixed residual layer (see fig. 4.2). For the CESAR2003 experiments we find that part of the aerosols are also located above the CBL till around noon. In this configuration aerosols reduce Q_{NET} and therefore the surface fluxes (see Fig. 4.5) without heating the shallow CBL compared to the residual layer. This effect explains the significantly shallower CBL for AERO+ (and CONTROL) during the morning. In turn, during the afternoon aerosols act as a second source of energy, warming the CBL in comparison to the free-troposphere. This effect counterbalances the decrease in the surface available energy. Warming the CBL leads to a weakening of $\Delta\theta$ and a subsequent faster CBL growth. As a result, the CBL for CONTROL and AERO+ reach a similar depth as in CLEAR experiment due to the different contributions in the heat budget.

Our findings indicate a series of connected effects of absorbing aerosols impacting the afternoon CBL depths: (i) the decrease of turbulent surface fluxes and entrainment (negative effect), (ii) weakening of $\Delta\theta$ by increasing the CBL potential temperature

(positive effect) and (iii) development of a deeper and less strongly stable inversion layer in the lower part of the entrainment zone (negative effect) due to the relatively stronger heating at the top of the CBL. The latter process leads to an earlier stabilization of the potential temperature, deepening the entrainment zone; and thereby increasing the resistance for the penetration of the eddies (Ackerman, 1977; Barbaro *et al.*, 2013). Aiming to further quantify the impact of upper CBL heating on the turbulent field we calculate the CBL anisotropy at 500 m, quantified by $\frac{\overline{w'^2}}{\overline{u'^2}+\overline{v'^2}}$, for 13.5 UTC. By doing so, we quantify the suppression of the upward movements in the CBL. We find 0.69, 0.66 and 0.60 for CLEAR, CONTROL and AERO+ respectively, indicating a greater conversion of vertical into horizontal motions in the AERO+ case. This shows that the turbulent kinetic energy diminishes and the turbulent structures find more resistance to develop if abundant aerosols heat the CBL.

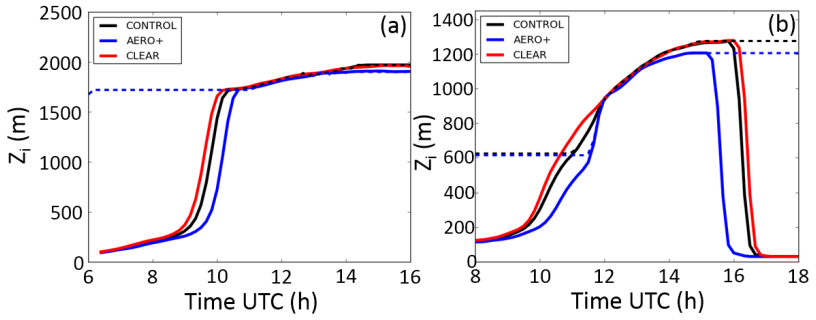

Figure 4.7: Temporal evolution of the boundary-layer depth for (a) CESAR2008 and (b) CESAR2003 cases. The dotted-lines represent the depth of the aerosol layer in the LES model.

The net effect of the aerosols, in these particular cases, is to slightly warm the afternoon CBL (up to 0.25K if compared to CONTROL, Fig. 4.6c) and to reduce the surface fluxes (down to 55% if compared to CONTROL, Fig. 4.5b), which leads to a slightly shallower CBL (down to 80 m if compared to CONTROL, Fig. 4.7). These results agree with Yu *et al.* (2002) and Wong *et al.* (2012) with respect to the net effect of scattering aerosols to slightly decrease the afternoon CBL depth. The reduced surface fluxes decrease the entrainment of dry air from the free troposphere. These effects combined result in negligible changes in the specific humidity (not shown).

4.4.2 Sensitivity analysis to aerosol optical properties

In the previous LES numerical experiments we studied only weakly absorbing aerosols, based on the CESAR2008 observations ($\omega > 0.9$). To complete our research, we employ the MXL model to extend the analysis to a wider range of aerosol conditions (τ and ω) by performing 336 experiments varying systematically τ (0.0 to 1.0) and ω (0.7 to 1.0) for both CESAR2008 (Fig. 4.8) and CESAR2003 (Fig. 4.9) cases. We base the choice of the τ and ω ranges on previous studies that characterized aerosol properties for different parts of the globe - see Kaufman (1993); Tripathi *et al.* (2005); Hewitt & Jackson (2009) and Israelevich *et al.* (2012). Note that these ranges encompass most situations, except for extreme events such as biomass burning or dust storms.

4.4.2.1 MXL model validation against LES results

To show the validity of this approach, we first compare the results of the MXL model to the LES model for CESAR2008 (10 UTC) and CESAR2003 (13.5 UTC) in Tables 4.2 and 4.3, respectively. Note that we performed an additional LES experiment similar to AERO+ but with $\omega = 0.7$ to further evaluate the response of the MXL model to strongly absorbing aerosols.

Table 4.2: MXL model and LES model results for CESAR2008 at 10 UTC. The brackets show the MXL model deviations from the LES results. Δt is the time delay of the CBL morning onset compared to the CLEAR case. The initial conditions of the AERO+$_{\omega=0.7}$ experiment are equal to the ones for AERO+, except $\omega = 0.7$. The LES results are the vertically averaged values from the surface until z_i.

Variable / Experiment	CONTROL	CLEAR	AERO+	AERO+$_{\omega=0.7}$
θ (K)	295.2 (+0.20)	295.2 (+0.15)	294.9 (+0.20)	293.9 (+0.20)
HR (K day^{-1})	0.7 (+0.3)	-	2.4 (+0.6)	10.5 (+0.8)
z_i (m)	1420 (-266)	1600 (-148)	730 (-230)	240 (-54)
Δt (min)	12 (+6)	0 (+9)	40 (+24)	156 (+30)

We observe that the MXL model properly captures the (thermo)dynamical responses to aerosol heating. Like the LES, in the MXL model the morning potential temperature response (Table 4.2) to aerosol forcing is small, unless strongly absorbing aerosols are abundant. In this situation - AERO+$_{\omega=0.7}$ - the morning CBL is cooled by 1 K in both models and the heating rates are similar (deviations $< 10\%$). The underestimation of the CBL height is due to the slight delay of the CBL morning onset observed in the MXL model results (see also Fig. 4.3d). The delay of the

Table 4.3: MXL model and LES model results for CESAR2003 at 13.5 UTC. The brackets show the MXL model deviations from the LES results. Δt is the time advance of the CBL afternoon collapse compared to the CLEAR case. The initial conditions of the AERO+$_{\omega=0.7}$ experiment are equal to the ones for AERO+, except $\omega = 0.7$. The LES results are the vertically averaged values from the surface until z_i.

Variable / Experiment	CONTROL	CLEAR	AERO+	AERO+$_{\omega=0.7}$
θ (K)	290.8 (-0.05)	290.7 (+0.05)	291.0 (-0.25)	291.8 (-0.15)
HR (K day^{-1})	1.3 (-0.10)	-	3.7 (+0.25)	11.4 (+0.45)
z_i (m)	1185 (+35)	1185 (+71)	1155 (+15)	1310 (+75)
Δt (min)	-13 (-2)	0 (-6)	-50 (+10)	-97 (+19)

CBL morning onset is explained by the slightly different initial conditions used for the LES and the MXL models (see Fig. 4.2). For the afternoon CBL (CESAR2003 - Table 4.3) a similar performance of the MXL model is found. The deepening of the afternoon CBL caused by strongly absorbing aerosols is slightly overestimated in the MXL model because the earlier stabilization of the potential temperature is not taken into account due to the well-mixed nature of the MXL model. Finally, the significant advance of the afternoon CBL collapse upon the presence of aerosols is well captured. In conclusion, the performance of the MXL suffices to map the aerosol effect on the CBL dynamics for a wider range of aerosol characteristics. The satisfactory performance of the MXL model indicates that the mixed-layer theory assumptions, i.e. infinitesimally thin inversion layer and the well-mixed CBL, do not dramatically change the CBL thermodynamics behavior, if compared to the LES results. Despite the good performance, we note, however, that the availability of an LES model remains important to validate the MXL model results, like presented in Tables 4.2 and 4.3.

4.4.2.2 Aerosol impacts on the morning CBL

As shown in Fig. 4.8, we find shallower morning CBLs if τ increases. For example, similar to the CONTROL experiment (black dot), for $\omega = 0.92$ and $\tau = 0.2$, the CBL height at 10 UTC reaches about 1400 m decreasing to around 700 m for $\omega = 0.92$ and $\tau = 0.6$ (AERO+ experiment, blue dot). We find that the sensitivity of the CBL growth (and irradiance) to τ increases if the aerosols become more absorbing, i.e ω decreases. In the case of scattering aerosols more energy reaches the surface because forward scattering prevails. If aerosols absorb instead of scatter SW radiation, some of this forward-scattered radiation is absorbed in the CBL, further reducing the SW radiation reaching the surface. By increasing the amount of strongly absorbing

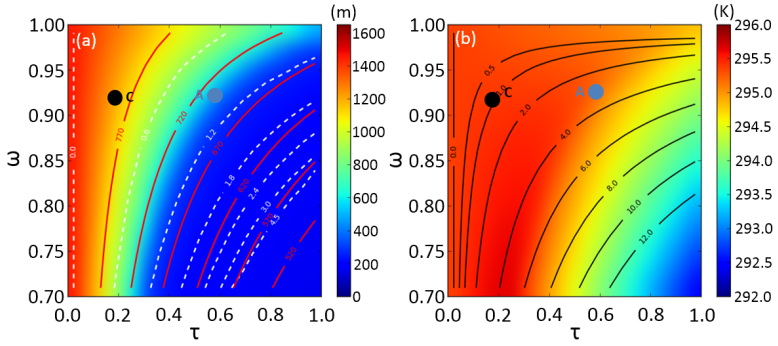

Figure 4.8: (a) CBL height (shades), downward irradiance (red continuous contour in Wm^{-2}) and time delay (in hours) of the morning inversion layer break-up compared to the CLEAR case (white-dashed contour). (b) Potential temperature (shades) and aerosol HR (black continuous contour in K day^{-1}) as a function of the aerosol optical depth and single scattering albedo. The black (blue) dots represent the CONTROL (AERO+) ω and τ conditions. All variables are shown for CESAR2008 case at 10 UTC, except the time delay of the morning inversion break-up, which is based on the morning onset time of CLEAR.

aerosols (towards the lower-right corner of Fig. 4.8), the sensible heat flux is reduced significantly (see Fig. 4.5b). Consequently, there is insufficient energy to overcome the temperature inversion and the residual layer remains present above the CBL (see also Fig. 4.10b) the entire day (dashed contours in Fig. 4.8a).

Our results also show that the morning CBL (10 UTC) is significantly warmer either for clear conditions (τ close to zero) or for purely scattering aerosols (ω close to unity). The physical explanation is the following: forward scattering aerosols (or clearer atmospheres) allow more SW radiation to reach the surface, leading to higher sensible heat fluxes, warming the morning CBL. As shown in Figs. 4.6a and 4.6b, at 10 UTC the heat budget is mainly driven by the combination of the surface and entrainment turbulent fluxes, explaining the increase in the CBL potential temperature. If τ increases, more SW radiation is absorbed within the aerosol layer (increasing the HR for absorbing aerosols). However, under the conditions of CESAR2008 case, the surface inversion layer jump is not weakened because part of the aerosols reside above the CBL, i.e. $\mathrm{h}_a > z_i$. The CBL remains therefore shallow, and θ is mainly driven by the turbulent surface fluxes, which are reduced due to aerosol extinction of SW radiation.

These findings emphasize the importance of representing adequately the aerosol

layer since its depth plays a crucial role in the surface energy partitioning and CBL growth.

4.4.2.3 *Aerosol impacts on the afternoon CBL*

Analogously, we explore in Fig. 4.9 the results for CESAR2003. For the aerosol impacts on the afternoon CBL we focus on the CESAR2003 case because for CESAR2008 the surface inversion is not broken for certain aerosol conditions (see Fig. 4.8a and Fig. 4.10). We select 13.5 UTC as a representative time for this case study because SH>0 and the aerosols are completely incorporated within the CBL for all the experiments.

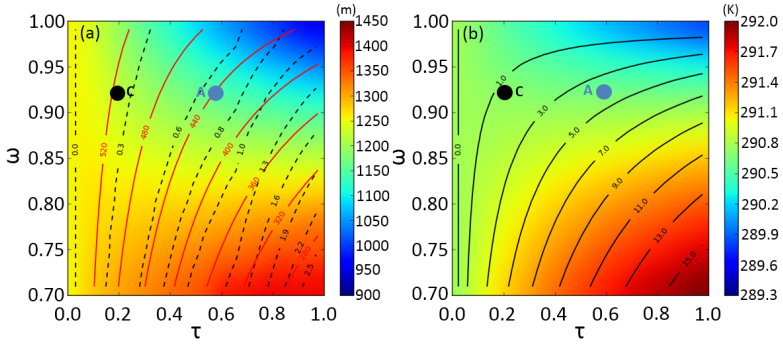

Figure 4.9: Same as Fig. 4.8 but for the CESAR2003 (13.5 UTC) except in (a) where the black dashed contours are the time advance (in hours) of the CBL afternoon collapse compared to the CLEAR case.

The main difference with Fig. 4.8 is the fact that during the afternoon the heating due to aerosols alters more significantly the heat budget (see Fig. 4.6b). Our results agree with the findings of Yu *et al.* (2002) pointing out that strongly scattering aerosols lead to an afternoon CBL that is shallower and colder. The physical explanation is the following: scattering aerosols reduce irradiance - back-scattering SW radiation - without incrementing the HR (solid contours in Fig. 4.9b). The opposite is observed for absorbing aerosols because the reduction of the irradiance is overcompensated by the increase of the HR. For the CBL height, the HR compensates the irradiance reduction at $\omega \sim 0.83$. Interestingly, for potential temperature - at 13.5 UTC - the effects counterbalance at $\omega \sim 0.91$. This value is slightly higher than $\omega \sim 0.86$ found by Lyamani *et al.* (2010).

We observe a shortening of the convective period - defined as the part of the diurnal cycle when SH> 0 - if aerosols are present (see also SH_{AERO+} ratio in Fig. 4.5b). Our results indicate that the earlier decay of turbulence advances the afternoon collapse of the CBL up to 2.5 hours for high loads of strongly absorbing aerosols (dashed contours in Fig. 4.9a). This effect has important implications for the establishment of the stable boundary layer, see Nair *et al.* (2011). As shown in Fig. 4.9a (lower-right portion), the stable boundary layer is formed earlier (up to 2.5 hours) if strongly absorbing aerosols are present.

4.4.2.4 Aerosol impacts on the diurnal evolution of the CBL

In this section we apply the MXL model to quantify the impact of aerosol optical properties - τ and ω - on surface and atmospheric variables. We present maxima and diurnal averages (denoted by an overbar) for the CESAR2008 case. Our purpose here is to study how aerosols affect important state variables that are normally used to investigate atmospheric phenomena with larger temporal and spatial scales than the boundary-layer scale. By doing so, we broaden our understanding on how the land-atmosphere system responds to aerosol forcing. The impacts of purely scattering ($\omega = 1.0$) and strongly absorbing ($\omega = 0.7$) aerosols on the diurnal evolution of the CBL are shown in Fig. 4.10. We use $SH > 0$ as a criterion to determine the duration of the convective period. Note that we quantify the aerosol impact by normalizing the differences by the CLEAR case value ($\frac{\phi_{CLEAR} - \phi_{\tau,\omega}}{\phi_{CLEAR}}$), where ϕ is the variable under study.

In Fig. 4.10a we show the diurnally averaged surface fluxes. Aerosols significantly diminish the amount of available energy at the surface. The reduction in $\overline{Q_{NET}}$ is more pronounced for strongly absorbing aerosols (44%) than for purely scattering aerosols (17%). Even for heavy loads of strongly scattering aerosols ($\tau = 1.0$ and $\omega = 1.0$) the reductions in $\overline{LE}$ (15%) and $\overline{SH}$ (22%) remain relatively small compared to CLEAR. In contrast, for heavy loads of strongly absorbing aerosols ($\tau = 1.0$ and $\omega = 0.7$), $\overline{LE}$ and $\overline{SH}$ diminish by 43% and by 50%, respectively. Note that, under the well-watered surface conditions, the percentage reduction is more significant for $\overline{SH}$ than for $\overline{LE}$ (see also Fig. 4.5 panels b and c).

The reduction observed for $\overline{LE}$ has direct implications for diurnal average evaporation (not shown), decreasing from 6.4 mm day^{-1} for the CLEAR case to 3.7 mm day^{-1} for heavy loads of strongly absorbing aerosols. For purely scattering aerosols a slight reduction of 1.0 mm day^{-1} is observed for $\tau = 1.0$. These results confirm the findings of Biasutti & Giannini (2006), where aerosols intensified dryness in the Sahel region.

As shown in Fig. 4.10b, we find for purely scattering aerosols that the reduction in $\overline{\mathrm{Q_{NET}}}$ diminishes the maximum CBL height with 95 m for $\tau = 1.0$. The total energy in the system integrated over the CBL and the residual layer also decreases with 17%. We define the CBL heat input (HI) similarly as Barbaro *et al.* (2013):

$$HI = SH + \int_0^{z_i} HR dz.$$

For purely scattering aerosols $\overline{\mathrm{HI}}$ also decreases to 78% of the CLEAR value. Depending on τ, strongly absorbing aerosols have a different impact on the growth of the CBL. We find that the maximum CBL height increases by up to 65 m and that the $\overline{\mathrm{HI}}$ increases by up to 46% compared to CLEAR for $\tau \leq 0.4$. Note the maxima in CBL height and CBL $\overline{\mathrm{HI}}$ for $\tau = 0.4$. For $\tau > 0.4$ the maximum CBL height diminishes because the reduction of $\overline{\mathrm{SH}}$ significantly delays the onset of the CBL growth. If $\tau > 0.6$ the heat introduced by $\overline{\mathrm{SH}}$ is insufficient to totally overcome the residual layer (see also Fig. 4.8a). Note that for $\tau > 0.8$ the increase of $\overline{HR}$ compensates the less acute decrease in both z_i and $\overline{\mathrm{SH}}$, leading to a nearly constant CBL $\overline{\mathrm{HI}}$. The maximum CBL height equals to 278 m for $\tau = 1.0$. For strongly absorbing aerosols, a significant part of the energy that does not reach the surface is absorbed by the aerosols located within the RL and the CBL. Therefore, we note an increase in the total energy up to 37% compared to CLEAR as τ increases. Note

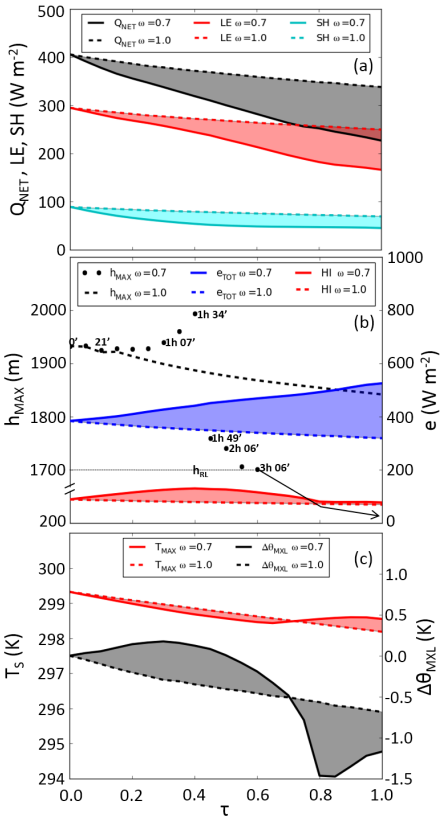

Figure 4.10: Surface and (thermo)dynamics variables as a function of the aerosol optical depth for CESAR2008. The shades indicate the range of variation between strong absorption $\omega = 0.7$ (continuous lines) and purely scattering aerosols $\omega = 1.0$ (dashed lines). (a) Diurnally averaged Q_{NET} (black), LE (red) and SH (cyan). (b) Maximum CBL height (black dots and dotted line) and diurnal averages of total energy (blue, right axis) and CBL heat input (red, right axis). In (b) the numbers next to the dots ($\omega = 0.7$) indicate the time delay of the morning inversion layer break-up compared to the CLEAR case; for $\tau > 0.6$ and $\omega = 0.7$ the response of h_{MAX} is schematized because the CBL does not overcome h_{RL} (1700 m, thin black dotted-line). Note the different scales for the y-axes. (c) Maximum (red) surface temperature and diurnally and mixed-layer averaged potential temperature difference compared to CLEAR (black, right axis).

that in spite of the shallower CBLs, the total energy in the system always increases because of the heating of the residual layer. The impact of aerosols on the total energy significantly modifies the effective albedo (α_{EFF}) by altering the irradiance and the outgoing SW radiation (see Fig. 4.5a). Compared to CLEAR, α_{EFF} decreases by 40% for strongly absorbing aerosols and increases by 64% for purely scattering aerosols.

We show in Fig. 4.10c the maximum surface temperature (T_{MAX}), and diurnally and mixed-layer averaged potential temperature difference compared to the CLEAR case ($\Delta\bar{\theta}_{MXL} = \bar{\theta}_{MXL} - \bar{\theta}_{MXL}^{CLEAR}$). We observe that, irrespective of their absorption properties, aerosols always reduce the daytime surface temperature. T_{MAX} diminishes, by 0.8 K ($\omega = 0.7$) and by 1.2 K ($\omega = 1.0$), for the entire τ range. The differences in T_{MAX} are small among the absorption regimes. T_{MAX} is always slightly larger for purely scattering aerosols except for high loads of absorbing aerosols due to the less accentuated reduction in $\overline{\text{HI}}$. The $\Delta\bar{\theta}_{MXL}$ evolution follows the CBL $\overline{\text{HI}}$. For strongly absorbing aerosols and $\tau > 0.8$ the CBL $\overline{\text{HI}}$ remains nearly constant and is used to heat a shallower CBL, increasing $\bar{\theta}_{MXL}$.

4.5 Conclusions

In this study we quantified the effects of aerosol scattering and absorption of shortwave (SW) radiation on the surface energy budget and on the convective boundary layer (CBL) dynamics. To this end, we coupled an atmospheric large-eddy simulation (LES) model and a mixed-layer (MXL) model to a (i) land-surface model and a (ii) SW radiation transfer model. We successfully validated our LES and MXL model results using measurements of (thermo)dynamic variables and aerosol properties for two typical CBL prototypes: CESAR2008 and CESAR2003. During CESAR2008, the early morning potential temperature profile was characterized by a well-mixed residual layer above a strong near surface inversion, leading to a rapid onset of the CBL during the morning transition. CESAR2003, in contrast, was characterized by a continuous growth of the CBL. Given the good agreement between the LES and MXL model results, we explored the aerosol effect on the land-atmosphere system for a wide range of optical depths and single scattering albedos.

The LES and MXL model results showed that over the studied well-watered grassland, aerosols reduced the sensible heat flux more than the latent heat flux. As a result, relatively scattering aerosols decreased the Bowen ratio from around 0.47 at 08 UTC down to values as low as 0.12 at 14 UTC. Aerosols also delayed (up to 4.5 hours) or even prevented the CBL morning onset and hasten (up to 2.5 hours) its

afternoon collapse. Not only the vertical distribution of the aerosols played an important role on the CBL evolution, but also the initial temperature profile. In the CESAR2008 case, for instance, we found that strongly absorbing aerosols in the residual layer could maintain a persistent near-surface inversion for the entire day. When the aerosols were entrained in the CBL, we observed a strong dependence of the single scattering albedo on the afternoon CBL (thermo)dynamics: for CESAR2003 the strongly absorbing aerosols ($\omega = 0.7$) deepened and warmed (+140 m and +1.2 K, respectively), while purely scattering aerosols shallowed and cooled (−280 m and −1.0 K, respectively) the afternoon CBL if compared to the CLEAR case. The diurnally averaged surface net radiation for CESAR2008 showed a strong dependence on the type of aerosol, decreasing by 68 Wm^{-2} for heavy loads of purely scattering aerosols and by 180 Wm^{-2} for the same load of strongly absorbing aerosols. Under the studied surface conditions, the diurnal average evaporation decreased by 16% and by 42% for purely scattering and strongly absorbing aerosols respectively, if compared to CLEAR.

Due to the comprehensiveness of the observational data set and the LES results discussed here, our study can be used as a benchmark to evaluate the coupling and the performance of the parameterizations for SW radiation, land-surface and boundary-layer schemes, implemented in mesoscale or global chemistry transport models. In particular, we showed the intrinsic non-linear couplings within the land-atmosphere system. The impact of aerosols for different surfaces and heterogeneous conditions as well their effects on the LW cooling will be investigated in a future study.

"But it's no joke
It's doing me harm, you know I can't sleep
I can't stop my brain, you know it's three weeks
I'm going insane
You know I'd give you everything I've got
For a little peace of mind"

Lennon, J.W. and McCartney, J.P. (1968). I'm so tired. *The Beatles*, **2(B)**, Apple Records.

5

Numerical simulation of the interaction between ammonium nitrate aerosol and convective boundary-layer dynamics

Published as:
Barbaro, E., Krol, M. & Vilà-Guerau de Arellano, J. (2015). Numerical simulation of the interaction between ammonium nitrate aerosol and convective boundary-layer dynamics. *Atmospheric Environment*, **105**, 202 – 211

Abstract

We investigate the interaction between the ammonium nitrate aerosol ($^{A}NO_3$) abundance and convective boundary-layer (CBL) dynamics by means of a large-eddy simulation (LES) framework. In our LES model the CBL dynamics is solved coupled with radiation, chemistry, and surface exchange. Concerning the aerosol coupling we assume a simplified representation that accounts for black carbon, aerosol water and inorganic aerosols, focusing on the semi-volatile ammonium nitrate aerosol within the CBL. The aerosol absorption and scattering of shortwave radiation is also taken into consideration. We use a data set of observations taken at the Cabauw Experimental Site for Atmospheric Research during the IMPACT/EUCAARI (European Integrated Project on Aerosol, Cloud, Climate, and Air Quality Interactions) campaign to successfully evaluate our LES approach. We highlight that our LES framework reproduces the observations of the ratio between gas-phase nitrate and total nitrate at the surface, with a diurnally-averaged overestimation of only $\approx 12\%$. We show that the dependence between gas-aerosol conversion of nitrate and CBL (thermo)dynamics produces highly non-linear concentration and turbulent flux vertical profiles. The flux profiles maximize at around 1/3 of the CBL. Close to the surface, we show that the outgassing of $^{A}NO_3$ affects the dry deposition of nitrate. This outgassing is responsible for the high deposition velocities obtained from the concentration and flux measurements during observational campaigns. To account for the influence of CBL (thermo)dynamics on gas-aerosol conversion we propose an effective turbulent exchange coefficient based on an analysis of the flux budget equation of aerosol nitrate calculated by our LES. The implementation of this effective turbulent exchange coefficient in a 1D model leads to a better agreement with the LES results and with surface observations.

5.1 Introduction

The role of tropospheric aerosols in the climate system has been exhaustively studied over the past decades (Jacobson, 1998; Kaufman *et al.*, 2002; Bellouin *et al.*, 2005). According to a recent overview of Baklanov *et al.* (2014), however, the online coupling of atmospheric dynamics, aerosol transport, chemical reactions, and atmospheric composition in numerical models will remain a challenge over the next years. Specifically for the convective boundary layer (CBL) only in the last decade a few integrating studies appeared that couple aerosols to boundary-layer dynamics, microphysics and chemistry (Jiang & Feingold, 2006; Barbaro *et al.*, 2014; Lee *et al.*, 2014). The same is noted from the observational perspective. Several measurement campaigns have established a comprehensive database of meteorological observations (Angevine *et al.*, 1998b; Masson *et al.*, 2008) often including radiosondes of the CBL vertical structure. However, only a few have combined these with detailed aerosol and chemical observations (Kulmala *et al.*, 2011; Jager, 2014).

In this Chapter we study the formation and transport of ammonium nitrate aerosol (henceforth called ${}^{A}NO_3$) within the CBL placing special emphasis on understanding and representing processes such as the deposition flux and turbulent transport. Extending previous studies (Vinuesa & Vilà-Guerau de Arellano, 2003; Vilà-Guerau de Arellano *et al.*, 2005; Aan de Brugh *et al.*, 2013; Barbaro *et al.*, 2014) we present here a Large-Eddy Simulation (LES) modeling framework. The novelty of this study lies in the dynamical coupling of the CBL (thermo)dynamics and turbulence with the surface, radiation, chemistry, and aerosols. At the surface, we explicitly solve the energy budget and account for bi-directional turbulent flux exchanges of chemical species.

Aan de Brugh *et al.* (2013) have shown by means of an LES (albeit without accounting for deposition effects and chemistry) that fast vertical mixing in the CBL in combination with a temperature-dependent partitioning of atmospheric nitrate between the gas and aerosol phases leads to interactions between dynamics and aerosol formation. Close to the top of the CBL (cooler) gaseous nitric acid (henceforth called ${}^{g}HNO_3$) and ammonia (NH_3) condense on ${}^{A}NO_3$, thus the gas-aerosol equilibrium shifts towards the aerosol phase. Close to the surface (warmer) ${}^{A}NO_3$ evaporates to ${}^{g}HNO_3$ shifting the equilibrium towards the gas-phase.

The outgassing of ${}^{A}NO_3$ close to the surface significantly affects the dry deposition of nitrate since its deposition velocity depends upon whether nitrate is in the gas or particle phase (Huebert & Robert, 1985; Mozurkewich, 1993; Nemitz & Sutton, 2004). This has implications especially for the measurement community since the gas-aerosol equilibrium may change below the measurements height (Huebert *et al.*, 1988; Wolff

et al., 2010). As a result, several studies report very high aerosol nitrate deposition velocities (Hanson, 1991) since the actual measurements reflect a so-called "apparent deposition" (Nemitz & Sutton, 2004).

According to previous studies (Harrison & Pio, 1983; Mozurkewich, 1993; Nemitz & Sutton, 2004; Morino *et al.*, 2006; Fountoukis & Nenes, 2007; Aan de Brugh *et al.*, 2013) the physical mechanisms that drive the gas-aerosol nitrate spatial distribution are: (i) the availability of NH_3 and SO_4^{2-}, (ii) CBL (thermo)dynamics, (iii) gas-aerosol equilibration timescale (τ_{eq}), and (iv) dry deposition of gas phase nitrate. As discussed in previous work (Morino *et al.*, 2006; Fountoukis & Nenes, 2007; Aan de Brugh *et al.*, 2012), τ_{eq} is the effective timescale required for ammonia and gaseous nitric acid to reach equilibrium with the inorganic aerosol particles. Several studies estimated that τ_{eq} for aerosol nitrate ranges from a few seconds to several minutes, i.e. τ_{eq} is of similar order of magnitude as the turbulent timescale of the CBL (Dassios & Pandis, 1999; Morino *et al.*, 2006; Aan de Brugh *et al.*, 2013). In such circumstances, non-linearities between CBL dynamics and chemistry are expected (Fitzjarrald & Lenschow, 1983; Krol *et al.*, 2000; Vinuesa & Vilà-Guerau de Arellano, 2003). Despite its importance, an accurate representation of τ_{eq} from the observational point of view remains challenging, since τ_{eq} depends on microphysical properties of aerosols, e.g. viscosity and particle size (Shiraiwa & Seinfeld, 2012; Saleh *et al.*, 2013), and CBL (thermo)dynamics (Morino *et al.*, 2006).

Most atmospheric models use standard diffusion theory (K-theory) to parametrize the vertical turbulent flux of chemical species (Hamba, 1993; Vilà-Guerau de Arellano & Duynkerke, 1995; Hesterberg *et al.*, 1996; Nemitz *et al.*, 2004; Aan de Brugh *et al.*, 2012). In this approach the exchange coefficient for heat or moisture is also used for chemical species. For inert scalars or long-lived species, standard diffusion theory has been proven sufficiently accurate to represent the turbulent vertical transport (Vilà-Guerau de Arellano & Duynkerke, 1995). For short-lived species, it has been suggested to adapt the exchange coefficient taking the chemical timescale into account (Vilà-Guerau de Arellano & Duynkerke, 1992).

In this Chapter, we revisit the gas-aerosol partitioning of nitrate in the CBL using our coupled LES framework. We focus on two outstanding issues concerning nitrate. First, we will investigate the impact of CBL turbulence and chemistry on nitrate deposition. LES results will be used to calculate the nitrate deposition velocity for two values of τ_{eq}. Second, we investigate the question how to parametrize turbulent vertical flux accounting for the interaction between turbulence and the gas-aerosol conversion of nitrate (both explicitly solved in our LES) in non-eddy-resolving models. Consequently, we will derive a parametrization for transport of gas and aerosol nitrate and apply it in the Wageningen University Single Column model (WUSCM).

5.2 Methods

5.2.1 Numerical modeling framework

We investigate the evolution of the ammonium nitrate concentration within the CBL by means of an LES framework. The use of LES allows us to solve explicitly the most energetic turbulent eddies and parametrize only the smallest scales (see Appendix 5A). We use the Dutch Atmospheric LES (DALES, version 3.2 - see Heus *et al.* (2010) for details). We implemented ISORROPIA2 (Nenes *et al.*, 1998; Fountoukis & Nenes, 2007) to interactively account for the equilibrium between gas-phase and aerosol nitrate. The aerosol properties (extinction, single scattering albedo - ω, and asymmetry factor - g) are dynamically calculated in DALES by means of an aerosol module, as explained in detail in Aan de Brugh *et al.* (2012). The aerosols are also coupled to the shortwave (SW) radiation calculations by means of the broadband two-stream Delta-Eddington model, as discussed in Barbaro *et al.* (2014). We parametrize dry deposition of gas-phase chemicals and aerosols similarly to Ganzeveld & Lelieveld (1995) and Slinn & Slinn (1980) respectively, and the surface energy budget equations are calculated based on van Heerwaarden *et al.* (2010). A detailed description of the SW radiation and land-surface modules, and their coupling in DALES, was already given by Barbaro *et al.* (2014). Therefore, we here focus on a description of the chemistry, aerosol, and dry deposition modules.

5.2.1.1 Chemistry module

The simple background gas-phase chemical utilized here was already used in several DALES studies (Vilà-Guerau de Arellano *et al.*, 2011) and we will show that realistic distributions of the main chemicals species are simulated. Our main goal is to ensure a satisfactory reproduction of the NO-NO_2-O_3 triad and an accurate formation rate of ${}^{g}HNO_3$ from the oxidation of NO_2 (OH + NO_2 $\longrightarrow$ ${}^{g}HNO_3$).

In the Appendix 5A we provide the 3D conservation equation for the resolved scalar spatial and temporal distributions in DALES. Here, as a process illustration of the coupling between dynamics and the chemistry, we show in Eq. 5.1 the 1D conservation equation of the aerosol nitrate for a horizontally averaged CBL explicitly including the gas-particle conversion:

$$\frac{\partial \overline{{}^{A}NO_3}}{\partial t} = -\frac{\partial \overline{w' {}^{A}NO_3'}}{\partial z} + \frac{\overline{{}^{A}NO_3^{eq}} - \overline{{}^{A}NO_3}}{\tau_{eq}}, \tag{5.1}$$

where the first term on the right hand side is the vertical turbulent flux divergence of nitrate explicitly solved by our LES (but parameterized in 1D models), and the

last term represents the temperature dependent gas-particle conversion. Similarly to Nemitz & Sutton (2004), we write the gas-particle conversion term as the difference between the ${}^{A}NO_3$ equilibrium (${}^{A}\mathrm{NO}_3^{eq}$) calculated by ISORROPIA2 and the actual ${}^{A}NO_3$ concentration divided by τ_{eq} for nitrate. The dependence of the gas-aerosol nitrate equilibrium on absolute temperature and relative humidity is carefully discussed in Mozurkewich (1993) and Nenes *et al.* (1998). The equilibrium is obtained provided the total concentrations of nitrate and ammonia, (TNO_3 and TNH_4, respectively) absolute temperature and relative humidity (Mozurkewich, 1993; Aan de Brugh *et al.*, 2013). These fields are dynamically obtained from the LES and serve as input parameters for the ISORROPIA2 calculations.

5.2.1.2 Aerosol module

The optical properties of inorganic and black carbon (BC) aerosols are calculated assuming two log-normal aerosol size distributions ($\bar{r} = 75$ nm and 37 nm, respectively and $\sigma = 2$, where r is the geometric radius and σ the geometric standard deviation of both the distributions). The first mode represents an accumulation soluble aerosol and the second mode an insoluble aerosol (containing only black carbon). Analogous to Aan de Brugh *et al.* (2012), we assume all the inorganic aerosols to be spherical and contain only water, ammonium nitrate and ammonium sulfate. The insoluble BC particles are assumed to be externally mixed with the soluble particles. Similarly to Aan de Brugh *et al.* (2012) our model does not take into account organic aerosol. The lack of organic aerosols can cause an underestimation of the extinction coefficient since it represents a significant component of particulate matter in the Netherlands (Dusek *et al.*, 2013). Since ultimately our intent is to reproduce the correct effect of the aerosols on the surface net-radiation (Barbaro *et al.*, 2014) we compensate the absence of organic aerosols by introducing aerosol nitrate, aerosol sulfate and black carbon in the free atmosphere according to the observations of aerosol optical depth (τ) and single scattering albedo as we detail in Sect. 5.3.

5.2.1.3 Dry-deposition module

The dry-deposition velocities for gaseous species (v_d) are parametrized as described in Ganzeveld & Lelieveld (1995). Similarly, we take $v_d = (r_a + r_b + r_c)^{-1}$ where r_a is the aerodynamic resistance between the first level of the LES model (15 m in our case) and the surface, r_b is the quasi laminar sublayer resistance (depending on the gas and its molecular diffusivity) and r_c the bulk surface resistance. The dry-deposition for aerosols is calculated as $v_d^a = (r_a + r_d)^{-1}$ and is based on Slinn & Slinn (1980). In their approach v_d^a is related directly to the resistance terms, where r_d accounts

for the contributions of Brownian diffusion and impaction. Our aerosols are submicron particles, and the gravitational term can be safely neglected. We perform our simulations over a typical grassland (90% vegetated) with a constant surface roughness of 15 cm. The dry-deposition model implemented in our framework is similar to the scheme implemented in the TM5 chemical transport model (Krol *et al.*, 2005) and has been widely used in several studies (Huijnen *et al.*, 2010).

5.2.2 Observational data set

We design our LES experiments based on observations taken on May 8, 2008 at CESAR (Cabauw Experimental Site for Atmospheric Research, www.cesar-observatory.nl), in the Netherlands during the IMPACT/EUCAARI intensive measurement campaign (Kulmala *et al.*, 2011). We choose May 8, 2008 (hereafter CESAR2008) due to the availability of observations and the appropriate synoptic situation, characterized by a persistent high pressure system above central Europe favoring clear-sky conditions during the entire day (Hamburger *et al.*, 2011). The observations were extensively validated by Wang *et al.* (2009) (direct/diffuse *SW* radiation), Hamburger *et al.* (2011) (synoptics and pollution), Aan de Brugh *et al.* (2012) (gas-aerosol conversion) and Barbaro *et al.* (2014) (thermodynamics, CBL height and energy/radiation budgets). The hourly integrated gas-phase and aerosol nitrate, as well as the ammonia observations used in this work were measured simultaneously by a MARGA (Monitor for AeRosols and Gases in ambient Air) system as described in Aan de Brugh *et al.* (2012) and Mensah *et al.* (2012). In a MARGA system, the airflow enters the equipment at a constant rate of 1 m^3h^{-1} via a Teflon-coated inlet, with a cut-off for particles smaller than 10 μm (PM_{10}). The gas-phase compounds are collected by a WRD (wet rotating denuder) whereas the particulate matter passes through the WRD to be collected subsequently by a SJAC (Steam-Jet Aerosol Collector). For more information about the MARGA system we refer the reader to ten Brink *et al.* (2007) and Thomas *et al.* (2009). The NO_X-O_3 observations were taken at the nearby RIVM station (National Institute for Public Health and the Environment - www.lml.rivm.nl) in Zegveld, located at 20 km from the CESAR site. The aerosol optical depth was taken from the AERONET Level 1.5 data for Cabauw. The single scattering albedo was taken from the AERONET inversion data.

5.2.3 Experimental design

Barbaro *et al.* (2014) showed that during the morning CESAR2008 is characterized by a distinctive 1500 m residual layer (RL) sitting above a strong surface inversion (located at around 200 m above the surface). They also showed that the well-mixed

vertical structure of the RL allows a very rapid growth of the CBL after the break up of the morning inversion. During the afternoon the CBL grows fairly little (at a rate of ≈ 60 m h^{-1}) and the thermodynamical conditions remain relatively constant. Based on this, and similar to Aan de Brugh *et al.* (2013), we focus only on the afternoon period (11-16 UTC), which shows little CBL growth. We use as initial conditions the (thermo)dynamics, radiation and land-surface fields obtained by Barbaro *et al.* (2014) at 11 UTC.

Due to the computational cost of this coupled-LES experiment, the spatial numerical domain that has been simulated is reduced to 4800 × 4800 × 3000 m aiming to maintain the same spatial resolution of 50 × 50 × 15 m as in Barbaro *et al.* (2014). We verified that results are almost identical despite the reduction in the horizontal domain (not shown). We assume in the domain periodic horizontal boundary conditions, and to prevent numerical instabilities due to the chemical differential equations we reduced the original time step from 3 s to 1 s throughout the whole simulation.

In Aan de Brugh *et al.* (2013) an effective equilibration timescale of 30 minutes was adopted. Following their results, and the good agreement with observations (discussed in Sect. 5.3) we also adopt a constant (with respect to time and height) effective aerosol equilibration timescale of 30 minutes. Note, however, that based exclusively on the aerosol properties described in Sect. 5.2.1.2, a mass accommodation coefficient for aerosol nitrate equal to 0.5 (Dassios & Pandis, 1999), and a particle number concentration of 1000 cm^{-3} (Hamburger *et al.*, 2011) we calculate a τ_{eq} of approximately 3.5 min (see Eq. 3 in Saleh *et al.* (2013)). A plausible explanation for the difference between the calculated and effective τ_{eq} is that other chemical species (e.g. viscous secondary organic aerosols), may increase τ_{eq} due to aerosol mass-transport limitation (Morino *et al.*, 2006; Shiraiwa & Seinfeld, 2012). Additionally, the larger ammonium nitrate particles in the mode adapt slowest to the new environmental thermodynamics (Saleh *et al.*, 2013), and therefore also augment τ_{eq}. The use of a larger τ_{eq} might also account for the complex relation between chemistry and the multiscale character of CBL turbulence and thermodynamics (Morino *et al.*, 2006). In the CBL, smaller eddies alter the local environment at the scale of individual particles, whereas larger eddies transport the aerosols to different thermodynamic conditions within the entire CBL. These processes are characterized by different timescales, and combined may result in a larger τ_{eq}. The explanation of a larger τ_{eq} is similar to the larger turbulent timescale compared to the Kolmolgorov timescale, affecting cloud droplet formation (Grabowski & Wang, 2013).

In the setup used by Barbaro *et al.* (2014), τ and ω were prescribed following the observations taken during the EUCAARI campaign. Here we use the aerosol module (Sect. 5.2.1.2) coupled to our LES to explicitly calculate these aerosol properties

for every time step based on the aerosol concentrations of black carbon, ammonium, nitrate, sulfate and aerosol water. As shown later, our τ and ω are in close agreement with the observations and the LES results discussed in Barbaro *et al.* (2014).

We impose for CESAR2008 a constant surface emission of NO_X equal to 0.23 ppb m s^{-1} to account for the highway emission nearby the CESAR site. Most of the NO_X emissions in the Netherlands are vehicular (Velders *et al.*, 2011), and 90% (10%) are assumed to be in the form of NO (NO_2). Our NH_3 surface exchange is modeled as a combination of typical spring emission and deposition, and amounts, on average during the day, to 0.38 ppb ms^{-1}. This value agrees with flux measurements taken at Cabauw (on average $\approx$ 0.3 ppb ms^{-1}) see Erisman *et al.* (1989). We use a constant small isoprene surface emission equal to 15 ppt ms^{-1} to account for advection of nearby forested areas, leading to mixing ratios around 30 ppt within the CBL. The CH_4 and CO initial mixing ratios are set equal to 1.8 ppm and 0.2 ppm, respectively. These values are in agreement with climatological observations taken at CESAR (Vermeulen *et al.*, 2011). We summarize the initial concentrations (CBL and free-troposphere) and surface fluxes (emission/deposition velocity) of the most important chemicals in Table 4.1.

Table 5.1: Boundary conditions and initial concentrations at the CBL and free-troposphere for the CESAR2008 experiment. The v_d values are dynamically calculated depending on the resistances but remain fairly constant during the whole simulation. Note the free-tropospheric values for black carbon, ammonium nitrate, and ammonium sulfate used to compensate for the lack of organic aerosol in our model. Also note that aerosol ammonium (NH_4^+) is formed by neutralization of H_2SO_4 and HNO_3.

Chemicals	**Surface**		**CBL (ppb)**	**FT (ppb)**
	Emission (ppb ms^{-1})	**v_d (cm s^{-1})**		
NO	0.21	0.10	1.0	0.1
NO_2	0.02	0.45	4.0	1.0
O_3	-	0.60	57	65
Isoprene	0.015	-	0.01	0.01
BC	-	0.004	1.5	1.5
^{g}HNO$_3$	-	1.86	0.9	0.9
^{A}NO$_3$	-	0.004	2.0	2.3
SO_4^{2-}	-	0.004	1.3	1.3
NH_3	0.5	1.01	11	1.0
NH_4^+	-	0.004	4.6	4.9
CH_4	-	-	1800	1800
CO	-	0.002	200	200

In addition to the CESAR2008 experiment we design another LES experiment prescribing the same boundary-layer and surface properties as CESAR2008, but shorten-

ing the equilibration timescale to 10 minutes (hereafter called CESAR2008-10). Our motivation is that the microphysical properties of aerosol nitrate have not been measured at Cabauw during CESAR2008, and the equilibration timescale plays a crucial role in the vertical transport of nitrate and on partitioning of TNO3 within the CBL (Dassios & Pandis, 1999; Morino *et al.*, 2006; Aan de Brugh *et al.*, 2012). The 10-min equilibration timescale is also closer to the value of 3.5 minutes, calculated according to Saleh *et al.* (2013). By performing these numerical experiments, we cover the situations where the turbulent time scale ($\tau_T \approx 17$ min) is either slightly longer or slightly shorter than the equilibration time scale. Therefore, strong interactions between gas-aerosol conversion and turbulence are expected (Fitzjarrald & Lenschow, 1983; Vinuesa & Vilà-Guerau de Arellano, 2003; Aan de Brugh *et al.*, 2012).

We use the WUSCM to investigate the ability of a non-eddy resolving model to reproduce our horizontally-averaged LES fields for the CESAR2008 experiment. In the WUSCM we use the same setup as in the work by Aan de Brugh *et al.* (2012). Similarly, the Medium Range Forecast (MRF) scheme is used to calculate the boundary-layer diffusion (Troen & Mahrt, 1986; Hong & Pan, 1996), and the momentum calculations are based on the parametrization proposed by Noh *et al.* (2003). To ensure consistency in the comparison between LES-averaged fields and the WUSCM vertical profiles, both the WUSCM and the LES model use the same free-tropospheric initial concentrations for ammonium nitrate and ammonium sulphate (Table 4.1). Besides that, the initial conditions for the (thermo)dynamics, land-surface, and net-radiation used in the WUSCM are taken from Barbaro *et al.* (2014). Also similarly to Aan de Brugh *et al.* (2012), the time step adopted in the WUSCM is 20 seconds. Note that reducing the time step in the WUSCM did not alter the results discussed here (not shown).

5.3 Evaluation of our LES results against surface observations

As described in the experimental design Section, the initial conditions for thermodynamics and radiation used in our LES are taken from Barbaro *et al.* (2014). Therefore, here we omit the evaluation of radiation and surface energy budgets, CBL height (based on the minimum of the buoyancy flux), and thermodynamics (potential temperature and specific humidity), which are shown in Fig. 3 of Barbaro *et al.* (2014). The evolution of the temperature and relative humidity at 2m height is shown in Fig. 1 of Aan de Brugh *et al.* (2013). In Fig. 5.1 we present an evaluation of the CBL chemistry and the aerosol properties against the available surface observations.

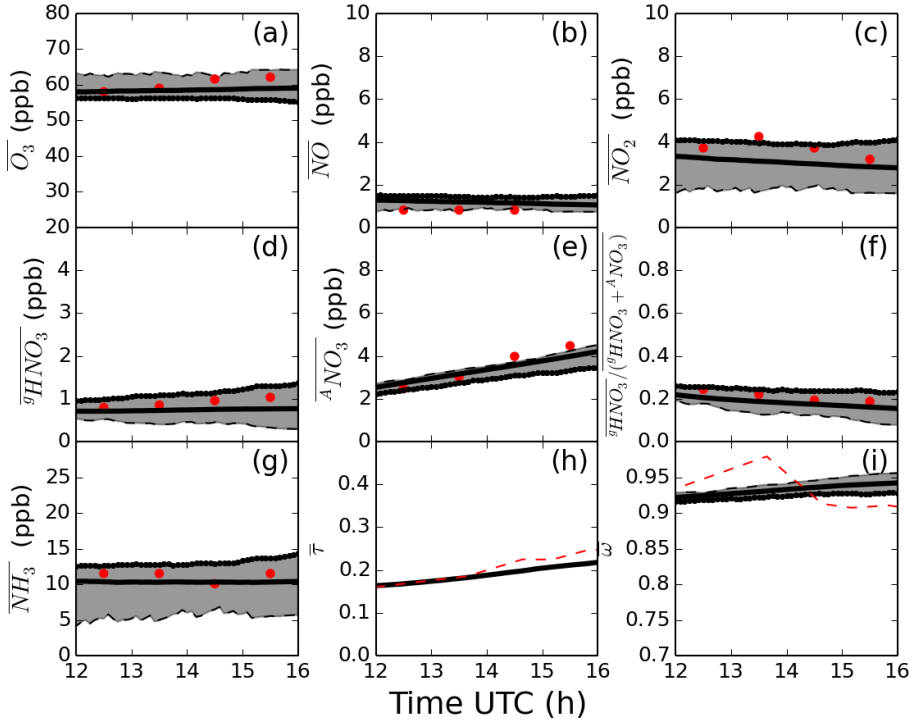

Figure 5.1: Time evolution of the chemistry (a-g) and aerosol properties (h-i) for our LES framework (CESAR2008) and surface observations taken at CESAR. The red dots represent the RIVM/CESAR hourly-averaged surface observations and the red dashes the EUCAARI continuous aerosol measurements (at 550 nm). The shades represent the difference between the horizontally-averaged values at the surface (black dots) and at the top of the CBL (dashes). The black lines represent the bulk values of the atmospheric compounds averaged over the CBL.

The results correspond to an aerosol equilibration time partitioning equal to 30 min (Aan de Brugh *et al.*, 2013). Note that we concentrate our analysis only in the afternoon CBL to reduce the role of diurnal variability (Barbaro *et al.*, 2014). The observations of ozone, NO_X, gas-aerosol nitrate and ammonia taken at CESAR are hourly averaged.

Based on Fig. 5.1 we conclude that our LES is able to adequately simulate the chemistry and the aerosol properties during the afternoon for CESAR2008. It can be observed that the NO_X-O_3 is well reproduced. Comparable O_3 mixing ratios during the afternoon are commonly observed in CESAR (Demuzere *et al.*, 2009) and similar NO_X-O_3 mixing ratios were recently reported throughout the whole Europe during

the PEGASOS campaign (Jager, 2014). The ${}^{g}HNO_3$ and ${}^{A}NO_3$ concentrations are also properly simulated in our LES (adopting a constant equilibration time scale equal to 30 min). The TNO_3 partitioning, defined as ${}^{g}HNO_3/({}^{g}HNO_3 + {}^{A}NO_3)$, is also well in agreement with the surface observations, with a diurnal average overestimation of ≈ 12 %. This result supports the use of the effective equilibration timescale equal to 30 minutes to simulate the partitioning of nitrate within the CBL for this case. Note, however, that the chemistry of the CESAR2008 case is characterized by a small diurnal variability (specially for NO_X-O_3). Therefore, the good match obtained with our LES framework compared to the surface observations is partly explained by our choice of initial concentrations (shown in Table 4.1).

The elevated NH_3 concentrations within the CBL (Fig. 5.1g) are explained by the high surface emissions due to the intense cattle farming in the Netherlands (Velthof *et al.*, 2012). The significant differences between the maximum-minimum (shades) concentrations observed for NH_3 are due to surface emissions and the small free-tropospheric concentrations (the latter also seen for NO_2) compared to the surface values (see Table 4.1). The fluctuations observed at the top of the CBL (dashes) are due to entrainment of cleaner air from the free-troposphere.

The aerosol properties are well reproduced during the whole simulation. Around 13.5 UTC advection of polluted air brings slightly more absorbing aerosols from Central Europe (Hamburger *et al.*, 2011), decreasing ω. Nevertheless, the aerosol optical depth remains almost unchanged. We are able to compensate for the lack of organic aerosol in our model and therefore to properly reproduce τ by adding ammonium nitrate and sulfate, and black carbon in the free atmosphere. We are aware that this may lead to excessive entrainment of aerosols from the free-troposphere. However, the CBL grows fairly little during the whole simulated period.

5.4 Impact of different equilibration timescales on the gas-aerosol conversion

In Fig. 5.2 we compare the vertical profiles of gas-phase and aerosol nitrate, total nitrate and ammonia obtained for CESAR2008 (τ_{eq} = 30 min) and CESAR2008-10 (τ_{eq} = 10 min) experiments. To ensure robustness, all the vertical profiles are horizontally- and time-averaged between 12.5 UTC - 14.5 UTC.

We observe in Fig. 5.2 that the gas-aerosol conversion mechanisms and the equilibration timescale significantly influence the vertical profiles of ${}^{g}HNO_3$ and ${}^{A}NO_3$ for both numerical experiments. Regardless of the well-mixed character of the CBL,

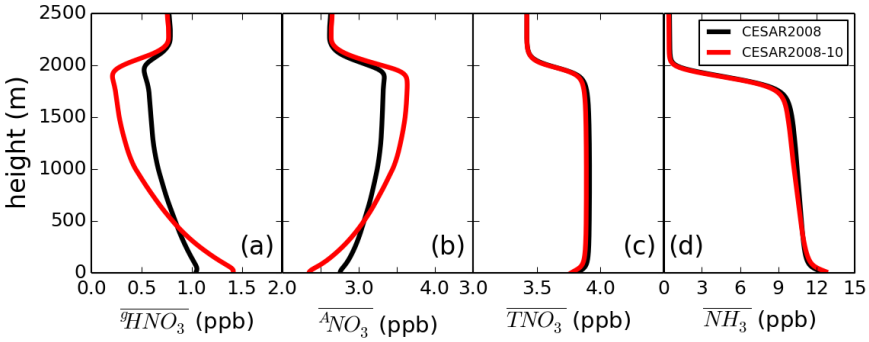

Figure 5.2: Horizontally-averaged vertical profiles of (a) ${}^{g}HNO_3$ (b) ${}^{A}NO_3$ (c) TNO_3 (d) NH_3. The legend indicates the experiment.

more ${}^{g}HNO_3$ is observed at the surface if compared with the top of the CBL. As expected, we note the opposite for ${}^{A}NO_3$.

We observe steeper gradients in the vertical profiles of gas-aerosol nitrate for the shorter equilibration time scale. This is explained by the faster gas-aerosol conversion. In that case, the equilibration time scale is shorter than the boundary-layer time scale ($\tau_T \approx 17$ min), creating a gradient that is maintained due to the relative slow turbulent motions. Note that more gas-phase nitrate is present close to the surface for the shorter equilibration timescale. That leads to higher values of TNO_3 partitioning at the surface, which is less consistent with observations (Fig. 5.2a and Fig. 5.2b, and Fig. 5.1f).

Since ${}^{g}HNO_3$ is converted into ${}^{A}NO_3$ and vice-versa, we note in Fig. 5.2c that the TNO_3 vertical profile is similar to a conserved variable. The small difference for the TNO_3 vertical profile between the two experiments is explained by larger quantities of ${}^{g}HNO_3$ close to the surface for CESAR2008-10 (Fig. 5.2a). In that case, more nitric acid deposits and by consequence the TNO_3 is slightly smaller than for CESAR2008. A well-mixed character is observed for NH_3 (Fig. 5.2d). Close to the surface and near the top of the CBL the profile is influenced by emission/deposition and detrainment, respectively. Due to the abundance of NH_3 we note that its association with ${}^{g}HNO_3$ has only a minor influence on its vertical distribution.

We present in Fig. 5.3 the ${}^{A}NO_3$-budget calculated based on Eq. 5.1. This budget quantifies the vertical contributions of (i) turbulent flux divergence and (ii) gas-aerosol conversion of nitrate to the tendency of ${}^{A}NO_3$ within the CBL.

Gas-aerosol conversion and vertical divergence of the turbulent flux contribute oppositely to the ${}^{A}NO_3$ evolution within the CBL. Close to the surface, aerosol ni-

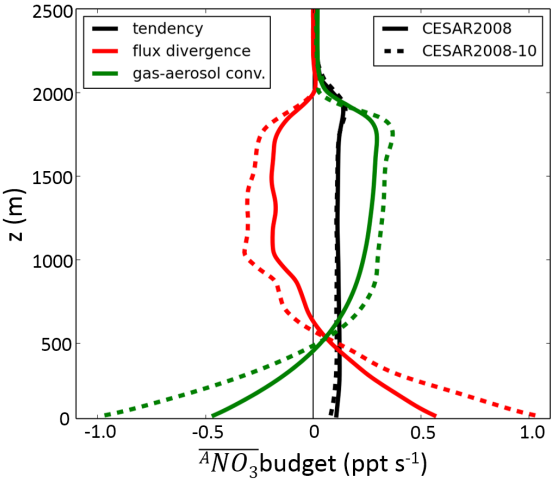

Figure 5.3: Vertical profile of the $^{A}NO_3$ budget time-averaged between 12.5-14.5 UTC. The budget terms and the experiments are indicated in the legends.

trate outgasses to $^{g}HNO_3$ and a strong positive $^{A}NO_3$ vertical gradient is created. From the mid-CBL up to the top of the CBL, downdrafts rich in $^{A}NO_3$ act towards homogenizing the $^{A}NO_3$ profile. As a net effect, the tendency term is positive and approximately constant with height indicating that aerosol nitrate is being produced throughout the CBL (see Fig. 5.1e).

As also shown by Aan de Brugh *et al.* (2012), reducing the equilibration timescale increases the contribution of the gas-aerosol conversion to the budget. Accordingly, the turbulent term reacts proportionally, implying in a larger turbulent vertical flux. Therefore, we show in Fig. 5.4 the influence of the equilibration timescale on the vertical profiles of the turbulent fluxes for the same variables discussed in Fig. 5.2.

The vertical fluxes for both $^{g}HNO_3$ and $^{A}NO_3$ are highly non-linear, driven by the spatial distributions of absolute temperature and relative humidity. Both maxima occur at around 1/3 of the CBL (Aan de Brugh *et al.*, 2013). In accordance to the vertical profiles of these concentrations (Fig. 5.2) the fluxes are larger for the shorter equilibration timescale. Since $^{g}HNO_3$ is converted into $^{A}NO_3$ and vice-versa, the turbulent fluxes for both variables are opposite and almost equal in magnitude. The small negative flux for total nitrate is caused by $^{g}HNO_3$ deposition since $^{A}NO_3$ deposition velocities are very small. As presented in Table 4.1, the net-turbulent flux of NH_3 depends on dry deposition and surface emission.

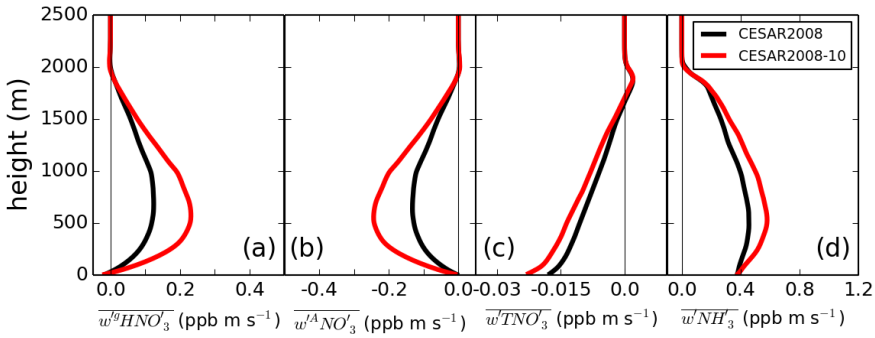

Figure 5.4: Same as Fig. 5.2 but for the turbulent vertical fluxes.

5.5 Aerosol nitrate deposition velocity

In our LES, we are able to explicitly calculate a height-dependent deposition velocity by taking the ratio between the turbulent vertical flux and the mean concentration at the surface (see Appendix 5A). We compare these velocities with the deposition velocities calculated at the surface based both on the atmospheric and surface resistances (see Table 4.1). We show in Fig. 5.5 the deposition velocities for $^{A}NO_3$, TNO_3 and O_3 within the surface layer for the CESAR2008 and CESAR2008-10 experiments.

We notice in Fig. 5.5a that $v_d^{^{A}NO_3}$ increases significantly with height within the surface layer and becomes even larger than the maximum deposition velocity - defined as the inverse of the atmospheric resistance (Ganzeveld & Lelieveld, 1995). The strong vertical gradient observed within the surface layer explains why several observational studies have reported significant deposition velocities for aerosol nitrate (see Hanson (1991) for an extensive review). This overestimation of the deposition velocity (known as "apparent deposition") is caused by the strong outgassing of $^{A}NO_3$ close to the surface (Huebert *et al.*, 1988; Nemitz & Sutton, 2004). Comparing our LES experiments we find that this effect becomes more important at shorter time scales since the outgassing of $^{A}NO_3$ becomes more efficient. We found in Fig. 5.5b a larger TNO_3 deposition velocity for the CESAR2008-10 experiment (0.75 cm s^{-1}) compared to the CESAR2008 experiment (0.56 cm s^{-1}). This is explained by the fact that the TNO_3 deposition velocity is calculated by a concentration-weighted average between aerosol nitrate and gas phase nitrate deposition velocities (Morino *et al.*, 2006). In Fig. 5.5c the nearly constant deposition velocity throughout the surface layer is in agreement with the calculated value at the surface for O_3 (0.6 cm s^{-1}).

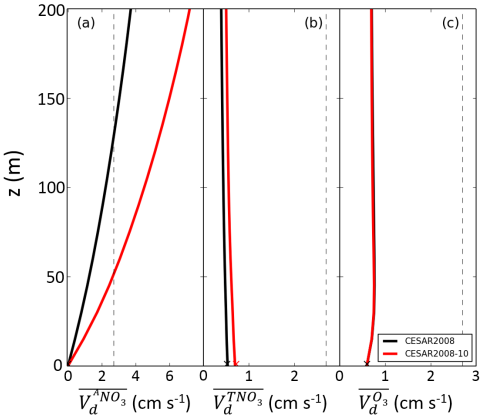

Figure 5.5: Vertical profiles of the effective deposition velocity calculated by our LES within the surface layer for (a) $^{A}NO_3$ (b) TNO_3 and (c) O_3. The thin dashed-lines refer to the maximum possible deposition velocity $v_d = 1/r_a$. The crosses refer to the deposition velocities calculated at the surface (Table 5.1). The deposition velocity for TNO_3 is explained in the text. The profiles are time-averaged between 12.5-14.5 UTC. The different experiments are indicated in the legend.

The $^{A}NO_3$ turbulent flux within the surface layer varies significantly with height. This indicates that the deposition velocity for $^{A}NO_3$ cannot be calculated using measurements of $^{A}NO_3$ made too far away from the surface (Fitzjarrald & Lenschow, 1983; Wolff *et al.*, 2010). The results shown in Fig. 5.5 for $^{A}NO_3$ deposition have implications from the measurement perspective. For example, $^{A}NO_3$ deposition velocities measured at around 30 m height can be of the order of 2 cm s $^{-1}$ depending on the equilibration time scale. To avoid that issue, we suggest the calculation of the deposition velocity for TNO_3 instead, since it can be treated as a conservative quantity, as shown in Fig. 5.5b. Our conclusion agrees with the observations presented by Huebert *et al.* (1988) and Wolff *et al.* (2010). For $^{g}HNO_3$, Huebert & Robert (1985) found a daytime average deposition velocity equal to 2.5 ± 0.9 cm s^{-1} under similar temperature and land-surface conditions. This value is comparable to $v_d^{gHNO3} = 1.9$ cm s^{-1} we calculated for our LES simulations. Our values are also within the range found by Nemitz *et al.* (2004). For NH_3, the calculated deposition velocity ($v_d^{NH_3} = 1.0$ cm s^{-1}) is also well within the range obtained by Hesterberg *et al.* (1996) for grassland. The calculated ozone deposition velocity (0.6 cm s^{-1}) agrees with the ones obtained by Meszaros *et al.* (2009) in terms of observations (0.44 ± 0.23 cm s^{-1}) and modeling (0.52 ± 0.08 cm s^{-1}) over grassland.

Our vertical resolution (15 m) suffices to capture the most important physical processes controlling the deposition process and interactions between surface and turbulence. Despite that, detailed higher resolution numerical studies, e.g. Nemitz & Sutton (2004) remain crucial to study the outgassing of nitrate aerosol close to the surface.

5.6 Representation of the transport of aerosol nitrate within the CBL

As shown in Figs. 5.2 and 5.4, the vertical distribution of aerosol nitrate depends on absolute temperature and on fluctuations with respect to the vertical velocity. In consequence, the turbulent transport of the aerosol nitrate (first term on the rhs in Eq. 5.1) might be influenced by the gas-aerosol conversion. This may affect the representation of the vertical turbulent flux of nitrate in 1D models. Our LES is used here (i) to explicitly resolve all the terms of the horizontally-averaged flux budget equation for aerosol nitrate, and (ii) to help us derive a new parameterization for the turbulent flux of aerosol nitrate (see Sects. 5A.2 and 5A.3).

In short, the results indicate that the ${}^{A}NO_3$ flux remains in steady-state because the transport of ${}^{A}NO_3$ and chemistry contributions are in close balance with the buoyancy term and production of ${}^{A}NO_3$ flux. Specially, the buoyancy term remains important within the entire CBL, and cannot be ignored. This is explained by the fact that the ${}^{A}NO_3$ flux depends not only on the turbulent transport, but also on the temperature dependent gas-aerosol conversion. Therefore, we ask ourselves whether the traditional representation (i.e. inert K-theory) of the turbulent flux is still valid for aerosol nitrate since this species explicitly depends on the CBL thermodynamics and on the equilibration timescale. To answer that question, we extend earlier research (Vilà-Guerau de Arellano & Duynkerke, 1992; Hamba, 1993; Verver, 1994; Vinuesa & Vilà-Guerau de Arellano, 2003) and propose here to calculate an exchange coefficient for ${}^{A}NO_3$. We do that by adding to the exchange coefficient for heat the effects of the gas-aerosol equilibration timescale and absolute temperature. The detailed derivation is given in the Appendix 5A. In Eq. 5.2 we show the proposed expression to close the turbulent flux of ${}^{A}NO_3$:

$$\overline{w' {}^{A}NO_3'} = -K_{{}^{A}NO_3} \frac{\partial \overline{{}^{A}NO_3}}{\partial z}$$
$$K_{{}^{A}NO_3} = K_H \frac{\widetilde{B}}{\widetilde{C}}, \tag{5.2}$$

where $K_{^A NO_3}$ is the inert exchange coefficient for heat (K_H) depending not only on turbulent characteristics but also on chemistry ($\widetilde{C}$) and gas-aerosol conversion of nitrate ($\widetilde{B}$).

The chemistry term $\widetilde{C}$ is equal to $(1+2Da)$, where Da is the Damköhler number, which relates the turbulent timescale to the chemical timescale (see Appendix 5A). Note that for very slow chemistry ($Da \ll 1$) this term vanishes from the equation. In our case ($Da \approx 1$) and chemistry tends to make $K_H > K_{^A NO_3}$. The physical meaning is that during the turbulent transport of the air parcel, the species are reacting and in consequence the exchange coefficient becomes smaller (Vilà-Guerau de Arellano & Duynkerke, 1992). The buoyant correction term $\widetilde{B}$ (see Appendix 5A) depends on a positive closure term adjustable to the LES results, and remains always positive. Consequently, $\widetilde{B}$ tends to make $K_{^A NO_3} > K_H$. The interpretation of a larger exchange coefficient is that for an adequate representation of the nitrate turbulent flux we need a larger characteristic mixing length scale that accounts not only the turbulent transport, but also for the temperature dependent gas-aerosol conversion of nitrate.

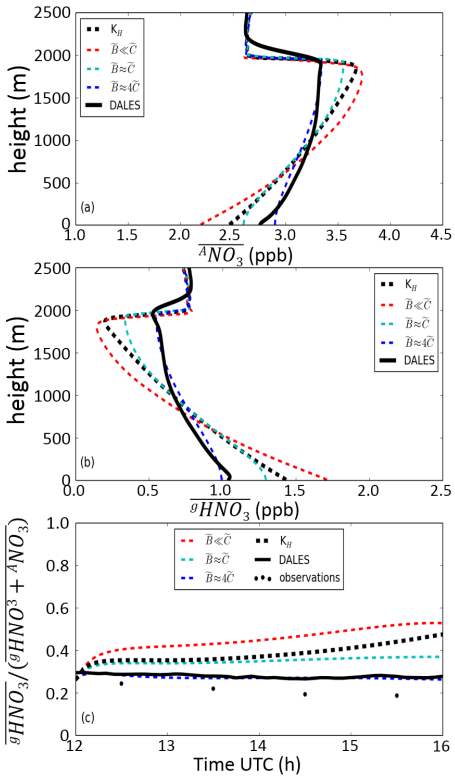

Figure 5.6: Vertical profiles of (a) $^A NO_3$ and (b) $^g HNO_3$ obtained by the LES (continuous lines) and the WUSCM (dashes) for different corrections time-averaged between 12.5-14.5 UTC. (c) Time evolution of the TNO_3 partitioning at the surface. The colored-dashes indicate the different corrections used in the WUSCM.

We evaluate the new exchange coefficient calculated using Eq. 5.2 by comparing the horizontally-averaged LES nitrate fields with the WUSCM nitrate profiles calculated with the new $K_{^A NO_3}$ profiles for the CESAR2008 case. We also examine the impact of the new exchange coefficient on the gas-aerosol partitioning of nitrate at the surface. Note that for long-lived species (i.e. $Da >> 1$) and thermodynamic variables (e.g. θ) there is enough time for the

turbulent eddies to mix the properties within the CBL. In these cases, (horizontally-averaged) well-mixed vertical distributions within the CBL are observed. Since the same boundary and initial conditions are used in the WUSCM and the LES model, the vertical profiles of long-lived species calculated by both models remain very similar throughout the entire simulation.

We notice in Fig. 5.6 that the use of K_H leads to an under(over)estimation of ${}^{A}NO_3$ (${}^{g}HNO_3$) close to the surface. Also, the comparison between LES and WUSCM profiles worsens for the chemistry correction much larger than the buoyant correction (i.e. $\widetilde{B} \ll \widetilde{C}$). This is because the chemistry solely tends to decrease the exchange coefficient and as a consequence, the vertical gradients tend to increase. In contrast, the effect of buoyancy enlarges the exchange coefficient, enhancing vertical mixing. Absolute temperature (decreases with height in the CBL) and aerosol nitrate (increases with height in the CBL) are anti-correlated, leading to a positive $\widetilde{B}$ term (see Appendix 5A). As a consequence, the vertical gradients for both gas-phase and aerosol nitrate diminish. We found the best match between LES and WUSCM for $\frac{\widetilde{B}}{\widetilde{C}} \approx 4$. Accordingly, the TNO_3 partitioning at the surface obtained by the WUSCM progressively approaches the LES values resulting in a better agreement with the observations taken at CESAR as the ratio $\frac{\widetilde{B}}{\widetilde{C}}$ increases.

Our intent here is to show that the impact of the temperature-dependent gas-aerosol conversion of nitrate in the buoyant term has a non-negligible effect on the vertical transport of nitrate (Verver, 1994). We alert the reader that different CBL thermodynamics and gas-aerosol equilibration timescale may alter the magnitude of the ratio $\frac{\widetilde{B}}{\widetilde{C}}$ found here. Future studies should therefore aim to extend this result, for example for warmer/cooler CBLs, as also discussed in Aan de Brugh *et al.* (2013).

5.7 Conclusions

We studied the transport and formation of ammonium nitrate aerosol within the convective boundary layer (CBL) using a large-eddy simulation (LES) in which radiation, aerosols, CBL dynamics and surface processes are coupled in the same framework. Our LES model was successfully evaluated against observations of chemistry and aerosol fields. We performed a sensitivity analysis on the impact of a shorter and a larger equilibration timescale compared to the characteristic turbulent time scale on the gas-aerosol conversion of nitrate within the CBL. Our LES results indicated that 30 minutes is an adequate equilibration timescale of nitrate for this case. We noted that the vertical distribution of gas-aerosol nitrate showed a significantly larger variability for shorter equilibration timescales, despite the well-mixed nature of the CBL.

Using our LES we quantified the effect of gas-aerosol conversion on the nitrate deposition flux within the surface layer. Our results confirmed that the large apparent deposition velocities for aerosol nitrate close to the surface are due to outgassing. As a consequence, the total nitrate deposition flux depends on the gas-phase nitrate concentration at the surface. We found that a shorter equilibration timescale resulted in a larger deposition velocity of total nitrate.

We found using our LES that the mixing between poor-nitrate updrafts (warm) and rich-nitrate downdrafts (cold) within the CBL significantly altered the vertical turbulent flux of gas-aerosol nitrate. The maximum of the gas-aerosol nitrate vertical flux was located at $\approx 1/3$ of the CBL height. The turbulent flux of aerosol nitrate was also influenced by the interaction between CBL dynamics and chemistry. The LES provided us with a framework to interpret the vertical profiles of gas-aerosol nitrate obtained by a 1D model. Based on the LES results, we proposed a new formulation to parameterize the turbulent flux of nitrate in the 1D model. The results indicated the need to increase the exchange coefficient used in non-eddy resolving models to better account for the complex interaction between gas-aerosol conversion of nitrate and turbulence within the CBL. Indeed, the new exchange coefficient also improved the comparison between gas-aerosol partitioning of nitrate calculated with our 1D model and surface observations.

Our findings indicate that to understand the evolution of gas-aerosol nitrate in the boundary layer, it is necessary to solve and represent simultaneously the CBL (thermo)dynamics, surface exchange processes, and gas-aerosol conversion of nitrate. Under this framework we were able to better interpret observations of nitrate deposition velocity close to the surface, and also to augment our understanding about the relation between turbulent transport and gas-aerosol conversion of nitrate.

5A Supplementary material

5A.1 Theoretical Framework

Here we introduce the fundamental concepts associated with the numerical tools used in the main manuscript. Our LES (DALES, see Heus *et al.* (2010)) solves the Navier-Stokes equations assuming the Boussinesq approximation (Deardorff, 1974; Moeng, 1984). In addition to these equations and the thermodynamic equations, DALES is able to resolve the governing equation for a given conserved scalar. In DALES, the numerical grid acts as a filter to determine the portion of the flow that is explicitly resolved. Phenomena smaller than the filter width (i.e. subgrid scale) will be parametrized (Wyngaard, 2010). Typically, under convective situations, an LES

with a grid size similar to ours (50 m in the horizontal and 15 m in the vertical) is able to explicitly resolve around 90% of the turbulent motions (Heus *et al.*, 2010). In DALES, the equation for a resolved conserved scalar whose mixing ratio is χ reads (Wyngaard, 2010):

$$\frac{\partial \widetilde{\chi}}{\partial t} = -\widetilde{U_j}\frac{\partial \widetilde{\chi}}{\partial x_j} - \frac{\partial \tau_{\chi j}}{\partial x_j} + \widetilde{S_C}, \tag{5A.1}$$

where the tildes denote the resolved-scale fields, $\widetilde{U_j}$ are the three components of the wind speed, τ_χ is the subgrid turbulent flux of χ (i.e. the part of the flow that is not explicitly solved), and the repeated indices are summed over the three spatial dimensions. The term on the left-hand side represents the tendency of χ on time. At the right hand side we have respectively, the advection of χ by the wind, the divergence of the subgrid turbulent flux of χ and a so-called "source term for additional processes" accounting for the resolved and subgrid parts (Wyngaard, 2010). Specifically for aerosol nitrate, S_C represents the gas-particle conversion of nitrate as we have shown in Sect. 5.2.

Contrarily to LES, non-eddy resolving models need to parametrize *all* the relevant scales of turbulence. Eq. 5A.1 written in a typical non-eddy resolving framework, i.e. under the assumption of horizontal homogeneity and neglecting subsidence motions, reads:

$$\frac{\partial \overline{\chi}}{\partial t} = -\frac{\partial \overline{w'\chi'}}{\partial z} + S_C. \tag{5A.2}$$

where w is the vertical wind velocity. Note that we have used Reynolds decomposition ($\chi = \overline{\chi} + \chi'$) to separate the χ field into a mean ($\overline{\chi}$) and a fluctuation from the mean $\left(\chi'\right)$ (Arya, 2001). For simplicity, throughout all the manuscript we extrapolate the use of the bar notation to also indicate the mean for the LES variables. Therefore, the total flux $\widetilde{\overline{w'\chi'}} + \overline{w'\chi'}_{subgrid}$ will be indicated simply by $\overline{w'\chi'}$.

The first term on the right-hand side of Eq. 5A.2 represents the divergence of the turbulent flux of χ. The relative importance of the source term (S_C) compared to the vertical divergence of the turbulent flux can be analyzed by non-dimensionalizing Eq. 5A.2 by a characteristic turbulent time scale τ_T - see Vilà-Guerau de Arellano *et al.* (2004) for details. In doing so, a dimensionless ratio called turbulent Damköhler number (Molemaker & Vilà-Guerau de Arellano, 1998) expresses the significance of the chemistry contribution compared to the turbulent one. This ratio is given by

$$Da = \frac{\tau_T}{\tau_C}, \tag{5A.3}$$

where τ_C is the chemical timescale. Other studies have shown that τ_C for aerosol nitrate is of the order of minutes (Dassios & Pandis, 1999; Morino *et al.*, 2006; Aan de Brugh *et al.*, 2013). Since τ_T is also within the same range (Garratt, 1992) Da is approximately equal to unity. Therefore, the gas-particle conversion is of the same order of magnitude as the divergence of the flux, and both quantities need to be treated simultaneously, as we have shown in Sect. 5.4.

In the main manuscript we use Eq. 5A.2 (explicitly solved in our LES) to obtain an effective deposition velocity V_d^{χ} by taking the ratio between the turbulent vertical flux and the mean concentration at the surface:

$$V_d^{\chi} = -\frac{\overline{w'\chi'}}{\overline{\chi}} \tag{5A.4}$$

By calculating this ratio within the surface layer with LES, we can provide a physical explanation and quantify the real deposition velocity for $^{A}NO_3$ (Nemitz & Sutton, 2004; Wolff *et al.*, 2010).

Closely related to the treatment of the turbulent flux in Eq. 5A.2, we investigate in Sect. 5.6 how well diffusion theory represents the nitrate vertical distribution calculated with LES. The LES model explicitly resolves the second-order moments in the CBL whereas non-eddy resolving models parametrize them. Using diffusion theory (Nieuwstadt & van Dop, 1982; Vilà-Guerau de Arellano & Duynkerke, 1992) the vertical turbulent flux of χ takes the form

$$\overline{w'\chi'} = -K_H \left(\frac{\partial \overline{\chi}}{\partial z} \right). \tag{5A.5}$$

This implies that the eddy-diffusion coefficient for heat (K_H) is used for all scalars. We have discussed in Sect. 5.6 the validity of this assumption for gas-aerosol nitrate. Note that the turbulent flux can also be parametrized by other means, for example using a mass-flux approach (Petersen & Holtslag, 1999).

To understand which physical processes determine the turbulent flux, we analyze in Eq. 5A.6 the budget equation for the vertical flux of χ (Fitzjarrald & Lenschow, 1983; Schumann, 1989; Vilà-Guerau de Arellano & Duynkerke, 1992):

$$\underbrace{\frac{\partial \overline{w'\chi'}}{\partial t}}_{Tendency} = \underbrace{-\overline{w'w'}\frac{\partial \overline{\chi}}{\partial z}}_{Production} + \underbrace{\frac{g}{T}\overline{\theta'\chi'}}_{Buoyancy} \underbrace{-\left(\frac{1}{\rho}\overline{\chi'\frac{\partial p'}{\partial z}} + \frac{\partial \overline{w'w'\chi'}}{\partial z} \right)}_{Total\ Transport} \underbrace{+\overline{R_i}}_{Chemistry} \underbrace{-\epsilon}_{Dissipation} \tag{5A.6}$$

where g is the acceleration of gravity, T is a reference temperature, θ is the potential temperature, p is the kinetic pressure, and ρ is the air density. In most of the

applications the flux is assumed to be in steady-state (Fitzjarrald & Lenschow, 1983) and that the dissipation of the flux can be neglected (Vilà-Guerau de Arellano & Duynkerke, 1995). A detailed derivation of the chemistry term for aerosol nitrate is given the next Section. We have shown in Sect. 5.6 for aerosol nitrate that the production and buoyant terms are responsible to strengthen the flux since they account, respectively for the vertical gradients within the CBL and the upward/downward movements carrying different mixing ratios. In contrast, the transport and chemistry terms act towards weakening the flux. Note that to obtain Eq. 5A.5, production and transport (neglecting the triple correlation) are assumed to be equivalent and the most significant terms in the flux budget equation (Holtslag & Moeng, 1991; Hamba, 1993).

Since the gas-aerosol conversion of nitrate explicitly depends upon the absolute temperature, we connect the buoyant term in Eq. 5A.6 directly to the absolute temperature by assuming fluctuations in potential and absolute temperature to be similar, $\overline{\theta'\chi'} \approx \overline{T'\chi'}$ (Garratt, 1992). A convenient way to show the relevance of this term is by relating it to the correlation between absolute temperature and χ, as shown in Eq. 5A.7:

$$\rho_{T\chi} = \frac{\overline{T'\chi'}}{\sigma_T \sigma_\chi}, \tag{5A.7}$$

where σ_T and σ_χ are the standard deviations of absolute temperature and χ, respectively. The sign of the correlation - positive or negative - determines the nature of the relationship between the variables, i.e. direct or inverse, respectively.

5A.2 Derivation of the new reactive exchange coefficient

Here we derive the exchange coefficient $K_{A_{NO_3}}$ accounting for effects of (i) temperature and (ii) timescale of the gas-aerosol conversion of nitrate within the CBL. Following earlier work on transport of chemically reactive species in the CBL (Fitzjarrald & Lenschow, 1983; Hamba, 1993; Verver, 1994; Vinuesa & Vilà-Guerau de Arellano, 2003) we start with the equation for the horizontally-averaged turbulent vertical flux of aerosol nitrate:

$$\underbrace{\frac{\partial \overline{w'^{A}NO_3'}}{\partial t}}_{Tendency} = \underbrace{-\overline{w'w'}\frac{\partial \overline{^{A}NO_3}}{\partial z}}_{Production} + \underbrace{\frac{g}{T}\overline{\theta'^{A}NO_3'}}_{Buoyancy} \underbrace{-\left(\frac{1}{\rho}\overline{^{A}NO_3'\frac{\partial p'}{\partial z}} + \frac{\partial \overline{w'w'^{A}NO_3'}}{\partial z}\right)}_{Total\ Transport} + \underbrace{\overline{R_i}}_{CHEM} \underbrace{-\epsilon}_{Diss} \tag{5A.8}$$

Similarly to Fitzjarrald & Lenschow (1983); Holtslag & Moeng (1991) and Vilà-Guerau de Arellano & Duynkerke (1995) we assume the flux to be in steady state

and neglect the dissipation contribution. We neglect the third order correlation term (Fitzjarrald & Lenschow, 1983; Hamba, 1993) and write the total transport term according to the Rotta's return-to-isotropy assumption.

$$\frac{\partial \overline{w' {}^{A}NO_3'}}{\partial t} = 0$$
$$Total\ Transport = -\frac{\overline{w' {}^{A}NO_3'}}{\tau_T} \tag{5A.9}$$

where τ_T is the turbulent time scale. Substituting Eq. 5A.9 in Eq. 5A.8:

$$0 = -\overline{w'w'}\frac{\partial \overline{{}^{A}NO_3}}{\partial z} + \frac{g}{T}\overline{\theta' {}^{A}NO_3'} - \frac{\overline{w' {}^{A}NO_3'}}{\tau_T} + \overline{R_i} \tag{5A.10}$$

We subsequently introduce the scaled eddy diffusivity term for heat (K_H):

$$K_H = \overline{w'w'}\tau_T = \frac{l^2}{\tau_T} \tag{5A.11}$$

where "l" is a characteristic length scale related to the size of the thermals. We multiply Eq. 5A.10 by τ_T in order to substitute Eq. 5A.11 in Eq. 5A.10. This gives:

$$0 = -\overline{w'w'}\tau_T\frac{\partial \overline{{}^{A}NO_3}}{\partial z} + \tau_T\frac{g}{T}\overline{\theta' {}^{A}NO_3'} - \overline{w' {}^{A}NO_3'} + R_i\tau_T$$
$$\overline{w' {}^{A}NO_3'} = -\frac{l^2}{\tau_T}\left(\frac{\partial \overline{{}^{A}NO_3}}{\partial z}\right) + \left[\tau_T\frac{g}{T}\overline{\theta' {}^{A}NO_3'}\right] + \overline{R_i}\tau_T \tag{5A.12}$$

Similarly to Vinuesa & Vilà-Guerau de Arellano (2003) (their Eqs. 5 and 11) we rewrite the chemistry term $\overline{R_i}\tau_T$ in terms of the turbulent fluxes involved in the equilibrium reaction between gas-phase and aerosol nitrate and their respective Damköhler numbers (defined as τ_T/τ_{eq}). Note that this reaction is explicitly calculated using ISORROPIA2 and no analytic formulation is feasible:

$$\overline{{}^{g}HNO_3} + \overline{NH_3} \longleftrightarrow \overline{{}^{A}NO_3}$$
$$\overline{R_i}\tau_T = \overline{w' {}^{g}HNO_3'}Da^{{}^{g}HNO_3} + \overline{w'NH_3'}Da^{NH_3} - \overline{w' {}^{A}NO_3'}Da^{{}^{A}NO_3} \tag{5A.13}$$

Due to the abundance of NH_3 within the CBL (Fig. 5.1g) and its long lifetime in the mixed-layer we take $Da^{NH_3} << 1$. We also take $Da^{{}^{g}HNO_3} \approx Da^{{}^{A}NO_3}$ since Eq. 5A.13 is an equilibrium reaction, and consider $\overline{w' {}^{g}HNO_3'} \approx -\overline{w' {}^{A}NO_3'}$ (as shown in Fig. 5.4). Equation 5A.13 now reads (loosing the index for $Da^{{}^{A}NO_3}$):

$$\overline{R_i}\tau_T = -2\overline{w'^A NO_3'}Da \tag{5A.14}$$

Substituting Eq. 5A.14 in Eq.5A.12:

$$\overline{w'^A NO_3'} = -\frac{l^2}{\tau_T}\left(\frac{\partial\overline{^A NO_3}}{\partial z}\right) + \left[\tau_T\frac{g}{T}\overline{\theta'^A NO_3'}\right] - 2\overline{w'^A NO_3'}Da$$

$$\overline{w'^A NO_3'} = -\frac{l^2/\tau_T}{(1+2Da)}\left(\frac{\partial\overline{^A NO_3}}{\partial z}\right) + \left[\frac{\tau_T}{(1+2Da)}\frac{g}{T}\overline{\theta'^A NO_3'}\right] \tag{5A.15}$$

We approximate the buoyant term (last term on the rhs) following the two-scale direct-interaction approximation, i.e. taking the covariance fluxes proportional to their vertical gradients (Hamba, 1993; Verver, 1994). We also assume fluctuations in potential and absolute temperature to be similar (Garratt, 1992):

$$\frac{g}{T}\overline{\theta'^A NO_3'} = \frac{g}{T}\overline{T'^A NO_3'} = \mu\frac{g}{T}\frac{\partial\overline{T}}{\partial z}\frac{\partial\overline{^A NO_3}}{\partial z}l^2, \tag{5A.16}$$

where μ is a positive closure constant. Hamba (1993) neglects the contribution of this term. However, Fitzjarrald & Lenschow (1983); Verver (1994) and the findings of this work (Figs. 5A.1 and 5A.2) suggest that the influence of gas-aerosol conversion of nitrate on the exchange coefficient cannot be neglected. Substituting Eq. 5A.16 in Eq. 5A.15 gives:

$$\overline{w'^A NO_3'} = -\frac{l^2/\tau_T}{(1+2Da)}\left(\frac{\partial\overline{^A NO_3}}{\partial z}\right) + \mu\tau_T\frac{g}{T}\frac{\partial\overline{T}}{\partial z}\frac{\partial\overline{^A NO_3}}{\partial z}l^2 \tag{5A.17}$$

Taking $\frac{\partial\overline{T}}{\partial z} = -\frac{g}{cp}$ and substituting Eq. 5A.11, we finally obtain the relation between the vertical turbulent flux and the vertical gradient of $^A NO_3$ including the effects of gas-particle conversion (Eq. 2 in the main text):

$$\overline{w'^A NO_3'} = -\frac{K_H}{(1+2Da)}\left[1+\frac{\mu(\tau_T g)^2}{(Tc_p)}\right]\frac{\partial\overline{^A NO_3}}{\partial z} \tag{5A.18}$$

$$\widetilde{C} = (1+2Da)$$

$$\widetilde{B} = \left[1+\frac{\mu(\tau_T g)^2}{(Tc_p)}\right]$$

5A.3 *Quantifying the impact of the gas-aerosol conversion on the vertical turbulent flux of nitrate*

The vertical distribution of aerosol nitrate depends on absolute temperature and on fluctuations with respect to the vertical velocity. The co-variance between temperature and aerosol nitrate enables us to quantify these effects. In doing so, we aim to gain understanding in (i) how the fluctuations in T correlate with the ones in aerosol nitrate - indicating transport by thermals or subsidence motions, and (ii) the influence of these fluctuations on the turbulent flux, as shown in Eq. 5A.8.

We show in Fig. 5A.1a the horizontally-averaged vertical profiles of the correlation between temperature and $^{A}NO_3$, NO_2 (reference for detrained species), TNO_3, and O_3 (reference for entrained species), as well as the normalized standard deviation for the same variables (Fig. 5A.1b).

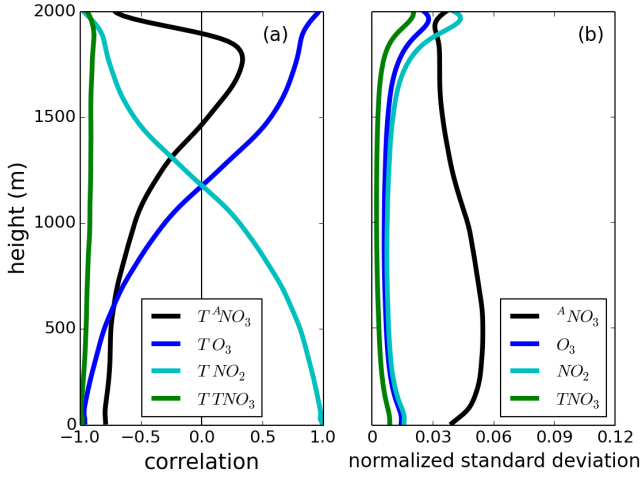

Figure 5A.1: Vertical profiles of (a) correlation coefficient between temperature and the variables indicated in the legend. (b) normalized standard deviation for the same variables. The profiles are shown for the CESAR2008 experiment and are time-averaged between 12.5UTC - 14.5UTC.

O_3 is strongly anti-correlated with temperature close to the surface since updrafts carry O_3-poor air influenced by deposition, whereas downdrafts transport O_3-rich air entrained from the free troposphere, increasing the correlation towards the top of the CBL. The same pattern but with an opposite magnitude is noticed for NO_2. These results corroborate the findings of Schumann (1989). The correlation sign crosses the

zero line around the middle of the CBL because of the change in the regime between downdrafts and updrafts. As indicated in Fig. 5.2, the temperature dependence is responsible for a sink of ${}^{A}NO_3$ near the surface and a source of ${}^{A}NO_3$ close to the top of the CBL. This process alters the vertical profile of the correlation for ${}^{A}NO_3$. We compare the aerosol nitrate correlation with the total nitrate correlation (long-lived species) with sinks both at the top (detrainment) and at the surface (dry deposition). We notice that outgassing of ${}^{A}NO_3$ close to the surface reduces the correlation from ≈ -1 to ≈ -0.8, whereas formation of ${}^{A}NO_3$ close to the top of the CBL (≈ 1800 m) reduces the correlation to ≈ 0.3. Note that a similar correlation (but with opposite sign) is observed for ${}^{g}HNO_3$ (not shown). Entrainment of NH_3-poor air close to the inversion layer reduces the ${}^{A}NO_3$ formation, leading to an anti-correlation between ${}^{A}NO_3$ and temperature above 1800 m. In the middle of the CBL, where turbulent mixing is most effective in destroying the correlation, the correlation between T and ${}^{A}NO_3$ increases compared to the other species. This is explained by the fact that the ${}^{A}NO_3$ field depends not only on transport by updrafts (${}^{A}NO_3$-poor) and downdrafts (${}^{A}NO_3$-rich) but also on gas-aerosol conversion controlled by the temperature itself (see Fig. 5.2). The effect of the gas-aerosol conversion can be seen in the vertical profiles of the standard deviation (normalized by the respective concentration profiles). We notice in Fig. 5A.1b for aerosol nitrate (similar for gas-phase nitrate) that the horizontal deviations reach up to $\approx 6\%$ of its average concentration at the height of the maximum turbulent flux (Aan de Brugh *et al.*, 2013). These values are significantly larger than for ozone, NO_2 and total nitrate.

Based on the findings discussed in Fig. 5A.1 we use our LES to explicitly resolve all the terms of the horizontally-averaged flux budget equation for aerosol nitrate (Eq. 5A.8). The results for CESAR2008 and CESAR2008-10 experiments are presented in Fig. 5A.2.

In Fig. 5A.2 we show that for both experiments the transport and chemistry contributions to the flux are counterbalanced by buoyancy and production of ${}^{A}NO_3$ flux. The tendency term is omitted because it is negligible (the steady state assumption is valid). Also, the dissipation and the numerical residual are omitted since they remain small throughout the whole CBL. The production and buoyant terms are negative and thus responsible for an overall negative ${}^{A}NO_3$ flux (see Fig. 4b in the main text). At the top of the CBL the ${}^{A}NO_3$ concentration decreases due to entrainment of NH_3-poor air and therefore this term becomes slightly positive. The buoyant term is also negative since temperature and ${}^{A}NO_3$ are anti-correlated. At the entrainment zone the magnitude of the buoyant term augments because of the interaction between warm air entrained from the free-troposphere and detrainment of aerosol nitrate from the CBL. The chemistry term is proportional to (minus) the ${}^{A}NO_3$ vertical flux.

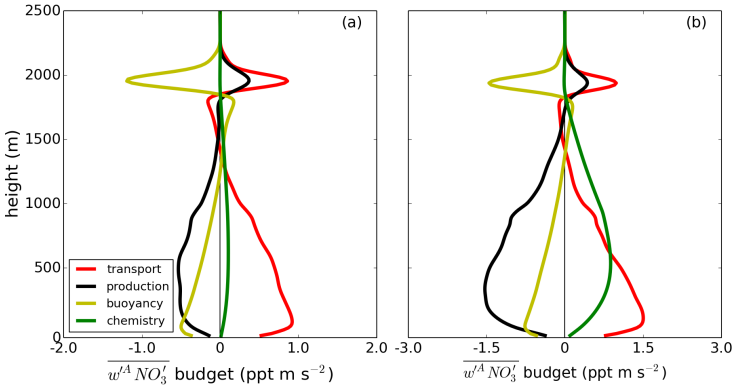

Figure 5A.2: ^{A}NO$_3$ flux budget time-averaged between 12.5-14.5 UTC for (a) CESAR2008 and (b) CESAR2008-10 experiments. The individual terms named according to Eq. 5A.6 are indicated in the legend. The tendency (steady-state) and the dissipation terms as well as the numerical residuum remain small throughout the CBL. Note in (a) and (b) the different scales for the x-axes.

Therefore, it remains positive throughout the CBL and contributes to a reduction of the $^ANO_3$ turbulent flux. The transport term is always positive (weakening the flux) since it acts to mix $^ANO_3$-poor air (updrafts) and $^ANO_3$-rich air (downdrafts). Comparing the flux budget profiles for the different equilibration timescales we notice that the shape of all the terms remain similar but their magnitudes increase for the shorter equilibration time scale.

"I've gotta get it right the first time
That's the main thing
I can't afford to let it pass
You get it right the next time that's not the same thing
Gonna have to make the first time last"

Joel, W.M. (1977). Get it right the first time. *The Stranger*, **4(B)**, Columbia Records.

6 Summary

In this Section we summarize the most important findings and relevant issues treated in detail in Chapters 2 to 5.

The primary conclusion of this thesis is that it is necessary to take aerosols into account to accurately describe the convective atmospheric boundary-layer (CBL) dynamics and the land-surface processes. We reached this conclusion by systematically studying the land-CBL system and its couplings, and employed a hierarchy of models ranging from an eddy-resolving model (large-eddy simulation; LES) to non-eddy resolving models (mixed-layer model, and single column model). In addition to the numerical component, we used a complete observational data set to help us design and evaluate our numerical framework.

Chapter 2 was devoted to the explanation of the radiative transfer code used in Chapters 4 and 5. We showed that despite the simplified treatment of solar radiation and its interactions with aerosols, our radiative code is in general agreement with a more sophisticated radiative transfer code, even for extreme aerosol loads. Moreover, our results reproduce observations of direct and diffuse radiation at the surface accordingly - as shown in Chapter 4.

Regarding the longwave band, we showed that aerosols are not relevant for the estimation of the incoming longwave radiation at the surface. We concluded that Brunt's formula, depending only on screen level temperature and vapor pressure, is

the most adequate to represent the incoming longwave radiation at the surface for the cases relevant for our studies.

In **Chapter 3** we investigated the impact of aerosol heat absorption on the dynamics of an idealized CBL with prescribed surface fluxes. We found that the structure and evolution of the CBL were influenced by the vertical distribution of the aerosols. Moreover, we showed that the aerosols influence the exchange of heat between the CBL and the free troposphere by (i) extinction of radiation and consequently reduced surface fluxes, and by (ii) deepening the entrainment zone depth. We highlighted the importance of high-resolution models to properly represent the effects of aerosol absorption of radiation on the dynamics of the CBL, especially in the entrainment zone. We demonstrated that, in addition to the properties of the aerosols, the vertical distribution is an important characteristic to properly describe the CBL height evolution and the dynamics of the upper part of the CBL. To further support the analysis of the LES results, we used a mixed-layer (MXL) model to calculate boundary-layer depth and the potential temperature jump at the inversion layer. In spite of the simplicity of this model, the mixed-layer results obtained for boundary-layer height and the inversion layer jump agreed well with the LES results.

Extending the knowledge acquired with the academical prototypical experiments performed in Chapter 3, in **Chapter 4** we quantified the effects of aerosol scattering and absorption of shortwave (SW) radiation both on the surface energy budget and on the CBL dynamics. To this end, we coupled our LES model and the MXL model to (i) a land-surface model and (ii) a broadband SW radiative transfer model, (described in Chapter 2). We successfully validated the results obtained with the LES model and MXL model using measurements of (thermo)dynamic variables and aerosol properties observed in Cabauw (the Netherlands). Our LES results showed that for Cabauw (over well-watered grassland) aerosols significantly alter the magnitude of the available energy at the surface and its partitioning. Under well-watered conditions, the sensible heat flux was more strongly reduced compared to the latent heat flux. Given the satisfactory agreement between the LES results and MXL model results, we further explored the sensitivity of the land-CBL system to a wide range of aerosol optical depths and single scattering albedos using the MXL model. Our results showed that higher loads of aerosols impose an energy restriction at the surface. As a result, we calculated a delay in the morning onset of the CBL and an advance in the CBL afternoon collapse. We also found that entrainment of aerosols from the residual layer plays a significant role in the development of the CBL dynamics during the day. An important aspect of Chapter 4 is the investigation of the different responses of the CBL dynamics depending on aerosol optical properties. Strongly absorbing aerosols

deepened and warmed the CBL, while purely scattering aerosols shallowed and cooled the CBL.

We highlighted that the results presented in Chapter 4 can be used as a benchmark to evaluate coupling and performance of the parametrizations for SW radiation, land-surface and boundary-layer schemes, implemented in mesoscale or global chemistry transport models.

In **Chapter 5** we increased the complexity of our land-CBL system representation by studying the formation and transport of ammonium nitrate aerosols. In doing so, we coupled in our LES radiation, chemistry, aerosols, CBL dynamics, and surface exchange processes of chemicals, heat and moisture. Our fully-coupled LES model was again evaluated against observations of chemistry and aerosol fields and showed a good correspondence. In particular, our results showed a satisfactory agreement between the simulated and observed nitrate partitioning at the surface.

We showed that gas-aerosol conversion of nitrate leads to highly non-linear profiles of nitrate concentrations and turbulent fluxes. Moreover, the shapes of the simulated profiles depended strongly on the time scale of gas-aerosol conversions. Note that the typical timescale of turbulent motions in the CBL is around 10-20 minutes. For shorter time scales of gas-aerosol conversion compared to the CBL dynamics timescale, we found that turbulent fluxes are larger and concentration profiles more tilted within the CBL. These results have a significant impact on the nitrate deposition flux at the surface. Our LES results confirmed that the large deposition velocities for aerosol nitrate close to the surface are actually due to outgassing of aerosol nitrate rather than a real deposition process.

An important aspect discussed in Chapter 5 concerns the inability of non-eddy resolving models to accurately model the turbulent transport of nitrate within the CBL. Based on a detailed analysis of the flux budget equation, we showed that the exchange coefficient of heat used in our 1D model has to be increased to better account for the complex interaction between gas-aerosol conversion of nitrate and 3D turbulence within the CBL. Indeed, the new exchange coefficient also improved the comparison between gas-aerosol partitioning of nitrate calculated with our 1D model and surface observations.

The results discussed in this thesis demonstrate the need for considering the influence of aerosols on the CBL dynamics. Specifically, aerosols influence important phenomena for the CBL evolution namely radiation, surface-atmosphere interactions, chemistry, and (thermo)dynamics. In addition to that, the availability of high-resolution numerical simulations is crucial to validate and evaluate results obtained by numerical models that do not explicitly resolve the turbulent field.

"You can't always get what you want
But if you try sometime you might find
You get what you need"

Jagger, M.P. and Richards, K. (1969). You can't always get what you want. *Let it Bleed*, **4(B)**, Decca Records.

7 General discussion & Outlook

In this Chapter we place our research in a broader perspective and provide some recommendations for future studies. We start by further discussing the treatment of radiation and aerosols in numerical models. Then, we move to the role of different surface characteristics and emissions of gas-phase precursors in the spatial distribution of aerosols. Further, we propose an observational campaign to investigate the coupling between aerosols land surface, chemistry and CBL dynamics. Lastly, we briefly discuss the role of aerosols in the climate system.

7.1 Radiation treatment

Under the specific conditions discussed in this thesis, our simplified broadband radiation treatment appeared accurate enough to represent the effect of aerosols in the shortwave radiation band. The most important assumptions concerning the broadband radiation calculations were (i) the use of a bulk formulation (Burridge & Gadd, 1974) to obtain the net-transmissivity of the free-atmosphere above the CBL, and (ii) the use of a single representative wavelength to account for the gas and aerosol

properties. Moreover, it is also assumed that the contributions from long wave emission (cooling) and shortwave radiation absorption by gas phase compounds (heating) cancel in the CBL. In view of that, we have some recommendations to improve the treatment of radiation in DALES for future studies.

A logical next step would be the implementation of a *multiband* radiative transfer code in DALES that explicitly accounts for the presence of the most abundant atmospheric gases (e.g. water vapor, O_2, CO_2, O_3). By implementing a more detailed radiative code that resolves the gases interaction with short- and longwave radiation, one would eliminate the assumption of exact cancellation between atmospheric heating and cooling due to gases during the convective period, see Chapter 2 and Angevine *et al.* (1998b). By means of a *multiband* radiative transfer, the wavelength dependent optical properties of aerosols can also be accounted for by following the Ångström equation (see Chapter 2). Furthermore, another advantage of calculating the radiative fluxes using a multiband model is the capability to quantify the influence of aerosols on the photosynthetically active radiation (PAR) at the surface. PAR (400-700 nm) is of great importance in plant biochemical processes and agricultural studies (Escobedo *et al.*, 2011) since it represents the solar radiation available for photosynthesis. Several studies have shown that an accurate estimate of PAR is crucial to the amount of carbon fixed by plants (Frouin & Pinker, 1995), marine ecosystems (Frouin & Murakami, 2007), and biomass production (Alados & Alados-Arboledas, 1999).

With respect to the longwave band, we have shown that aerosols in Cabauw (the Netherlands) and Sao Paulo (Brazil) do not affect the incoming longwave radiation at the surface during the convective period. However, if the aerosol particles are large enough (Tegen *et al.*, 1996) or are present in extreme quantities (Zhou & Savijärvi, 2014) an effect has been detected (e.g. larger than 20 $\mathrm{W}m^{-2}$). Dufresne *et al.* (2002) showed that the longwave radiative forcing of aerosols is significant only within the atmospheric window (8-13 μm), and for particles with diameters larger than 2 μm. In their calculations the aerosol forcing in the longwave band maximized for particles as large as 20 μm. Therefore, we recommend to take the aerosol interaction with longwave radiation into account only when large particles such as dust are present. Note, however, that to perform a full spectrally resolved radiation transfer calculation is computationally expensive. To avoid this expense, the calculations could be simplified by grouping the spectrum of radiation into a fixed number of bands (Kato *et al.*, 1999). Other simplifications commonly found in literature (Bozzo *et al.*, 2014) are to perform calculations in a reduced time frequency and on a coarser resolution than the dynamics or chemistry of the CBL. Concerning an efficient *multiband* radiative transfer code we suggest the implementation of LibRadTran - used in Chapter 2 to

evaluate our assumptions (Mayer & Kylling, 2005) - or the Rapid Radiation Transfer Model (RRTM) described in detail by Mlawer *et al.* (1997) and Iacono *et al.* (2008). The RRTM is currently the radiation scheme used in the ECMWF model and provides a fast and accurate representation of the short- and longwave radiation fields, also accounting for the presence of aerosols (Morcrette *et al.*, 2008). Aiming for the best compromise between performance and computational cost, the RRTM uses in its operational version 14 and 16 spectral bands to represent the shortwave and longwave spectrum, respectively (Bozzo *et al.*, 2014). This amount of bands can be used as a reference in DALES.

We have shown in this thesis that aerosols are very important to calculate the SEB. However, a full calculation of aerosol formation, dynamics, and removal, remains computationally very expensive and involves many uncertainties. Other uncertainties are introduced by the radiative properties of aerosols, including their wavelength dependent characteristics. Therefore, an alternative would be to constrain numerical calculations using data from the AERONET network or by using similar observations measured during observational campaigns.

Another important assumption in our research was to divide the atmosphere into parallel layers of infinite extensions in the horizontal directions (plane-parallel atmosphere). This assumption is sound in our case because we deal only with homogeneous land-surfaces and atmospheric conditions. For instance, under heterogeneous land-surface conditions, the interaction between radiation and the different surface characteristics may need a three-dimensional radiative transfer treatment. Such code would be able to account for clouds and the interactions between aerosols and radiation also for heterogeneous atmospheric situations. However, three-dimensional radiative transfer is very expensive computationally, and its explicit coupling in DALES will provide a challenge.

In the next section we discuss how heterogeneous land characteristics may influence the spatial aerosol distribution.

7.2 Surface characteristics

7.2.1 Impact of different land-surfaces and emissions heterogeneity on the nitrate distribution

In this thesis we dealt only with aerosols over homogeneous land-surfaces and homogeneous emissions. However, an interesting question is how horizontal variations in (i) soil moisture and (ii) surface emissions influence formation and transport of aerosols in the CBL. To deal with (i) and (ii) we extend the research done in Chapter 5 for

gas-phase ($^{g}HNO_3$) and aerosol ($^{A}NO_3$) nitrate fields within the CBL (CESAR2008 experiment). We do so, by introducing two extra LES experiments (HETER1 and HETER2). Most importantly, for both HETER1 and HETER2, all the settings of the CESAR2008 experiment (see Chapters 4 and 5) are kept the same, except the domain size, surface water content, wind speed, and NH_3 surface emission (the latter only for HETER2). The nitrate equilibration timescale between gas-phase and aerosols is also kept equal to 30 minutes (like in Chapter 5).

In order to induce a moderate secondary circulation in HETER1 and HETER2 we simulate a wetter patch besides a dryer patch if compared to CESAR2008 soil conditions. By doing so, the sensible heat flux is lower over the wetter patch compared to the drier patch. In contrast, the latent heat flux is higher over the wetter patch. Note that the average surface water content in HETER1 and HETER2 remains equal to the CESAR2008 experiment. The Bowen ratio (β) of the dry patch during the day remains within the range 0.45-0.2, whereas for the wet patch β varies from 0.25-0.1 throughout the simulation. Similar differences in the β range were obtained by Patton *et al.* (2005); Ouwersloot *et al.* (2011). Following Patton *et al.* (2005) we also double the CESAR2008 horizontal domain ($9600 \times 9600 \times 3000$ m) to maintain the same spatial resolution as CESAR2008. We do so to ensure that the ratio of the wavelength of one complete dry-wet cycle and the CBL height is within the optimum range proposed in Patton *et al.* (2005) (4 to 9). In the current setup our ratio is ≈ 5. For HETER2 we keep the same configuration as HETER1 but similarly to Auger & Legras (2007) we restrain the NH_3 surface emissions to only one half of the domain (in this case the wet patch). To keep the total NH_3 emission equal among the experiments we double the NH_3 surface emission at the wet patch if compared to the other experiments. Here the abundance of NH_3 in the CBL for all experiments is enough to associate with $^{g}HNO_3$.

We present in Fig. 7.1 the 2-hour-averaged (13.5-15.5 UTC) contours for $^{g}HNO_3$ and $^{A}NO_3$ and wind fields within the CBL. Here we show the LES results for CESAR2008 (see Chapter 5) as a reference and discuss the results for HETER1 and HETER2 experiments.

We observe in Fig. 7.1 more $^{A}NO_3$ at the (cold) top of the CBL for all the experiments (see Chapter 5). The opposite is noted for $^{g}HNO_3$. For the CESAR2008 experiment both $^{g}HNO_3$ and $^{A}NO_3$ are equally distributed in the horizontal domain (as expected) due to the surface horizontal homogeneity. In contrast, for HETER1 and HETER2 experiments the dry-wet patch configuration induces a secondary circulation. The higher sensible heat flux over the dry patch favors upward motions, whereas over the wet patch subsiding motions are dominant. It is clear for both heterogeneous cases that more $^{g}HNO_3$ is located over the dry patch, compared to the wet

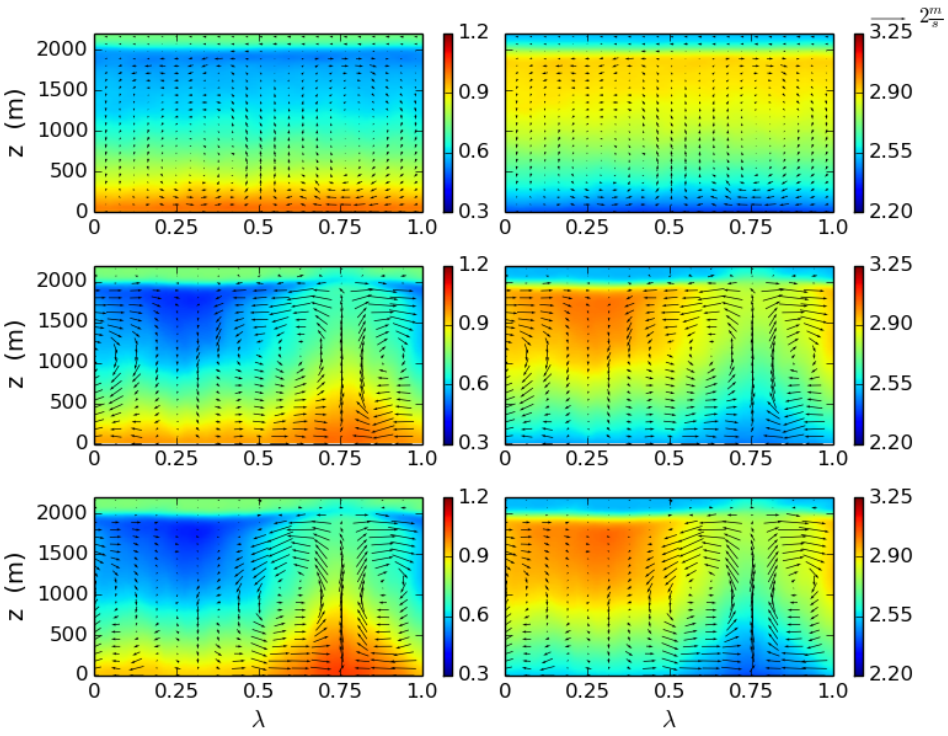

Figure 7.1: ${}^{g}HNO_3$ (left-hand side) and ${}^{A}NO_3$ (right-hand side) x-z LES fields for CESAR2008 (upper), HETER1 (middle) and HETER2 (bottom) experiments. In all the contours the arrows represent the wind magnitude. All the x-axes are displayed in terms of the wavelength of one complete dry-wet cycle.

patch. Consistently, the opposite is observed for ${}^{A}NO_3$. This distribution is explained by the fact that the maximum ${}^{A}NO_3$ outgassing occurs close to the surface and above the dry patch (warmest area). The warm patch induces a ${}^{g}HNO_3$-rich updraft that forms ${}^{A}NO_3$ as the eddies rise to the colder top of the wet patch. Consistently, the ${}^{A}NO_3$-rich downdraft outgasses as it gets close to the surface. For CESAR2008 the vertical distributions of ${}^{A}NO_3$ and ${}^{g}HNO_3$ vary by $\approx 20\%$ and $\approx 45\%$ within the CBL. These values are of the same order as the ones found for the heterogeneous experiments.

We note a considerable variability of aerosol nitrate between the patches for both HETER1 and HETER2 compared to CESAR2008. Interestingly, the well-mixed CBL efficiently transports NH_3 from the wet patch (HETER2) to the dry patch and we do not see significant changes between HETER1 and HETER2 for the ${}^{g}HNO_3$ and

$^{A}NO_3$ fields. Therefore, we conclude that the aerosol and gas-phase nitrate concentrations are relatively independent of the way NH_3 emissions are introduced in the model. This result corroborates the findings of Auger & Legras (2007) who showed very little impact of the emission pattern on the distribution of species after allowing enough time for turbulent mixing. However, with lower NH_3 emissions the formation of aerosol nitrate may become limited by the availability of NH_3 and a more heterogeneous distribution may be expected.

Note that these results were already qualitatively discussed in Aan de Brugh *et al.* (2013). They suggested that these features may appear in observations - both at the surface and airborne - and recommended those to be taken under steady and weak wind conditions. They have also reported the strongest differences in the concentrations at higher altitudes - as also noted in Fig. 7.1.

For all the experiments aerosols also reduce the solar radiation at the surface with ≈ 40 Wm^{-2} if compared to the same cases without the aerosols (not shown). A similar effect has been found by Yu *et al.* (2002), see also Feingold *et al.* (2005); Haywood *et al.* (2011). Despite that, the aerosol horizontal heterogeneity induces very little differences in the distribution of surface radiation (< 5 Wm^{-2} comparing dry/wet patches). However, Lee *et al.* (2014) have shown that depending on the aerosol vertical distribution, the size of the patches, absorptivity and optical thickness, aerosols can strengthen (or even create) a secondary circulation by locally reducing the surface fluxes or altering cloud formation. Next, we discuss how different environments influence aerosol formation and surface emissions of gasses.

7.2.2 Aerosols in different environments

In this thesis we limited ourselves to quantify the role of aerosols altering the land-CBL system over a well-watered, and homogeneous grassland in Cabauw. However, the role of aerosols may be different over different land-surfaces, e.g. urbanized areas, or tropical forests. Concerning the aerosol impact on the surface energy budget, for an urbanized area aerosols would strongly decrease the surface sensible heat, since the evaporation in urban areas is generally very small. For a forested site, where the latent heat flux is the dominant flux at the surface, we expect a strong decrease in evaporation when large amounts of aerosols are present, and therefore a drier CBL. Our mixed-layer model is a good tool to analyze the impact of aerosols in different environments (e.g. dry and wet surfaces), in a similar fashion as discussed in Sect. 4.4.2.

Under different environmental conditions the aerosol properties would be significantly different due to the surface emissions. Whereas in the urbanized area the

predominant particles would be strongly absorbing anthropogenic aerosols (Castanho & Artaxo, 2001), in a forested area more scattering aerosols are expected due to the different surface emissions (e.g. isoprene, terpenes) and formation of secondary organic aerosols (Janssen *et al.*, 2012; Li *et al.*, 2014). Closely connected with our study in Chapter 5, dry deposition and a warmer/cooler environment would strongly influence the partitioning of semi-volatile organic vapors (Hodzic *et al.*, 2013). Also, temperature influences emissions of organic gases such as isoprene, which creates an interesting coupling between surface emissions, aerosols, radiation, and CBL dynamics (Janssen *et al.*, 2012). Back to grassland, ammonia emissions are also strongly temperature dependent, which introduces additional feedbacks in the coupled system (Skjoth & Geels, 2013).

7.3 Designing a field experiment

In the previous sections we have shown that the study of aerosols coupled to the land-CBL system forms a challenge from the numerical point of view (see Fig.1.4). Therefore, we propose the design of an integrating observational campaign (Angevine *et al.*, 1998a; Masson *et al.*, 2008; Kulmala *et al.*, 2009; Jager, 2014) aiming to facilitate the design of numerical experiments and to help their interpretation. Such observational effort can be used to constrain some characteristics as well as to evaluate the performance of a numerical framework (see Chapters 4 and 5).

We propose to perform simultaneous measurements over adjacent urbanized and vegetated areas, during periods of cloudy and clear-sky conditions. In doing so, one is able to quantify how aerosols impact on (i) two different environments, and (ii) disturbing the urban-rural secondary circulation. Previous observational campaigns have already investigated individually some of the issues mentioned above, however the couplings remain poorly understood.

As a starting point we mention the FLATLAND experiment (Angevine *et al.*, 1998a). The focus during the FLATLAND campaign was to understand the CBL dynamics over a very flat rural area in Illinois (USA). The emphasis was on aspects such as the calculation of the CBL height and entrainment zone characteristics. The role of aerosols was also studied, and found to be responsible for a significant heating of the boundary layer during the day (Angevine *et al.*, 1998b). Concerning observations of aerosol particles over the city we highlight the CAPITOUL (*C*anopy and *A*erosol *P*articles *I*nteractions in *TO*ulouse *U*rban *L*ayer) experiment (Masson *et al.*, 2008). Their aim was to explore the diurnal and seasonal variability of urban climate processes with special emphasis on the (urban) surface energy budget quantification. In this campaign, however, the CBL chemistry was not fully explored.

In contrast, the EUCAARI (*EU*ropean integrated project on aerosol cloud *C*lim*A*te and *A*ir quality inte*R*act*I*ons) campaign (Kulmala *et al.*, 2011) provided a rich database containing detailed information (including airborne measurements) about aerosols and gas-phase chemistry observed in Europe during 2008. Despite the very complete data set, this campaign explored mostly rural sites. The PEGASOS (*P*an *E*uropean *G*as-*A*ero*SO*ls-climate interaction *S*tudy) campaign (Jager, 2014) also provided the community with a rich data set containing mainly information about the chemical composition of the CBL. During PEGASOS, some data about the CBL thermodynamical vertical structure was sampled, by means of a zeppelin platform. However, most of the time, the zeppelin would remain at lower altitudes not flying close enough to the upper layers of the CBL (> 1000 m) during the afternoon. Despite that limitation, the zeppelin collected important observations of the vertical structure of the boundary layer during the morning transition.

To bridge the gap between these campaigns we suggest to design an observational campaign accounting for simultaneous high-resolution surface and upper air observations of (i) radiation, (ii) surface exchanges, (iii) CBL (thermo)dynamics, (iv) CBL chemistry, and (v) aerosols. Concerning the duration of the observational campaign we suggest one month of continuous observations with intensive observational periods depending on meteorological and air quality conditions. This duration is similar to other boundary-layer campaigns, such as CASES-99 (Poulos *et al.*, 2002) and BBLAST (Lothon *et al.*, 2014).

At the surface, similar to what has been done in Cabauw (rural) (Beljaars & Bosveld, 1997; Bosveld, 2010), and Sao Paulo (urban) (Ferreira *et al.*, 2012, 2013), we suggest measurements of all the components of the SEB (sensible, latent, and ground heat fluxes) as well as short- and longwave radiation during the entire convective period. Specifically, we suggest independent measurements of the direct and diffuse components (as discussed in Oliveira *et al.* (2002)), and PAR (Escobedo *et al.*, 2009) of the shortwave radiation. In that way, these observations would also provide a continuous database, and may help to deduce empirical expressions and relations between these variables (Escobedo *et al.*, 2011). The SEB will be also significantly different due to the urban/rural surface characteristics and aerosols, and simultaneous measurements will provide an interesting quantification. Surface stations measuring gaseous emissions (e.g. CO, NO_x, and NH_3) also provide important information about the gas-phase precursors of aerosols for both environments. Note that these precursors will be very different between the urbanized and vegetated areas.

Concerning the CBL vertical structure, we suggest to launch radiosondes every 3 hours to capture the thermodynamical profile of the CBL. In addition to the radiosondes, a wind profiler and a ceilometer would be valuable additions to obtain

reliable estimates of the CBL height and cloud base height. A LIDAR instrument would provide extra information about the aerosol height, backscattering, and extinction (Povey *et al.*, 2014). By estimating the aerosol layer height, one could compare it to the wind profiler data to determine the extension of a possible residual layer from the night before (as we have discussed in Chapter 4). The use of LIDAR and the wind profiler together could also help to better understand the development of the CBL during the first hours of the morning. The LIDAR would be also useful to estimate the entrainment zone thickness (Mok & Rudowicz, 2004). We recommend the use of an aircraft platform flying several times per day over the urban and the rural area. The aircraft should sample aerosol composition and size (Bahreini *et al.*, 2003) within the CBL, since these characteristics are crucial to calculate the role of aerosols disturbing the radiative field. The aircraft is useful to provide information about the upper layers of the CBL, specifically the entrainment zone. With information such as entrainment flux, velocity, and depth (Angevine *et al.*, 1998a) one could investigate the role of aerosols disturbing the heat budget at the entrainment zone (see Chapter 3). By sampling both over the rural and urban patches one could shed some light on the transport of aerosols between patches and their interactions with updrafts and downdrafts (see Sect. 7.2.1). The aircraft is also useful to measure gas-phase chemistry and cloud properties (Zhang *et al.*, 2007). We advise measurements of actinic flux using, for instance, tethered-balloons (De Roode *et al.*, 2001) or ground stations and the aircraft platform (Kylling *et al.*, 2005). In that way one could obtain detailed information of the amount of radiation available for photo-chemistry (Madronich, 1987; Landgraf & Crutzen, 1998), and biology and health (Nielsen *et al.*, 2006). One should pay special attention to the role of clouds disturbing the radiative field and therefore altering the photolysis frequencies (Kylling *et al.*, 2005).

Last, we suggest the use of a satellite instrument to retrieve aerosol optical thickness and thus complement the in-situ measurements of aerosols in the CBL. Moreover, remote sensing may bridge the gap between the in-situ, local boundary-layer observations and the effects of aerosols on climate (Kaufman, 1993). Using a satellite instrument could help to quantify the long-range advection of aerosols towards the experimental site (e.g. dust and anthropogenic aerosol). In addition to that, a satellite instrument (e.g. MODIS or CALIOP) could be useful to investigate the effect of aerosols on clouds. One could combine simultaneous in-situ observations of cloud fraction and base (ceilometer), and aerosol concentration (LIDAR), with satellite information of the effective radius of cloud drops (Painemal & Zuidema, 2011). Also, aircraft measurements below cloud base, at different levels within the cloud, and above the cloud (Duong *et al.*, 2011) synchronized with the satellite overpass would help to

quantify the effect of aerosols on cloud formation (Kaufman & Nakajima, 1993), and cloud drop size (Feingold *et al.*, 2001).

In the next section we further comment on the feedback between aerosols-clouds and the impact for larger-scale processes.

7.4 The role of aerosols in the climate system

Aerosols play an important role altering the SEB and the Earth's climate. Overall, it is expected that aerosols have a cooling effect on climate due to backscattering of solar radiation (Coakley *et al.*, 1983; Kaufman, 1993). In addition to the direct backscattering of solar radiation, Lohmann & Feichter (2005) and Boucher *et al.* (2013) showed that aerosols disturb the climate system by altering cloud characteristics. Indeed, one of the most prominent issues concerning aerosols and the climate system (but not treated in this thesis) is the aerosol indirect effect (Feingold *et al.*, 2003). By acting as cloud condensation nuclei, aerosols significantly increase the droplet concentration in the cloud. In contrast, the droplet size is reduced, as well as the precipitation efficiency (Xue & Feingold, 2006; Stevens & Feingold, 2009). For example, due to more/less clouds (Kylling *et al.*, 2005) or scattering/absorbing aerosols and gases (Jacobson, 1998) the photolysis frequencies and heating rates may change significantly (Landgraf & Crutzen, 1998). In addition, clouds may change in a future climate (Boucher *et al.*, 2013), therefore the role of clouds altering important chemical budgets, e.g. tropospheric ozone, and tropospheric oxidizing capacity need to be investigated (Voulgarakis *et al.*, 2009). Interestingly, according to Rosenfeld & Feingold (2003) factors such as variability in cloud liquid water path and boundary-layer dynamics need to be accounted for in the calculations of the indirect effect of aerosols on clouds.

Stevens & Feingold (2009) discussed the aerosol-cloud interactions in the context of the entire Earth system. They highlighted several uncertainties, such as the impact of thermodynamics and aerosols in cloud formation. They also showed that the interaction between the microscale (e.g. cloud formation) and macroscale (e.g. precipitation) remains very uncertain. Future numerical studies need to bridge the gap between these scales by, for example, coupling these processes in the same numerical framework, in combination with observational campaigns (as exemplified above). As a first step, we suggest here the use of an LES framework to couple aerosols to the formation of shallow cumulus clouds, accounting for the chemical composition of the aerosols.

Although there is still much to investigate about aerosols and their coupling with the land-atmosphere system (ranging from micro- to larger-scales), we have explored in this thesis how aerosols interact with the CBL chemistry and dynamics, also through their impact on the surface energy budget. Our approach was based on the study of the processes that occur at daily scale as a key element to better understand phenomena at larger scales. A unique aspect of this thesis has been the systematic design of high-resolution numerical experiments by means of LES, together with the use of detailed observations from the CESAR site.

References

Aan de Brugh, J.M.J., Henzing, J.S., Schaap, M., Morgan, W.T., van Heerwaarden, C.C., Weijers, E.P., Coe, H. & Krol, M.C. (2012). Modelling the partitioning of ammonium nitrate in the convective boundary layer. *Atmospheric Chemistry and Physics*, **12**, 3005–3023. 11, 103, 104, 105, 106, 109, 113

Aan de Brugh, J.M.J., Ouwersloot, H.G., Vilà-Guerau de Arellano, J. & Krol, M.C. (2013). A large-eddy simulation of the phase transition of ammonium nitrate in a convective boundary layer. *J Geophys Res: Atmospheres*, **118**, 826–836. 8, 9, 10, 11, 13, 78, 102, 103, 105, 107, 109, 110, 113, 118, 121, 126, 138

Ackerman, T.P. (1977). A model of the effect of aerosols on urban climate with particular applications to the Los Angeles basin. *J Atmos Sci*, **34**, 531–547. 9, 10, 12, 48, 60, 61, 74, 90

Alados, I. & Alados-Arboledas, L. (1999). Direct and diffuse photosynthetically active radiation: measurements and modelling. *Agricultural and Forest Meteorology*, **93**, 27 – 38. 134

Andreae, M. & Rosenfeld, D. (2008). Aerosol-cloud-precipitation interactions. part 1. the nature and sources of cloud-active aerosols. *Earth-Science Reviews*, **89**, 13–41. 3

Andreae, M.O. & Crutzen, P.J. (1997). Atmospheric aerosols: Biogeochemical sources and role in atmospheric chemistry. *Science*, **276**, 1052–1058. 4, 8

Andrews, E., Sheridan, P.J., Fiebig, M., McComiskey, A., Ogren, J.A., Arnott, P., Covert, D., Elleman, R., Gasparini, R., Collins, D., Jonsson, H., Schmid, B. & Wang, J. (2006). Comparison of methods for deriving aerosol asymmetry parameter. *J. Geophys. Res.*, **111**. 21, 27

Angevine, W.M., Grimsdell, A.W., Hartten, L.M. & Delany, A.C. (1998a). The flatland boundary layer experiments. *Bulletin of the American Meteorological Society*, **79**, 419–431. 139, 141

Angevine, W.M., Grimsdell, A.W. & Mckeen, S.A. (1998b). Entrainment results from the FLATLAND boundary layer experiments. *J Geophys Res*, **103**, 13689–13701. 4, 8, 10, 17, 21, 29, 48, 49, 50, 57, 58, 75, 76, 88, 102, 134, 139

Arneth, A., Harrison, S.P., Zaehle, S., Tsigaridis, K., Menon, S., Bartlein, P.J., Feichter, J., Korhola, A., Kulmala, M., O'Donnell, D., Schurgers, G., Sorvari, S. & Vesala, T. (2010). Terrestrial biogeochemical feedbacks in the climate system. *Nature Geoscience*, **3**, 525–532. 1, 5, 74

Arnfield, A.J. & Grimmond, C. (1998). An urban canyon energy budget model and its application to urban storage heat flux modeling. *Energy and Buildings*, **27**, 61 – 68. 38

Arya, S.P. (2001). *Introduction to Micrometeorology*. Academic Press 420 pp. 120

Athanasopoulou, E., Tombrou, M., Pandis, S.N. & Russell, A.G. (2008). The role of sea-salt emissions and heterogeneous chemistry in the air quality of polluted coastal areas. *Atmospheric Chemistry and Physics*, **8**, 5755–5769. 3

Auger, L. & Legras, B. (2007). Chemical segregation by heterogeneous emissions. *Atmos. Environ.*, **41**, 2302–2318. 136, 138

Bahreini, R., Jimenez, J.L., Wang, J., Flagan, R.C., Seinfeld, J.H., Jayne, J.T. & Worsnop, D.R. (2003). Aircraft-based aerosol size and composition measurements during ace-asia using an aerodyne aerosol mass spectrometer. *Journal of Geophysical Research: Atmospheres*, **108**. 141

Baklanov, A., Schlünzen, K., Suppan, P., Baldasano, J., Brunner, D., Aksoyoglu, S., Carmichael, G., Douros, J., Flemming, J., Forkel, R., Galmarini, S., Gauss, M., Grell, G., Hirtl, M., Joffre, S., Jorba, O., Kaas, E., Kaasik, M., Kallos, G., Kong, X., Korsholm, U., Kurganskiy, A., Kushta, J., Lohmann, U., Mahura, A., Manders-Groot, A., Maurizi, A., Moussiopoulos, N., Rao, S.T., Savage, N., Seigneur, C., Sokhi, R.S., Solazzo, E., Solomos, S., Sørensen, B., Tsegas, G., Vignati, E., Vogel, B. & Zhang, Y. (2014). Online coupled regional meteorology chemistry models in Europe: Current status and prospects. *Atmospheric Chemistry and Physics*, **14**, 317–398. 4, 8, 74, 102

Bangert, M., Kottmeier, C., Vogel, B. & Vogel, H. (2011). Regional scale effects of the aerosol cloud interaction simulated with an online coupled comprehensive chemistry model. *Atmos. Chem. Phys.*, **11**, 4411–4423. 3

Barbaro, E., Oliveira, A.P., Soares, J., Codato, G., Ferreira, M.J., Mlakar, P., Boznar, M.Z. & Escobedo, J.F. (2010). Observational characterization of the downward atmospheric longwave radiation at the surface in the city of Sao Paulo. *Journal of Applied Meteorology and Climatology*, **49**, 2574–2590. 33, 34

Barbaro, E., Vilà-Guerau de Arellano, J., Krol, M.C. & Holtslag, A.A.M. (2013). Impacts of Aerosol Shortwave Radiation Absorption on the Dynamics of an Idealized Convective Atmospheric Boundary Layer. *Boundary-Layer Meteorology*, **148**, 31–49. 74, 77, 88, 90, 96

Barbaro, E., Vilà-Guerau de Arellano, J., Ouwersloot, H.G., Schroter, J.S., Donovan, D.P. & Krol, M.C. (2014). Aerosols in the convective boundary layer: Shortwave radiation effects on the coupled land-atmosphere system. *Journal of Geophysical Research: Atmospheres*, **119**, 5845–5863. 102, 104, 105, 106, 107, 108, 109, 110

Barbaro, E., Krol, M. & Vilà-Guerau de Arellano, J. (2015). Numerical simulation of the interaction between ammonium nitrate aerosol and convective boundary-layer dynamics. *Atmospheric Environment*, **105**, 202 – 211.

Bateni, S.M. & Entekhabi, D. (2012). Relative efficiency of land surface energy balance components. *Water Resources Research*, **48**, 10.1029/2011WR011357. 87

Beljaars, A.C. & Bosveld, F. (1997). Cabauw Data for the Validation of Land Surface Parameterization Schemes. *Journal of Climate*, **10**, 1172–1193. 77, 78, 83, 140

Bellouin, N., Boucher, O., Haywood, J. & Reddy, M.S. (2005). Global estimate of aerosol direct radiative forcing from satellite measurements. *Nature*, **438**, 1138–1141. 102

Bellouin, N., Quaas, J., Morcrette, J.J. & Boucher, O. (2013). Estimates of aerosol radiative forcing from the MACC re-analysis. *Atmospheric Chemistry and Physics*, **13**, 2045–2062. 7, 26

Betts, A.K. (1974). Reply to comment on the paper "non-precipitating Cumulus convection and its parameterization". *Q J R Meteorol Soc*, **100**, 469–471. 51, 52, 53, 63, 77

Bianco, L. & Wilczak, J. (2002). Convective boundary layer depth: Improved measurement by doppler radar wind profiler using fuzzy logic methods. *J Atmos Oceanic Technol*, **19**, 1745–1758. 83

Biasutti, M. & Giannini, A. (2006). Robust sahel drying in response to late 20th century forcings. *Geophys Res Lett*, **33**, L11706. 95

Biavati, G., Di Donfrancesco, G., Cairo, F. & Feist, D.G. (2011). Correction scheme for close-range lidar returns. *Applied optics*, **50**, 5872–82. 80

Bierwirth, E., Wendisch, M., Jäkel, E., Ehrlich, A., Schmidt, K.S., Stark, H., Pilewskie, P., Esselborn, M., Gobbi, G.P., Ferrare, R., Müller, T. & Clarke, A. (2010). A new method to retrieve the aerosol layer absorption coefficient from airborne flux density and actinic radiation measurements. *J Geophys Res*, **115**. 57

Bilbao, J. & de Miguel, A.H. (2007). Estimation of Daylight Downward Longwave Atmospheric Irradiance under Clear-Sky and All-Sky Conditions. *Journal of Applied Meteorology and Climatology*, **46**, 878–889. 32

Bosveld, F. (2010). Observering the surface energy budget at Cabauw: A status report. Tech. rep., Koninklijk Nederlands Meteorologish Instituut. 140

Bosveld, F.C., Baas, P., Steeneveld, G.J., Holtslag, A.A.M., Angevine, W.M., Bazile, E., de Bruijn, E.I.F., Deacu, D., Edwards, J.M., Ek, M., Larson, V.E., Pleim, J.E., Raschendorfer, M. & Svensson, G. (2014). The third GABLS intercomparison case for evaluation studies of boundary-layer models. part b: Results and process understanding. *Boundary-Layer Meteorology*, **152**. 32

Boucher, O. & Anderson, T. (1995). General circulation model assessment of the sensitivity of direct climate forcing by anthropogenic sulfate aerosols to aerosol size and chemistry. *J Geophys Res*, **100**, 26117 – 16134. 74

Boucher, O., Randall, D., Artaxo, P., Bretherton, C., Feingold, G., Forster, P., Kerminen, V.M., Kondo, Y., Liao, H., Lohmann, U., Rasch, P., Satheesh, S., Sherwood, S., Stevens, B. & Zhang, X. (2013). Clouds and aerosols. In *Climate Change 2013: The Physical Science Basis. Contribution of Working Group I to the Fifth Assessment Report of the Intergovernmental Panel on Climate Change*, Cambridge University Press. 3, 7, 21, 142

Bozzo, A., Pincus, R., Sandu, I. & Morcrette, J.J. (2014). Impact of a spectral sampling technique for radiation on ecmwf weather forecasts. *Journal of Advances in Modeling Earth Systems*. 134, 135

Bretherton, C., Macvean, M., Bechtold, P., Chlond, A., Cotton, W., Cuxart, J., Cuijpers, H., Khairoutdinov, M., Kosovic, B., Lewellen, D., Moeng, C.H., Sibiesma, P., Stevens, B., Stevend, D., Sykes, I. & Wyant, M. (1999). An intercomparison of radiatively driven entrainment and turbulence in a smoke cloud, as simulated by different numerical models. *Q J R Meteorol Soc*, **125**, 391–423. 12, 50, 51, 56

Brunt, D. (1932). Notes on radiation in the atmosphere I. *Q. J. R. Meteorol. Soc.*, **58**, 389–420. 17, 32, 39, 77

Brutsaert, W. (1975). On a derivable formula for long-wave radiation from clear skies. *Water Resources Research*, **11**, 742–744. 31, 32

Burns, S.P., Sun, J., Delany, A.C., Semmer, S.R., Oncley, S.P. & Horst, T.W. (2003). A Field Intercomparison Technique to Improve the Relative Accuracy of Longwave Radiation Measurements and an Evaluation of CASES-99 Pyrgeometer Data Quality. *Journal of Atmospheric and Oceanic Technology*, **20**, 348–361. 38

Burridge, D.M. & Gadd, A.J. (1974). The meteorological office operational 10 level numerical weather prediction model (december 1974). Tech. rep., U.K. Met. Office Tech. Notes 12 and 48. 26, 76, 133

Carslaw, K.S., Boucher, O., Spracklen, D.V., Mann, G.W., Rae, J.G.L., Woodward, S. & Kulmala, M. (2010). A review of natural aerosol interactions and feedbacks within the earth system. *Atmos. Chem. Phys.*, **10**, 1701–1737. 1, 8

Casso-Torralba, P., Vilà-Guerau de Arellano, J., Bosveld, F., Soler, M.R., Vermeulen, A., Werner, C. & Moors, E. (2008). Diurnal and vertical variability of the sensible heat and carbon dioxide budgets in the atmospheric surface layer. *J Geophys Res*, **113**, D12119. 78, 86

Castanho, A.D. & Artaxo, P. (2001). Wintertime and summertime sao paulo aerosol source apportionment study. *Atmospheric Environment*, **35**, 4889–4902. 4, 33, 36, 139

Chamecki, M., Meneveau, C. & Parlange, M.B. (2009). Large eddy simulation of pollen transport in the atmospheric boundary layer. *Journal of Aerosol Science*, **40**, 241–255. 1

Charlson, R., Schwartz, S., Hales, J., Cess, R., Coakley, J., Hansen, J. & Hoffmann, D. (1992). Climate forcing by anthropogenic aerosols. *Science*, **255**, 423–430. 48

Chen, J.P., Tsai, I.C. & Lin, Y.C. (2013). A statistical-numerical aerosol parameterization scheme. *Atmospheric Chemistry and Physics Discussions*, **13**, 12033–12087. 74

Cirino, G.G., Souza, R.A.F., Adams, D.K. & Artaxo, P. (2014). The effect of atmospheric aerosol particles and clouds on net ecosystem exchange in the amazon. *Atmos. Chem. Phys.*, **14**, 6523–6543. 2

Coakley, J.A., Cess, R.D. & Yurevich, F.B. (1983). The effect of tropospheric aerosols on the earth's radiation budget: A parameterization for climate models. *Journal of the Atmospheric Sciences*, **40**, 116–138. 21, 142

Codato, G., Oliveira, A.P., Soares, J., Escobedo, J.F., Gomes, E.N. & Pai, A.D. (2008). Global and diffuse solar irradiances in urban and rural areas in southeast Brazil. *Theoretical and Applied Climatology*, **93**, 57–73. 5, 34

Conant, W.C. (2002). Black carbon radiative heating effects on cloud microphysics and implications for the aerosol indirect effect 1. extended Köhler theory. *J Geophys Res*, **107**. 17, 50

Costabile, F., Barnaba, F., Angelini, F. & Gobbi, G.P. (2013). Identification of key aerosol populations through their size and composition resolved spectral scattering and absorption. *Atmospheric Chemistry and Physics*, **13**, 2455–2470. 74

Crawford, T.M. & Duchon, C.E. (1999). An Improved Parameterization for Estimating Effective Atmospheric Emissivity for Use in Calculating Daytime Downwelling Longwave Radiation. *J. Appl. Meteor.*, **38**, 474–480. 32

Cuijpers, J.W.M. & Holtslag, A.A.M. (1998). Impact of skewness and nonlocal effects on scalar and buoyancy fluxes in convective boundary layers. *J Atmos Sci*, **55**, 151–162. 10, 49

D'Amato, G., Spieksma, F.T.M., Liccardi, G., Jäger, S., Russo, M., Kontou-Fili, K., Nikkels, H., Wüthrich, B. & Bonini, S. (1998). Pollen-related allergy in europe. *Allergy*, **53**, 567–578. 1

Dassios, K.G. & Pandis, S.N. (1999). The mass accommodation coefficient of ammonium nitrate aerosol. *Atmospheric Environment*, **33**, 2993–3003. 103, 107, 109, 121

De Roode, S.R., Duynkerke, P.G., Boot, W. & Van der Hage, J.C.H. (2001). Surface and tethered-balloon observations of actinic flux: Effects of arctic stratus, surface albedo, and solar zenith angle. *J Geophys Res*, **106**, 27497–27507. 50, 141

de Wekker, S.F.J., Steyn, D.G. & Nyeki, S. (2004). A comparison of aerosol-layer and convective boundary-layer structure over a mountain range during STAAARTE 1997. *Boundary-Layer Meteorol*, **113**, 249–271. 75

Deardorff, J. (1974). Three-dimensional numerical study of the height and mean structure of a heated planetary boundary layer. *Boundary-Layer Meteorology*, **7**, 81–106. 119

Demuzere, M., Trigo, R.M., Vilà-Guerau de Arellano, J. & van Lipzig, N.P.M. (2009). The impact of weather and atmospheric circulation on O3 and PM10 levels at a rural mid-latitude site. *Atmos. Chem. Phys.*, **9**, 2695–2714. 110

Dentener, F. & Crutzen, P. (1994). A three-dimensional model of the global ammonia cycle. *Journal of Atmospheric Chemistry*, **19**, 331–369. 7

Derksen, J., Roelofs, G.J., Otjes, R., de Leeuw, G. & Röckmann, T. (2011). Impact of ammonium nitrate chemistry on the AOT in Cabauw, the Netherlands. *Atmospheric Environment*, **45**, 5640–5646. 78

Dilley, A.C. & Obrien, D.M. (1998). Estimating downward clear sky long-wave irradiance at the surface from screen temperature and precipitable water. *Q.J Royal Met. Soc.*, **124**, 1391–1401. 32

Dufresne, J.L., Gautier, C., Ricchiazzi, P. & Fouquart, Y. (2002). Longwave scattering effects of mineral aerosols. *Journal of the Atmospheric Sciences*, **59**, 1959–1966. 134

Duong, H.T., Sorooshian, A. & Feingold, G. (2011). Investigating potential biases in observed and modeled metrics of aerosol-cloud-precipitation interactions. *Atmos. Chem. Phys.*, **11**, 4027–4037. 141

Dürr, B. & Philipona, R. (2004). Automatic cloud amount detection by surface longwave downward radiation measurements. *J Geophys Res*, **109**, D05201. 32, 86

Dusek, U., ten Brink, H., Meijer, H., Kos, G., Mrozek, D., Röckmann, T., Holzinger, R. & Weijers, E. (2013). The contribution of fossil sources to the organic aerosol in the Netherlands. *Atmospheric Environment*, **74**, 169–176. 105

Duynkerke, P.G. (1991). Radiation fog: A comparison of model simulation with detailed observations. *Monthly Weather Review*, **119**, 324–341. 77

Duynkerke, P.G., Zhang, H. & Jonker, P. (1995). Microphysical and turbulent structure of nocturnal Stratocumulus as observed during ASTEX. *J Atmos Sci*, **52**, 2763–2777. 50, 51

Edwards, J., Basu, S., Bosveld, F. & Holtslag, A. (2014). The impact of radiation on the gabls3 large-eddy simulation through the night and during the morning transition. *Boundary-Layer Meteorology*, **152**, 189–211. 40

Ek, M. & Mahrt, L. (1994). Daytime evolution of relative humidity at the boundary layer top. *Mon. Wea. Rev.*, **122**, 2709–2721. 6

Elterman, L. (1968). UV, visible and IR for altitudes to 50 km (AFCR-68-0153). Tech. rep., Air Force Cambridge Res. Lab. Bedford, Mass. 26, 76

Erisman, J.., De Leeuw, F.A.A.M. & Van Aalst, R.M. (1989). Deposition of the most acidifying components in the netherlands during the period 1980-1986. *Atmospheric Environment*, **23**, 1051–1062. 108

Escobedo, J.F., Gomes, E.N., Oliveira, A.P. & Soares, J. (2009). Modeling hourly and daily fractions of UV, PAR and NIR to global solar radiation under various sky conditions at Botucatu, Brazil. *Applied Energy*, **86**, 299 – 309. 140

Escobedo, J.F., Gomes, E.N., Oliveira, A.P. & Soares, J. (2011). Ratios of UV, PAR and NIR components to global solar radiation measured at Botucatu site in Brazil. *Renewable Energy*, **36**, 169–178. 134, 140

Fairall, C.W., Persson, P.O.G., Bradley, E.F., Payne, R.E. & Anderson, S.P. (1998). A New Look at Calibration and Use of Eppley Precision Infrared Radiometers. Part I: Theory and Application. *Journal of Atmospheric and Oceanic Technology*, **15**, 1229–1242. 38

Feingold, G., Remer, L.A., Ramaprasad, J. & Kaufman, Y.J. (2001). Analysis of smoke impact on clouds in brazilian biomass burning regions: An extension of twomey's approach. *Journal of Geophysical Research: Atmospheres*, **106**, 22907–22922. 142

Feingold, G., Eberhard, W.L., Veron, D.E. & Previdi, M. (2003). First measurements of the twomey indirect effect using ground-based remote sensors. *Geophysical Research Letters*, **30**. 3, 142

Feingold, G., Jiang, H. & Harrington, J.Y. (2005). On smoke suppression of clouds in Amazonia. *Geophysical Research Letters*, **32**, 1–4. 9, 138

Feingold, G., Koren, I., Wang, H., Xue, H. & Brewer, W.A. (2010). Precipitation-generated oscillations in open cellular cloud fields. *Nature*, **466**, 849–852. 3

Fernando, H. (1991). Turbulent mixing in stratified fluids. *Annu Rev Fluid Mech*, **23**, 455–493. 63, 64

Ferreira, M., Oliveira, A., Soares, J., Codato, G., Barbaro, E. & Escobedo, J. (2012). Radiation balance at the surface in the city of Sao Paulo, Brazil: diurnal and seasonal variations. *Theoretical and Applied Climatology*, **107**, 229–246. 140

Ferreira, M.J., Oliveira, A.P. & Soares, J. (2013). Diurnal variation in stored energy flux in Sao Paulo city, Brazil. *Urban Climate*, **5**, 36–51. 140

Finch, J.W. & Best, M.J. (2004). The accuracy of downward short- and long-wave radiation at the earths surface calculated using simple models. *Meteorol. Appl.*, **11**, 33–39. 32

Fitzjarrald, D.R. & Lenschow, D.H. (1983). Mean concentration and flux profiles for chemically reactive species in the atmospheric surface layer. *Atmospheric Environment*, **17**, 2505 – 2512. 103, 109, 115, 121, 122, 123, 124

Flerchinger, G.N., Xaio, W., Marks, D., Sauer, T.J. & Yu, Q. (2009). Comparison of algorithms for incoming atmospheric long-wave radiation. *Water Resour. Res.*, **45**. 32

Foken, T. (2008). Eddy flux measurements the energy balance closure problem : an overview. *Ecological Applications*, **18(6)**, 1351–1367. 83

Forster, P., Ramaswamy, V., Artaxo, P., Berntsen, T., Betts, R., Fahey, D., Haywood, J., Lean, J., Lowe, D., Myhre, G., Nganga, J., Prinn, R., Raga, G., Schulz, M. & Dorland, R.V. (2007). Changes in atmospheric constituents and in radiative forcing. In *Climate Change 2007: The Physical Science Basis. Contribution of Working Group I to the Fourth Assessment Report of the Intergovernmental Panel on Climate Change*, Cambridge University Press. 7, 16, 48, 74

Fountoukis, C. & Nenes, A. (2007). ISORROPIAII: A computationally efficient thermodynamic equilibrium model for K+ Ca2+ Mg2+ NH4+ Na+ SO42- NO3- Cl- H2O aerosols. *Atmospheric Chemistry and Physics*, **7**, 4639–4659. 103, 104

Frouin, R. & Murakami, H. (2007). Estimating photosynthetically available radiation at the ocean surface from adeos-ii global imager data. *Journal of Oceanography*, **63**, 493–503. 134

Frouin, R. & Pinker, R.T. (1995). Estimating photosynthetically active radiation (par) at the earth's surface from satellite observations. *Remote Sensing of Environment*, **51**, 98 – 107, remote Sensing of Land Surface for Studies of Global Chage. 134

Ganzeveld, L. & Lelieveld, J. (1995). Dry deposition parameterization in a chemistry general circulation model and its influence on the distribution of reactive trace gases. *Journal of Geophysical Research*, **100**, 20,999–21,012. 7, 104, 105, 114

Ganzeveld, L., Lelieveld, J. & Roelofs, G.. (1998). A dry deposition parameterization for sulfur oxides in a chemistry and general circulation model. *Journal of Geophysical Research D: Atmospheres*, **103**, 5679–5694. 11

Gao, R.S., Hall, S.R., Swartz, W.H., Schwarz, J.P., Spackman, J.R., Watts, L.A., Fahey, D.W., Aikin, K.C., Shetter, R.E. & Bui, T.P. (2008). Calculations of solar shortwave heating rates due to black carbon and ozone absorption using in situ measurements. *J Geophys Res*, **113**. 16, 17, 50

Garratt, J.R. (1992). *The atmospheric boundary layer*. Cambridge University Press, U.K., 316 pp. 4, 49, 50, 51, 53, 77, 121, 122, 124

Gentine, P., Entekhabi, D. & Polcher, J. (2011). The Diurnal Behavior of Evaporative Fraction in the Soil-Vegetation-Atmospheric Boundary Layer Continuum. *Journal of Hydrometeorology*, **12**, 1530–1546. 87

Grabowski, W.W. & Wang, L.P. (2013). Growth of cloud droplets in a turbulent environment. *Annual Review of Fluid Mechanics*, **45**, 293–324. 107

Gregory, J.M., Ingram, W.J., Palmer, M.A., Jones, G.S., Stott, P.A., Thorpe, R.B., Lowe, J.A., Johns, T.C. & Williams, K.D. (2004). A new method for diagnosing radiative forcing and climate sensitivity. *Geophysical Research Letters*, **31**. 7

Grell, G. & Baklanov, A. (2011). Integrated modeling for forecasting weather and air quality: A call for fully coupled approaches. *Atmospheric Environment*, **45**, 6845 – 6851, modeling of Air Quality Impacts, Forecasting and Interactions with Climate. 4

Grell, G.A., Peckham, S.E., Schmitz, R., McKeen, S.A., Frost, G., Skamarock, W.C. & Eder, B. (2005). Fully coupled online chemistry within the WRF model. *Atmospheric Environment*, **39**, 6957 – 6975. 10

Grob, S., Esselborn, M., Abicht, F., Wirth, M., Fix, A. & Minikin, A. (2013). Airborne high spectral resolution lidar observation of pollution aerosol during EUCAARI-LONGREX. *Atmospheric Chemistry and Physics*, **13**, 2435–2444. 78

Grobner, J., Wacker, S., Vuilleumier, L. & Kampfer, N. (2009). Effective atmospheric boundary layer temperature from longwave radiation measurements. *J. Geophys. Res.*, **114**. 32, 35

Guenther, A., Hewitt, C.N., Erickson, D., Fall, R., Geron, C., Graedel, T., Harley, P., Klinger, L., Lerdau, M., Mckay, W.A., Pierce, T., Scholes, B., Steinbrecher, R., Tallamraju, R., Taylor, J. & Zimmerman, P. (1995). A global model of natural volatile organic compound emissions. *J. Geophys. Res.*, **100**, 8873. 7

Halthore, R.N., Crisp, D., Schwartz, S.E., Anderson, G.P., Berk, A., Bonnel, B., Boucher, O., Chang, F.L., Chou, M.D., Clothiaux, E.E., Dubuisson, P., Fomin, B., Fouquart, Y., Freidenreich, S., Gautier, C., Kato, S., Laszlo, I., Li, Z., Mather, J.H., Plana-Fattori, A., Ramaswamy, V., Ricchiazzi, P., Shiren, Y., Trishchenko, A. & Wiscombe, W. (2005). Intercomparison of shortwave radiative transfer codes and measurements. *Journal of Geophysical Research: Atmospheres*, **110**. 29

Hamba, F. (1993). A Modified K Model for Chemically Reactive Species in the Planetary Boundary Layer. *Journal of Geophysical Research*, **98-D3**, 5173–5182. 103, 116, 122, 123, 124

Hamburger, T., McMeeking, G., Minikin, a., Birmili, W., Dall'Osto, M., O'Dowd, C., Flentje, H., Henzing, B., Junninen, H., Kristensson, a., de Leeuw, G., Stohl, a., Burkhart, J.F., Coe, H., Krejci, R. & Petzold, a. (2011). Overview of the synoptic and pollution situation over Europe during the EUCAARI-LONGREX field campaign. *Atmospheric Chemistry and Physics*, **11**, 1065–1082. 3, 78, 106, 107, 111

Hanson, P.J. (1991). Dry Deposition of Reactive Nitrogen Compounds: A Review of Leaf, Canopy and Non-Foliar Measurements. *Atmos. Environ.*, **25A**. 103, 114

Harman, H. (1976). *Modern Factor Analysis*. University of Chicago Pres 508 pp. 37

Harrison, R.M. & Pio, C.A. (1983). An investigation of the atmospheric HNO3-NH3-NH4NO3 equilibrium relationship in a cool , humid climate. *Telus*, **35B**, 155–159. 8, 103

Hatzianastassiou, N., Matsoukas, C., Fotiadi, A., Pavlakis, K.G., Drakakis, E., Hatzidimitriou, D. & Vardavas, I. (2005). Global distribution of Earth surface shortwave radiation budget. *Atmospheric Chemistry and Physics*, **5**, 2847–2867. 7, 75

Haywood, J. & Boucher, O. (2000). Estimates of the direct and indirect radiative forcing due to tropospheric aerosols: A review. *Reviews of Geophysics*, **38**, 513–543. 8

Haywood, J., Ramaswamy, V. & Soden, B. (1999). Tropospheric Aerosol Climate Forcing in Clear-Sky Satellite Observations over the Oceans. *Science*, **283**, 1299–1303. 74

Haywood, J., Francis, P., Martin, G. & Taylor, J. (2001). Optical properties and direct radiative effect of Saharan dust : A case study of two Saharan dust outbreaks using aircraft data. *J Geophys Res*, **106**, 18417,18430. 26, 86

Haywood, J.M., Osborne, S.R., Francis, P.N., Keil, A., Formenti, P., Andreae, M.O. & Kaye, P.H. (2003). The mean physical and optical properties of regional haze dominated by biomass burning aerosol measured from the C-130 aircraft during SAFARI 2000. *Journal of Geophysical Research: Atmospheres*, **108**. 7, 8, 10

Haywood, J.M., Johnson, B.T., Osborne, S.R., Baran, a.J., Brooks, M., Milton, S.F., Mulcahy, J., Walters, D., Allan, R.P., Klaver, a., Formenti, P., Brindley, H.E., Christopher, S. & Gupta, P. (2011). Motivation, rationale and key results from the GERBILS Saharan dust measurement campaign. *Quarterly Journal of the Royal Meteorological Society*, **137**, 1106–1116. 138

Henry, R.H.P.e. (1991). *Multivariate Receptor Models, In: Receptor Modeling for Air Quality Management*. Elsevier Science Publishers 117-147. 37

Hesterberg, R., Blatter, A., Fahrni, M., Rosset, M., Neftel, A., Eugster, W. & Wanner, H. (1996). Deposition of nitrogen-containing compounds to an extensively managed grassland in central switzerland. *Environmental Pollution*, **91**, 21–34. 103, 115

Heus, T., van Heerwaarden, C.C., Jonker, H.J.J., Siebesma, A.P., Axelsen, S., van den Dries, K., Geoffroy, O., Moene, A., Pino, D., de Roode, S.R. & Vilà-Guerau de Arellano, J. (2010). Formulation of the Dutch Atmospheric Large-Eddy Simulation (DALES) and overview of its applications. *Geosci Model Dev*, **3**, 415–444. 11, 17, 26, 52, 76, 77, 104, 119, 120

Hewitt, C.N. & Jackson, A. (2009). *Atmospheric Science for Environmental Scientists*. Wiley-Blackwell, 300 pp. 22, 56, 74, 81, 91

Hodzic, A., Madronich, S., Aumont, B., Lee-Taylor, J., Karl, T., Camredon, M. & Mouchel-Vallon, C. (2013). Limited influence of dry deposition of semivolatile organic vapors on secondary organic aerosol formation in the urban plume. *Geophysical Research Letters*, **40**, 3302–3307. 139

Holtslag, A. & de Bruin, H. (1988). Applied modeling of the nighttime surface energy balance over land. *Journal of Applied Meteorology*, **27**, 689–704. 18, 32, 77

Holtslag, A.A.M. & Moeng, C.H. (1991). Eddy diffusivity and countergradient transport in the convective atmospheric boundary layer. *Journal of the Atmospheric Sciences*, **48**, 1690–1698. 122

Hong, S.Y. & Pan, H.L. (1996). Nonlocal boundary layer vertical diffusion in a medium-range forecast model. *Mon. Wea. Rev.*, **124**, 2322–2339. 109

Hosseinpour, F. & Wilcox, E.M. (2014). Aerosol interactions with african/atlantic climate dynamics. *Environ. Res. Lett.*, **9**, 075004. 1

Huang, X., Cole, J.N.S., He, F., Potter, G.L., Oreopoulos, L., Lee, D., Suarez, M. & Loeb, N.G. (2013). Longwave Band-By-Band Cloud Radiative Effect and Its Application in GCM Evaluation. *Journal of Climate*, **26**, 450–467. 31

Huebert, B. & Robert, C. (1985). The Dry Deposition of Nitric Acid to Grass. *Journal of Geophysical Research*, **90**, 2085–2090. 102, 115

Huebert, B.J., Luke, W.T., Delany, A.C. & Brost, R.A. (1988). Measurements of concentrations and dry surface fluxes of atmospheric nitrates in the presence of ammonia. *Journal of Geophysical Research*, **93**, 7127–7136. 102, 114, 115

Huijnen, V., Williams, J., Van Weele, M., Van Noije, T., Krol, M., Dentener, F., Segers, A., Houweling, S., Peters, W., De Laat, J., Boersma, F., Bergamaschi, P., Van Velthoven, P., Le Sager, P., Eskes, H., Alkemade, F., Scheele, R., Nédélec, P. & Pätz, H.. (2010). The global chemistry transport model tm5: Description and evaluation of the tropospheric chemistry version 3.0. *Geoscientific Model Development*, **3**, 445–473. 106

Iacono, M.J., Delamere, J.S., Mlawer, E.J., Shephard, M.W., Clough, S.A. & Collins, W.D. (2008). Radiative forcing by long-lived greenhouse gases: Calculations with the AER radiative transfer models. *J. Geophys. Res.*, **113**. 135

Israelevich, P., Ganor, E., Alpert, P., Kishcha, P. & Stupp, a. (2012). Predominant transport paths of Saharan dust over the Mediterranean Sea to Europe. *J Geophys Res*, **117**, D02205. 2, 74, 81, 91

Iziomon, M., Mayer, H. & Matzarakis, A. (2003). Downward atmospheric longwave irradiance under clear and cloudy skies: Measurement and parameterization. *Journal of Atmospheric and Solar-Terrestrial Physics*, **65**, 1107–1116. 32

Jacobson, M.Z. (1998). Studying the effects of aerosols on vertical photolysis rate coefficient and temperature profiles over an urban airshed. *J Geophys Res*, **103**. 6, 8, 48, 61, 102, 142

Jacobson, M.Z. (2001a). Strong radiative heating due to the mixing state of black carbon in atmospheric aerosols. *Nature*, **409**, 695–697. 9

Jacobson, Z. (2001b). Global direct radiative forcing due to multicomponent anthropogenic and natural aerosols. *J Geophys Res*, **106**, 1551–1568. 21, 74

Jacovides, C.P., Kaltsounides, N.A., Asimakopoulos, D.N. & Kaskaoutis, D.G. (2005). Spectral aerosol optical depth and angstrom parameters in the polluted athens atmosphere. *Theoretical and Applied Climatology*, **81**, 161–167. 27

Jager, J.E. (2014). *Airborne VOC measurements on board the Zeppelin NT during the PEGASOS campaigns in 2012 deploying the improved Fast-GC-MSD System*. Forschungszentrum Julich GmbH, Germany, 182 pp. 8, 102, 111, 139, 140

James, P.M. (2006). An objective classification method for Hess and Brezowsky Grosswetterlagen over Europe. *Theoretical and Applied Climatology*, **88**, 17–42. 78

Janssen, R.H.H., de Arellano, J.V.G., Ganzeveld, L.N., Kabat, P., Jimenez, J.L., Farmer, D.K., van Heerwaarden, C.C. & Mammarella, I. (2012). Combined effects of surface conditions, boundary layer dynamics and chemistry on diurnal SOA evolution. *Atmos. Chem. Phys.*, **12**, 6827–6843. 139

Jarvis, P.G. (1976). The interpretation of the variations in leaf water potential and stomatal conductance found in canopies in the field. *Philosophical Transactions of the Royal Society of London. B, Biological Sciences*, **273**, 593–610. 77

Jiang, H. & Feingold, G. (2006). Effect of aerosol on warm convective clouds: Aerosol-cloud-surface flux feedbacks in a new coupled large eddy model. *Journal of Geophysical Research*, **111**, D01202. 10, 102

Jochum, A., Rodriguez Camino, E., De Bruin, H. & Holtslag, A.A.M. (2004). Performance of HIRLAM in a semiarid heteregeneous region: Evaluation of the land surface and boundary layer description using EFEDA observations. *Mon Weather Rev*, **132**, 2745–2760. 58

Johnson, B.T., Heese, B., McFarlane, S.A., Chazette, P., Jones, A. & Bellouin, N. (2008). Vertical distribution and radiative effects of mineral dust and biomass burning aerosol over West Africa during DABEX. *J Geophys Res*, **113**. 48, 49, 75

Jonsson, P., Eliasson, I., Holmer, B. & Grimmond, C.S.B. (2006). Longwave incoming radiation in the Tropics: results from field work in three African cities. *Theoretical and Applied Climatology*, **85**, 185–201. 33, 36, 38

Joseph, J., Wiscombe, W. & Weinman, J. (1976). The delta-eddington approximation for radiative flux transfer. *J Atmos Sci*, **33**, 2452–2459. 11, 12, 17, 22, 23, 24, 26, 76

Junge, C.E., Chagnon, C.W. & Manson, J.E. (1961). A world-wide stratospheric aerosol layer. *Science*, **133**, 1478–1479. 20

Karam, H.A., Pereira Filho, A.J., Masson, V., Noilhan, J. & Marques Filho, E.P. (2010). Formulation of a tropical town energy budget (t-teb) scheme. *Theoretical and Applied Climatology*, **101**, 109–120. 38

Kassianov, E.I., Flynn, C.J., Ackerman, T.P. & Barnard, J.C. (2007). Aerosol single-scattering albedo and asymmetry parameter from MFRSR observations during the ARM Aerosol IOP 2003. *Atmos. Chem. Phys.*, **7**, 3341–3351. 21

Kato, S., Ackerman, T.P., Mather, J.H. & Clothiaux, E.E. (1999). The k-distribution method and correlated-k approximation for a shortwave radiative transfer model. *Journal of Quantitative Spectroscopy and Radiative Transfer*, **62**, 109 – 121. 26, 134

Kaufman, Y., Tanré, D. & Boucher, O. (2002). A satellite view of aerosols in the climate system. *Nature*, **419**, 215–223. 1, 49, 74, 102

Kaufman, Y.J. (1993). Aerosol optical thickness and atmospheric path radiance. *J Geophys Res*, **98**, 2677. 20, 27, 74, 91, 141, 142

Kaufman, Y.J. & Nakajima, T. (1993). Effect of amazon smoke on cloud microphysics and albedo-analysis from satellite imagery. *J. Appl. Meteor.*, **32**, 729–744. 142

Kessler, C.J., Porter, T.H., Firth, D., Sager, T.W. & Hemphill, M. (1992). Factor analysis of trends in Texas acidic deposition. *Atmospheric Environment. Part A. General Topics*, **26**, 1137–1146. 37

Kinne, S., O'Donnel, D., Stier, P., Kloster, S., Zhang, K., Schmidt, H., Rast, S., Giorgetta, M., Eck, T.F. & Stevens, B. (2013). MAC-v1: A new global aerosol climatology for climate studies. *Journal of Advances in Modeling Earth Systems*, **5**. 8, 81

Klett, J. (1985). Lidar inversion with variable backscatter/extinction ratios. *Applied Optics*, **24**, 1638–1643. 80

Knap, W., Hinssen, Y., Los, A., van Oort, C., Warmer, J. & Worrell, E. (2010). Baseline surface radiation network (BSRN) station at the Cabauw observatory. Tech. rep., Koninklijk Nederlands Meteorologish Instituut. 78

Knapp, K.R., Haar, T.H.V. & Kaufman, Y.J. (2002). Aerosol optical depth retrieval from GOES-8 : Uncertainty study and retrieval validation over South America. *J Geophys Res*, **107**, 10.1029/2001JD000505. 74

Krol, M., Houweling, S., Bregman, B., van den Broek, M., Segers, A., van Velthoven, P., Peters, W., Dentener, F. & Bergamaschi, P. (2005). The two-way nested global chemistry-transport zoom model TM5: algorithm and applications. *Atmos. Chem. Phys.*, **5**, 417–432. 106

Krol, M.C., Molemaker, M.J. & Vilà-Guerau de Arellano, J. (2000). Effects of turbulence and heterogeneous emissions on photochemically active species in the convective boundary layer. *J. Geophys. Res.*, **105**, 6871–6884. 7, 10, 103

Kulmala, M., Asmi, A., Lappalainen, H.K., Carslaw, K.S., Pöschl, U., Baltensperger, U., Hov, O., Brenquier, J.L., Pandis, S.N., Facchini, M.C., Hansson, H.C., Wiedensohler, A. & O'Dowd, C.D. (2009). Introduction: European Integrated Project on Aerosol Cloud Climate and Air Quality interactions (EUCAARI): integrating aerosol research from nano to global scales. *Atmospheric Chemistry and Physics*, **9**, 2825–2841. 10, 78, 139

Kulmala, M., Asmi, A., Lappalainen, H.K., Baltensperger, U., Brenguier, J.L., Facchini, M.C., Hansson, H.C., Hov, O., O'Dowd, C.D., Pöschl, U., Wiedensohler, A., Boers, R., Boucher, O., de Leeuw, G., Denier van der Gon, H.A.C., Feichter, J., Krejci, R., Laj, P., Lihavainen, H., Lohmann, U., McFiggans, G., Mentel, T., Pilinis, C., Riipinen, I., Schulz, M., Stohl, A., Swietlicki, E., Vignati, E., Alves, C., Amann, M., Ammann, M., Arabas, S., Artaxo, P., Baars, H., Beddows, D.C.S., Bergström, R., Beukes, J.P., Bilde, M., Burkhart, J.F., Canonaco, F., Clegg, S.L., Coe, H., Crumeyrolle, S., D'Anna, B., Decesari, S., Gilardoni, S., Fischer, M., Fjaeraa, A.M., Fountoukis, C., George, C., Gomes, L., Halloran, P., Hamburger, T., Harrison, R.M., Herrmann, H., Hoffmann, T., Hoose, C., Hu, M., Hyvärinen, A., Hõrrak, U., Iinuma, Y., Iversen, T., Josipovic, M., Kanakidou, M., Kiendler-Scharr, A., Kirkevå G, A., Kiss, G., Klimont, Z., Kolmonen, P., Komppula, M., Kristjánsson, J.E., Laakso, L., Laaksonen, A., Labonnote, L., Lanz, V.A., Lehtinen, K.E.J., Rizzo, L.V., Makkonen, R., Manninen, H.E., McMeeking, G., Merikanto, J., Minikin, A., Mirme, S., Morgan, W.T., Nemitz, E., O'Donnell, D., Panwar, T.S., Pawlowska, H., Petzold, A., Pienaar, J.J., Pio, C., Plass-Duelmer, C., Prévôt, A.S.H., Pryor, S., Reddington, C.L., Roberts, G., Rosenfeld, D., Schwarz, J., Seland, O., Sellegri, K., Shen, X.J., Shiraiwa, M., Siebert, H., Sierau, B., Simpson, D., Sun, J.Y., Topping, D., Tunved, P., Vaattovaara, P., Vakkari, V., Veefkind, J.P., Visschedijk, A., Vuollekoski, H., Vuolo, R., Wehner, B., Wildt, J., Woodward, S., Worsnop, D.R., van Zadelhoff, G.J., Zardini, A.A., Zhang, K., van Zyl, P.G., Kerminen, V.M., S Carslaw, K. & Pandis, S.N. (2011). General overview: European Integrated project on Aerosol Cloud Climate and Air Quality interactions (EUCAARI): integrating aerosol research from nano to global scales. *Atmospheric Chemistry and Physics*, **11**, 13061–13143. 8, 10, 12, 78, 102, 106, 140

Kylling, A., Webb, A.R., Kift, R., Gobbi, G.P., Ammannato, L., Barnaba, F., Bais, A., Kazadzis, S., Wendisch, M., Jäkel, E., Schmidt, S., Kniffka, A., Thiel, S., Junkermann, W., Blumthaler, M., Silbernagl, R., Schallhart, B., Schmitt, R., Kjeldstad, B.,

Thorseth, T.M., Scheirer, R. & Mayer, B. (2005). Spectral actinic flux in the lower troposphere: measurement and 1-d simulations for cloudless, broken cloud and overcast situations. *Atmospheric Chemistry and Physics*, **5**, 1975–1997. 141, 142

Landgraf, J. & Crutzen, P.J. (1998). An efficient method for online calculations of photolysis and heating rates. *J Atmos Sci*, **55**, 863–878. 50, 141, 142

Lee, S.S., Feingold, G., McComiskey, A., Yamaguchi, T., Koren, I., Martins, J.V. & Yu, H. (2014). Effect of gradients in biomass burning aerosol on shallow cumulus convective circulations. *Journal of Geophysical Research: Atmospheres*. 10, 102, 138

Li, K., Wang, W., Ge, M., Li, J. & Wang, D. (2014). Optical properties of secondary organic aerosols generated by photooxidation of aromatic hydrocarbons. *Scientific Reports*, **4**. 139

Li, Z., Moreau, L. & Arking, A. (1997). On solar energy disposition: A perspective from observation and modeling. *Bulletin of the American Meteorological Society*, **78(1)**, 53–70. 6, 8, 75

Li, Z., Xia, X., Cribb, M., Mi, W., Holben, B., Wang, P., Chen, H., Tsay, S.C., Eck, T.F., Zhao, F., Dutton, E.G. & Dickerson, R.E. (2007). Aerosol optical properties and their radiative effects in northern China. *J Geophys Res*, **112**. 48

Lilly, D.K. (1968). Models of cloud-topped mixed-layer under a strong inversion. *Q J R Meteor Soc*, **94**, 292–309. 11, 12, 50, 51, 53, 77

Liou, K. (2002). *An Introduction to Atmospheric Radiation*. Academic Press, 583 pp. 6, 16, 18, 19, 21, 22, 26, 28, 31, 51, 76

Liu, C. & Ou, S.S. (1990). Effects of Tropospheric Aerosols on the Solar Radiative Heating in a Clear Atmosphere. *Theoretical and Applied Climatology*, **106**, 97–106. 74

Liu, H., Pinker, R.T. & Holben, B.N. (2005). A global view of aerosols from merged transport models, satellite, and ground observations. *J Geophys Res*, **110**. 48, 49

Liu, J. & Mauzerall, D.L. (2007). Potential influence of inter-continental transport of sulfate aerosols on air quality. *Environ. Res. Lett.*, **2**, 045029. 2

Lohmann, U. & Feichter, J. (2005). Global indirect aerosol effects: a review. *Atmospheric Chemistry and Physics*, **5**, 715–737. 142

Long, C.N. & Turner, D.D. (2008). A method for continuous estimation of clear-sky downwelling longwave radiative flux developed using ARM surface measurements. *J. Geophys. Res.*, **113**. 32, 34

Longo, K.M., Freitas, S.R., Andreae, M.O., Yokelson, R. & Artaxo, P. (2013). *Biomass Burning in Amazonia: Emissions, Long-Range Transport of Smoke and Its Regional and Remote Impacts*, 207–232. American Geophysical Union. 2

Lothon, M., Lohou, F., Pino, D., Couvreux, F., Pardyjak, E.R., Reuder, J., Vilà-Guerau de Arellano, J., Durand, P., Hartogensis, O., Legain, D., Augustin, P., Gioli, B., Lenschow, D.H., Faloona, I., Yague, C., Alexander, D.C., Angevine, W.M., Bargain, E., Barrie, J., Bazile, E., Bezombes, Y., Blay-Carreras, E., van de Boer, A., Boichard, J.L., Bourdon, A., Butet, A., Campistron, B., de Coster, O., Cuxart, J., Dabas, A., Darbieu, C., Deboudt, K., Delbarre, H., Derrien, S., Flament, P., Fourmentin, M., Garai, A., Gibert, F., Graf, A., Groebner, J., Guichard, F., Jimenez, M.A., Jonassen, M., van den Kroonenberg, A., Magliulo, V., Martin, S., Martinez, D., Mastrorillo, L., Moene, A.F., Molinos, F., Moulin, E., Pietersen, H.P., Piguet, B., Pique, E., Roman-Cascon, C., Rufin-Soler, C., Said, F., Sastre-Marugan, M., Seity, Y., Steeneveld, G.J., Toscano, P., Traulle,

O., Tzanos, D., Wacker, S., Wildmann, N. & Zaldei, A. (2014). The bllast field experiment: Boundary-layer late afternoon and sunset turbulence. *Atmospheric Chemistry and Physics*, **14**, 10931–10960. 140

Lyamani, H., Olmo, F.J. & Alados-Arboledas, L. (2010). Physical and optical properties of aerosols over an urban location in Spain: seasonal and diurnal variability. *Atmospheric Chemistry and Physics*, **10**, 239–254. 75, 94

Madronich, S. (1987). Photodissociation in the atmosphere 1. actinic flux and the effects of ground reflections and clouds. *J Geophys Res*, **92**, 9740–9752. 26, 50, 52, 77, 141

Malavelle, F., Pont, V., Mallet, M., Solmon, F., Johnson, B., Leon, J.F. & Liousse, C. (2011). Simulation of aerosol radiative effects over west africa during DABEX and AMMA SOP-0. *J Geophys Res*, **116**. 48

Malek, E. (1997). Evaluation of effective atmospheric emissivity and parameterization of cloud at local scale. *Atmospheric Research*, **45**, 41–54. 32, 34

Martilli, A., Clappier, A. & Rotach, M. (2002). An urban surface exchange parameterisation for mesoscale models. *Boundary-Layer Meteorology*, **104**, 261–304. 38

Marty, C. (2003). Downward longwave irradiance uncertainty under arctic atmospheres: Measurements and modeling. *J. Geophys. Res.*, **108**. 38

Masson, V., Gomes, L., Pigeon, G., Liousse, C., Pont, V., Lagouarde, J.P., Voogt, J., Salmond, J., Oke, T.R., Hidalgo, J., Legain, D., Garrouste, O., Lac, C., Connan, O., Briottet, X., Lachérade, S. & Tulet, P. (2008). The Canopy and Aerosol Particles Interactions in TOulouse Urban Layer (CAPITOUL) experiment. *Meteorol and Atmos Phys*, **102**, 135–157. 8, 17, 48, 49, 75, 102, 139

Matthias, V. & Bosenberg, J. (2002). Aerosol climatology for the planetary boundary layer derived from regular lidar measurements. *Atmospheric Research*, **63**, 221–245. 74

Mauritsen, T., Svensson, G., Zilitinkevich, S.S., Esau, I., Enger, L. & Grisogono, B. (2007). A total turbulent energy closure model for neutrally and stably stratified atmospheric boundary layers. *J Atmos Sci*, **64**, 4113–4126. 66

Mayer, B. & Kylling, A. (2005). The libradtran software package for radiative transfer calculations description and examples of use. *Atmos. Chem. Phys.*, **5**, 1855–1877. 17, 22, 26, 76, 135

Mensah, A., Holzinger, R., Otjes, R., Trimborn, A., Mentel, T.F., ten Brink, H., Henzing, B. & Kiendler-Scharr, A. (2012). Aerosol chemical composition at Cabauw, The Netherlands as observed in two intensive periods in May 2008 and March 2009. *Atmospheric Chemistry and Physics*, **12**, 4723–4742. 78, 106

Meszaros, R., Horvath, L., Weidinger, T., Neftel, A., Nemitz, E., Dammgen, U., Cellier, P. & Loubet, B. (2009). Measurement and modelling ozone fluxes over a cut and fertilized grassland. *Biogeosciences*, **6**, 1987–1999. 115

Meywerk, J. & Ramanathan, V. (1999). Observations of the spectral clear-sky aerosol forcing over the tropical Indian Ocean. *J Geophys Res*, **104**, 24359. 75

Mlawer, E.J., Taubman, S.J., Brown, P.D., Iacono, M.J. & Clough, S.A. (1997). Radiative transfer for inhomogeneous atmospheres: Rrtm, a validated correlated-k model for the longwave. *Journal of Geophysical Research: Atmospheres*, **102**, 16663–16682. 135

Moeng, C.H. (1984). A large-eddy-simulation model for the study of planetary boundary-layer turbulence. *J Atmos Sci*, **41**, 2052–2062. 49, 76, 119

Moeng, C.H. & Wyngaard, J.C. (1988). Spectral analysis of large-eddy simulations of the convective boundary layer. *J Atmos Sci*, **45**, 3573–3587. 49

Mok, T. & Rudowicz, C. (2004). A lidar study of the atmospheric entrainment zone and mixed layer over hong kong. *Atmospheric Research*, **69**, 147–163. 141

Molemaker, M.J. & Vilà-Guerau de Arellano, J. (1998). Control of chemical reactions by convective turbulence in the boundary layer. *J. Atmos. Sci*, **5**, 568–579. 120

Morcrette, J.J., Barker, H.W., Cole, J.N.S., Iacono, M.J. & Pincus, R. (2008). Impact of a new radiation package, McRad, in the ECMWF integrated forecasting system. *Mon. Wea. Rev.*, **136**, 4773–4798. 135

Morino, Y., Kondo, Y., Takegawa, N., Miyazaki, Y., Kita, K., Komazaki, Y., Fukuda, M., Miyakawa, T., Moteki, N. & Worsnop, D.R. (2006). Partitioning of HNO 3 and particulate nitrate over Tokyo: Effect of vertical mixing. *Journal of Geophysical Research*, **111**, D15215. 103, 107, 109, 114, 121

Mozurkewich, M. (1993). The dissociation constant of ammonium nitrate and its dependence on temperature, relative humidity and particle size. *Atmospheric Environment. Part A. General Topics*, **27**, 261–270. 102, 103, 105

Myhre, G., Berntsen, T., Haywood, J., Sundet, J., Holben, B., Johnsrud, M. & Stordal, F. (2003). Modeling the solar radiative impact of aerosols from biomass burning during the Southern African Regional Science Initiative (SAFARI-2000) experiment. *J Geophys Res*, **108**, 8501. 26, 81, 87

Myhre, G., Shindell, D., Bréon, F.M., Collins, W., Fuglestvedt, J., Huang, J., Koch, D., Lamarque, J.F., Lee, D., Mendoza, B., Nakajima, T., Robock, A., Stephens, G., Takemura, T. & Zhang, H. (2013). Anthropogenic and natural radiative forcing. In *Climate Change 2013: The Physical Science Basis. Contribution of Working Group I to the Fifth Assessment Report of the Intergovernmental Panel on Climate Change*, Cambridge University Press. 1, 7

Nair, U.S., Mcnider, R., Patadia, F., Christopher, S.A. & Fuller, K. (2011). Sensitivity of nocturnal boundary layer temperature to tropospheric aerosol surface radiative forcing under clear sky conditions. *J Geophys Res*, **116**, 1–16. 95

Nemitz, E. & Sutton, M.A. (2004). Gas-particle interactions above a Dutch heathland: III. Modelling the influence of the NH3-HNO3-NH4NO3 equilibrium on size-segregated particle fluxes. *Atmos. Chem. Phys.*, **4**, 1025–1045. 102, 103, 105, 114, 116, 121

Nemitz, E., Sutton, M.A., Wyers, G.P. & Jongejan, P.A.C. (2004). Gas-particle interactions above a Dutch heathland: I. Surface exchange fluxes of NH3, SO2, HNO3 and HCl. *Atmos. Chem. Phys.*, **4**, 989–1005. 103, 115

Nenes, A., Pandis, S.N. & Pilinis, C. (1998). Isorropia: A new thermodynamic equilibrium model for multiphase multicomponent inorganic aerosols. *Aquatic Geochemistry*, **4**, 123–152. 8, 104, 105

Neuman, J.A., Nowak, J.B., Brock, C.A., Trainer, M., Fehsenfeld, F.C., Holloway, J.S., Hu, G., Hudson, P.K., Murphy, D.M., Jr, D.K.N., Orsini, D., Parrish, D.D., Ryerson, T.B., Sueper, D.T., Sullivan, A. & Weber, R. (2003). Variability in ammonium nitrate formation and nitric acid depletion with altitude and location over California. *Journal of Geophysical Research*, **108**. 8

Nielsen, K.P., Zhao, L., Stamnes, J.J., Stamnes, K. & Moan, J. (2006). The importance of the depth distribution of melanin in skin for {DNA} protection and other photobiological processes. *Journal of Photochemistry and Photobiology B: Biology*, **82**, 194 – 198, current {UVA} research topics. 141

Niemela, S., Raisanen, P. & Savijarvi, H. (2001). Comparison of surface radiative flux parameterizations: Part I: Longwave radiation. *Atmospheric Research*, **58**, 1 – 18. 32, 33, 38

Nieuwstadt, F.T.M. & Brost, R.A. (1986). The decay of convective turbulence. *J Atmos Sci*, **43**, 532 – 545. 49

Nieuwstadt, F.T.M. & van Dop, H.e. (1982). *Atmospheric turbulence and air pollution modelling*. D. Reidel. 121

Niyogi, D., Chang, H.I., Chen, F., Gu, L., Kumar, A., Menon, S. & Pielke, R.A. (2007). Potential impacts of aerosol land-atmosphere interactions on the indian monsoonal rainfall characteristics. *Nat Hazards*, **42**, 345–359. 1

Noh, Y., Cheon, W., Hong, S. & Raasch, S. (2003). Improvement of the k-profile model for the planetary boundary layer based on large eddy simulation data. *Boundary-Layer Meteorology*, **107**, 401–427. 109

Noilhan, J. & Planton, S. (1989). A simple Parameterization of Land Surface Processes for Meteorological Models. *Monthly Weather Review*, **117**, 536–549. 77

Oakes, J.M., Breen, E.C., Scadeng, M., Tchantchou, G.S. & Darquenne, C. (2014). Mri-based measurements of aerosol deposition in the lung of healthy and elastase-treated rats. *Journal of Applied Physiology*, **116**, 1561–1568. 1

Oberdorster, G., Maynard, A., Donaldson, K., Castranova, V., Fitzpatrick, J., Ausman, K., Carter, J., Karn, B., Kreyling, W., Lai, D., Olin, S., Monteiro-Riviere, N., Warheit, D., Yang, H. & report from the ILSI Research Foundation/Risk Science Institute Nanomaterial Toxicity Screening Working Group, A. (2005). Principles for characterizing the potential human health effects from exposure to nanomaterials: elements of a screening strategy. *Particle and Fibre Toxicology*, **2**, 8. 1

Offerle, B., Grimmond, C.S.B. & Oke, T.R. (2003). Parameterization of net all-wave radiation for urban areas. *J. Appl. Meteor.*, **42**, 1157–1173. 38

Ohmura, A. (2001). Physical basis for the temperature-based melt-index method. *J. Appl. Meteor.*, **40**, 753–761. 32

Oliveira, A.P., Machado, A.J., Escobedo, J.F. & Soares, J. (2002). Diurnal evolution of solar radiation at the surface in the city of Sao Paulo: seasonal variation and modeling. *Theoretical and Applied Climatology*, **71**, 231–249. 5, 33, 140

Ouwersloot, H.G., Vilà-Guerau de Arellano, J., van Heerwaarden, C.C., Ganzeveld, L.N., Krol, M.C. & Lelieveld, J. (2011). On the segregation of chemical species in a clear boundary layer over heterogeneous land surfaces. *Atmos. Chem. Phys.*, **11**, 10681–10704. 136

Ouwersloot, H.G., de Arellano, J.V., H. van Stratum, B.J., Krol, M.C. & Lelieveld, J. (2013). Quantifying the transport of subcloud layer reactants by shallow cumulus clouds over the amazon. *Journal of Geophysical Research: Atmospheres*, **118**, 13,041–13,059. 9

Paasonen, P., Asmi, A., Petäjä, T., Kajos, M.K., Äijälä, M., Junninen, H., Holst, T., Abbatt, J.P.D., Arneth, A., Birmili, W., van der Gon, H.D., Hamed, A., Hoffer, A., Laakso, L., Laaksonen, A., Richard Leaitch, W., Plass-Dülmer, C., Pryor, S.C., Räisänen, P., Swietlicki, E., Wiedensohler, A., Worsnop, D.R., Kerminen, V.M. & Kulmala, M. (2013). Warming-induced increase in aerosol number concentration likely to moderate climate change. *Nature Geoscience*, **6**, 438–442. 74

Painemal, D. & Zuidema, P. (2011). Assessment of modis cloud effective radius and optical thickness retrievals over the southeast pacific with vocals-rex in situ measurements. *Journal of Geophysical Research: Atmospheres*, **116**, n/a–n/a. 141

Palmer, J. & Bass, M.e. (1994). *Handbook of Optics: The Measurement of Transmission, Absorption, Emission and Reflection. 2nd Ed.*. McGraw-Hill. 20, 21

Patton, E.G., Sullivan, P.P. & Moeng, C.H. (2005). The influence of idealized heterogeneity on wet and dry planetary boundary layers coupled to the land surface. *J. Atmos. Sci.*, **62**, 2078–2097. 136

Payne, R.E. & Anderson, S.P. (1999). A New Look at Calibration and Use of Eppley Precision Infrared Radiometers. Part II: Calibration and Use of the Woods Hole Oceanographic Institution Improved Meteorology Precision Infrared Radiometer. *Journal of Atmospheric and Oceanic Technology*, **16**, 739–751. 38

Penner, J., Charlson, R., Schwartz, S., Hales, J., Launiainen, S., Travis, L., Leifer, R., Novakov, T., Ogren, J. & Radke, L. (1994). Quantifying and minimizing uncertainty of climate forcing by anthropogenic aerosols. *Bull. Amer. Meteor. Soc.*, **75**, 375–400. 89

Petersen, A.C. & Holtslag, A. (1999). A first-order closure for covariances and fluxes of reactive species in the convective boundary layer. *J. Appl. Meteor.*, **38**, 1758–1776. 121

Philipona, R., Dutton, E.G., Stoffel, T., Michalsky, J., Reda, I., Stifter, A., Wendung, P., Wood, N., Clough, S.A., Mlawer, E.J., Anderson, G., Revercomb, H.E. & Shippert, T.R. (2001). Atmospheric longwave irradiance uncertainty: Pyrgeometers compared to an absolute sky-scanning radiometer, atmospheric emitted radiance interferometer, and radiative transfer model calculations. *J. Geophys. Res.*, **106**, 28129–28141. 38

Philipona, R., Durr, B. & Marty, C. (2004). Greenhouse effect and altitude gradients over the Alps - by surface longwave radiation measurements and model calculated LOR. *Theoretical and Applied Climatology*, **77**, 1–7. 38

Pinker, R.T. & Laszlo, I. (1992). Modeling surface solar irradiance for satellite applications on a global scale. *Journal of Applied Meteorology*, **31**, 194–211. 19

Pino, D. & Vilà-Guerau de Arellano, J. (2008). Effects of shear in the convective boundary layer: analysis of the turbulent kinetic energy budget. *Acta Geophys*, **56**, 167–193. 51, 63, 64

Pino, D., Jonker, H.J.J., Vilà-Guerau de Arellano, J. & Dosio, A. (2006). Role of shear and the inversion strength during sunset turbulence over land: characteristic length scales. *Bound.-Lay. Meteorol.*, **121**, 537–556. 86

Pino, D., Vilà-Guerau de Arellano, J., Peters, W., Schröter, J., van Heerwaarden, C.C. & Krol, M.C. (2012). A conceptual framework to quantify the influence of convective boundary layer development on carbon dioxide mixing ratios. *Atmos. Chem. Phys.*, **12**, 2969–2985. 79, 85

Poulos, G.S., Blumen, W., Fritts, D.C., Lundquist, J.K., Sun, J., Burns, S.P., Nappo, C., Banta, R., Newsom, R., Cuxart, J., Terradellas, E., Balsley, B. & Jensen, M. (2002). CASES-99: A comprehensive investigation of the stable nocturnal boundary layer. *Bulletin of the American Meteorological Society*, **83**, 555–581. 140

Povey, A.C., Grainger, R.G., Peters, D.M. & Agnew, J.L. (2014). Retrieval of aerosol backscatter, extinction, and lidar ratio from raman lidar with optimal estimation. *Atmospheric Measurement Techniques*, **7**, 757–776. 141

Prata, A.J. (1996). A new long-wave formula for estimating downward clear-sky radiation at the surface. *Quarterly Journal of the Royal Meteorological Society*, **122**, 1127–1151. 32, 38

Priemus, H. & Schutte-Postma, E. (2009). Notes on the particulate matter standards in the european union and the netherlands. *Int J Environ Res Public Health*, **6**, 1155–1173. 36

Quijano, A.L., Sokolik, I.N. & Toon, O.B. (2000). Radiative heating rates and direct radiative forcing by mineral dust in cloudy atmospheric conditions. *J Geophys Res*, **105**, 12207–12219. 9, 48

Raga, G., Castro, T. & Baumgardner, D. (2001). The impact of megacity pollution on local climate and implications for the regional environment: Mexico City. *Atmos Environ*, **35**, 1805–1811. 9, 10, 12, 48, 56, 58, 60, 61

Ramanathan, V. (2001). Aerosols, Climate, and the Hydrological Cycle. *Science*, **294**, 2119–2124. 2

Ramanathan, V., Crutzen, P.J., Lelieveld, J., Mitra, A.P., Althausen, D., Anderson, J., Andreae, M.O., Cantrell, W., Cass, G.R., Chung, C.E., Clarke, A.D., Coakley, J.A., Collins, W.D., Conant, W.C., Dulac, F., Heintzenberg, J., Heymsfield, A.J., Holben, B., Howell, S., Hudson, J., Jayaraman, A., Kiehl, J.T., Krishnamurti, T.N., Lubin, D., McFarquhar, G., Novakov, T., Ogren, J.A., Podgorny, I.A., Prather, K., Priestley, K., Prospero, J.M., Quinn, P.K., Rajeev, K., Rasch, P., Rupert, S., Sadourny, R., Satheesh, S.K., Shaw, G.E., Sheridan, P. & Valero, F.P.J. (2001). Indian ocean experiment: An integrated analysis of the climate forcing and effects of the great indo-asian haze. *Journal of Geophysical Research: Atmospheres*, **106**, 28371–28398. 7, 28

Raut, J.C. & Chazette, P. (2008). Radiative budget in the presence of multi-layered aerosol structures in the framework of AMMA SOP-0. *Atmospheric Chemistry and Physics Discussions*, **8**, 12461–12528. 74

Riemer, N., Vogel, H., Vogel, B. & Fiedler, F. (2003). Modeling aerosols on the mesoscale-y: Treatment of soot aerosol and its radiative effects. *Journal of Geophysical Research*, **108**. 10

Rodhe, H., Persson, C. & Akesson, O. (1972). An investigation into regional transport of soot and sulfate aerosols. *Atmospheric Environment (1967)*, **6**, 675–693. 3

Roelofs, G.J. & Jongen, S. (2004). A model study of the influence of aerosol size and chemical properties on precipitation formation in warm clouds. *Journal of Geophysical Research: Atmospheres*, **109**. 3

Rosenfeld, D. & Feingold, G. (2003). Explanation of discrepancies among satellite observations of the aerosol indirect effects. *Geophysical Research Letters*, **30**. 142

Sakaeda, N., Wood, R. & Rasch, P.J. (2011). Direct and semidirect aerosol effects of southern African biomass burning aerosol. *J Geophys Res*, **116**, D12205. 74, 88

Saleh, R., Donahue, N.M. & Robinson, A.L. (2013). Time scales for gas-particle partitioning equilibration of secondary organic aerosol formed from alpha-pinene ozonolysis. *Environmental Science & Technology*, **47**, 5588–5594. 103, 107, 109

Sanchez-Ccoyllo, O.R., Ynoue, R.Y., Martins, L.D., Astolfo, R., Miranda, R.M., Freitas, E.D., Borges, A.S., Fornaro, A., Freitas, H., Moreira, A. & Andrade, M.F. (2008). Vehicular particulate matter emissions in road tunnels in Sao Paulo, Brazil. *Environmental Monitoring and Assessment*, **149**, 241–249. 33

Satheesh, S. & Ramanathan, V. (2000). Large differences in tropical aerosol forcing at the top of the atmosphere and Earth's surface. *Nature*, **405**, 60–63. 48

Schaap, M., Apituley, A., Timmermans, R.M.A., Koelemeijer, R.B.A. & Leeuw, G.D. (2009). Exploring the relation between aerosol optical depth and PM 2.5 at Cabauw, the Netherlands. *Atmos. Chem. Phys.*, **9**, 909–925. 79

Schaap, M., Weijers, E., Mooibroek, D., Nguyen, L. & Hoogerbrugge, R. (2010). Composition and origin of Particulate Matter in the Netherlands: results from the Dutch Research Programme on Particulate Matter. Tech. rep., PBL Netherlands Environmental Assessment Agency. 3

Schepanski, K., Tegen, I. & Macke, A. (2009). Saharan dust transport and deposition towards the tropical northern atlantic. *Atmospheric Chemistry and Physics*, **9**, 1173–1189. 2

Schumann, U. (1989). Large-eddy simulation of turbulent diffusion with chemical reactions in the convective boundary layer. *Atmos Environ*, **23**, 1713–1727. 121, 125

Seinfeld, J. & Pandis, S. (2006). *Atmospheric Chemistry and Physics: From Air Pollution to Climate Change: 2nd Ed.*. A Wiley-Interscience. 18, 22

Shettle, E. & Weinman, J. (1970). The transfer of solar irradiance through inhomogeneous turbid atmospheres evaluated by eddington's approximation. *J Atmos Sci*, **27**, 1048–1055. 12, 17, 22, 23, 24, 25, 26, 76

Shiraiwa, M. & Seinfeld, J.H. (2012). Equilibration timescale of atmospheric secondary organic aerosol partitioning. *Geophysical Research Letters*, **39**. 103, 107

Singh, S., Soni, K., Bano, T., Tanwar, R.S., Nath, S. & Arya, B.C. (2010). Clear-sky direct aerosol radiative forcing variations over mega-city Delhi. *Annales Geophysicae*, **28**, 1157–1166. 75

Skjoth, C.A. & Geels, C. (2013). The effect of climate and climate change on ammonia emissions in europe. *Atmos. Chem. Phys.*, **13**, 117–128. 139

Slinn, S.A. & Slinn, W. (1980). Predictions for particle deposition on natural waters. *Atmos. Environ.*, **14**, 1013–1016. 104, 105

Solomon, S., Schmeltekopf, A.L. & Sanders, R.W. (1987). On the interpretation of zenith sky absorption measurements. *J. Geophys. Res.*, **92**, 8311. 29

Staley, D.O. & Jurica, G.M. (1972). Effective atmospheric emissivity under clear skies. *J. Appl. Meteor.*, **11**, 349–356. 33

Stamnes, K., Tsay, S., Wiscombe, W.J., & Laszlo, I. (2000). DISORT, a general-purpose Fortran program for discrete-ordinate-method radiative transfer in scattering and emitting layered media: documentation of methodology. Tech. rep., Dept. of Physics and Engineering Physic, Stevens Institute of Technology. 26

Stevens, B. & Feingold, G. (2009). Untangling aerosol effects on clouds and precipitation in a buffered system. *Nature*, **461**, 607–613. 2, 8, 142

Stier, P., Seinfeld, J.H., Kinne, S. & Boucher, O. (2007). Aerosol absorption and radiative forcing. *Atmosphere*, **7**, 5237–5261. 74

Stockwell, W. & Goliff, W. (2004). Measurement of actinic flux and calculation of photolysis rate parameters for the central California Ozone study. *Atmos Environ*, **38**, 5169–5177. 50

Stull, R.B. (1988). *An Introduction to Boundary Layer Meteorology*. Kluwer Academic Publishers, 680 pp. 4, 5, 26, 49, 50, 53, 66, 67, 76, 77

Sullivan, P., McWilliams, J. & Moeng, C.H. (1994). A subgrid scale model for large-eddy simulation of planetary boundary-layer flows. *Boundary-Layer Meteorol*, **71**, 276–276. 49, 52

Sullivan, P.P., Moeng, C.H., Stevens, B., Lenschow, D.H. & Mayor, S.D. (1998). Structure of the entrainment zone capping the convective atmospheric boundary layer. *J Atmos Sci*, **55**, 3042–3064. 51, 52, 58, 63, 64, 65

Swap, R., Garstang, M., Greco, S., Talbot, R. & Kallberg, P. (1992). Saharan dust in the Amazon Basin. *Tellus B*, **44**, 133–149. 2

Swinbank, W.C. (1963). Long-wave radiation from clear skies. *Q.J Royal Met. Soc.*, **89**, 339–348. 32

Swinehart, D.F. (1962). The beer-lambert law. *Journal of Chemical Education*, **39**, 333. 20

Takemura, T., Nakajima, T., Dubovik, O., Holben, B. & Kinne, S. (2002). Single-Scattering Albedo and Radiative Forcing of Various Aerosol Species with a Global Three-Dimensional Model. *Journal of Climate*, **15**, 333–352. 75

Tegen, I., Lacis, A.A. & Fung, I. (1996). The influence on climate forcing of mineral aerosols from disturbed soils. *Nature*, **380**, 419–422. 33, 134

ten Brink, H., Otjes, R., Jongejan, P. & Slanina, S. (2007). An instrument for semi-continuous monitoring of the size-distribution of nitrate, ammonium, sulphate and chloride in aerosol. *Atmospheric Environment*, **41**, 2768 – 2779. 106

Tennekes, H. (1973). A model for the dynamics of the inversion above a convective boundary layer. *J Atmos Sci*, **30**, 558–567. 11, 12, 51

Thomas, R.M., Trebs, I., Otjes, R., Jongejan, P.A.C., Ten Brink, H., Phillips, G., Kortner, M., Meixner, F.X. & Nemitz, E. (2009). An automated analyzer to measure surface-atmosphere exchange fluxes of water soluble inorganic aerosol compounds and reactive trace gases. *Environmental Science and Technology*, **43**, 1412–1418. 106

Toledano, C., Cachorro, V.E., Berjon, A., de Frutos, A.M., Sorribas, M., de la Morena, B.A. & Goloub, P. (2007). Aerosol optical depth and Angstrom exponent climatology at El Arenosillo AERONET site (Huelva, Spain). *Q.J.R. Meteorol. Soc.*, **133**, 795–807. 27

Tripathi, S.N., Dey, S., Tare, V. & Satheesh, S. (2005). Aerosol black Carbon radiative forcing at an industrial city in northern India. *Geophys Res Lett*, **32**, L08802. 7, 21, 48, 58, 74, 75, 81, 86, 91

Troen, I. & Mahrt, L. (1986). A simple model of the atmospheric boundary layer; sensitivity to surface evaporation. *Boundary-Layer Meteorology*, **37**, 129–148. 109

Tunved, P., Partridge, D.G. & Korhonen, H. (2010). New trajectory-driven aerosol and chemical process model Chemical and Aerosol Lagrangian Model (CALM). *Atmospheric Chemistry and Physics*, **10**, 10161–10185. 74

Twine, T., Kustas, W., Norman, J., Cook, D., Houser, P., Meyers, T., Prueger, J., Starks, P. & Wesely, M. (2000). Correcting eddy-covariance flux underestimates over a grassland. *Agricultural and Forest Meteorology*, **103**, 279–300. 83

Uijlenhoet, R. & Sempere Torres, D. (2006). Measurement and parameterization of rainfall microstructure. *Journal of Hydrology*, **328**, 1–7. 2

Ulden, A.P.V. & Holtslag, A.A.M. (1985). Estimation of atmospheric boundary layer parameters for diffusion applications. *J. Climate Appl. Meteor.*, **24**, 1196–1207. 39

van Beelen, A.J., Roelofs, G.J.H., Hasekamp, O.P., Henzing, J.S. & Röckmann, T. (2014). Estimation of aerosol water and chemical composition from AERONET Sun-Sky radiometer measurements at Cabauw, the Netherlands. *Atmospheric Chemistry and Physics*, **14**, 5969–5987. 78

van Heerwaarden, C.C. & Vilà-Guerau de Arellano, J. (2008). Relative humidity as an indicator for cloud formation over heterogeneous land surfaces. *J. Atmos. Sci.*, **65**, 3263–3277. 18

van Heerwaarden, C.C., Vilà-Guerau de Arellano, J., Moene, A.F. & Holtslag, A.A.M. (2009). Interactions between dry-air entrainment , surface evaporation and convective boundary-layer development. *Quart. J. R. Met. Soc.*, **1291**, 1277–1291. 11, 32

van Heerwaarden, C.C., Vilà-Guerau de Arellano, J., Gounou, A., Guichard, F. & Couvreux, F. (2010). Understanding the daily cycle of evapotranspiration: A method to quantify the influence of forcings and feedbacks. *Journal of Hydrometeorology*, **11**, 1405–1422. 76, 77, 78, 83, 104

Van Zanten, M.C., Duynkerke, P.G. & Cuijpers, J.W.M. (1999). Entrainment parameterization in convective boundary layers. *J Atmos Sci*, **56**, 813–828. 51, 63

Velasco, P. (2005). Characterization of Ambient PM10 and PM2.5 in California. Tech. rep., California Environmental Protection Agency. 33

Velders, G.J.M., Geilenkirchen, G.P. & Lange, R.D. (2011). Higher than expected NOx emission from trucks may affect attainability of NO2 limit values in the Netherlands. *Atmospheric Environment*, **45**, 3025–3033. 108

Velthof, G.L., Bruggen, C.V., Groenestein, C.M., Haan, B.J.D., Hoogeveen, M.W. & Huijsmans, J.F.M. (2012). A model for inventory of ammonia emissions from agriculture in the Netherlands. *Atmospheric Environment*, **46**, 248–255. 111

Venkatram, A. & Viskanta, R. (1977). Effects of aerosol-induced heating on the convective boundary layer. *J Atmos Sci*, **34**, 1918–1932. 10, 74, 75

Vermeulen, A.T., Hensen, A., Popa, M.E., van den Bulk, W.C.M. & Jongejan, P.A.C. (2011). Greenhouse gas observations from cabauw tall tower (1992-2010). *Atmospheric Measurement Techniques*, **4**, 617–644. 108

Verver, G. (1994). Comment on "A modified K model for chemically reactive species in the planetary boundary laye" by Fujihiro Hamba. *Journal of Geophysical Research*, **99**, 21–23. 116, 118, 122, 124

Vilà-Guerau de Arellano, J. & Cuijpers, J.W.M. (2000). The chemistry of a dry cloud: The effects of radiation and turbulence. *J Atmos Sci*, **57**, 1573–1584. 51

Vilà-Guerau de Arellano, J. & Duynkerke, P. (1992). Influence of Chemistry on the flux gradient relationships for the NO-O3-NO2 system. *Boundary-Layer Meteorology*, **61**, 375–387. 103, 116, 117, 121

Vilà-Guerau de Arellano, J. & Duynkerke, P.G. (1995). Atmospheric surface layer similarity theory applied to chemically reactive species. *J. Geophys. Res.*, **100**, 1397–1408. 9, 103, 122

Vilà-Guerau de Arellano, J., Dosio, A., Vinuesa, J.F., Holtslag, A.A.M. & Galmarini, S. (2004). The dispersion of chemically reactive species in the atmospheric boundary layer. *Meteorol. Atmos. Phys.*, **87**, 23–38. 120

Vilà-Guerau de Arellano, J., Kim, S.W., Barth, M.C. & Patton, E.G. (2005). Transport and chemical transformations influenced by shallow cumulus over land. *Atmos. Chem. Phys.*, **5**, 3219–3231. 102

Vilà-Guerau de Arellano, J., Patton, E.G., Karl, T., van den Dries, K., Barth, M.C. & Orlando, J.J. (2011). The role of boundary layer dynamics on the diurnal evolution of isoprene and the hydroxyl radical over tropical forests. *Journal of Geophysical Research: Atmospheres*, **116**. 8, 11, 104

Vinuesa, J.F. & Vilà-Guerau de Arellano, J. (2003). Fluxes and (co-)variances of reacting scalars in the convective boundary layer. *Tellus B*, **55**, 935–949. 102, 103, 109, 116, 122, 123

Voulgarakis, A., Wild, O., Savage, N.H., Carver, G.D. & Pyle, J.A. (2009). Clouds, photolysis and regional tropospheric ozone budgets. *Atmospheric Chemistry and Physics*, **9**, 8235–8246. 142

Wallace, J.M. & Hobbs, P.V. (2006). *Atmospheric Science: An introductory Survey (2nd Ed.)*. Elsevier 483 pp. 20, 21, 30, 31

Wallin, J.E., Segerström, U., Rosenhall, L., Bergmann, E. & Hjelmroos, M. (1991). Allergic symptoms caused by long-distance transported birch pollen. *Grana*, **30**, 265–268. 1

Wang, P., Knap, W.H., Kuipers Munneke, P. & Stammes, P. (2009). Clear-sky shortwave radiative closure for the Cabauw Baseline Surface Radiation Network site, Netherlands. *J Geophys Res*, **114**, D14206. 7, 74, 75, 78, 83, 106

Wilks, D. (2011). *Statistical Methods in the Atmospheric Sciences*. Academic Press 704 pp. 37

Willmott, C.J. (1982). Some Comments on the Evaluation of Model Performance. *Bulletin of the American Meteorological Society*, **63**, 1309–1313. 39

Wolff, V., Trebs, I., Foken, T. & Meixner, F.X. (2010). Exchange of reactive nitrogen compounds : concentrations and fluxes of total ammonium and total nitrate above a spruce canopy. *Biogeosciences*, **7**, 1729–1744. 102, 115, 121

Wong, D.C., Pleim, J., Mathur, R., Binkowski, F., Otte, T., Gilliam, R., Pouliot, G., Xiu, A., Young, J.O. & Kang, D. (2012). WRF-CMAQ two-way coupled system with aerosol feedback: software development and preliminary results. *Geoscientific Model Dev*, **5**, 299–312. 10, 49, 57, 60, 74, 90

Wyngaard, J.C. (2010). *Turbulence in the Atmosphere*. Cambridge University Press, U.S.A, 393 pp. 9, 119, 120

Xue, H. & Feingold, G. (2006). Large-eddy simulations of trade wind cumuli: Investigation of aerosol indirect effects. *Journal of the Atmospheric Sciences*, **63**, 1605–1622. 142

Yu, H., Liu, S.C. & Dickinson, R.E. (2002). Radiative effects of aerosols on the evolution of the atmospheric boundary layer. *J Geophys Res*, **107**. 5, 6, 7, 10, 48, 49, 56, 60, 75, 90, 94, 138

Yu, S. & Zhang, Y. (2011). An Examination of the Effects of Aerosol Chemical Composition and Size on Radiative Properties of Multi-Component Aerosols. *Atmospheric and Climate Sciences*, **01**, 19–32. 74

Zdunkowski, W., Welch, R. & Paegle, J. (1976). One-dimensional numerical simulation of the effects of air pollution on the planetary boundary layer. *J Atmos Sci*, **33**, 2399–2414. 9, 48, 61

Zhang, J., Gong, W., Leaitch, W.R. & Strapp, J.W. (2007). Evaluation of modeled cloud properties against aircraft observations for air quality applications. *Journal of Geophysical Research: Atmospheres*, **112**. 141

Zhang, Y., Wen, X.Y. & Jang, C. (2010). Simulating chemistry-aerosol-clouds-radiations-climate feedbacks over the continental U.S. using the online-coupled Weather Research Forecasting Model with chemistry (WRF/Chem). *Atmospheric Environment*, **44**, 3568–3582. 4, 8, 74, 75

Zhou, Y. & Savijärvi, H. (2014). The effect of aerosols on long wave radiation and global warming. *Atmospheric Research*, **135–136**, 102 – 111. 134

Zilitinkevich, S., Elperin, T., Kleeorin, N. & Rogachevskii, I. (2007). Energy- and flux-budget (EFB) turbulence closure model for stably stratified flows. part I: steady-state, homogeneous regimes. *Boundary-Layer Meteorol*, **125**, 167–191. 66

Zilitinkevich, S.S., Elperin, T., Kleeorin, N., Rogachevskii, I., Esau, I., Mauritsen, T. & Miles, M.W. (2008). Turbulence energetics in stably stratified geophysical flows : Strong and weak mixing regimes. *Q J R Meteorol Soc*, **134**, 793–799. 66

Zubler, E.M., Folini, D., Lohmann, U., Lüthi, D., Muhlbauer, a., Pousse-Nottelmann, S., Schär, C. & Wild, M. (2011a). Implementation and evaluation of aerosol and cloud microphysics in a regional climate model. *J Geophys Res*, **116**, D02211. 74

Zubler, E.M., Lohmann, U., Lüthi, D. & Schär, C. (2011b). Intercomparison of aerosol climatologies for use in a regional climate model over Europe. *Geophysical Research Letters*, **38**. 1, 81

Samenvatting

Dit hoofdstuk bevat een overzicht van de belangrijkste resultaten in dit proefschrift.

De belangrijkste conclusie van dit proefschrift is dat aerosolen essentieel zijn voor een accurate beschrijving van de dynamica van de convectieve grenslaag (CBL) en de processen aan het landoppervlak. We zijn tot deze conclusie gekomen op basis van een systematische studie van het gekoppelde land-CBL systeem. Voor deze studie maakten we gebruik van een hiërarchie aan modellen, variërend van een turbulentie-oplossend model (large-eddy simulatie, LES) tot modellen die de turbulentie niet oplossen, maar parametriseren (menglaagmodel en kolomsmodel). Naast de numerieke modellen hebben we een complete observationele dataset gebruikt voor het ontwerp en de evaluatie van onze numerieke studies.

Hoofdstuk 2 beschrijft de korte golf (SW) stralingscode die gebruikt wordt in Hoofdstukken 4 en 5. We laten zien dat, ondanks de versimpelde wijze waarop wij inkomende zonnestraling en haar interactie met aerosolen behandelen, onze stralingscode grotendeels dezelfde resultaten geeft als een complexere code, zelfs voor extreme concentraties aerosolen. Onze modelresultaten reproduceren waarnemingen van directe en diffuse straling aan het landoppervlak, hetgeen wij laten zien in Hoofdstuk 4.

Wij laten zien dat aerosolen niet van belang zijn voor de bepaling van de inkomende langgolvige straling aan het landoppervlak. We concluderen dat de formule van Brunt, die alleen van de screenlevel temperatuur en dampspanning afhangt, de meest adequate methode is om de inkomende langgolvige straling aan het landoppervlak te benaderen.

In **Hoofdstuk 3** hebben we onderzocht hoe warmteabsorptie door aerosolen de dynamica van een geïdealiseerde CBL met constante fluxen aan het landoppervlak beïnvloedt. We vinden dat de structuur en de evolutie van de CBL beïnvloed worden door de verticale verdeling van de aerosolen. Aerosolen beïnvloeden de uitwisseling van warmte tussen de CBL en de vrije atmosfeer (i) door de reductie van fluxen aan het landoppervlak door middel van de uitdoving van kortgolvige straling en (ii) door

het dieper maken van de entrainment zone. We benadrukken het belang van modellen met een hoge verticale resolutie in het correct representeren van de effecten van de absorptie van straling door aerosolen, met name in de entertainment zone. We laten zien dat, naast de eigenschappen van de aerosolen zelf, hun verticale verdeling van belang is om de evolutie van de CBL diepte en de dynamica van het bovenste deel van de CBL te beschrijven. Om de analyse van onze LES resultaten kracht bij te zetten, hebben we een menglaagmodel (MXL) gebruikt om de diepte van de grenslaag en de grootte van de temperatuursprong in de inversielaag te berekenen. Ondanks de eenvoud van dit model komen de resultaten ervan goed overeen met de LES resultaten.

In **Hoofdstuk 4** bouwen we verder op de resultaten van de prototype-experimenten die we in Hoofdstuk 3 hebben uitgevoerd. Hier kwantificeren we de effecten van lichtverstrooiing door aerosolen en de invloed van absorptie van kortgolvige straling op de energiebalans aan het landoppervlak en de CBL dynamica. Hiervoor hebben we ons LES model gekoppeld aan (i) een landoppervlaktemodel en (ii) een breedband SW stralingsmodel (beschreven in Hoofdstuk 2). We hebben de resultaten succesvol gevalideerd met behulp van meetdata van (thermo)dynamische variabelen en de eigenschappen van aerosolen, als waargenomen in Cabauw (Nederland). Onze LES-resultaten laten zien dat voor Cabauw (over nat gras) de aerosolen de hoeveelheid energie die het landoppervlak bereikt, maar ook de spatiële/temporele verdeling hiervan, significant beïnvloeden. Als het landoppervlak goed bewaterd is, wordt de voelbare warmteflux meer gereduceerd dan de latent warmte flux. Vanwege de goede overeenkomst tussen de resultaten van LES en MXL, hebben we MXL gebruikt om de gevoeligheid van het gekoppelde land-CBL system te verkennen voor een grote spreiding aan optische dieptes en single-scattering-albedos. Onze resultaten laten zien dat een hogere concentratie aerosolen leidt tot een groter energieverlies aan het landoppervlak. Het resultaat hiervan is een vertraging van de grenslaaggroei in de morgen en een versnelling van het inzakken van de grenslaag aan in de namiddag. We vonden ook dat de entrainment van aerosolen een belangrijke rol speelt in de dagelijkse ontwikkeling van de CBL. Een belangrijk onderdeel van Hoofdstuk 4 vormt het onderzoek naar de relatie tussen de eigenschappen van de grenslaag en die van de aerosolen. Aerosolen die sterk absorberen maken de grenslaag dieper en warmer, terwijl aerosolen die enkel verstrooien de grenslaag juist ondieper en koeler maken.

We benadrukken dat de resultaten in Hoofdstuk 4 gebruikt kunnen worden als een referentie voor numerieke schema's/modellen voor kortgolvige straling, landoppervlak en grenslaag, geïmplementeerd in meso-schaal of globale chemie transportmodellen, alsmede als een benchmark voor de koppeling tussen deze schema's.

In **Hoofdstuk 5** hebben we de complexiteit van ons land-CBL systeem opgevoerd door de formatie en het transport van ammoniumnitraat te bestuderen. Hierdoor

hebben we in ons LES model zowel straling, chemie, aerosolen en CBL dynamica gekoppeld, als ook uitwisselingsprocessen aan het land van chemische stoffen, warmte en vocht. Ons volledig gekoppelde LES-model hebben wij nogmaals succesvol geëvalueerd met observaties van chemie en aerosolen. In het bijzonder laten onze resultaten een goede match zien tussen de gesimuleerde en waargenomen verdeling van nitraat aan het landoppervlak.

We vinden dat de conversie van gas naar aerosol van nitraat leidt tot sterk niet-lineaire profielen van concentraties en turbulente fluxen van nitraat. De gesimuleerde profielen hangen met name sterk af van de tijdschaal van de conversie van gas naar aerosolen en terug. De typische tijdschaal van turbulentie in de CBL is 10 tot 20 minuten. Wanneer de tijdschaal van de conversies korter is dan deze CBL dynamica tijdschaal, vinden we dat de turbulente fluxen groter zijn en de concentratieprofielen sterker gekanteld zijn in de CBL. Deze resultaten hebben een sterke invloed op de nitraatdepositie aan het landoppervlak. Onze LES resultaten bevestigen dat de hoge depositiesnelheden voor aerosolnitraat dicht bij het landoppervlak meer door het uitgassen van aerosolnitraat komt dan door daadwerkelijke depositie.

Een belangrijk aspect dat besproken wordt in Hoofdstuk 5 is de matige representatie van het turbulente transport van nitraat in de CBL in modellen die turbulentie niet oplossen, maar parametriseren. Met een gedetailleerde analyse van de fluxbudgetvergelijking laten we zien dat de uitwisselingscoëfficiënt van warmte in ons 1D model verhoogd dient te worden om de complexe interacties tussen de gas-aerosolconversie van nitraat en de driedimensionale turbulentie in de CBL mee te nemen. De nieuwe uitwisselingscoëfficiënt verbetert ook inderdaad de match tussen de gas-aerosol verdeling van nitraat, als berekend door ons 1D model en waargenomen aan het landoppervlak.

De resultaten in dit proefschrift laten dus zien dat het belang van aerosolen op de CBL dynamica in ogenschouw genomen dient te worden. Met name beïnvloeden aerosolen fenomenen die belangrijk zijn voor de CBL ontwikkeling, namelijk straling, land-atmosfeerinteracties, chemie en (thermo)dynamica. Bovendien is de beschikbaarheid van numerieke simulaties met een hoge resolutie cruciaal om de resultaten van modellen met geparametriseerd turbulent transport te valideren en te evalueren.

Sumário

Esta seção sumariza os aspectos mais importantes discutidos nos Capítulos 2 a 5 desta tese.

A principal conclusão desta tese refere-se à necessidade de se considerar a presença dos aerossóis para descrever a dinâmica da camada limite planetária convectiva (CLP), bem como dos processos relacionados à interação superfície e CLP. Nesta tese, discute-se o sistema acoplado superfície-CLP, utilizando-se uma hierarquia de modelos numéricos, desde o modelo LES (large-eddy simulation ou simulação dos grandes turbilhões), que explicitamente resolve a campo turbulento, até modelos que parametrizam a turbulência (modelos de camada de mistura e unidimensional). Além de modelagem, utilizou-se um conjunto de observações detalhadas para caracterizar e avaliar os experimentos numéricos.

No **Capítulo 2** discutiu-se o código de transferência radiativa (Delta-Eddington) utilizado nos Capítulos 4 e 5. Constatou-se que, apesar do tratamento simplificado da radiação solar e sua interação com os aerossóis, os resultados obtidos com este código de transferência radiativa concordam com outros códigos mais sofisticados, mesmo para condições de extrema poluição. Mais ainda, os resultados reproduzem observações de radiação direta e difusa em superfície, como detalhado no Capítulo 4.

Em relação a radiação de onda longa em superfície, mostrou-se que a representação dos aerossóis não é relevante. Concluiu-se também que a formulação de Brunt, função somente da temperatura e da pressão de vapor em nível de abrigo, é a mais adequada para estimar a radiação de onda longa em superfície para os casos avaliados neste estudo.

No **Capítulo 3** investigou-se o impacto da absorção de energia pelos aerossóis na dinâmica de uma CLP idealizada, onde foram prescritos os fluxos turbulentos em superfície. Mostrou-se que a estrutura e a evolução da CLP foram influenciadas pela distribuição vertical dos aerossóis. Mais ainda, os resultados indicam que os aerossóis influenciam as trocas de calor entre a CLP e a atmosfera livre através da (i) extinção da radiação solar e consequente redução dos fluxos em superfície e (ii)

aprofundamento da camada de entranhamento. Demonstrou-se a importância do uso de modelos de alta resolução para representar o efeito da absorção de energia pelos aerossóis na dinâmica da CLP, em especial na camada de entranhamento. Além das propriedades dos aerossóis, sua distribuição vertical também é uma característica importante para a descrição da evolução da CLP, altura da camada e dinâmica de camadas superiores. Para auxiliar na análise dos campos tridimensionais do modelo LES, utilizou-se também um modelo de camada de mistura para o cálculo da altura da camada e da inversão térmica no topo da camada. Apesar da simplicidade do modelo de camada de mistura, os resultados obtidos para altura da camada e inversão térmica na camada de entranhamento foram compatíveis com os obtidos pelo modelo LES.

Utilizando o conhecimento adquirido com os experimentos acadêmicos discutidos no Capítulo 3, no **Capítulo 4** quantificou-se os efeitos da reflexão e absorção de radiação de onda curta no balanço de energia em superfície e na dinâmica da CLP. Para este fim, acoplou-se o modelo LES e o modelo de camada de mistura a (i) um modelo de superfície e (ii) um modelo Delta-Eddington de banda larga (descrito no Capítulo 2). Validaram-se os resultados obtidos pelo LES e o modelo de camada de mistura utilizando-se observações das variáveis (termo)dinâmicas e propriedades dos aerossóis observadas em Cabauw (Holanda). Os resultados obtidos com o LES mostraram que para Cabauw (superfície gramada sem restrição hídrica) os aerossóis alteraram significativamente a magnitude da variabilidade da energia disponível em superfície e sua partição. Sem restrições hídricas, o fluxo de calor sensível foi mais intensamente reduzido se comparado com o fluxo de calor latente. Dado a concordância entre os resultados obtidos com o modelo LES e com o modelo de camada de mistura, explorou-se a sensitividade do sistema superfície-CLP à presença dos aerossóis, variando a profundidade óptica e o albedo simples utilizando o modelo de camada de mistura. Esta análise mostrou que aerossóis impõe uma restrição energética em superfície. Como resultado, verificou-se um atraso no início do crescimento da CLP durante a manhã, e um avanço em seu colapso durante a tarde. Mostrou-se também que o entranhamento dos aerossóis da camada residual noturna é importante no desenvolvimento da dinâmica da CLP durante o dia. Um aspecto importante explorado no Capítulo 4 é a investigação da resposta da dinâmica da CLP dependendo das propriedades ópticas dos aerossóis. Aerossóis altamente absortivos aprofundam e aquecem a CLP, enquanto que aerossóis refletivos reduzem a altura da camada e resfriam a CLP.

Mostrou-se que o caso apresentado no Capítulo 4 pode ser utilizado como referência para a avaliação do acoplamento e da performance de parametrizações para (i) radiação de onda curta, (ii) esquemas de solo-superfície e (iii) esquemas de camada limite, implementados em modelos de mesoescala ou modelos químicos de transporte em escala global.

No **Capítulo 5** aumentou-se a complexidade da representação do sistema superfície-CLP incluindo a formação e transporte de nitrato de amônia na CLP. Dessa maneira, acoplou-se no modelo LES: radiação, química, aerossóis, dinâmica da CLP e processos de troca (i) química e (ii) termodinâmica em superfície. Os resultados obtidos pelo modelo LES acoplado a estes módulos foram satisfatoriamente comparados com um conjunto observacional de dados de química e aerossóis na CLP. Particularmente, os resultados obtidos para nitrato estão de acordo com as observações em superfície.

Mostrou-se que a conversão de nitrato entre gás e aerossol resulta em perfis verticais de concentração e fluxo turbulento de nitrato não-lineares. Mais ainda, a forma desses perfis verticais depende da escala temporal da conversão entre gás e aerossol. Destaca-se que a escala temporal típica dos grandes turbilhões na atmosfera é de aproximadamente 10-20 minutos. Para escalas temporais de conversão de nitrato entre gás e aerossol mais curtas que a escala dos grandes turbilhões, observou-se que os perfis verticais dos fluxos turbulentos são mais intensos bem como o gradiente vertical de concentração na CLP. Esses resultados têm um impacto significativo na compreensão da deposição de nitrato em superfície. Os resultados obtidos com o modelo LES confirmaram que as altas velocidades de deposição para nitrato próximo a superfície são, na verdade, devidas à evaporação do nitrato, ao invés de deposição, como sugerido em diversos estudos observacionais.

Um dos aspectos discutidos no Capítulo 5 é a inabilidade de modelos numéricos que parametrizam turbulência de resolver o transporte de nitrato na CLP. Baseado na análise da equação do balanço do fluxo vertical de nitrato, mostrou-se que o valor do coeficiente de troca de calor utilizado no modelo unidimensional teve que ser aumentado para considerar-se adequadamente as interações entre nitrato, nas formas de gás e aerossol, e o caráter tridimensional da turbulência da CLP. De fato, o novo coeficiente de troca turbulenta melhorou a comparação entre os campos de nitrato (para gás e aerossol) calculados pelo modelo unidimensional e obtidos através de observações.

Os resultados discutidos nesta tese demonstram a necessidade de considerar a influência dos aerossóis na dinâmica da CLP. Em específico, aerossóis influenciam a fenomenologia da CLP, nominalmente radiação, interação superfície-atmosfera, química e termodinâmica. Mais ainda, a disponibilidade de observações ou de simulações de alta resolução é crucial para a validação de resultados obtidos por modelos numéricos que não resolvem explicitamente o fenômeno da turbulência na CLP.

Acknowledgments

The whole process of making and publishing a PhD thesis resembles me composing and publishing a music album. Each Chapter is a new and original song never heard before. All the figures, derivations and explanations, meaning the different instruments, voices and sounds, are carefully layered to amuse the ears. Similarly, after writing every "new song" you go on tour, presenting it to different audiences, making sure they will understand - and appreciate - both your music and your lyrics.

As every singer needs his/her "Brian Epstein" to succeed, a PhD candidate needs good guidance. Therefore, I gratefully thank my direct supervisor Dr. Jordi Vilà-Guerau de Arellano. Jordi, I am most grateful to you since you were *always promptly there* when I needed to discuss science: from minor textual details to major structural aspects. I explicitly want to tell you that this work sounds like it does, to a great extend, because of your critique and comments. You are also an excellent teacher and a source of inspiration when it comes to education. I thoroughly enjoyed sharing the boundary-layer turbulence course with you the last two years.

I would also like to thank my first promotor, Prof. Maarten Krol, a man constantly looking for the perfect beat. Maarten, I spent undoubtedly the most unpleasant and productive times of my PhD research with you. Your razor-sharp attitude elevated the motto "improving the paper" above any social constraint, such as feelings or gentleness. That said, I want to stress that I learned a great deal about science and about scientific writing with you. I also want to thank you for your critical remarks, and for still being able to take off your "professor shoes" and help us PhD students with mundane, everyday issues, like debugging a code or eating *speculaas* cookies. I am also grateful to my second promotor, Prof. Bert Holtslag, for giving me the ticket to ride on this magical mystery tour. We met in Rio de Janeiro in 2009 during a summer school and thanks to you I could come to the Netherlands and meet Jordi a couple of months later.

Since this is a permanent record, I have allowed myself to be a little more verbose than perhaps necessary.

During my years as a PhD candidate, I also found some good friends in the Netherlands. I am especially happy to have two of them as my paranymphs. Chiel, it was very nice to discuss a broad variety of topics with you, ranging from science and literature to Branco's free-kick skills. Besides the nice talks, I also had a great time playing some music with you. Ivar, it was great that you also joined several of those sessions with your electric guitar. It certainly gave a more rock 'n' roll feeling to the songs we chose to cover. We also had very nice talks about our research and about how to move on after the PhD years, and I have always appreciated your honest opinion. I am also glad that I could join some of the nice movie nights you co-organized.

I also want to thank Joel Schröter for a friendship that I deeply cherish. Joel, know that your passion for science was always an example to me. It was also nice to learn and discuss *Geopolitik* with you. I should also say *obrigado* to Ruud for joining most of these talks, and for the opportunity to listen to his refined collection of vinyl records. Natalie, I also had a nice time sharing three offices with you, or being at your place, just talking and listening to Dean Martin, or watching Monty-Python. Marina, it was so cool to play guitar alongside your singing. I hope you enjoyed that as much as I did. Michał, I think we have quite some good stories to remember, either in Cyprus or during the BBOS symposia. Alba, Denica, Folmer, Ingrid, and Marie, the 3pm coffee breaks with you were always a lot of fun. I wish you all the best in finishing your PhDs. Marie, I will not forget how much we laughed with the *ze Frènch*, uhm?

Joost, thanks for your insightful comments about bitter misery and aerosol formation. It was also a great honor to be your paranymph. Huug, thanks for the friendship, discussions about LES and mixed-layer theory, as well as all the help with Gitorious. I also want to thank you and Ivar for the very tuneful teamwork during the organization of the "Bridging the gap" conference in 2012. Something that could potentially be a stressful activity was actually a very pleasant task. Thanks to Folkert and Michiel of the Mill for the very nice conversations and the informative AQ meetings, organized by Prof. Wouter Peters. Wouter, thanks for all the interesting talks during lunch, and the help with Python and the Dutch translations. I'd also like to thank you for checking on me when the discussions with Maarten got too heated.

Thanks to the KNMIers: Dave Donovan, Ping Wang, Wouter Knap, Fred Bosveld, and Henk Klein Baltink for the LIDAR profiles and the CESAR/EUCAARI data set. Gert-Jan, *danke schön* for helping me with the CESAR data and with the new PhD regulations. Leo, thanks for checking my propositions for proper English, and Oscar, it was always fun to try to talk in Mexican with you. Sweet Caroline, thanks for the support with hundreds of declarations, and for always knowing the exact person to phone when needed. I also thank Kees for always being available to solve any kind

of computer issue. I also want to thank Dimitra for the nice challenge of supervising her MSc thesis. I think we both learned a good deal from it.

A Spanish invasion occurred at the MAQ during my PhD years: David, Pablo, Mariano, and Carlos, it was great to interact with you and to practice my *Portunhol*. Carla, it was nice sharing an office in Atlas with you. You also convinced me that we actually speak Brazilian in Brazil. Chiel and Ruud, thanks for the "little help" with the samenvatting, and Anneke, thanks for the very thorough parenthesis checking.

Apesar da enorme distância, algumas pessoas no Brasil foram especialmente importantes durante esses últimos anos. Primeiramente eu gostaria de agradecer aos professores Amauri Oliveira e Jacyra Soares pela excelente introdução à ciência, discussões, e a grande amizade desde que comecei a iniciação científica na USP. Eu realmente devo *muito* do que aprendi a vocês. Eu não poderia deixar de agradecer ao grande amigo Fábio e a sua esposa Letícia. Fábio, eu fico feliz que a nossa amizade desde os tempos de graduação tenha continuado por todos esses anos. Queria agradecer também à Beatriz pelos momentos que passamos juntos. Bia, o respeito e a admiração que tenho por você dizem tudo.

A música diz que "vida é o que acontece enquanto você está ocupado fazendo outros planos". Portanto eu agradeço a toda minha família por compreender minha decisão de estudar tão longe de casa. O apoio de vocês foi fundamental. Pai e mãe, obrigado pelas conversas no Skype. Sempre é muito bom vê-los e ouvi-los. Agradeço muito ao meu irmãozinho Gabriel por ser *tão legal* comigo. Gabriel e Kelly, saibam que os dias que passamos juntos na Itália e na Holanda foram muito especiais. Yvonninha e Benê, muito obrigado por tudo que vocês fazem por mim. Assim como num álbum de música, a capa de uma tese de doutorado também é fundamental. Por isso, Yvonninha, eu te agradeço pelo lindo trabalho. Basta dizer que nem na minha imaginação a capa tinha ficado tão boa. And now, I need to switch back to English to thank my *schatje* Daniëlle. Daan, having you in my life is such a joy that it's hard to put into words. Thanks for all the support and love. I am glad we are so much in tune and happy together. I also want to thank your family for accepting me so fast, and for the nice time we've spent together. I appreciate all the effort you make to communicate with me.

List of journal publications

Barbaro, E., Oliveira, A.P., Soares, J., Codato, G., Ferreira, M.J., Mlakar, P., Boznar, M.Z. & Escobedo, J.F. (2010). Observational characterization of the downward atmospheric longwave radiation at the surface in the city of Sao Paulo. *Journal of Applied Meteorology and Climatology*, **49**, 2574–2590.

Ferreira, M., Oliveira, A., Soares, J., Codato, G., **Barbaro, E.** & Escobedo, J. (2012). Radiation balance at the surface in the city of Sao Paulo, Brazil: diurnal and seasonal variations. *Theoretical and Applied Climatology*, **107**, 229–246.

Barbaro, E., Vilà-Guerau de Arellano, J., Krol, M.C. & Holtslag, A.A.M. (2013). Impacts of Aerosol Shortwave Radiation Absorption on the Dynamics of an Idealized Convective Atmospheric Boundary Layer. *Boundary-Layer Meteorology*, **148**, 31–49.

Barbaro, E., Vilà-Guerau de Arellano, J., Ouwersloot, H.G., Schroter, J.S., Donovan, D.P. & Krol, M.C. (2014). Aerosols in the convective boundary layer: Shortwave radiation effects on the coupled land-atmosphere system. *Journal of Geophysical Research: Atmospheres*, **119**, 5845–5863.

Barbaro, E., Krol, M. & Vilà-Guerau de Arellano, J. (2015). Numerical simulation of the interaction between ammonium nitrate aerosol and convective boundary-layer dynamics. *Atmospheric Environment*, **105**, 202–211.

Netherlands Research School for the
Socio-Economic and Natural Sciences of the Environment

D I P L O M A

For specialised PhD training

The Netherlands Research School for the
Socio-Economic and Natural Sciences of the Environment
(SENSE) declares that

Eduardo Wilde Barbaro

born on 16 September 1986 in São Paulo, Brazil

has successfully fulfilled all requirements of the
Educational Programme of SENSE.

Wageningen, 20 March 2015

the Chairman of the SENSE board	the SENSE Director of Education
Prof. dr. Huub Rijnaarts	Dr. Ad van Dommelen

The SENSE Research School has been accredited by the Royal Netherlands Academy of Arts and Sciences (KNAW)

KONINKLIJKE NEDERLANDSE
AKADEMIE VAN WETENSCHAPPEN

The SENSE Research School declares that **Mr Eduardo Barbaro** has successfully fulfilled all requirements of the Educational PhD Programme of SENSE with a work load of 57.6 EC, including the following activities:

SENSE PhD Courses

- Autumn School: biogeochemistry and biophysics of the lower atmosphere (2010)
- Environmental Research in Context (2011)
- Research in Context Activity: 'Co-organising PhD course Bridging the gap between atmospheric scales and developing best practices on the organisation of the course', Wageningen (2012)

Other PhD and Advanced MSc Courses

- Atmospheric Chemistry and Air Quality, Wageningen University (2011)
- Boundary-layer processes, Wageningen University (2012)
- Scientific Writing, Wageningen University (2012)

Management and Didactic Skills Training

- PhD representative at the Meteorology and Air quality group (2012)
- Co-supervision of MSc thesis entitled 'Model simulation of the morning transition effect on boundary layer dynamics and chemistry during the PEGASOS campaign in the Netherlands' (2013)
- Teaching assistance of the BSc course 'Boundary-Layer Processes' (2013-2014)
- Member of the American Meteorological Society Committee on Boundary Layers and Turbulence (2013-2014)

Selection of Oral Presentations

- *Impacts of aerosol radiation absorption on the heat budget and dynamics of the atmospheric boundary layer.* 32nd NATO/SPS International Technical Meeting on Air Pollution Modelling and its applications, 07-11 May 2012, Utrecht, The Netherlands.
- *Impact of aerosol radiation absorption on the dynamics of an atmospheric boundary layer in equilibrium.* 20th Symposium on boundary layers and turbulence, 09-13 July 2012, Boston, United States.
- *Effects of aerosols on convective boundary-layer dynamics and land-atmosphere system.* 21st Symposium on boundary layers and turbulence, 09-13 June 2014, Leeds, United Kingdom.
- *Interaction between aerosols and convective boundary-layer dynamics.* Pan-European Gas-AeroSOls-climate interaction Study (PEGASOS) 4th annual meeting, 17-18 December 2014, Athens, Greece

SENSE Coordinator PhD Education

Dr. ing. Monique Gulickx

This study was sponsored by the National Computing Facilities Foundation (NCF project SH-060) for the use of supercomputer facilities.

Financial support from Wageningen University for printing this thesis is gratefully acknowledged.